ALMA MATER STUDIORUM
UNIVERSITÀ DI BOLOGNA

DOTTORATO DI RICERCA IN

AUTOMOTIVE ENGINEERING FOR INTELLIGENT MOBILITY

Ciclo 38

Settore Concorsuale: 09/B1 - TECNOLOGIE E SISTEMI DI LAVORAZIONE

Settore Scientifico Disciplinare: ING-IND/16 - TECNOLOGIE E SISTEMI DI LAVORAZIONE

LASER CUTTING AND WELDING OF LITHIUM-ION BATTERIES FOR E- MOBILITY APPLICATIONS

Presentata da: Caterina Angeloni

Coordinatore Dottorato

Davide Moro

Supervisore

Alessandro Fortunato

Co-supervisore

Federico Poli

Erica Liverani

Esame finale anno 2026

Finanziato dall'Unione europea – Next Generation EU, Missione 4, Componente 2, Investimento 3.3 (D.M. 117/2023) CUP J33C22001350009

Preface

Batteries are the beating heart of the global energy system, empowering both transport and energy sectors. They are central to the EU's clean energy transition, industrial future and strategic autonomy. While European battery sector benefits from strong support for research and development, it still faces major challenges, particularly in supply chain geopolitical issues and labor costs. Access to batteries is crucial for ensuring the competitiveness of the automotive industry, as they are the most critical component of electric vehicles, accounting for 25-40% of their total cost [1]. Staying competitive in this field demands continuous examination, adaptation, and the development of new production models that balance often conflicting priorities: sustainability, complexity, cost, time, and quality. Hence, expanding knowledge and deepen the understanding in these areas is crucial.

The research activities at the Laser Group of University of Bologna address these objectives through the optimization of advanced manufacturing processes, leveraging expertise in laser technologies ranging from welding to the cutting of innovative materials for next-generation batteries. Additionally, we integrate monitoring sensors to enhance automation levels, working toward the implementation of digital twin frameworks.

This thesis presents the outcomes of research carried out across four universities, made possible by the PNRR scholarship's support for international mobility. Research areas covered span from the development of manufacturing systems to the application of laser technologies in the fabrication and assembly of battery packs. Across all studies, quality, productivity and sustainability are overreaching priorities, with the ultimate goal of fostering stronger knowledge transfer between academia and industry.

I wish to express my sincere gratitude to my principal supervisor, Alessandro Fortunato, and my co-supervisor, Erica Liverani, for the profession and personal support they have shown me throughout these years. I have greatly benefit from their guidance and experience to transform ideas into scientific papers. I would also like to thank Federico Poli for his support in deepening my understanding of the challenges related to industrial automation and the control of laser processing when integrated into automatic machines. I am truly grateful to my lab colleagues for all the constructive discussions, the exchange of ideas, and their daily support.

Caterina Angeloni
Bologna, 2025

Contents

List of Abbreviations

LIBs	lithium-ion batteries
EVs	electric vehicles
HAZ	heat affected zone
PW	pulsed laser radiation
CW	continuous-wave laser
SM	single mode
Li	lithium
SSB	solid state battery
Al	aluminum
Cu	copper
fps	frames per second
EDS	Energy-dispersive spectroscopy
SEM	scanning electron microscopy
EDM	Electrical Discharge Machining
LM	light microscopy
PRRs	pulse repetition rates
CC	current collectors
EP	equal pulse
IP	increasing pulse
SEI	solid electolyte interphase
Ps	scientific publications
SOs	scientific objectives

List of Symbols

Symbol	Unit	Description
P	W	laser power
BPP	m rad	beam parameter product
λ	nm	laser wavelength
BPP	m rad	beam parameter product
M^2	a.u.	beam quality factor
w_0	μm	laser beam radius
θ	$mrad$	laser beam divergence angle
P_P	W	peak power
P_{avg}	W	average output power
f_p	Hz	pulse repetition rate
τ	ns	pulse duration
F_{max}	Jcm^{-2}	laser peak fluence
w	μm	beam spot radius
E_p	J	laser pulse energy
F_{th}	Jcm^{-2}	threshold fluence
S	a.u.	incubation factor
N	a.u.	number of pulses per spot

Chapter 1

Introduction

1.1 Motivation

Lithium-ion batteries (LIBs) are a key cornerstone of the technological landscapes in modern societies. Since their commercialization by Sony Corporation in 1991, they have seen widespread application in smartphones, laptops, and other portable electronic devices [2]. During the last decade, LIBs have also emerged as a pivotal enabler of electromobility [3] and will be essential to the forthcoming transition to renewable energy sources, allowing for balancing of their inherent fluctuations in energy supply [4]. The development of LIBs has been acknowledged by awarding the 2019 Nobel Prize in Chemistry to the scientists John B. Goodenough, M. Stanley Whittingham, and Akira Yoshino [5]. LIBs exhibit several distinct advantages setting them apart from other battery technologies. Their exceptional energy density and specific energy permit the efficient storage of substantial energy quantities within compact and lightweight configurations. Additionally, LIBs possess a low self-discharge and nearly-zero memory effect, allowing them to retain their charge over long periods of inactivity [6]. As a result, global LIB production capacities are predicted to increase remarkably in the near future [7]. The development is mainly driven by the global battery market for automotive applications, which is expected to continue growing in the upcoming years [8]. At the same time, battery prices are declining as deployments increase [9].

Despite the aforementioned beneficial characteristics of LIBs, further advances of the technology are essential to meet future customer demands in the automotive industry. Batteries needs higher energy density for longer driving ranges, faster charging capabilities, improved safety, and lower costs. To remain competitive, manufacturers must enhance battery performance while simultaneously increasing production rates and ensuring consistent, high-quality output. These requirements have a direct impact on manufacturing processes, where precision, efficiency, flexibility, and reliability become paramount .

In this context, the quality of fundamental assembly and component fabrication steps that could be covered or supported by laser technology, such as electrode cutting and tab welding, is crucial [10].

Conventional battery designs incorporate an anode and a cathode tab (see Figure 1.1a) which provide electrical connections to the battery casing. These connections are typically established through laser welding. At this stage of battery manufacturing, evaluating the weld quality is crucial for ensuring the reliable operation of the entire battery pack. Therefore, industrial online monitoring systems for weld inspection will

be discussed.

Inside each battery case, the electrodes are housed. These are a sandwich composite materials, where the mean layer is typically a current collector foil made of copper for the anode and aluminum for the cathode, with thicknesses ranging between 8 and 30 µm. A significant innovation in cylindrical battery design is the tab-less architecture, which features a full-flag configuration (Figure 1.1b). Here, the tab extends along the entire foil length, separated by slits. This design improves the energy density of the battery pack in terms of reducing localized heating, improved thermal stability, and enhanced overall safety. High-quality cut edges are essential to ensure reliable electric connections and prevent defects like spatter and dross (Figure 1.1c).

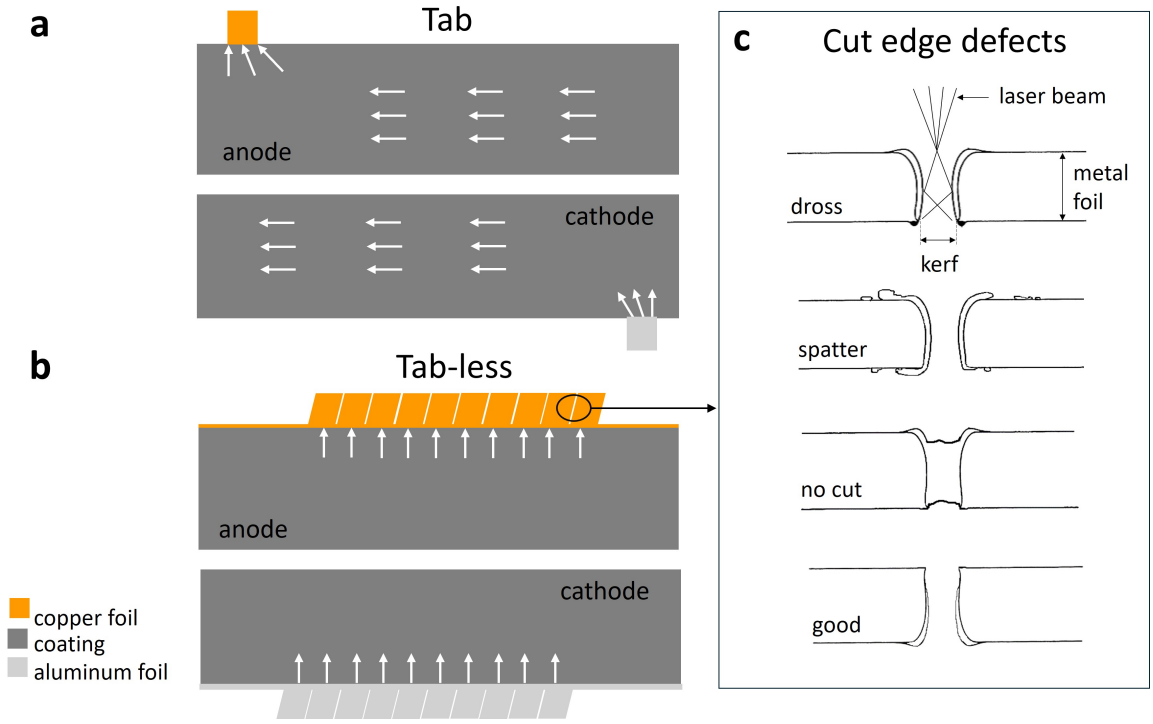

Figure 1.1: Electrode design with a (a) single-tab, where electrons travel along the entire distance; (b) tabless, where electrons travel shorter distances thanks to the full flags along the foil. Major cut edge defects are classified in (c)

Poor edge quality increases electrical stress, leading to heat generation and potential thermal runaway [11]. Internal short circuits and significant heat generation can eventually result in catastrophic failures of the entire system. Additionally, optimizing kerf width is crucial to minimizing material waste during electrode cutting and trimming.

Currently, die cutting and rotary knife slitting have been used to cut the prismatic and cylindrical electrodes, respectively. Both techniques require relatively expensive tooling that wears over time [12]. This tool wear results in process instability and requires additional cost and downtime to replace the worn tools. Furthermore, redesign of mechanical cutting processes demanding extra expenses is an inevitable step, since cell specifications vary depending on applications such as electronic devices and electric vehicles.

The abovementioned problems can be solved by using laser cutting, which is proven and widely utilized in industry [13] as an efficient and reliable manufacturing method. It has many advantages, such as no tool wear due to the contact-free process, high energy concentration and precision for different cutting patterns, low noise level, fast processing speed, very narrow Heat Affected Zone (HAZ), applicability to nearly all materials, and flexibility of laser power [10]. Most importantly, laser cutting is relatively easily applicable to different cell specifications with less cost, since redesign of laser cutting processes is relatively simple and cheap compared to mechanical cutting processes.

However, as a thermal process, laser cutting of thin current collectors is inherently associated with thermal defects on the edge profile. Therefore, it is essential to conduct research to determine the optimal cutting conditions for battery current collector production in both aluminum and copper.

1.2 Objective

Up to date, laser cutting of current collectors and real-time monitoring of laser welding in lithium-ion battery (LIB) manufacturing face several industrial limitations. Firstly, the formation of thermal defects during high-speed laser cutting of thin copper and aluminum foils is not yet fully understood, especially regarding the influence of laser parameters such as pulse duration, repetition rate, and beam shaping. In addition, optimal cutting conditions are difficult to define due to the complex interdependencies between material properties, processing speed, and laser source. While ultrafast-pulsed lasers (pulse length $<$10 ps) can improve edge quality, their high cost and limited throughput hinder industrial integration. On the other hand, quality assurance in laser welding remains a major concern, as poor welds can lead to battery failure. Despite the availability of monitoring tools, the implementation of robust, inline, and scalable solutions is still lacking. Moreover, correlations between monitoring signals and actual weld quality require further investigation to support automated process control.

This dissertation addresses the above-mentioned challenges through a combination of experimental and modeling approaches. Initially, copper and aluminum foils were cut using both pulsed and continuous-wave laser sources, comparing process outcomes over a wide range of parameters (up to 25 m/s in scanning speed). To further understand defect formation, computational fluid dynamics (CFD) model was developed, offering insight into melt dynamics and thermal effects. Ultrafast and burst-mode lasers were also explored during my period abroad in South Korea to assess their potential for high-speed, defect-free cutting.

In parallel, monitoring strategies for laser welding were investigated using photodiodes, high-speed imaging, and optical microphones. Signal analysis techniques were applied to detect instabilities and correlate them with weld quality. The feasibility of implementing such monitoring tools in industrial environments was evaluated with a focus on reliability and responsiveness. This work was conducted with the support of the laboratories facilities at used in Luleå University of Technology (Sweden) and the University of Warwick (England). In conclusion, this dissertation advances the industrial applicability of laser-based processes in LIB manufacturing by addressing

material-process interdependencies, optimizing process design, integrating real-time monitoring, and assessing the scalability and robustness of both cutting and welding operations.

1.3 Thesis structure

This publication-based thesis is divided into six chapters. Following the introduction given in this chapter, the theoretical foundations of LIBs and laser technology are detailed in Chapter 2. Subsequently, the research gap is defined in Chapter 3 based on the current state of literature covering laser-based current collector cutting and monitoring systems of the tab-welding. Chapter 4 gives an overview of the research approach and methodology used in this dissertation. In the following, Chapter 5 presents and discusses the results obtained in this thesis based on the embedded publications. Finally, the key insights of the dissertation are summarized and an outlook on potential future areas of research is given in Chapter 6.

Chapter 2

Fundamentals

This chapter provides the theoretical foundations for this thesis. In the first Section 2.1, technical parameters, components, operating principle, and production of LIBs are explained. Subsequently, the generation, propagation, and interaction with solid matter of laser radiation are detailed in Section 2.2.

2.1 Lithium-ion batteries

2.1.1 Terminology

Batteries are galvanic systems that store energy chemically and enable its conversion into electrical energy on demand. Electron transfer from one species to another can be thought of as the mechanism behind a wide range of inorganic compound reactions. The gain in electrons is called reduction and the loss in electrons is called oxidation; the joint process is called the *redox reaction* [14].

Batteries are classified into two main categories: primary and secondary. Primary batteries are non-rechargeable, where the redox are irreversible processes, making them pure energy conversion systems. In contrast, secondary batteries are rechargeable, as they undergo reversible redox processes. In this case, external energy is required to drive these reactions in reverse, allowing energy storage. As a result, they function as both energy conversion and storage systems. Lithium ion batteries (LIBs) are a particular type of rechargeable battery is in which lithium ions move from the negative electrode to the positive electrode during discharge and back when charging. The smallest functional galvanic element is a *cell*, which is made up of two distinct solid electrodes submerged in an electrolyte solution.

Although this classification is inaccurate for the charging process from an electrochemical standpoint, the labels *anode* and *cathode* are applied to the electrodes as components based on their role during discharge.

2.1.2 Structure and Composition

Conventional lithium-ion batteries use a liquid electrolyte to transport lithium ions between the anode and the cathode. While mature and widely used, these systems pose safety risks due to the flammability of the liquid electrolyte and are limited in energy density. In contrast, solid-state batteries (SSBs) replace the liquid electrolyte with

a solid-state electrolyte (ceramic, polymer, or composite). This allows for the use of lithium metal anodes, which significantly increases the energy density and reduces the risk of leakage or combustion. Specifically, lithium (Li) metal anodes have a theoretical capacity of 3865 $mAhg^{-1}$, approximately 10 times higher than graphite, possessing the lowest reduction potential (3.04 V vs. the standard hydrogen electrode) and density (0.535 gcm^{-3}) [15]. Solid-state systems offer improved thermal and mechanical stability, but current challenges include unpredictable dendrite growth on Li metal surfaces during operation and manufacturing complexity since it has to be handled within a very low relative humidity environment such as a dry room or glove box.

A conventional liquid electrolyte LIB is made up of various components, including cathode, anode, electrolyte and separator, each composed of different materials (see Figure 2.1). Additionally, LIBs have a shell to protect the internal components of the cell from the atmospheric environment.

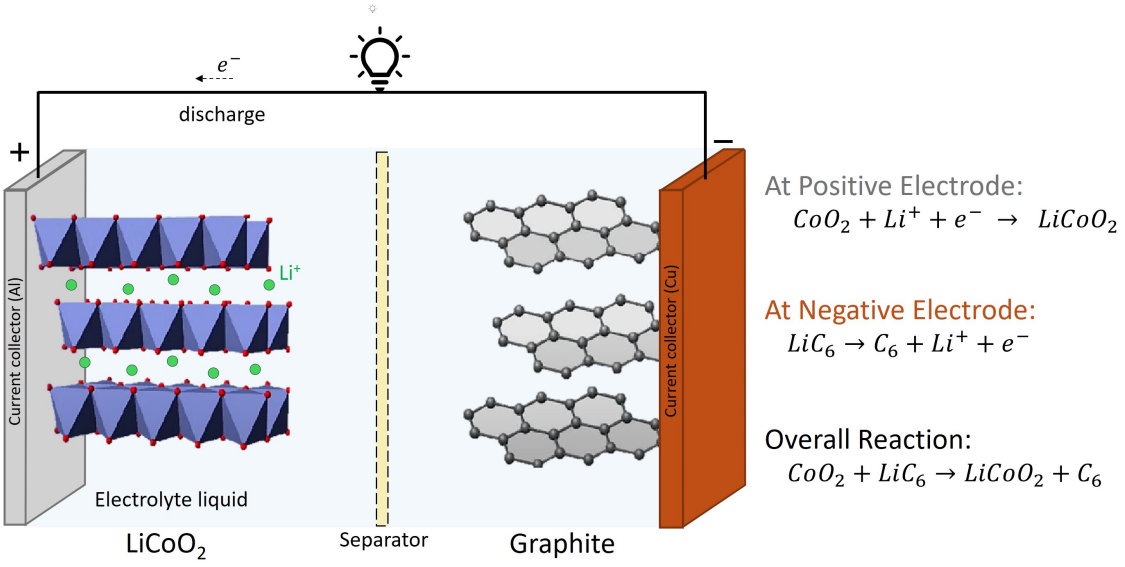

Figure 2.1: Schematic representation of the composition and redox reactions of a discharging LIB where lithium ions Li^+ move from the anode to the cathode and the electron e^- flow direction.

Electrodes

Anode active materials for electrochemical storage used in LIBs allow for reversible insertion of lithium ions (Li^+) into their layered structure during battery charge and discharge cycles. This mechanism is called intercalation. Nowadays graphite is the anode material employed in nearly all LIBs with different particle sizes and shapes, domain sizes, crystallinity and coating [16]. Other carbon-based anode materials have been investigated, such as hard and soft carbon, graphene and carbon nanotubes (CNT). Compared to anode materials, the choice of cathodes offers a wider range of possibilities, including lithium iron phospate (LFP), lithium cobalt oxide (LCO), lithium manganese oxide (LMO), lithuim nickel manganese cobalt oxides (NMC) [17]. Besides the active material, a LIB electrode also includes conductive carbon and binder. The binder is pre-dissolved in a solvent and binds all particles together on a current collector. Polyvinylidene difluoride (PVDF) processed with N- methyl-2-pyrrolidone (NMP)

is a common polymer binder for cathodes, while water-based carboxymethyl cellulose (CMC) combined with styrene butadiene rubber (SBR) is often used for anodes [18]. The conductive carbon particles and binder form an electronic conductive network within the entire layer.

The charge storage process can be greatly affected by electrode properties given by the material used. Just to mention some: active material mass loading [mg cm-2] determines the energy density, adhesion and cohesion between the coating and the current collector is crucial for maintaining good electrical contact and electrode performance, charge transfer resistance which determines the quality of the exchange process between solvated Li ions in the electrolyte and Li atoms in the electrodes, etc. The electrode architectural parameters play a crucial role in determining electrode properties, such as thickness, porosity, pore size and particle size [19].

Current Collectors

Metallic foils are commonly employed as current collectors in LIBs. They should have strong electrical conductivity, good adhesion of the active components, good mechanical, chemical, electrochemical stability, and moderate material prices. Typically, aluminum foil is sandwiched between two cathodes with a thickness of 12 to 20 μm and a copper foil with a thickness of 6 to 10 μm is employed as current collector for the cathode. The cost-effective and lightweight aluminum is limited to the cathode side since it develop lithium aluminum alloys at low anode potentials.

For higher energy density batteries, lighter and thinner current collectors gradually have become the focus. Considering the preparation difficulty of ultra-thin electrolytic copper foil, the limiting thickness of copper foil is about 4 μm and cannot be further reduced. Meanwhile, further reduction in the thickness of copper foil may result in complete peeling off from the cathode roller, and copper foil is prone to wrinkling and cracking [20]. In recent years, with the gradual maturity of thin film deposition technology and the limited development of copper foil current collectors, the non-metallic carbon-based and polymer-derived materials emerge as promising alternatives to conventional metallic counterparts [21].

Electrolyte

In lithium-ion batteries, the electrolyte plays a crucial role by enabling the transport of lithium ions between the anode and cathode during charging and discharging, primarily through diffusion. It must exhibit high ionic conductivity and electrochemical stability across a broad voltage and temperature range. Compatibility with the battery's components, safety, environmental sustainability, and low-cost production are also essential requirements.

Liquid electrolytes are the most widely used and typically consist of a mixture of organic carbonate solvents. The organic solvent is a key factor for battery performance because it increases the mobility of lithium ions. A common formulation includes ethylene carbonate (EC) and ethyl methyl carbonate (EMC) in a 1:1 ratio, with approximately 2 with vinylene carbonate (VC) added as an additive. EC and VC are particularly valued for their film-forming abilities, facilitating the formation of the

solid electrolyte interphase (SEI) on the graphite anode, which is essential for battery stability and longevity.

Lithium hexafluorophosphate ($LiPF_6$) is the standard conducting salt in these electrolytes, offering a good balance between conductivity and chemical compatibility. Alongside carbonates, ethers and esters are also common solvent choices in advanced formulations. Additives like VC further enhance the cycle life of the battery by improving SEI quality and mitigating degradation. While solid-state and polymer electrolytes present promising alternatives, their use remains limited in conventional LIBs [18].

Separator

The separator is a safety component between the cathode and the anode. It prevents direct contact, hence short circuiting, while being permeable to lithium ions owing to its microporous membrane. The most common separator materials are polyethylene and polypropylene. When the cell heats excessively, which is an early sign of thermal runaway, these materials melts due to the high temperature and fills its micro pores to stop lithium-ion flow between anode and cathode. This “shutdown” function damages the cell irreparably, but avoids major negative consequences [22]. It accounts as the third most expensive component in the cell, after the cathode and the can header and terminals. Nowadays, many new businesses are emerging, offering novel materials to improve battery safety, cost efficiency and sustainability. To name a few, QuantumScape introduced a new ceramic separator called "cobra" that functions both as a barrier between the cathode and anode and a Li-ion conductor [23]. Additionally, the startup 24M unveiled a separator called "Impervio", designed to prevent dendrite formation and control heat during battery failure. Compared to traditional separators, tests revealed that cells employing Impervio maintained significantly lower temperatures under stress, reducing fire and explosion risks [24].

Casing

LiBs cells, after being manufactured, are interconnected in series and/or parallel to create a battery module, which also requires various housing components, depending on the LIBs type (cylindrical, prismatic, or pouch). The final battery pack requires a cooling system and casing made of aluminum, steel or composite materials to protect against mechanical stress and thermal impacts [25].

2.1.3 Chemistry Basics

The ability of lithium-ion batteries (LIBs) to store and release electrical energy relies on the reversible intercalation of lithium ions into the active electrode materials. A redox reaction example that occurs during charging in a lithium-ion battery with a $LiCoO_2$ cathode can be expressed as:

$$\mathrm{LiCO_2(s) + 6C(s) \rightarrow LiC_6}(s) + \mathrm{CoO_2}(s) \tag{2.1}$$

In this solid-state reaction, the compound Li_6C indicates that Li^+ ions have penetrated between the sheets of carbon atoms in graphite [14]. At the microscopic level, battery operation is governed by the coordinated movement of lithium ions and electrons (see

Figure 2.1). During charging, lithium is deintercalated from the $LiCoO_2$ cathode and diffuses through the electrolyte toward the graphite anode, where it intercalates between the carbon layers. Simultaneously, electrons are extracted from the cathode and flow through an external circuit to the anode, where they recombine with Li^+ ions to maintain charge balance. The reverse process occurs during discharge, where lithium leaves the graphite structure and diffuse in the electrolyte through the separator and re-enters the cathode into the host lattice, performing electrical work. One electron from the external circuit is supplied to the cathode for each intercaled lithium ion maintaing charge neutrality.

2.1.4 Manufacturing

High-throughput production methods for small LIBs, which are often used in consumer electronics, have been well-established since the 1990s. Process expertise has now been applied to the manufacturing of larger cells (>20 Ah) for EV applications. For large size EV cells, it is still challenging to build progressively cost-effective facilities with faster throughput and better product quality. The manufacturing process can be clustered into three major segments characterized by a high degree of complexity and interdependency: electrode production, cell assembly and cell conditioning (see Figure 2.2.

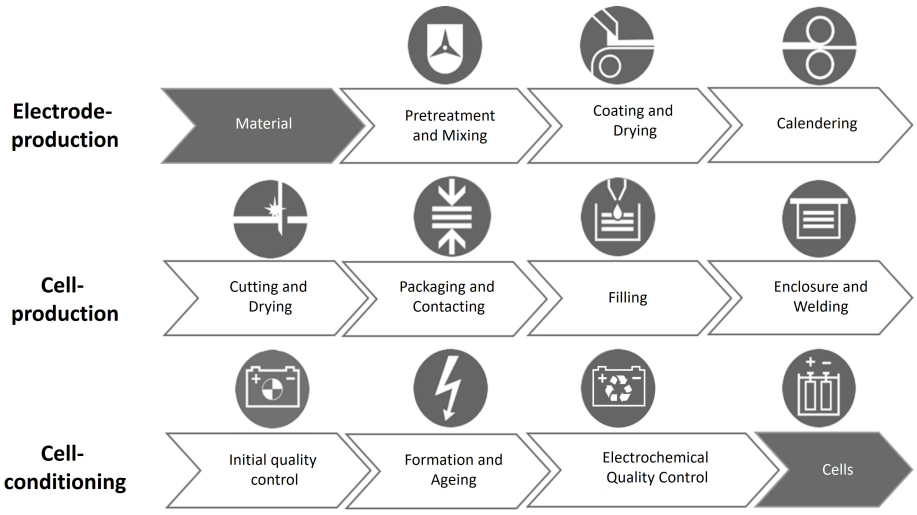

Figure 2.2: Generalized battery production chain for LIB manufacturing (adapted from [18]).

Electrode production

The first step in making an electrode begins with a viscous paste preparation, known as slurry, in which the active material powder, a binder additive (such as PVDF), and a conductive additive (e.g. carbon black) are dispersed in a solvent. The choice of solvent depends on the electrode chemistry: purified water is commonly used for anode slurries, while N-methyl-2-pyrrolidone (NMP) is typical for cathodes due to its compatibility with fluorinated binders. Once homogenized, the slurry is applied onto the metallic current collector foil-copper for the anode and aluminum for the cathode-using precise

coating techniques such as slot dies or doctor blade coating. For high-capacity, large-format LIBs, the electrodes are often coated on both sides of the foil to maximize energy density.

The coated foils are then *dried* to evaporate the solvent. Drying conditions depend on the slurry chemistry: cathodes such as NMC require NMP solvent recovery systems and dry-air or nitrogen environments, due to NMP's toxicity and flammability. Anode, like graphite, typically uses aqueous slurries, making drying less hazardous but still requiring strict moisture control. Drying is usually conducted using convection ovens, often enhanced by laser radiation which enables an infrared (IR) heating. A typical drying profile uses a high–low–high temperature sequence to balance throughput, adhesion, and microstructure. Standard drying times range from 1–2 minutes, with line speeds of 25–50 m/min [18, 19].

The dried electrode laminates undergo calendering, a densification process that compresses the electrodes in a two-roller calendar at line speeds of 30-100 m/min to achieve the desired thickness, enhancing energy density and other physical electrode properties (such as adhesion, porosity, conductivity) [18].

After calendering, electrodes are slit into appropriate widths using mechanical punching or laser radiation [26, 27] and subjected to a final drying. Sometimes subjected to vacuum drying to remove residual moisture, an essential step to prevent undesirable reactions with the electrolyte in the later stages of cell assembly [28]. The electrode cutting strategy strongly depends on the final cell format: pouch, cylindrical, or prismatic, as each design imposes specific dimensional and geometric requirements. In general, tailoring of any battery foil can be divided into three different types of cutting processes: notching, slitting, and separating (see Figure 2.3). For pouch cells, these are already divided into area that will later roughly correspond to their cell size, while the coated rolls for cylindrical and prismatic cells have a continuous coating. The baby coils of coated aluminium and coated copper must next be separated to the desired formats of the cells.

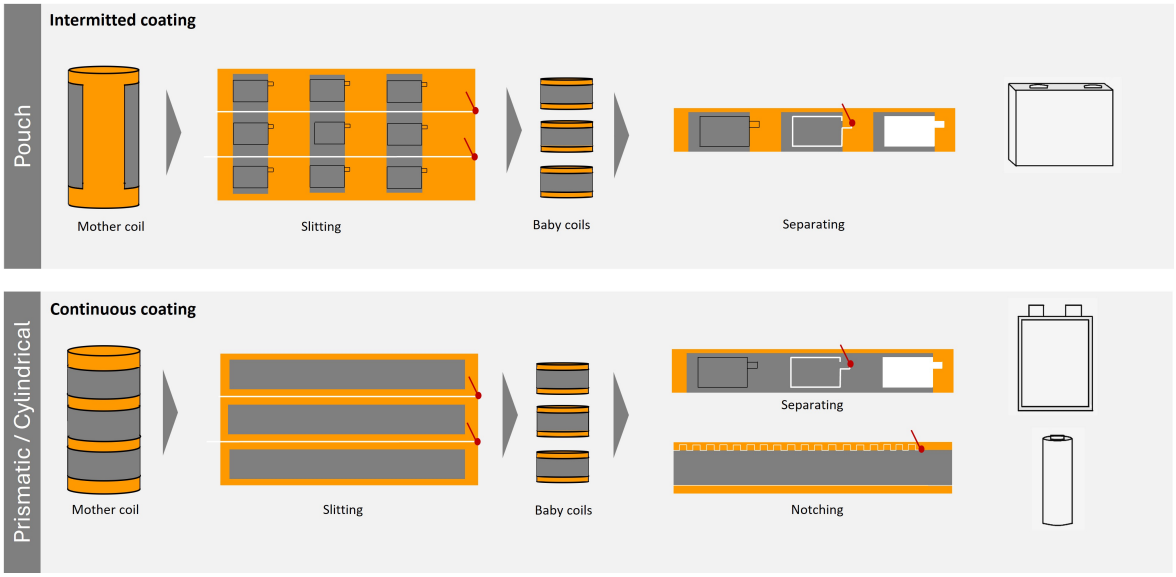

Figure 2.3: Process solutions for battery copper foil cutting for different type of cells (pouch, prismatic and cylindrical).

Cell production

After final drying, electrodes and separator materials are transferred into a dry room (ambient temperature ∼20 °C, dew point −40 °C to −60 °C) for cell assembly depending on the desired format (round wound, prismatic wound, stacked, Z-folded) as illustrated in Figure 2.4. The specific production line depends on the cell type (cylindrical, prismatic, or pouch). There are three main electrode stack assembly (ESA) processes:

- **Stacking** offers uniform mechanical load distribution, enabling the use of thicker electrodes (>100 µm) and achieving higher energy density. However, it is a discrete process that requires more effort to match the productivity and precision of winding.
- **Z-folding** involves continuously feeding the separator, folding it in a zigzag shape, and inserting discrete electrode sheets. It combines the energy density benefits of stacking with improved safety and higher automation. In some variants, electrodes are laminated onto the separator for faster and more accurate assembly (up to one sheet per second).
- **Winding** is the standard method for small cylindrical cells and is also used in prismatic EV cells. However, it is limited by bending stress and cracking risks in thick electrodes and is highly sensitive to defects due to the long electrode webs.

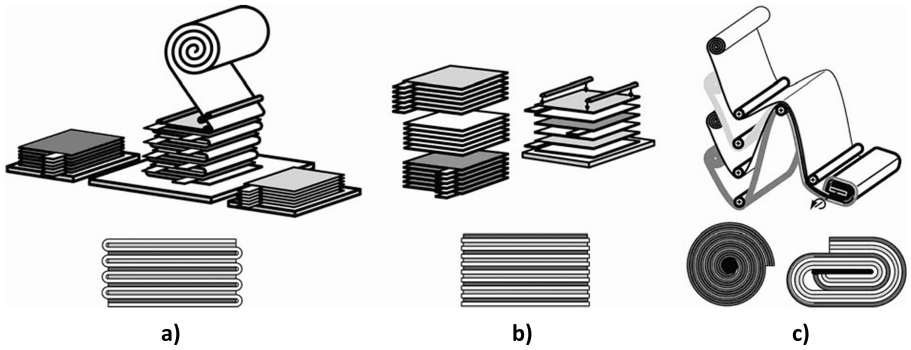

Figure 2.4: Cell production by a) stacking, b) z-folding and c) winding processes. Reproduced from ref. [29].

Once assembled, electrodes are electrically connected to metal tabs (aluminum for cathodes, nickel-plated copper for anodes), typically by ultrasonic or laser welding [30]. These tabs act as current collectors and external terminals. Failures induced by uncontrolled welding quality lead to three main disadvantages: (1) battery damage, i.e. uncontrolled welding penetration carries the risk of perforation of the battery cell, resulting in the release of harmful gases and fire; (2) scrapping of the entire battery pack since even a single defective welding, if not detected, can cause the failure of the entire battery pack (e.g. voltage drop); (3) welding dissimilar materials lead to the formation of intermetallic phases, resulting in lower mechanical and electrical properties. This highlights the need to detect welding defects through real-time in-process joint quality measurements using a closed-loop monitoring system that implements corrective

and/or preventive actions in order to achieve a reliable, "zero waste" process. Nowadays different type of sensors are implemented in industry, some of them are discussed in Section 2.3.

The electrode stack is then encased in a pouch or hard case, with only the tabs extending out. One side remains open for electrolyte filling.

The electrolyte (15–20 wt%) is filled under weak vacuum (<300 mbar below ambient), in extremely dry conditions (dew point $\sim -60\,^{\circ}\mathrm{C}$). The *filling* process requires careful control of dosage precision, foaming, and evaporation losses. The cell is then *sealed* and stored under controlled temperature to enhance wetting and gas diffusion.

Cell conditioning

Next comes the *formation* process, where the solid electrolyte interphase (SEI) on the anode is developed, typically starting with low charge rates that gradually increase. This takes about a day and is followed by aging, a stabilization phase that may last 2–3 weeks. Throughout these steps, quality control (voltage, capacity, impedance) is performed to screen out defective cells.

2.2 Laser technology

Light Amplification by Stimulated Emission of Radiation - LASER, an acronym destined to make scientific literature bloom across diverse fields for centuries. It was published for the first time at a conference in 1959 by Gordon Gould. Technically, this describes the underlying physical mechanism, but it is also used to characterize the radiation emitted by technical devices. Laser radiation can be categorized into two types: pulsed laser radiation (PW), which exhibits periodic variations in power over time, and continuous-wave (CW) radiation, which maintains a constant power. In materials processing, pulsed laser radiation is often further classified as either short-pulsed or ultrashort-pulsed, depending on the pulse duration. These distinctions result in different ablation behaviors, as discussed in Section 2.2.4.

2.2.1 Laser beam generation

Stimulated Emission

Stimulated emission is the fundamental physical mechanism that enables photon multiplication, enabling the amplification of the electromagnetic radiation. First introduced by Albert Einstein in his 1917 paper on the quantum theory of radiation, this process complements the spontaneous emission and absorption phenomena that govern atomic transitions.

As described in Figure 2.5a), in stimulated emission, an electron occupying an excited energy level E_1 in an atom or molecule can be induced to transition to a lower energy level E_0 when it interacts with an incoming photon whose energy $hv = E_1 - E_0$. A key aspect of stimulated emission, compared to spontaneous emission, is that the emitted photon is not random in its properties but is identical to the incident photon in phase, direction of propagation, frequency, and polarization. This coherence between photons is what ultimately gives laser light its unique properties, such as high monochromaticity, directionality, and temporal and spatial coherence.

For stimulated emission to dominate over spontaneous emission and absorption, a condition called *population inversion* must be achieved. The latter condition is achieved when the medium (the matter irradiated by an induced emission) must be brought in a state of non-equilibrium, where a greater number of particles N occupy the excited state (N_1) than the ground state (N_0). In thermal equilibrium, this condition is not naturally achieved, as described by the Boltzmann distribution, which predicts a lower population in higher energy states:

$$\frac{N_1}{N_0} = \exp\left(-\frac{E_1 - E_0}{k_B T}\right) \tag{2.2}$$

Where T is the absolute temperature and k_B is the Boltzmann constant. From equation (2.2) is clear that a population inversion $N_1 > N_0$ requires non-equilibrium state, which is possible only by continuously supplying energy, a process referred to as *pumping*. In solid-state lasers, optical pumping is used, where an external light source supplies photons that excite atoms in the active medium.

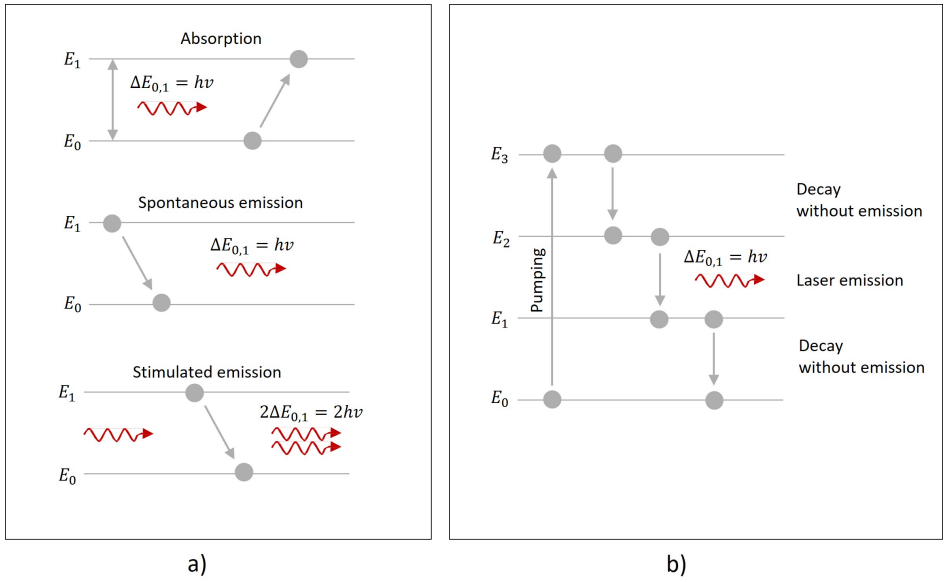

Figure 2.5: Energy-level diagrams of a laser system: a) two-level and b) four-level configuration.

For effective amplification, it is crucial that the excited state be metastable, meaning that atoms remain in this state long enough for stimulated emission to occur, rather than decaying immediately through spontaneous emission. The use of a metastable level increases the likelihood of coherent photon generation and thus laser emission.

However, there are fundamental limitations in two-level systems. When N_0 and N_1 approach each other, the rate of pumping equals the rate of de-excitation (via spontaneous and stimulated emission), a condition known as *saturation*. Under these circumstances, the medium becomes transparent to the stimulating radiation, preventing any net amplification and thus blocking laser operation.

To overcome this limitation, laser media must utilize at least a three-level system to separate the pumping process from the lasing transition. Even more effective is the four-level architecture: it represents the most efficient and practical framework for continuous and high-intensity laser generation, forming the backbone of many modern laser systems. As illustrated in Figure 2.5b), from the ground level E_0, the particles are pumped to the highest energy level E_3, from where the majority quickly relaxes to E_2, mostly via non-radiative processes. The stimulated emission then occurs from E_2 to E_1, and from E_1 the particles rapidly return to the ground state E_0, typically without emission of radiation. Thus, in a four-level system, occupation inversion is easier to produce than in a three-level system, since E_1 is essentially empty. It is of particular importance that the relaxation from E_3 to E_2 happens significantly quicker than the laser transition E_2 to E_1 in order to build up a stable population in the upper laser level E_2.

Laser components

All types of laser sources consist of three main components: the laser medium, a pump source and a optical resonator. The laser active medium within the optical cavity amplifies light by stimulated emission and can exist in different phases: a gas (gas laser), liquid (liquid lasers) and a crystal or glass doped with active ions (solid-state

lasers). A pump source supply energy to the laser-active medium to excite atoms or molecule, creating the population inversion. This energy can come from electrical or optical sources (e.g., a lamp or another laser source). The resonator is formed by two mirrors which trap the light. As the photons bounce back and forth between the mirrors of the resonator through the laser-active medium, they stimulate more emissions from the excited atoms, leading to photon amplification. The resonator allows for the continuous buildup of light intensity. One of the two mirror is fully reflective, while the other is partially transparent, allowing some of the light to escape as the laser output. When the light inside the resonator has been amplified sufficiently and the conditions for population inversion are met (more atoms are in the excited state than in the ground state), the photons escape through the partially transparent mirror as coherent laser light [31]. The properties of the laser beam are governed by the laser-active medium, which determines the wavelength λ and by the laser resonator, which determines the geometric characteristics of the beam, which will be explained in Section 2.2.2.

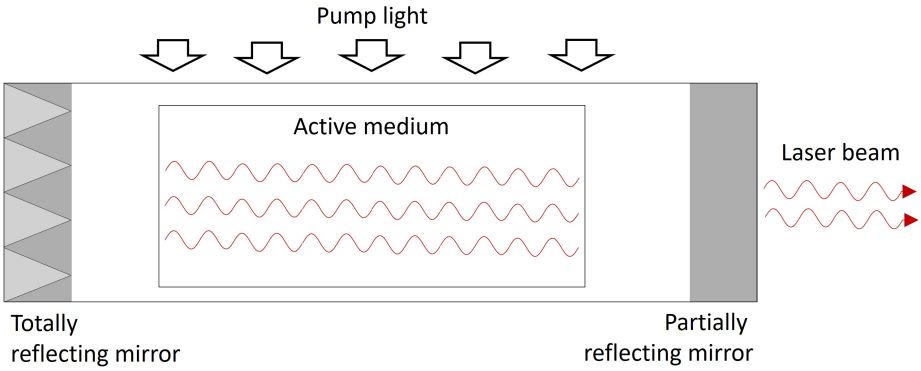

Figure 2.6: Resonator schematic representation for laser generation.

Continuous and pulsed mode

Laser systems can operate either in continuous wave or in pulsed mode, depending on how energy is stored and delivered over time. These two regimes differ significantly in terms of energy delivery, temporal profile, and interaction with matter, and they are selected according to the specific requirements of the application.

In continuous wave operation, the laser emits a steady and uninterrupted beam of light. This is made possible by maintaining a constant population inversion in the gain medium.The laser power generated depends on the amount of power used by the pumping source and the amount of active medium used.

In contrast, pulsed operation involves the emission of light in short, intense bursts, rather than a continuous beam. This is achieved by allowing energy to build up in the gain medium and then releasing it rapidly. The method used to create these pulses depends on the desired pulse duration.

For nanosecond pulses, the technique of *Q-switching* is commonly used. It is based on a fast optical switch in the laser resonator blocking laser light while pumping energy is stored in the gain medium. A closed shutter is placed in front of one of the mirrors, known as Q-switch within the cavity. As a result, laser beam cannot move between

the mirrors and the population inversion increases and exceeds the usual threshold value in the cavity by continuously pumping in the laser medium (low-Q state). Now, when the shutter is suddenly opened, all the stored energy is released in a very short, high-energy pulse (high-Q state). The switching device can be either mechanical or electro-optic shutter.

For ultrashort pulses (in picosecond and femtosecond range) a technique called *mode-locking* is used. This technique forces the different resonant modes of the cavity to oscillate with a fixed phase relationship. When these modes combine constructively, they generate a train of extremely short pulses. Passive mode-locking techniques, such as using a saturable absorber or nonlinear effects (e.g., Kerr-lens mode-locking), are typically employed to achieve pulse durations in the femtosecond range [32].

2.2.2 Definition of laser intensity and fluence variables

Gaussian beams

Lasers can operate in different transverse electromagnetic modes, which represent distinct spatial distributions of the optical field within the resonator. Among them, the TEM_{00} mode is the fundamental mode in resonators with spherical mirrors, characterized by a bell-shaped Gaussian intensity profile across the beam section expressed as [33]:

$$I_l = I_{l,0} \exp\left(-\frac{2r^2}{w^2(z)}\right) \tag{2.3}$$

Figure 2.7 shows the radial intensity distribution of a Gaussian beam that travels in z-direction, w is the beam radius at which the intensity has decreased to $1/e^2 \approx 13.5\%$ of its peak value $I_{l,0}$. Hence, 86% of the total power is concentrated within the area determined by the beam diameter.

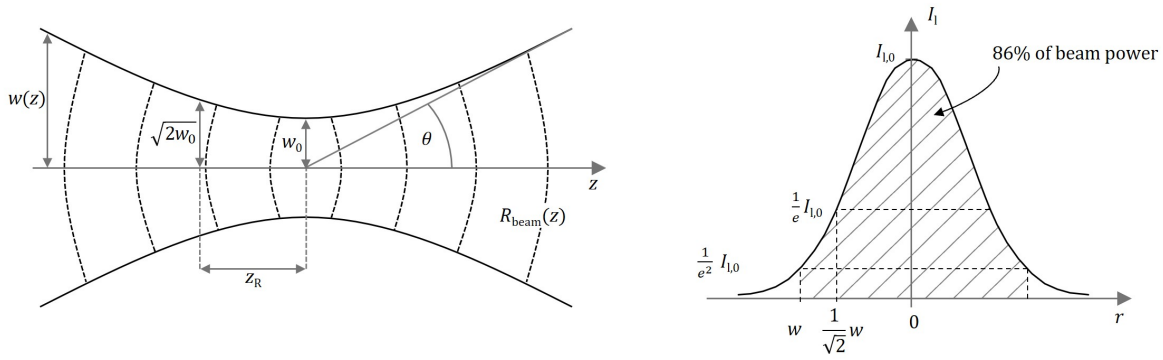

Figure 2.7: Left: Laser beam geometry along the z-axis with a beam radius w, the minimal beam radius w_0, the Rayleigh length z_R, the divergence angle θ. Right: Gaussian distribution of irradiance: beam radius and power (adapted from [33]

The radius of a Gaussian beam w(z) at any position along the z-axis can be derived from the beam waist w_0, which represents the minimum beam radius occurring at z=0:

$$w(z) = w_0 \sqrt{1 + \frac{z^2}{z_R^2}} \tag{2.4}$$

$$w_0 = w(z = 0) = \sqrt{\frac{z_R \lambda}{\pi}} \tag{2.5}$$

The parameter Z_R is called Rayleigh length and it is the distance from the beam waist (at z = 0) where the intensity drops to half of its maximum value. It is related to the beam waist as:

$$z_R = \frac{\pi w_0^2}{\lambda} \tag{2.6}$$

As illustrated in Figure 2.7, the beam is characterized by a converging-diverging geometry and features a point of minimum beam diameter at the waist.
For $z \gg z_R$, the beam has a conical geometry with straight generatrices and a vertex angle equal to:

$$\Theta = \lim_{z \gg Z_R} \frac{w(z)}{z} = \frac{w_0}{z_R} = \frac{\lambda}{\pi w_0} \tag{2.7}$$

The quality of a laser beam is commonly characterized by two parameters: the beam quality factor M^2 and the Beam Parameter Product BPP. The parameter M^2 is dimensionless and quantifies the deviation of a real beam from an ideal Gaussian beam. A perfect Gaussian beam has $M^2 = 1$, while higher values indicate increased divergence and reduced focusability. This makes M^2 particularly useful for comparing the intrinsic quality of beams generated by different laser sources, independent of their wavelength.

On the other hand, the Beam Parameter Product is defined as the product of the beam waist radius w_0 and the far-field divergence angle θ:

$$BPP = \theta w_0 = \frac{\lambda}{\pi} \tag{2.8}$$

It has physical units (e.g., mm·mrad) and is wavelength-dependent. For most laser beams, the intensity distribution deviates from the TEM_{00} mode, leading to an expansion of the beam radius and an increase in the divergence angle:

$$BPP_{real} = M^2 \frac{\lambda}{\pi} \tag{2.9}$$

Hence, the BPP provides a direct indication of the trade-off between beam size and divergence, making it more suitable for practical applications involving beam delivery or focusing optics.

Pulsed Laser Radiation

Laser can be operated in pulsed or continuous (wave) mode. Figure 2.8 depict the operational differences between the two modes. For CW lasers, the output power (given in Watt) is an important parameter. For PW lasers, various important quantities come into play: the pulse duration τ, the time between successive pulses T_p and the pulse energy E_p (in Joule). These define the pulse peak power P_p and the average output power of a pulsed laser source P_{avg} as:

$$P_p = \frac{E_p}{\tau} \tag{2.10}$$

$$P_{avg} = E_p \cdot f_p \tag{2.11}$$

where $f_p = 1/T$ is the pulse repetition frequency, also called pulse repetition rate.

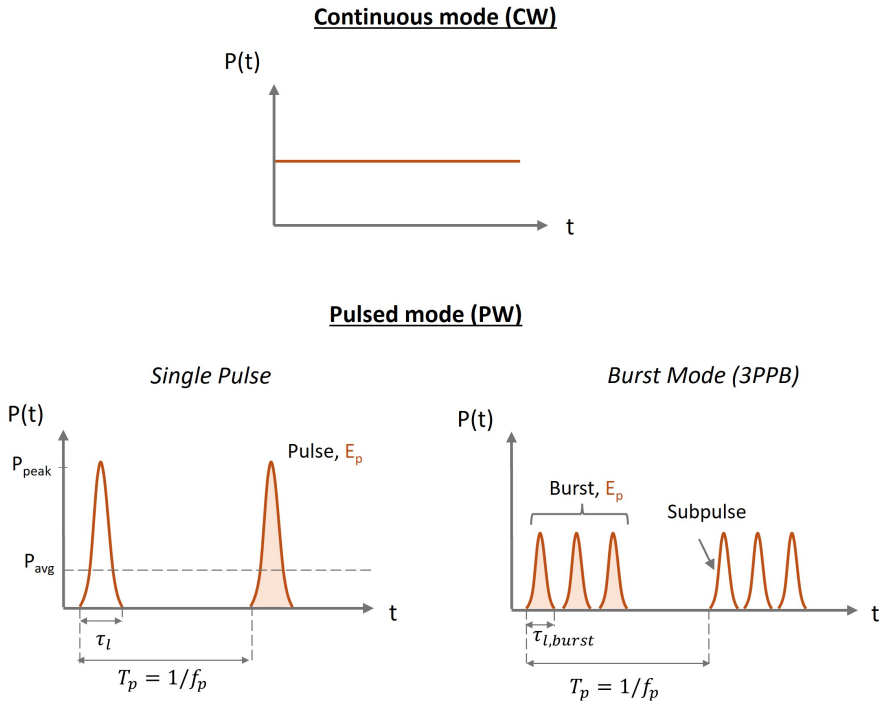

Figure 2.8: Schematic representation of continuous and pulsed mode. The pulsed radiation is characterized by a gaussian shape in conventional (bottom left) and burst mode (bottom right) operation denoting the peak power P_{peak}, average power P_{avg}, pulse repetition rate f_p, pulse period time T_p, pulse energy E_p, pulse length τ and burst pulse length τ_{burst} (PPB pulses per burst).

Although single-pulse operation at repetition rates of up to a few MHz typically maximizes ablation efficiency in most practical cases [34], burst operation—where two or more pulses are delivered in rapid succession with pulse-to-pulse separations corresponding to frequencies up to GHz range—can, in certain cases, improve surface morphology by enabling controlled heating of the workpiece [35].

2.2.3 Transport and focusing system

There are two possible beam delivery systems: a series of appropriately oriented mirrors forming an optical chain, or a waveguide known as an optical fiber [31] (see Figure 2.9).

Fiber delivery, used in fiber and disk lasers, offers high flexibility and easy integration, while free-space setups, typical of femtosecond lasers, preserve pulse quality but require precise alignment and a stable environment.

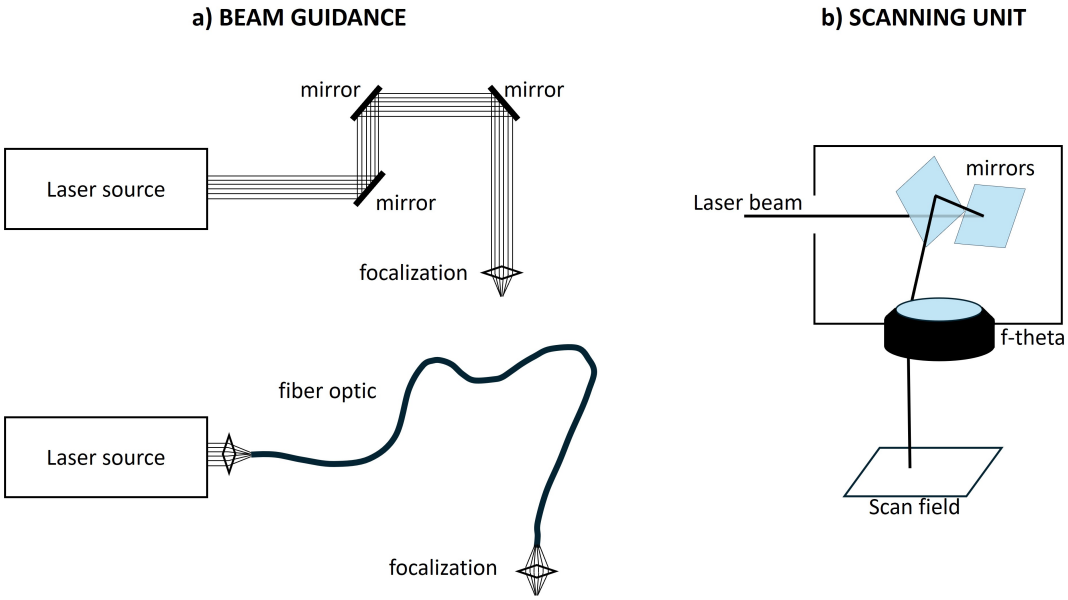

Figure 2.9: Beam transport configurations: a) optical chain at the top and optical fiber at the bottom (adapted from [31]), highlighting the focusing stage with the b) scanning unit comprising galvanometric mirrors and an f-theta lens.

Both beam focusing and deflection are combined in one technical unit, the so-called *scanner* optics. The beam is typically focused by f-theta lenses for distortion-free scanning and galvanometer-driven mirrors for rapid beam movement.

The f-theta component is a multi-element lens designed such that the focal plane remains flat and the spot position is linearly proportional to the scan angle of the deflecting mirrors. Unlike simple focusing lenses, f-theta optics correct for field curvature and other aberrations, ensuring consistent focus quality and spot size across large scan fields.

Mirrors in the scanner head are generally made of copper and can be coated with a highly reflective material that also possesses strong anti-oxidant properties. The high thermal conductivity of copper, combined with its high reflectivity and the fact that the beam is not focused, helps prevent the mirrors from reaching excessively high temperatures that could damage them (see Figure 2.9b). When higher speeds are employed, polygonal scanners or beam splitting are used. The former uses rotating multifacets wheels, enabling beam deflection speeds of several hundreds of meters per second [36], while the latter is used when larger sample areas have to be processed, for instance using so called DOEs or spatial light modulators (SLMs) [37, 38].

2.2.4 Laser-materia interaction

When electromagnetic radiation strikes a surface, a part of the incident energy is reflected, part is transmitted and part is absorbed within the material. The distribution of these interactions depends on the material's optical properties, the laser wavelength, and the surface condition. The absorbed radiation is attenuated according to Beer-Lambert law, $I = I_0 e^{-\beta z}$. The absorption coefficient β depends on the medium, the wavelength of the radiation and the intensity. Absorption is the process by which laser energy is converted into internal energy within the material, primarly as heat. At

the microscopic level, electromagnetic radiation can be described as oscillating electric and magnetic vector fields. These fields interact with charged particles—mainly electrons—within the material. The electric field component induces oscillatory motion in electrons. This mechanism for energy coupling is called "inverse bremsstrahlung effect". Specifically, the bremsstrahlung effect is the emission of photons from excited electrons.

If the frequency of the radiation does not match a natural resonance frequency of the electron system, the interaction results in forced vibrations, not fluorescence. These oscillating electrons either re-radiate energy (scattering, reflection, or transmission) or, if impeded by the material's atomic lattice (phonons), convert the energy into lattice vibrations—i.e., heat. This is known as the inverse bremsstrahlung effect, in which photons transfer their energy to electrons, which then couple to the lattice. When a sufficient amount of energy is absorbed, atomic vibrations intensify to the point where intermolecular bonds are significantly weakened, causing the material to lose its mechanical integrity—this marks the onset of melting. With continued energy input, the vibrational energy further disrupts the bonding forces, leading to vaporization. The resulting vapor can still absorb laser radiation to a limited extent due to the presence of bound electrons. However, with additional absorption, these electrons can be liberated, ionizing the gas and forming a plasma. If the resulting free-electron density is sufficiently high, the plasma becomes a highly absorbing medium, shielding the surface [39].

Reflection or Absorption

The fraction of laser radiation which is absorbed by the metal free electrons will vary with the same effects that affect reflectivity. The incident laser power P interacting with the substrate is partitioned into three components: a reflected portion P_{ref}, an absorbed portion P_{abs}, and a transmitted portion P_{tra}, such that:

$$P = P_{ref} + P_{abs} + P_{tra} \tag{2.12}$$

At shorter wavelengths, the higher photon energy enables interaction with a larger number of bound electrons, leading to increased absorption. As a result, the surface reflectivity decreases while the absorptivity correspondingly increases.

As the temperature of the material increases, the phonon population within the lattice rises, enhancing phonon–electron interactions. This increases the likelihood that excited electrons will transfer energy to the lattice rather than re-radiate it. Consequently, for certain metals, this results in a decrease in reflectivity and a corresponding increase in absorptivity with temperature.

Pulsed laser ablation of solids

The processing of solid substrates using continuous wave (CW) laser radiation can be effectively modeled through classical heat transfer approaches, as detailed by Mazumder et al. [39]. These models rely on macroscopic thermal conduction principles, assuming quasi-steady energy deposition. In contrast, the interaction of pulsed laser radiation, particularly with metallic substrates, must be described at the microscopic scale due to the rapid and localized nature of energy transfer.

Upon irradiation with a pulsed laser beam, energy is first absorbed by the free electrons in the material. This leads to rapid excitation and subsequent thermalization within the electron subsystem. The absorbed energy is then transferred to the atomic lattice via electron–phonon coupling, followed by thermal diffusion deeper into the material. This process is accurately captured by the two-temperature model (TTM), which treats the electrons and lattice as two distinct subsystems with separate temperatures, T_e and T_i respectively. The model assumes rapid internal equilibration of the electron subsystem and negligible heat conduction within the lattice over ultrashort timescales:

$$C_e \frac{\partial T_e}{\partial t} = -\frac{\partial Q(z)}{\partial z} - \gamma(T_e - T_i) + S \tag{2.13}$$

$$C_i \frac{\partial T_i}{\partial t} = \gamma(T_e - T_i) \tag{2.14}$$

$$Q(z) = -k_e \frac{\partial T_e}{\partial z} \tag{2.15}$$

$$S(z) = I(t) A \beta \exp(-\beta z) \tag{2.16}$$

Specifically, in 2.13, the changes in electron temperature are calculated considering the heat flow $Q(z)$ in the z direction perpendicular to the surface, the energy transferred to the lattice $\gamma(T_e - T_i)$, and the energy supplied by the laser $S(z)$. In equation 2.14 the lattice is heated only by energy transfer from the electrons. Moreover, C_e and C_i are the heat capacities (per unit volume) of the electron and lattice subsystems and γ is the parameter characterizing the electron–lattice coupling.

Equations 2.15 and 2.16 describe how the electron heat flux propagates within the metal and how the laser source heats the material, with k_e being the electronic thermal conductivity, β denotes the material's ability to absorb light, $I(t)$ is the laser intensity and $A = 1 - R$ the surface absorptivity [35].

These three equations are associated with three characteristic time scales: τ_e, τ_i, and τ_L, where $\tau_e = \frac{C_e}{\gamma}$ is the electron cooling time, $\tau_i = \frac{C_i}{\gamma}$ is the lattice heating time (with $\tau_e \ll \tau_i$), and τ_l is the laser pulse duration. These parameters define three distinct regimes of laser–metal interaction, commonly referred to as the femtosecond, picosecond, and nanosecond regimes:

- **Nanosecond regime**: For $\tau_l \gg \tau_i$, thermal equilibrium is established between electrons and phonons, such that $T_e = T_i$. As a result, the material is sequentially heated to its melting point and then to its vaporization temperature. In this case, thermal conduction is the main energy loss mechanism, and the threshold fluence for material evaporation scales with $\sqrt{\tau_L}$. Due to the formation of a substantial melt pool, ablation predominantly occurs from the liquid phase, which significantly reduces the precision of the processed features.[35]

- **Picosecond regime**: When timescales satisfy $\tau_e \ll \tau_l \ll \tau_i$, a partial electron–lattice coupling occurs, leading to a transient quasi-equilibrium state between the two subsystems. During this stage, hot electrons exhibit a significantly higher temperature than the lattice ($T_e \gg T_i$). Although surface ablation is still dominated by a solid-vapor transition, localized melting may occur below the surface, slightly compromising processing precision [35].

- **Femtosecond regime**: When $\tau_l \ll \tau_e$ a strong non-equilibrium condition is established between the electronic and lattice subsystems, therefore both electron–lattice interactions and thermal diffusion into the bulk can be neglected. Under these conditions, the maximum lattice temperature is predominantly governed by the electron cooling time, typically on the order of a few picoseconds. In this ultra-fast regime, the ablation depth per pulse follows a logarithmic dependence on the laser fluence. Material removal occurs via direct solid-to-vapor or solid-to-plasma transitions, allowing a high precision in the created structures during processing [35].

As discussed earlier, the mechanisms of laser ablation vary significantly depending on pulse duration, leading to a distinction between *short-pulsed* (nanosecond, ns) and *ultrashort-pulsed* (picosecond/femtosecond, ps/fs) regimes (see Figure 2.10).

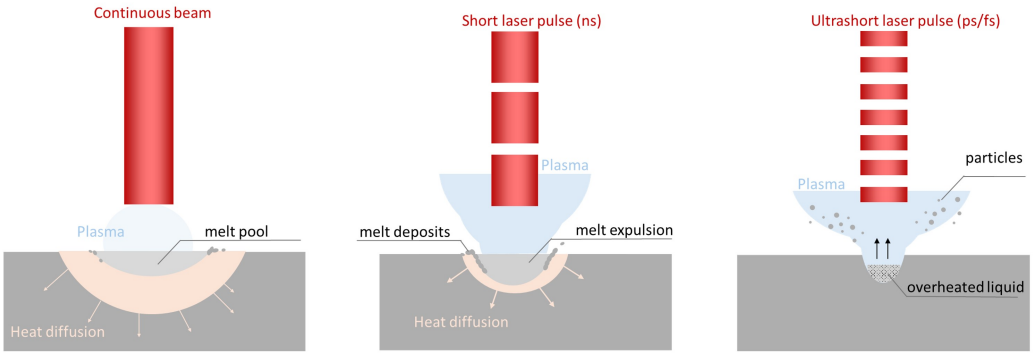

Parameter	CW	PW ns	PW ps/fs
Melt Pool	Wide and shallow	Narrow, deep, unstable	Negligible (cold ablation)
Material Ejection	Slow dripping	Violent spattering (ejecta)	Minimal debris (ultra-clean removal)
Heat Diffusion	Extensive (large HAZ)	Moderate (localized HAZ)	Minimal (no HAZ)
Plasma	Weak or absent	Dense, bright plasma	Transient, ionized plasma
Key Mechanisms	Conduction + melting	Vaporization + melt expulsion	Non-thermal ablation

Figure 2.10: Beam-Matter ablation dynamics by short (left) and ultrashort (right) laser pulses (adapted from [40].

In nanosecond laser processing, the absorbed laser energy heats the material, leading to melting and vaporization. The vaporized material exerts pressure on the molten layer, displacing it toward the edges of the ablation crater, where it is ejected as liquid droplets or re-solidifies as debris. Due to the relatively long pulse duration (typically >1 ns), thermal diffusion plays a dominant role, resulting in a pronounced heat-affected zone (HAZ) that extends beyond the ablated region. This thermal diffusion can cause undesirable effects such as recast layers, micro-cracking, and collateral damage to surrounding material, particularly in heat-sensitive applications [41, 42].

In contrast, ultra-short pulses (typically $\leq$ 10 ps) interact with matter in a fundamentally different way. The extremely short pulse duration confines energy deposition to a timescale shorter than electron-phonon coupling (typically a few picoseconds), minimizing thermal diffusion. This leads to non-thermal ablation mechanisms, where the material is directly ionized into a highly energetic plasma before significant heat conduction occurs.

The rapid energy deposition generates extreme pressures ($> GPa$) and temperatures, accelerating ionized material at supersonic velocities. Since the pulse ends before significant heat transfer to the lattice, continuous vaporization is suppressed, creating a metastable, superheated state that undergoes phase explosion or explosive boiling [43]. This process ejects a mixture of vapor, liquid droplets, and fragmented solid particles, significantly reducing the HAZ and producing cleaner, more precise ablation features.

Ablation model for ultra-short pulsed lasers

Ultrashort pulsed lasers have became of industrial interest thanks to their ability to remove material with minimal thermal damage, high spatial resolution, and reduced heat-affected zones. Understanding the processes of the laser-material interaction is necessary to enable efficient laser processing. Unlike longer pulse processing, this interaction is controlled via direct sublimation for ultrashort pulses, bypassing the liquid phase. By adopting the approach in Ref [44] the laser beam at the entrance of the scanner is characterized by a two-dimensional Gaussian shape with a fluence distribution described by:

$$F(r) = F_{max}\, e^{\frac{2r^2}{w^2}}\ [J/cm^2] \tag{2.17}$$

$$F_{max} = \frac{2\,E_p}{\pi w^2}\ [J/cm^2] \tag{2.18}$$

With $F_{max}[Jcm^{-2}]$ being the laser peak fluence in the center, r is the radial distance from the beam center, w is the laser spot radius and $E_p[J]$ is laser pulse energy, described as $E_p = P/f$. In ultrashort pulse lasers not all the energy is efficiently used to remove the material, part remains in the latter as residual heat and part of the energy is emitted from the surface with the hot liquid/gaseous matter [45, 46]. To ensure efficient material removal, laser has to work near its optimum fluence, which is a function of the material's fluence threshold. Threshold fluence F_{th} is the value of local fluence F(r) after which material ablation occurs, hence when $r = D/2$ where D is the diameter of the ablated crater. In this case, as illustrated in Figure 2.11, the measured diameter of the crater D can indicate the exact value of F_{th} by fitting the linear equation of $D^2(ln(F_{max})$ [47]:

$$D^2 = 2w^2 ln(F_{max}) - 2w^2 ln(F_{th}) \tag{2.19}$$

However, the threshold value can drop due to progressive irradiation. The most common way to describe this phenomenon, known as the heat incubation effect, is by the material-dependent incubation factor S when calculating F_{th} at different numbers of pulses per spot N. The multi-pulse ablation threshold is represented as:

$$F_{th}(N) = F_{th}(1) \cdot N^{S-1} \tag{2.20}$$

where $F_{th}(1)$ is the single pulse ablation threshold. The accumulation coefficient S is extracted experimentally and varies depending on the laser wavelength, laser pulse and pulse repetition rate.

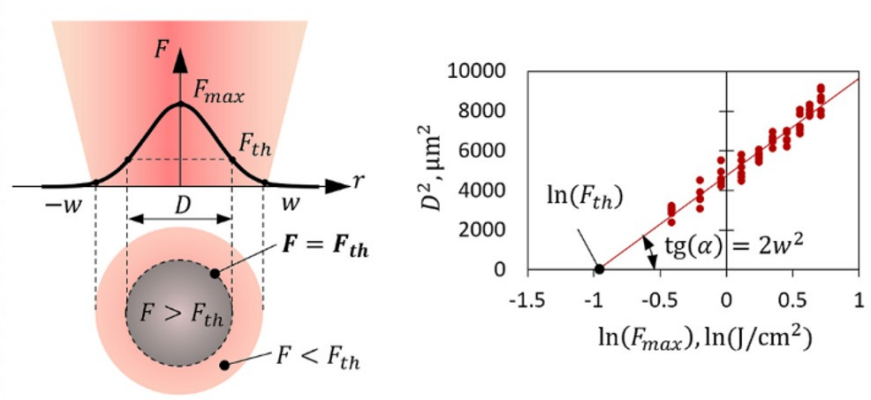

Figure 2.11: Ablation threshold calculation for ultrashort pulsed laser beams (adapted from [47]).

2.3 Monitoring systems

The internal structure of a battery system is made up of several cells which, when connected efficiently, form a module and ultimately a pack, ensuring a reliable and continuous energy supply. Specifically, in each cell, electrical current generated within the electrodes, is collected by a tab, which is a metal strip welded to the electrode foils. Each tab functions a bridge, enabling the transfer of the current to a busbar, a thicker conductor that connects multiple tabs or cells together. From the busbar, the current flows to the terminal which serves as an external connection point to the external load. These tab-to-busbar applications require the weld seams to resist thermal expansion and vibration for the entire life of the car. In this context, the connections between cells play a fundamental role in certifying the stability, duration, and efficiency of the battery.

Typical materials for these applications are aluminum (Al) and copper (Cu). Since the difference in physical and chemical performances, it is difficult for Cu to dissolve into Al during welding, and results in defects such as cracks, porosity, and brittle IMCs in the welded joint. Laser beam welding is a fusion welding technique [48] allowing for the material to absorb the energy of laser radiation, convert it into heat, melt the metal, and form a molten pool. Process parameters need to be thoroughly optimized to allow defect-free weld seams.

Failures induced by uncontrolled weld quality lead to three main disadvantages: (1) damage to the battery, i.e. uncontrolled penetration of the weld leads to the risk of puncture of the battery cell, resulting in the leakage of harmful gases and fire, and (2) the scrapping of the entire battery pack as even a single faulty weld, if undetected, can cause the entire battery pack to malfunction (e.g. voltage drop) (3) formation of intermetallic phases in the welding of dissimilar materials resulting in sag of mechanical and electrical properties.

Nowadays it is well known how to conduct lap- or butt-joint weldings with dissimilar highly reflective metals, as shown by Katayama et al. [49]. The challenge today is when it comes to high production rates and high demand of quality required by a zero-defect process. Industrial production speeds can reach up to 5–10 batteries/sec and the assembly of a single battery pack can contain up to 20,000 welds [50]. It

is estimated that each Gigafactory produces 6% circa of defected cells and battery modules [51]. Since most of the materials (electrodes, cell separators, electrolytes) are not fully recyclable and the whole disposal process is pricy, the quality target of the process has been set to 99.7% [52]. This highlights the central role of a monitoring system that gathers information from the process improving the understanding of the detecting phenomena. It uses the collected data to create quality control methods and adaptive, closed loop control of the process [53]. Hence, as the number of destructive samples inspections are minimized, the implementation of a monitoring system can be seen as a product certification.

A lot of studies of online quality control have been carried out aiming at reducing or eliminating product quality defects and process errors. Nowadays monitoring systems range from simple systems using single sensors to more sophisticated systems which utilize a great deal of sensors and detection methods, as shown by You et al. [54] and Cai et al. [55]. The latter reviewed three-hundred-ish papers describing the typical sensors used for laser welding and adaptive control: it ranges from photodiodes, visual sensor, spectrometer, acoustical sensor, pyrometer, plasma charge sensor to the application of artificial intelligence algorithms.

The following three sections will focus specifically on photodiodes, optical microphone technology and high-speed imaging, as these represent the technologies I was able to examine in greater detail during my research period abroad.

2.3.1 Photodiodes

Online laser welding quality control can be assessed based on photodiodes, which measures the electromagnetic emissions from the welding process. Mostly, three photodiodes are employed, each of which monitors a particular range of wavelengths, as shown in Figure 2.12a).

Laser light is transmitted through a 90° dichromatic folding mirror (which is transparent to the laser wavelength) towards the focusing lens that focuses the laser beam on the weld zone. The light emitted from the weld process is captured by the same focusing lens and reflected by the folding mirror towards the sensors. The coaxial setup makes it easy to align the sensors which register different wavelengths.

For processes utilizing near-infrared (NIR) laser sources, the characteristic detenction bandwidths are as follows: a S_P sensor (∼300nm-700nm) aimed to monitor plasma activity, a S_T sensor (∼1200nm-2000nm) acting as an IR detector (temperature) and an S_R sensor with a narrow band pass filter at the laser wavelength (∼1020nm-1090nm). The S_R sensor monitors the reflected light from the weld zone area and can be used as an indicator if conduction welding or keyhole welding is used. The signals from the diodes are sampled and processed in a computer. In practice, the systems sold today are of the 'golden template' type. The monitoring system records the sensors' values during welding. After a large number of good welds, a golden template signal is created (often the mean signal). Afterwards the monitoring simply compares the current sensor signal with the golden template, if the difference is too big, an alarm is triggered. One problem with this technique is that it requires a long learning period for the monitoring system, so it is not suitable for small batch production.

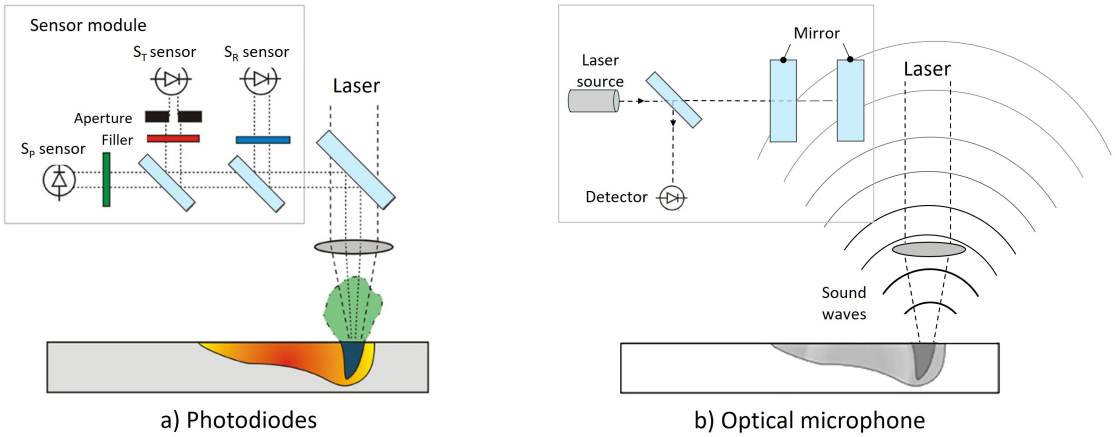

Figure 2.12: Monitoring sensors in laser welding: a) Photodiodes which captures three different signals in three wavelengths (adapted from [56]); b) Optical microphone and its detention principle from Fabry-Pérot interferometer (adapted from [57]).

2.3.2 Optical Microphone

Acoustic monitoring has been explored to detect welding defects. However, the main issue was related with its high sensitivity to the background noise, making it challenging to isolate relevant weld features [58].

The advancement of optical microphone technology, which can detect acoustic signals across an exceptionally wide frequency spectrum (extending from approximately 10 Hz to several tens of MHz) has sparked renewed interest in non-invasive acoustic monitoring of laser welding. Unlike conventional microphones that rely on a mechanically vibrating membrane, optical microphones operate entirely without moving parts, which substantially reduces their sensitivity to ambient noise. This allows for improved signal fidelity and clearer distinction between relevant process-generated acoustic emissions and environmental interference. Notably, this frequency range surpasses that of human auditory perception (20 Hz to 20 kHz), enabling detailed analysis of ultrasonic events related to laser–material interactions.

The core operating principle of these sensors is based on a Fabry-Pérot interferometric setup, as schematically illustrated in Figure 2.12b. The system comprises a micro-scale optical cavity formed by two parallel, partially reflective mirrors. A continuous-wave monochromatic laser is directed into this cavity. When acoustic pressure waves, originating from the welding process, propagate through the cavity, they modulate the density (ρ) of the medium (typically air or another transparent gas), and therefore also its optical refractive index (n) between the mirrors. In a medium, the wavelength of light (λ) depends on the refractive index as [57]:

$$\lambda(n) = \frac{c}{n(\rho)}\frac{1}{f} = \frac{\lambda_0}{n(\rho)} \tag{2.21}$$

where f denotes the frequency, c the speed of light and λ_0 the vacuum wavelength. The measurement laser beam propagating through the medium is exposed to an acoustic field and experiences a slight modulation of its optical wavelength, which is directly related to the local density and, consequently, to the sound pressure.

Therefore, the sound field induces changes in the laser wavelength and hence on its light intensity reflected by the cavity. This changing can be detected by a photodiode, which transduces the signal into an electrical voltage.

The acoustic emissions themselves arise from the intense thermomechanical activity occurring in the weld zone. As the high-energy laser beam interacts with the workpiece, rapid heating causes localized vaporization and the formation of a transient vapor cavity, commonly referred to as the keyhole. The oscillatory behavior and periodic collapse of the keyhole, along with recoil pressure fluctuations and molten metal flow, generate acoustic waves across a broad frequency range. Specifically, low-frequency components are typically attributed to unstable keyhole dynamics and turbulent fluid motion within the melt pool. In contrast, higher-frequency signals are associated with more abrupt phenomena such as droplet ejection, rapid solidification fronts, or phase transformations within the molten or semi-solid material.

2.3.3 Highspeed camera

High-speed imaging is a powerful tool for monitoring laser welding processes, allowing the capture of rapid phenomena such as keyhole dynamics, melt pool behavior, and spatter generation. A high-speed camera records thousands to millions of frames per second (fps), enabling detailed visualization of events that occur on microsecond timescales. The main components of a high-speed camera system include the lens (to collect and focus light), the sensor (typically a CMOS sensor capable of readout speeds greater than 10 Gbps), an internal memory buffer (typically 8 to 64 GB for temporary storage), a processor (for image management and triggering control), a cooling system (to stabilize sensor temperature during high-speed operation), and various input/output ports for synchronization and data transfer.

Several key parameters characterize the performance of high-speed imaging.

- **Frame rate:** determines the temporal resolution and it is commonly between 5,000–100,000 fps for laser welding (higher rates >500,000 fps are used for very fast phenomena like plasma dynamics).
- **Exposure time:** typically in the range of 1–10 microseconds, short enough to "freeze" motion without blur.
- **Spatial resolution:** depends on the sensor's pixel count and size, often requiring a trade-off between resolution and frame rate. For instance, 1024×768 pixels at 10,000 fps, dropping to 256×128 pixels at 500,000 fps.
- **Pixel size:** Typically between 10–20 microns, balancing sensitivity and resolution

Integration of the high-speed camera with the laser welding system is critical for effective monitoring and depending on the process, what different set up must be conducted, as summarized in the following table.

The camera can be installed coaxially with the laser beam by using a dichroic beam splitter (reflecting visible light while transmitting the laser wavelength) placed in the optical path. Alternatively, it is often mounted with a small *inclination* (around

Phenomena Observed	*Need of*	*Resolution*	*fps*	*Shutter*
Keyhole, spatter, plasma	Very high fps	Low	>100k	Very short (<1μs)
Fusion and dynamic pool	Balance quality/speed	Mid (ex. 1024x1024)	5-20k	1-5μs
Slow movements or general analyses	High resolution	High	1-4k	10-20 μs

Table 2.1: Sum up for laser welding processes

10–45°C from the beam axis) to minimize direct reflections, protect the sensor, and improve visibility of the melt pool and keyhole dynamics.

The camera is synchronized with the laser pulses and, if used, with the motion control system (robot, scanner) through an external triggering device, ensuring that the image acquisition matches precisely the welding events.

Additional illumination sources are required when very high frames rate are set to ensure sharp and clear images. Specifically, at high frame rates, exposure time per frame decreases drastically. For example, ranging from 1,000 fps to 100,000 fps, the exposure time decreases from 1 ms to 10 μs. As the exposure time shortens, less light reaches the sensor, resulting in darker images and increased noise unless compensated with strong illumination. There is no hard cutoff, but typically for >20,000fps specialized light sources (e.g. LED arrays, lasers) become crucial. In these cases, where micro-sized details must be captured, a pulsed coherent laser illumination is often preferred due to its high optical power density and narrow spectral bandwidth, as shown in Figure 2.13.

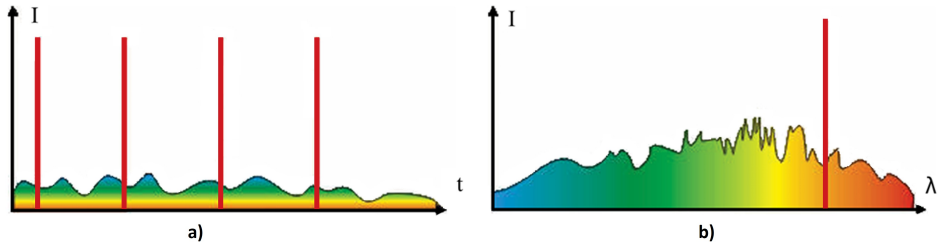

Figure 2.13: Monochromatic pulsed laser radiation effectively suppresses background process light by: a) delivering short, high-intensity pulses, and b) emitting within a narrow spectral bandwidth. (adapted from [59]).

When combined with narrow bandpass filters mounted on the camera lens, laser illumination enables selective imaging by suppressing broadband process emissions and ambient light. This approach is particularly effective for isolating the melt pool from the surrounding thermal radiation or plasma, enhancing contrast without increasing sensor gain [60].

Instead, for large-scale processes, such as directed energy deposition (DED) or laser welding with wide melt pools, the use of high-power LED arrays or diffused halogen sources is often more appropriate. These light sources offer broad, uniform illumination over larger fields of view and reduce coherence-related artifacts. In addition, pulsed or strobed LED lighting can be synchronized with the camera's exposure window to minimize motion blur and thermal noise, particularly at frame rates up to 20,000 fps. LEDs are also safer and more flexible in terms of installation and beam shaping compared to lasers, making them suitable for robust industrial setups.

As introduced earlier, in cases where imaging must be performed in the presence of intense plasma or arc emissions, such as in hybrid laser-arc welding or plasma-enhanced processes, bandpass-filtered monochromatic illumination (from either lasers or narrow-band LEDs) remains essential to reject background light and improve signal-to-noise ratio. Usually, these filters are centered at 808 nm, 1064 nm, or visible emissions.

High-speed imaging provides invaluable insights into transient process instabilities and defect formation. However, it also presents challenges, including the high cost of equipment (cameras ranging from 20,000 to over 100,000 €), the need for careful optical alignment and synchronization, large data generation, and complex image interpretation due to light emission phenomena during welding [54].

Chapter 3

State of the Art

In this chapter, the relevant scientific literature of two different manufacturing steps of LIBS are presented. First, in Section 3.1, cut edge quality of current collectors and electrodes is discussed along with laser-material interaction and production engineering aspects. Subsequently, in Section 3.2, three types of monitoring systems that assess tab-welding product quality are presented. Based on the state of the art, the research gap is identified at the end of this chapter in Section 3.3.

3.1 Laser cutting

Trimming of current collectors

The production of LIBs for automotive applications integrates several laser-based processes, among which current collector cutting plays a central role. Laser technology has become widely adopted thanks to its high flexibility, processing speed, and cut quality, which are crucial factors to meet the increasing productivity requirements of gigafactories [10].

Current collectors are thin metallic foils, typically copper (6–10 μm) for the anode and aluminum (12–30 μm) for the cathode, which act as conductive supports for the active material layers. Traditionally, these foils can be processed either mechanically, through die cutting or rotary knife slitting, or thermally, by means of a laser beam. Mechanical methods are cost-effective but limited by frequent tool wear, burr formation, and process interruptions. In contrast, laser cutting is a non-contact thermal process that enables high throughput (several meters of foil per second), pattern flexibility, and high cut quality by minimizing defects linked to laser–material interaction [61].

The main industrial concern in current collector cutting is related to edge defects, such as spatter, dross formation, and burrs, which can compromise battery safety. Spatter may redeposit on the electrode surface and induce uneven current distribution, promoting dendrite growth and short circuits [62].

Dross, on the other hand, results from incomplete vaporization and may remain attached to the cut edge, later detaching as metallic particles that risk piercing the separator [63]. Consequently, the elimination or strong reduction of these defects is a primary requirement.

Several studies have analyzed the mechanisms behind defect formation. Lee and Mazumder [64] explained spatter generation as the result of molten metal flow dynamics around the keyhole, where liquid is ejected and resolidifies. Similarly, the transition

between dross formation and spatter detachment has been correlated to the recoil pressure and Weber number, which describe whether the melt breaks into droplets or continuous jets. The choice of laser source (CW vs. PW), beam quality, and process parameters strongly affects these dynamics.

Different laser sources have been investigated. Luetke et al. [13] compared CW and nanosecond PW lasers for cutting thin Cu and Al foils, reporting cutting speeds up to 5 m/s. However, to satisfy the throughput targets of the automotive sector, scanning speeds of at least 16 m/s are required, corresponding to one battery per second in gigafactory production. Only recently, CW single-mode fiber lasers have enabled ultra-high-speed remote cutting, reaching scanning speeds of 20–30 m/s, and demonstrating the feasibility of industrially relevant production rates. At such speeds, understanding the interplay between irradiance, fluence, melt pool dynamics, and defect formation is still an active research field.

To minimize thermal effects and improve cutting quality many studies have been conducted using ultrashort pulsed laser beams (pulse length $< 10ps$). The main challenge of ultrashort laser power limitation or efficient ablation evolved gradually over time: the average power doubles every three years, with pulse repetition rates (PRRs) reaching tens of megahertz [65]. Even at such high pulse repetition rates, the resulting fluence exceeds the optimal one. A practical solution to reduce pulse energy (and fluence) without sacrificing the average power is temporal pulse division, which creates *pulse bursts*. These bursts typically feature intra-burst repetition rates in the MHz-GHz range, significantly enhancing ablation efficiency and reducing surface roughness [66]. However, the use of such techniques for cutting LIB electrodes remains limited, being applied intensively in micromachining. The primary challenges for industrial implementation up to now include relatively low processing speeds, high investment costs and the delicate requirements of the equipment and environment (e.g., a controlled atmosphere). Pico-second lasers in burst mode have improved cutting speeds of Cu current collectors (CCs) up to 3.8 m/s and reduced heat-affected zones HAZ [67]. Heidari Orujo et al. [68] optimized burst fluence in 10 ps laser cutting of CCs, achieving peak speeds of 4.7 m/s and 2.1 m/s for Al and Cu, respectively. It was not observed any improvement when varying the burst shape, namely equal pulse (EP) and increasing pulse (IP).

Cutting of electrodes

The sandwich-like structure of electrodes makes laser processing more challenging, as differences in melting point, thermal conductivity and optical absorptivity between the metallic collector and the active material can lead to delamination, HAZ enlargement, and active material loss. Laser processing on electrodes, as for CCs, is advantageous compared to mechanical cutting, since it avoids tool wear and downtime, while enabling higher precision and throughput [13]. However, as a thermal process, it may induce spatter, burrs, HAZ, and microstructural changes in the active layers, which negatively impact battery performance.

Nanosecond pulsed fiber lasers have historically dominated due to their ability to combine high beam quality with reduced thermal load, producing narrow kerfs at moderate speeds.

Lutey et al [69] explored five different laser sources to optimize the trade-off between

cut quality and productivity, including near-infrared (NIR) nanosecond pulsed fiber lasers, continuous wave laser and green lasers on both LFP and NMC cathodes. They found that in the pulsed mode, in order to minimize the heat conduction losses in the metallic layers, shorter pulse length and high speeds are preferred.

More recent research has investigated ultrashort pulsed lasers (ps–fs regime), which enable ablation-dominated material removal with minimal HAZ, though their limited productivity and high cost hinder large-scale industrial adoption. Gu et al. [70] showed that femtosecond laser cutting of LFP cathodes at high power can cause delamination and severe remelting, while Zhang et al. [71] reported increased HAZ and delamination for higher pulse energies and pulse width in graphite anodes. Laser source manufacturers have introduced an innovative burst mode feature, allowing control over pulse energy. Heidari et al.[68] found that increasing the number of pulses per burst and frequency lowers the peak fluence of each pulse, making it easier to fine-tune the optimal peak fluence and achieving higher processing speeds. Audouard et al. [72] applied GHz-burst mode for anode cutting and stated that the cutting time is mainly driven by the metal collector of the electrode (Cu- foil for anode, Al-foil for cathode).

Conversely, single-mode CW fiber lasers have emerged as promising candidates for high-speed electrode cutting, reaching powers above 1 kW and scanning speeds up to 5 m/s while still maintaining acceptable cut quality on both graphite and LCO cathode [73]. Challenges remain in balancing the energy input between the metallic collector and the active coating. Since the foil requires longer exposure to achieve full penetration, the active material often undergoes overheating, delamination, and capacity loss. Computational models [64] have further highlighted how melt pool flow, absorptivity, and temperature distribution differ significantly at the collector–active material interface, making process optimization highly material-dependent.

Overall, while ultrafast lasers guarantee maximum cut quality and CW lasers provide superior throughput, defining the optimal parameter window for electrode cutting when materials are changing rapidly remains a key research direction, especially under the industrial constraints of speed, cost, and scalability.

3.2 Monitoring systems

Monitoring methods for laser processing rely on detecting the physical phenomena generated by the interaction between the laser and the material. These methods are typically based on acoustic, optical, or thermal signals, and are often combined to enhance monitoring accuracy and effectiveness. For example, a microphone is used to collect the acoustic signal. Vision sensors like charge-coupled devices (CCD), complementary metal-oxide semiconductors (CMOS) and high-speed cameras with special filters are applied to capture the images of the keyhole, molten pool, spatters and plasma. Spectrometers, and photodiodes are utilized to collect the optical signals include visible light (VIS), infrared light (IR), and ultraviolet light (UV). The IR cameras, near-infrared (NIR) cameras, and pyrometers can be exploited to gather the thermal signal. In this thesis, the application of these sensors will be restricted to laser welding.

3.2.1 High-speed cameras

The need of improving efficient laser welding monitoring calls for a deep knowledge of the process. For this reason, high-speed cameras are widely used for laser welding process diagnosis since it is possible to observe the morphology of the melt pool area and keyholes. For instance, Fabbro et al. [74] observed that the bottom aperture of the keyhole was visible from the top, and the angle of the front keyhole wall varied with processing speed. Kim et al. [75] investigated laser keyhole welding of zinc-coated and uncoated steel sheets, revealing that keyhole position and size changed based on process conditions and material properties. Huang et al. [76] employed transparent glass to observe keyhole behavior and porosity formation in aluminum alloys, finding that increased magnesium content led to more stable keyhole formation due to higher internal pressure. Moreover, Hellwiga et al. [77] investigated the relationship between spatter dimensions and their detachment mechanisms as a function of the scanning speed.

To further understand and predict weld outcomes, numerical simulations such as finite element methods (FEM) and computational fluid dynamics (CFD) have been integrated with high-speed imaging results [78]. These simulations allow detailed exploration of temperature gradients, melt pool convection, and vapor recoil pressure, which are otherwise difficult to quantify experimentally. When paired with imaging data, simulations can be calibrated more accurately, improving the reliability of models for parameter optimization of laser welding of dissimilar materials. For instance, Rong et al. [79] investigated the effect of welding speed on the three-dimensional geometries of weld pool and keyhole using high speed imaging and simulation.

Recent advances include the application of AI and deep learning models trained on high-speed video datasets to automatically classify keyhole states and predict defect likelihood. For example, Ma et al. [80] research developed real-time method to predict porosity during laser welding of aluminum alloys by analyzing the 3D shape fluctuations of the keyhole using a high-speed camera. The signals were processed with advanced algorithms (EEMD, PCA) and used a neural network, optimized by a genetic algorithm, to predict local porosity. The model proved accurate and showed that pores form slightly after keyhole fluctuations, due to molten metal flow.

3.2.2 Photodiodes

The influence of process parameters can be effectively mitigated by using sensors that passively monitor emissions generated during laser processing. Among these, photodiodes are particularly advantageous due to their simple design, low cost, and ability to capture various types of radiative signals. Specifically, they can detect emissions from metal vapor and plasma plumes (S_P signal), thermal radiation from the processing zone (S_t signal), and reflected laser light (S_R signal). A typical photodiode configuration is shown in Figure 2.12a), where three separate sensors are employed to capture radiation within distinct spectral ranges. For processes utilizing near-infrared (NIR) laser sources, the characteristic detection bandwidths are as follows: S_P sensor (300–700 nm); S_R sensor (1020–1090 nm); S_T sensor (1200–2000 nm).

The signals recorded by the sensors can then be processed using AI algorithms

to correlate the process outcome quality with the statistical analysis of the signals. Lee et al. [81] employed a support vector machine alongside two deep learning models—a fully connected neural network and a convolutional neural network—to classify weld penetration quality based on photodiode signals, categorizing them as insufficient, transient, or satisfactory. A bandpass filter was applied to isolate the emission wavelength specific to copper. The models produced predictions at 50 ms intervals and achieved classification accuracies exceeding 90%. The convolutional neural network, in particular, was validated experimentally by progressively increasing the laser power, demonstrating its effectiveness for estimating penetration in Al/Cu laser welding.

While photodiode-based monitoring has been widely adopted in structural applications—such as automotive door assemblies, seat frames, and body side structures—its application to thin foils and dissimilar metal welding remains largely unexplored. Recent findings suggest that variations in part-to-part gap and laser power can be detected through abrupt changes in the plasma signal [52]. In a recent study, Chianese et al.[82] investigated whether photodiodes combined with supervised machine learning algorithms could automatically identify weld defects induced by simultaneous variations in part gap and laser power during remote laser welding of copper to steel, a process relevant for battery tab connections. Their approach achieved a classification accuracy of 97%. However, when scaled to high-volume manufacturing—where a single battery pack may contain up to 20,000 welds—even a 3% error rate could result in approximately 500 misclassified welds. Extrapolating this to annual production volumes in the hundreds of thousands, the implications of such misclassification rates become substantial.

One of the main issues in welding dissimilar metals such as aluminum and copper is the formation of intermetallic compounds (IMCs), which increase brittleness and electrical resistance at the joint. Seibold et al.[83] developed a real-time process control system for pulsed laser beam welding that uses material (specific optical emissions detected by photodiodes with band-pass filters) to dynamically shape each laser pulse. The control system, with a response time under 10 µs, interrupts the laser pulse once the emission signal indicates the onset of melting in the lower joining partner. Experimental results show that this approach significantly reduces mixing and IMC formation. Micrographs confirmed a minimal melt depth in the copper layer, though at the expense of reduced mechanical strength due to the limited fusion area.

3.2.3 Optical Microphone

Besides optical emissions, the acoustic process emissions serve as a valuable source of information [84].

In addition to conventional measures for describing central tendency of the signal (mean, median, and mode) and variability (interquartile range, range, variance, and standard deviation), the application of L-statistical features was considered. These moments were used by Yusolf et al. [85] when analyzing the sound signal acquired from a microphone during a butt joined steel plate laser welding using a pulsed mode. Specifically, L-Cv (scale) was found to be an indicator for the weld bead surface condition, with the larger values registered when large underfill occurred. Moreover, L-kurtosis values were found to give insights into irregularities of the weld bead and depth.

Additionally, the AE count (AEc) as a measure developed by Luo et al. [86] was applied. The latter monitored acoustic emissions generated during pulsed laser beam welding of stainless steel. AE counts represents the total number of signal pulses with a peak value exceeding a threshold of 0.5. It was found that a higher AE count value and higher amplitudes in the power spectrum exhibited a higher energy content within the plasma plume.

The use of optical microphones as a tool for monitoring industrial laser welding processes remains largely unexplored. However, first results demonstrated that also higher ultrasound frequencies can be accessed to evaluate the process condition and detect process deviations, free from interference of low-frequency disturbances. Notably, Authier et. al [87] conducted bead on plates experiments on stainless steel or titanium and found that for different laser power integrated over the 40 to 90 kHz band frequency shows a remarkably linear correlation with welding penetration depth. Since it is high above the audio range, it is of special interest in an industrial noisy environment.

Tomcic et al. [88] recorded high-frequency acoustic signals up to 1 MHz and extracted 17 acoustic features, which were then used to train a Gaussian process regression model. They found a strong correlation between weld depth and the zero-crossing rate of the acoustic signal, particularly in the 40 to 90 kHz range, regardless of laser power or feed rate.

In order to mitigate the influence of noise, signal processing was conducted in several studies before extracting signal features. Weiiss et al. [89] applied different denoising procedures and extract time and frequency-domain features to detect, ultimatly, burn-through, humping, and lack of fusion during laser beam welding of thin stainless-steel foils. Wavelet denoising technique was applied [90] to filter acoustic emissions originating from machine. However, it is not always possible to filter out the background noise, as it often shares overlapping frequency bands with the signal of interest [91]. Therefore, careful microphone placement is essential to minimize interference from background noise.

3.3 Conclusion and research gap

As outlined in the previous section, each manufacturing step in Li-ion battery production must aim toward the fabrication of zero-defect parts. This applies to both laser cutting and laser welding processes.

While laser cutting is a widely adopted technology, the continuous evolution of scanner heads, optics, and laser sources necessitates a systematic comparison between pulsed (from nanosecond to femtosecond) and continuous-wave lasers. Given the wide variety of electrode materials and foil thicknesses, recent studies have also explored continuous-wave cutting for both cathodes and anodes, revealing differences in cutting performance and the occurrence of thermal defects, which remain a critical concern.

Laser welding, on the other hand, is demonstrated to be a sustainable method due to its high energy efficiency and potential to minimize defect formation when combined with closed-loop real-time monitoring systems. Hence, the monitoring sensors have the central role of gathering information from the process, which is very sensitive to variations in material stack-up, joint geometry, laser parameters and occurring environment

defects (dust on the plate or gap between the parts to be joint).

A number of research gaps still hinder the reliable and large-scale industrial integration of both processes, particularly with respect to monitoring strategies, processing speed, and quality assurance. These challenges can be categorized into the following key areas:

- **Material-laser interactions:** The performance of laser cutting and welding strongly depends on the physical properties of the materials involved, including thermal conductivity, reflectivity, and thickness. For cutting, the onset of thermal defects such as burrs, dross, and spatters- especially in ultra-thin foils requires further investigation, particularly in relation to different laser regimes (e.g., burst mode, ultrashort pulses).

- **Monitoring strategy and data processing:** Although a variety of sensors have been employed for laser welding monitoring, a clear strategy for selecting the most suitable sensor(s) for specific defects or dynamic process changes is still lacking. Each sensor provides only a partial perspective, and the potential of signal complementarity and sensor fusion remains unexplored. At the same time, the increasing data throughput from high-resolution sensors demands robust, automated, and real-time signal processing methods capable of detecting defects, such as excessive dust on the surface or the gap between the plates to be joint. Developing an integrated and intelligent monitoring system is essential to enable closed-loop control and enhance process reliability.

- **Laser sustainability**: fiber laser welding faces some issues when working with aluminum alloys. Inadequate welding parameters and processes, unreliable welding monitoring, material inhomogeneities, and incorrect alignment or setup all contribute to defects in the manufacturing and assembly of battery packs. Even though achieving defect-free production in a real-world scenario remains a significant concern, it is crucial to investigate the relationship between bead performance and energy consumption to ensure a high-quality joint and enhanced sustainability.

In conclusion, the successful deployment of advanced laser cutting and welding in battery production depends on a deeper understanding of material-process interactions, the establishment of reliable and application-specific monitoring strategies, the development of scalable signal processing frameworks, the integration into high-throughput manufacturing lines, and a comprehensive techno-economic evaluation. These research gaps define the scope of this thesis and have guided the experimental and methodological choices presented in the following chapters.

Chapter 4

Research Approach

This chapter outlines the research approach and methodology used in this dissertation. After defining scientific objectives (SOs) at the beginning, the embedded publications are assigned to these objectives. Subsequently, the experimental and theoretical methods used throughout the research project are detailed.

4.1 Scientific objectives

Based on the research gap identified in Section 3.3, three SOs are defined in the following, outlining the scope of this thesis:

- SO1 Material-laser interaction: The first step is to investigate the cut edge quality of metal foils under different process parameter conditions. It is essential to clarify whether pulsed or continuous-wave lasers are more suitable for this application, along with the advantages and limitations of each technology. Additionally, the distinct physical interactions between short/ultrashort pulsed lasers and continuous-wave lasers with thin metal foils must be described in order to achieve both high processing speed and/or high-quality cut edges. To support this analysis, computational tools and a simplified ablation model are employed, respectively. The interaction will also be studied in the presence of an electrode coating on the current collector.

- SO2 Monitoring strategy and data processing: Study the signal acquisition hardware of various laser welding monitoring sensors, such as photodiodes and optical microphones, while varying the irradiated material, process parameters, laser sources, and beam shaping. This will be followed by a comparison between the acquired photodiode signals and the quality of the resulting weld bead geometries.

- SO3 Laser sustainability: Investigation of laser welding of dissimilar aluminum alloy sheets using linear scanning and laser beam wobbling, both with and without filler wire. Different process parameters are tested for various configurations, with the main aim of identifying the optimal welding configuration that achieves the required strength, minimal defects, suitable morphology, and low equivalent carbon emissions.

Collectively, the three SOs defined above aim at enabling laser cutting of electrodes and laser welding for industrial Li-ion battery manufacturing. They further represent

the conceptual framework for the studies conducted and publications written throughout this dissertation project.

4.2 Contribution of embedded publications

Within the author's research, eight scientific publications (Ps) were issued. Their allocation to the SOs defined in Section 4.1 is visualized in Figure 4.1 and detailed in the following. A granular description of the obtained results is provided in Section 5.1.

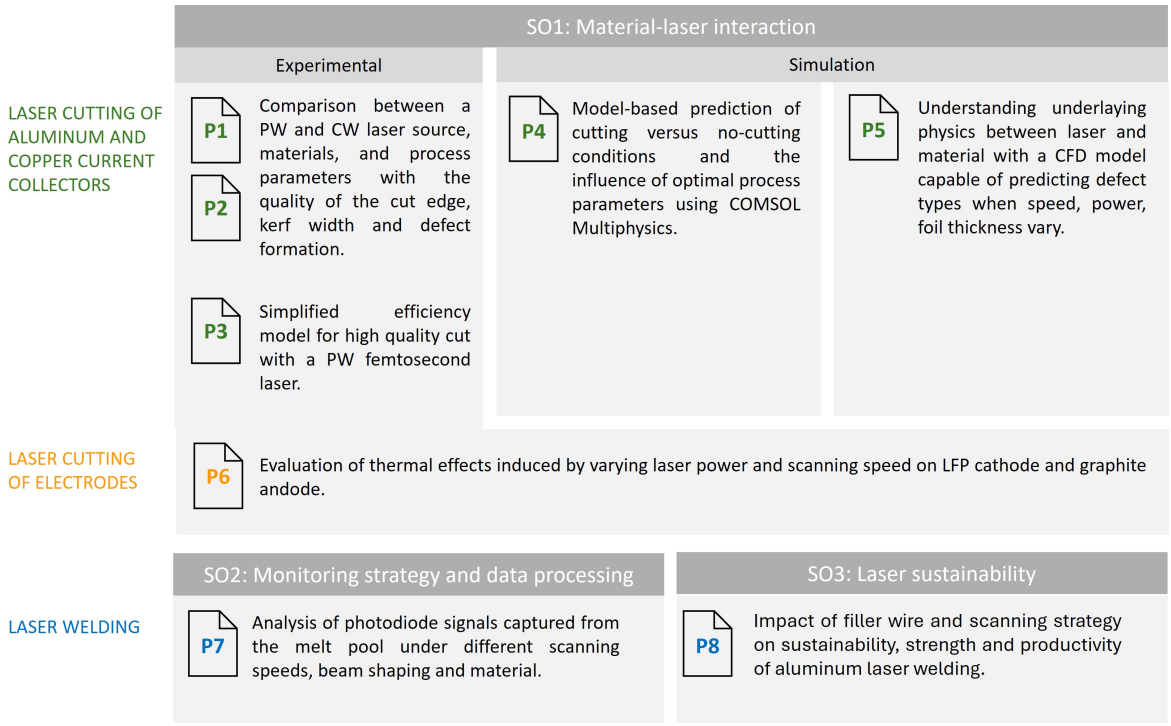

Figure 4.1: Allocation of the publications (Ps) created within this dissertation to the scientific objectives (SOs) defined in Section 4.1

Chapter 5

Results

Expanding upon the scientific approach, goals, and methodology detailed in Chapter 4, this chapter showcases the research outcomes achieved within this dissertation. The results are presented as concise summaries of the author's publications in Section 5.1 while highlighting novelty, consistency, and transferability.

5.1 Summary of embedded publications

5.1.1 P1: High speed laser cutting of ultrathin metal foils for battery cell production

Contenent

The first paper P1 investigates high-speed remote laser cutting of ultrathin aluminum (12 μm) and copper (6 μm) foils, which are key materials in battery cell manufacturing since they are used as LIB current collectors. According to literature, no studies are available on the laser cutting of these materials at speeds higher than 5 m/s.

P1 begins by identifying the limits of current cutting technologies. Mechanical methods, while free from thermal defects, suffer from wear and limited flexibility. Laser cutting, in contrast, offers high throughput, geometric adaptability, and non-contact operation.

The experimental analysis aimed to compare the performance of two laser sources and set-ups in terms of cutting quality and maximum achievable speed. Specifically, a continuous wave and a nanosecond pulsed wave laser sources were employed. For CW laser trials, power ranged from 170 to 1000 W and scanning speed from 1 to 15 m/s. In the case of PW setup, cutting speed was pushed up to 21 m/s while pulse duration was kept constant at 30 ns. The experimental campaign pointed out specific process parameter conditions that led to good cut edges and to specific macroscopic defects. Results showed that CW cutting of aluminum always produced a thin resolidified layer whose uniformity and thickness ($<$10 μm) depended on the specific energy, with optimal value set at 0.33 J/cm. Below this threshold, incomplete or inconsistent cuts occurred, while higher energy led to wider kerfs, thicker resolidified layers, and spatter formation. On copper, the behavior was similar but more sensitive to higher energy input, leading to burns and edge irregularities. An higher optimal specific energy (approximately 0.44 J/cm) was found due to its higher reflectivity and thermal conductivity. For PW cutting, both aluminum and copper yielded clean and regular

cuts when peak power was well tuned (1.7 kW for Al and 1.3 for Cu), even at speeds up to 21 m/s. However, outside the optimized process window, defects were observed, such as burns, spatters and oxidation. Comparing the two technologies, the nanosecond PW laser gave better cut quality at lower speeds for both materials, although some spattering remained evident. On the other hand, CW cutting provided more stable edge quality along the entire cut length at very high speeds and produced zero-defect on the front side of the copper foil.

5.1.2 P2: Characterization and process optimization of remote laser cutting of current collectors for battery electrode production

Contenent

This paper is an extension of paper P1, using the same experimental setups, materials, and methodology, but extending the investigation to scanning speeds up to 28 m/s.

A central innovation of the study lies in introducing a systematic comparison model of fluence and irradiance for CW and PW regimes over the same beam area. Irradiance is calculated as laser power per equivalent area, while fluence is irradiance times the equivalent interaction time. Once the quality was assessed via optical microscopy, the design of detailed process maps for defect classification was carried out. For each combination of material and laser source used, four different maps were designed. Each map effectively correlates defect type with energy input. The identification of the optimal cutting window for each combination of set up and material was identified.

Furthermore, after the assessment of process parameter influence on cut edge quality, an analysis of kerf width was also carried out to assess the amount of material "wasted" during the process.

The main outcome was that CW single mode fiber lasers enabled higher cut quality under all tested conditions, surpassing the current state-of-the-art in metal foil cutting. It performed especially well at very high speeds and was less sensitive to spatter and melt instability. PW laser cutting, while capable of smaller kerf widths due to its tighter focus, is more susceptible to irregular remelting and spatter formation, especially at the high-power densities required for full penetration. However, under low-speed conditions, PW lasers outperformed CW mode in minimizing dross on copper foils.

The work stands out for its experimental completeness, its innovative energy modeling across different laser regimes, and for pushing the operational limits of high-speed laser cutting in battery manufacturing.

5.1.3 P3: Simplified efficiency model for high quality cut with a PW femtosecond laser

Contenent

P3 of this dissertation analyses femtosecond laser cutting of copper and aluminum current collectors, with a focus on the different interaction between single pulse mode (SP) and burst mode (BM) at high frequencies (MHz and GHz).

The aim was to enhance ablation efficiency and cut edge quality, keeping aside the productivity demands. The experimental campaigns were carried out on 8 μm (Cu) and 12 μm (Al) in a controlled environment, with a laser pulse fixed at 200 fs and average power at 40 W. Different levels of scanning speed, frequency and number of pulses per burst (from 1 to 10) were studied to evaluate the performance in terms of ablation threshold, thermal accumulation, kerf width and defects such as burrs, spattering and heat affected zone (HAZ).

The study carried out a dual analysis of cut efficiency and quality, which led to the development of a simplified model that quantified the fraction of laser energy effectively used for ablation and the portion retained in the material.

The results showed that in SP mode the maximum efficiency was reached at the pulse repetition rate of 400 kHz for both Al (0.76) and Cu (0.86). The higher cutting efficiency in copper was due to its higher thermal conductivity, making it less sensitive to thermal accumulation. BM improved cutting speed: up to 3.0 m/s for Al and 3.4 m/s for Cu, approximately 3.8 times faster than SP. However, it involved thermal side effects, such as the formation of molten zones and spattering, especially in Al, losing the benefits of "cold" ablation.

Cutting quality deteriorates at high frequencies with excessive pulse overlap, resulting in the formation of burrs on the cut edges, spattering, and HAZ. The use of shielding gas (argon) has shown that HAZ can be attributed to thermal reactions between the hot metal and the environment.

While the proposed efficiency model is intentionally simplified, it enables efficient rapid extraction of key insights into SP experimental quality with minimal computational cost. The research confirms that, despite the technical challenges, the BM femtosecond laser represents a promising solution for the high-quality and high-speed fabrication of electric vehicle batteries if the average power of the laser will be increased. P3 approach captures the main trends related to intra-burst pulse separation and repetition rate, offering a practical tool for analyzing process conditions and cut edge quality without requiring complex simulations.

5.1.4 P4: Remote laser cutting of metal foils for battery electrodes fabrication: modeling of the process and experimental validation

Contenent

For P4 of this dissertation, a simplified thermal model for remote laser cutting current collectors was presented. The main goal was to optimize process parameters and predict cutting thresholds, the onset of defects, and kerf widths while minimizing thermal damage and material waste for both aluminum and copper foils.

The experimental setup includes a 1200 W CW single-mode laser with a 65 µm spot size, focused through a 340 mm F-theta lens and steered by a galvanometric scanner. Cutting tests were conducted at speeds ranging from 1 to 20 m/s and laser powers from 50 to 1200 W, resulting in energy densities from 4.9 to 2350 J/cm^2. CUT/NO-CUT thresholds were experimentally identified for each speed/power/material combination. Despite being thicker, aluminum required lower power than copper to achieve full cuts

under identical speeds. Consistently with the results obtained from previous studies, the main defects observed included dross and melted edges at low speeds and moderate irradiance, and spatter at high speeds (≥12 m/s for Al, ≥20 m/s for Cu). Burn defects were observable in copper at powers above 830 W, though with negligible width. The optimal process window was found for fluences just above the no-cut condition.

The thermal model, developed in COMSOL Multiphysics®, solves the time-dependent Fourier equation over a refined 3D domain (max mesh size 3 μm). Cutting is considered successful when the temperature reaches the material's boiling point (2467°C for Al, 2570°C for Cu) at both the surface and the bottom of the foil. Calibrated absorptivity values were 0.31 for aluminum and 0.19 for copper. The model demonstrated high accuracy in predicting CUT/NO-CUT thresholds, defect formation, and kerf width, with a maximum error below 10%.

Results demonstrate that the proposed model accurately predict optimal process parameters for cutting thin, highly reflective foils with CW lasers, while requiring low computational time. High-quality edges are achieved even at ultra-high speeds (≥10 m/s). The main bottleneck for cutting beyond 20 m/s is the limitation of the scanning system.

5.1.5 P5: Numerical and experimental study of highspeed laser cutting of copper current collectors

Contenent

P5 investigates the interaction between a CW laser and copper current collectors using a CFD framework that has been tuned and validated through experimental analysis. Previous research defined working areas of good cutting and macro-defects. However, the main challenge with the CW cutting of copper foils, when optimal parameters were set, was avoiding spatter and dross formation. Hence, P5 investigated the physics of matter interaction to understand the protagonist forces that led to the onset of defects. In particular, it was examined the impact of laser power (200-1000 W), cutting speed (2-25 m/s) and foil thickness (8-16μm) on cutting quality.

The CFD model takes into account temperature-dependent properties, (such as surface tension, laser absorptivity, viscosity, etc.), phase change, interface tracking via the Volume of Fluid method and laser multiple reflection inside the keyhole. In order to decrease computational time, only half of the domain was considered as only half of the cut edge was sufficient to assess the final quality trend. To calibrate the CFD model, three sets of process parameters were selected based on their ability to produce distinctly different edge geometries (A,B,C). Subsequently, it was validated using samples processed under parameter conditions at the boundaries of the operating window (C,D). Model predictions were compared with experimental data obtained via optical microscopy and SEM, using performance metrics such as Relative Root Mean Square Error (RRMSE) and Mean Absolute Percentage Error (MAPE). The results showed good agreement, especially for kerf width and dross height.

From simulations, five distinct process zones were identified: No cut, Recast, Dross, Good Cut, and Spatter. The formation of defects in the cutting process can be attributed to the varying amounts of evaporated over melted material and the latter

dynamics governed by the recoil pressure force.

It was observed that when low power and low speed were set, the recoil pressure was at its lowest. Although it was sufficient to induce material evaporation and enable cutting, this condition favors melting over evaporation. The weak force exerted on the molten pool results in minimal downward kinetic energy, leading to the accumulation of molten material along the cutting path. This material re-solidifies into bubble-shaped recast, producing an inconsistent kerf. The increase in power triggered higher recoil pressure values, promoting a narrower and more consistent kerf width. At even higher power and speed combinations, the recoil pressure reaches its peak, leading to a stable kerf but also imparting excessive kinetic energy to the molten pool. This condition favors evaporation rather than melting,as demonstrated by cross sections of the thin foils where the dross height was measured. However, with this value of recoil pressure exerted within the kerf, molten material can be ejected onto the front and back surfaces as irregular spatters.

To further understand the influence of foil thickness on laser cutting outcomes, simulations were also conducted on 16 μm thick copper foils using the same power and speed range. It was found that as the thickness increased, the parameters required to obtain a clean cut also changed. The increased thickness demands more energy to penetrate fully through the material, altering the dynamics of the cutting process and necessitating adjustments in operational parameters to maintain cutting efficiency and quality.

This study could be utilized as a guideline for achieving optimal cutting condition when input specifications undergo slight variations, such as changes in material characteristics, spot dimensions, speed and thickness. Utilizing this approach can save time and resources by reducing the need for extensive experimental campaigns.

5.1.6 P6: The effects of process parameters on high-speed cut quality of Li-ion electrodes using a single mode continuous laser

Contenent

The increasing demand for LIBs calls for efficient and high-quality electrode cutting technologies. Given the wide variety of electrode materials currently used in industry (differing in thickness, composition, and compactness) this study investigates the performance of high-speed laser cutting of LIB electrodes using a single-mode continuous-wave fiber laser.

Commercial electrodes were analyzed, consisting of graphite-coated copper anodes (66 μm total thickness, 8 μm Cu current collector) and $LiFePO_4$ - coated aluminum cathodes (80 μm total thickness, 14 μm Al). A SM-CW laser (λ = 1064 nm, 1.2 kW, 22 μm spot size) was employed, with cutting parameters varied across laser powers (190–1140 W) and scanning speeds (0.3–11 m/s). Cut quality was evaluated through digital microscopy and SEM/EDS analysis.

Quality metrics included the clearance width on the anode, the extent of the heat-affected zone (HAZ) on both anode and cathode, and the number and diameter of spherical droplets ejected from the cathode.

Key results identified optimal processing windows at 950 W and 5.5 m/s for the anode (with a clearance of 17 μm) and 1140 W at 6.6 m/s for the cathode (HAZ= 24 μm, 1–2 droplets $\leq$ 11μm). Critical thresholds of fluence and irradiance were established, beyond which defects such as recast layers, dross, spatter, and droplet formation were observed.

From a physical standpoint, cut quality was governed by the interplay of fluence and irradiance, recoil pressure of the molten material, and thermal conductivity differences between Cu/Al and graphite/LFP layers.

From a manufacturing perspective, scanning speeds above 5 m/s significantly reduced thermal defects and enabled productivity gains of 30–40% compared to nanosecond-pulsed lasers, confirming the SM-CW laser as a high-performance and cost-effective solution for industrial LIB production.

5.1.7 P7: Laser welding in e-mobility: process characterization and monitoring

Contenent

P7 addresses one of the key challenges in electric mobility: high-speed, defect-free laser welding of dissimilar thin metal sheets (Cu-Al) in battery pack manufacturing. Given industrial targets of up to 10 batteries/s and a 99.7% quality threshold, the development of a reliable and integrable in-line monitoring system is critical. This paper introduces a significant advancement over existing literature by validating a low-cost, industrial-ready monitoring system based on commercial photodiodes (Precitec LWM 4.0), in contrast with prior approaches relying on complex systems such as OCT, infrared imaging, and deep learning architectures. The novelty lies in correlating in-process sensor signals (plasma plume, temperature, back-reflection) with process parameters (laser power, welding speed, track length), across different material stack-ups (Al-Cu and Cu-Al) and beam qualities (single-mode and multimode). The experimental campaign comprised 54 welds per configuration, with three power levels (e.g., 900–1500 W), three speeds (100–300 mm/s), and two spot sizes (49–68 μm), resulting in consistent datasets for both Al-Cu and Cu-Al cases.

Key findings include:

- Laser power is identified as the most influential process parameter affecting both weld quality and signal stability.
- A strong linear correlation ($R^2 > 0.90$) is observed between laser power and both plasma and temperature signals for multimode sources.
- High welding speeds ($\geq$300 mm/s) result in lower signal standard deviation (T_{std},P_{std}), indicating improved process stability and weld homogeneity.
- Aluminum-on-top (Al-Cu) configurations generate significantly higher plasma intensities (P_m up to 2.8 V at 1500 W), due to lower phase change temperature (660 °C) compared to copper (1083 °C).

- Back-reflection signals (BS) exhibit a bell-shaped trend along the weld track, due to sensor beam alignment constraints; hence, BS is not considered suitable for real-time feedback control.
- Statistical analysis reveals that TS_{std} increases with power, regardless of speed, suggesting power should be the primary feedback variable in closed-loop control systems.

5.1.8 P8: Environmental impact, mechanical properties, and productivity: considerations on filler wire and scanning strategy in laser welding

Contenent

This study investigates the trade-off between weld quality, environmental sustainability, and industrial productivity in laser welding of dissimilar aluminum alloys for e-mobility battery applications. The paper introduces a multi-level decision-making model linking welding strategies (filler wire use and scanning method) to joint quality and carbon emissions, advancing beyond prior literature, which typically treats these factors separately. Four set-ups were compared: with/without filler wire and with linear/wobbling scanning. Key findings include:

- The wobbling + filler wire configuration achieves the highest weld quality (porosity <1%, ultimate strength up to 204 MPa) but leads to 140% higher CE_{eq} than the most sustainable option. The use of filler wire led to a more significant increase in carbon emissions than the power consumption.
- The linear scanning without filler setup minimizes environmental impact (as low as 45.4 gCO_2eq/m) with acceptable mechanical performance.

A novel aspect is the integration of productivity ratio (process time t_p over standby time t_s) as a selection criterion after the weld quality requirements. When t_p/t_s is high, sustainable configurations are preferred; when t_p/t_s is low, mechanical quality becomes dominant. A threshold of $t_p/t_s \approx 2\%$ is identified for process equivalence in CE_{eq}. The paper also proposes a detailed carbon emission model, accounting for operational and non-operational energy loads of the laser system, robot, chillers, wire feeder, and shielding gas. The methodology enables accurate CE_{eq} estimation under variable welding lengths, speeds, and industrial scenarios. This integrated approach advances the state of the art by combining process optimization, environmental assessment, and scenario-based decision support into a unified methodology.

Chapter 6

Conclusion

This chapter concludes the dissertation by summarizing the key contents and providing an outlook on potential future fields of research and development.

6.1 Summary

This PhD thesis investigates laser processing techniques within the manufacturing chain of lithium-ion batteries. The latter are key components for diverse technical applications, such as consumer electronics or electromobility. They enable electrochemical storage and release of energy through the movement of lithium ions between two electrodes Section 2.1.2. These electrodes consist of a thin metal foil acting as current collector and a slurry-coated active layer. The precision cutting of these electrodes into specific geometries, which vary based on battery type (prismatic, cylindrical, pouch), is a critical step that directly impacts both productivity throughput and the electrochemical performance of the final cell Section 2.1.4.

This dissertation first explores the fundamental interaction of laser beams with current collectors and electrodes to optimize cutting processes, with a specific focus on maximizing edge quality while maintaining high processing speed. Second, it examines laser welding of similar and dissimilar materials, aiming to develop a near zero-defect and sustainable joining process.

The initial studies (P1 and P2) addressed a gap in the literature concerning the high-speed laser cutting of ultrathin aluminum (12 μm) and copper (6 μm) foils, pushing cutting speeds well beyond the previously reported 5 m/s. P1 compared continuous wave (CW) and nanosecond pulsed wave (PW) lasers, demonstrating that CW lasers achieve superior cut quality at very high speeds, whereas PW lasers allow finer kerf control at moderate speeds but are more sensitive to spatter and defects. P2 extended this work, developing an innovative analytical energy-based model that compares fluence and irradiance across different regimes. This study also created comprehensive defect maps to define optimal processing windows, establishing a new operational benchmark for high-speed cutting of battery current collectors.

Despite parameter optimization, thermal defects occur because material ablation is mainly governed by melt ejection and evaporation rather than direct solid-vapor transition, as in ultra-short pulsed laser systems. Hence, P3 study introduced ultrashort femtosecond pulses and burst mode operation to leverage “cold ablation” mechanisms and minimize thermal effects. A simplified cutting efficiency model was developed to quantify the fraction of laser energy contributing to material removal versus residual

heating. Experiments showed that single-pulse mode maximizes efficiency at intermediate frequencies, while burst mode can triple cutting speed at the expense of thermal side effects such as spattering and molten zones.

Complementary to experimental analysis, P4 and P5 developed numerical models to describe CW laser interaction with thin metal foils. P4 presented a thermal model capable of predicting cut thresholds, defect formation, and kerf widths with less than 10% error. P5 introduced a CFD framework accounting for recoil pressure, molten pool dynamics, and multiple reflections. These studies elucidated the underlying physics of defect formation (distinguishing between insufficient material ejection leading to dross and excessive kinetic energy causing spatter) and provided practical guidance for adjusting laser power, speed, and foil thickness to optimize quality.

Moving from current collectors to full electrodes, P6 investigated CW laser cutting of commercial LIB electrodes (graphite-coated Cu anodes and $LiFePO_4$-coated Al cathodes). Critical fluence and irradiance thresholds were identified to minimize HAZ, spatter, delamination and recast layers. The study demonstrated that scanning speeds above 5 m/s significantly enhance productivity while reducing thermal defects, confirming SM-CW lasers as a cost-effective solution for industrial battery fabrication.

In summary, the most suitable setup for the notching line is driven by the priorities of the specific production line. When speed is the primary driver, a CW laser is the best solution, capable of achieving up to 20 m/s with good quality on both aluminum and copper. Conversely, when quality is prioritized over productivity (dross$<1\mu m$), ultrashort pulsed lasers in single-pulse mode emerge as the preferred choice, albeit at higher integration cost due to requirements for more precise fine-tuning of the system and a controlled temperature and humidity environment.

After the cutting process, laser technology has also become the state-of-art for subsequent welding steps. Laser welding is involved both at the cell level (e.g., tab-to-tab welding for cell sealing) and at the module/pack level (e.g., tab-to-busbar connections). P7 analyzes correlations between in-process photodiode signals (Plasma and Temperature) and the formation of defects during laser welding of aluminum and copper tabs, linking these to process parameters and laser set up.

P8 addressed the laser welding of aluminum sheets for battery assembly by investigating the relationship between weld bead performance, energy consumption ($CO_{2,eq}$ emissions) and productivity. A multi-level decision-making model was developed to optimize filler wire use and scanning strategies, effectively balancing weld quality, $CO_{2,eq}$ emissions, and process efficiency. This represents a significant step forward in aligning industrial feasibility with sustainability goals.

6.2 Outlook

Although this thesis has advanced the knowledge of both laser welding and cutting for battery manufacturing, further technological development is needed, and academic research fields remain to be explored.

For the cutting process, achieving dross-free results below 1 μm requires investigating integrated solutions. For example, a dual-laser approach could be tested, where one source pre-heats the material to facilitate absorption for a second, lower-energy ultrashort pulsed laser. Furthermore, the influence of plasma shielding effects on cutting

efficiency and final quality must be incorporated into future models.

As outlined in this dissertation, laser cutting of battery current collectors and electrodes is characterized by intricate relationships between processing parameters and product properties. Therefore, developing models for pulsed laser modes (both short and ultrashort) would greatly facilitate process design and deepen the understanding of underlying physical phenomena.

These models can be either purely data-based, applying artificial intelligence, for instance, or physics-based, e.g., by considering the two-temperature model Section 2.2.4. The latter could provide valuable insights into the complex ablation phenomena, such as selective binder evaporation in electrodes, but is challenging to implement and simulate due to the multi-material, porous composition of electrodes. In contrast, data-based process models are easier to set up and train and would presumably deliver precise predictions for resulting cut geometries, though they would not contribute to a physical understanding of the process.

Regarding laser welding, the integration of advanced monitoring devices (high speed cameras, photodiodes) is essential. These systems must be able to recognize distinct weld features to enable real time, closed-loop control of process parameters via AI algorithms, allowing for online adaptation and ensuring consistent, high-quality, defect-free welds.

Bibliography

[1] E. Parliament, *Powering the eu's future: Strengthening the battery industry*, 2025. [Online]. Available: %5Curl%7Bhttps://www.europarl.europa.eu/RegData/etudes/BRIE/2025/767214/EPRS_BRI(2025)767214_EN.pdf%7D

[2] G. E. Blomgren, "The development and future of lithium ion batteries", *Journal of The Electrochemical Society*, vol. 164, no. 1, A5019–A5025, Dec. 2016, ISSN: 1945-7111. DOI: 10.1149/2.0251701jes

[3] A. Masias, J. Marcicki, and W. A. Paxton, "Opportunities and challenges of lithium ion batteries in automotive applications", *ACS Energy Letters*, vol. 6, no. 2, pp. 621–630, Jan. 2021, ISSN: 2380-8195. DOI: 10.1021/acsenergylett.0c02584

[4] C. Xu et al., "Electric vehicle batteries alone could satisfy short-term grid storage demand by as early as 2030", *Nature Communications*, vol. 14, no. 1, Jan. 2023, ISSN: 2041-1723. DOI: 10.1038/s41467-022-35393-0

[5] The Royal Swedish Academy of Sciences, *The nobel prize in chemistry 2019*, 2019. [Online]. Available: https://www.nobelprize.org/prizes/chemistry/2019/press-release

[6] H. Budde-Meiwes et al., "A review of current automotive battery technology and future prospects", *Proceedings of the Institution of Mechanical Engineers, Part D: Journal of Automobile Engineering*, vol. 227, no. 5, pp. 761–776, Apr. 2013, ISSN: 2041-2991. DOI: 10.1177/0954407013485567

[7] L. Mauler, F. Duffner, and J. Leker, "Economies of scale in battery cell manufacturing: The impact of material and process innovations", *Applied Energy*, vol. 286, p. 116 499, Mar. 2021, ISSN: 0306-2619. DOI: 10.1016/j.apenergy.2021.116499

[8] International Energy Agency, *Global ev outlook 2024: Catching up with climate ambitions*, 2024. [Online]. Available: https://www.iea.org/reports/global-ev-outlook-2024

[9] J. T. Frith, M. J. Lacey, and U. Ulissi, "A non-academic perspective on the future of lithium-based batteries", *Nature Communications*, vol. 14, no. 1, Jan. 2023, ISSN: 2041-1723. DOI: 10.1038/s41467-023-35933-2

[10] W. Pfleging, "A review of laser electrode processing for development and manufacturing of lithium-ion batteries", *Nanophotonics*, vol. 7, no. 3, pp. 549–573, Feb. 2018, ISSN: 2192-8614. DOI: 10.1515/nanoph-2017-0044

[11] J. Grabow, J. Klink, R. Benger, I. Hauer, and H.-P. Beck, "Particle contamination in commercial lithium-ion cells—risk assessment with focus on internal short circuits and replication by currently discussed trigger methods", *Batteries*, vol. 9, no. 1, p. 9, Dec. 2022, ISSN: 2313-0105. DOI: 10.3390/batteries9010009

[12] Y. Liu, R. Zhang, J. Wang, and Y. Wang, "Current and future lithium-ion battery manufacturing", *IScience*, vol. 24, no. 4, 2021.

[13] M. Luetke et al., "A comparative study on cutting electrodes for batteries with lasers", *Physics Procedia*, vol. 12, pp. 286–291, 2011, ISSN: 1875-3892. DOI: 10.1016/j.phpro.2011.03.135

[14] M. Weller, M. T. Weller, T. Overton, J. Rourke, and F. Armstrong, *Inorganic chemistry*. Oxford University Press, USA, 2014.

[15] M. J. Wang, E. Carmona, A. Gupta, P. Albertus, and J. Sakamoto, "Enabling "lithium-free" manufacturing of pure lithium metal solid-state batteries through in situ plating", *Nature communications*, vol. 11, no. 1, p. 5201, 2020.

[16] D. Andre, H. Hain, P. Lamp, F. Maglia, and B. Stiaszny, "Future high-energy density anode materials from an automotive application perspective", *Journal of materials chemistry A*, vol. 5, no. 33, pp. 17 174–17 198, 2017.

[17] D. Andre et al., "Future generations of cathode materials: An automotive industry perspective", *Journal of Materials Chemistry A*, vol. 3, no. 13, pp. 6709–6732, 2015.

[18] A. Kwade, W. Haselrieder, R. Leithoff, A. Modlinger, F. Dietrich, and K. Droeder, "Current status and challenges for automotive battery production technologies", *Nature Energy*, vol. 3, no. 4, pp. 290–300, 2018.

[19] P. Zhu, P. R. Slater, and E. Kendrick, "Insights into architecture, design and manufacture of electrodes for lithium-ion batteries", *Materials & Design*, vol. 223, p. 111 208, 2022.

[20] L.-L. Lu et al., "Advances in electrolytic copper foils: Fabrication, microstructure, and mechanical properties", *Rare Metals*, vol. 44, no. 2, pp. 757–792, Oct. 2024, ISSN: 1867-7185. DOI: 10.1007/s12598-024-02965-6 [Online]. Available: http://dx.doi.org/10.1007/s12598-024-02965-6

[21] N. Xu, J. You, H. Ying, G. Han, and Y. Shi, "Exploring composite current collectors: From academic research to industrial application", *Journal of Alloys and Compounds*, vol. 1038, p. 182 761, Aug. 2025, ISSN: 0925-8388. DOI: 10.1016/j.jallcom.2025.182761 [Online]. Available: http://dx.doi.org/10.1016/j.jallcom.2025.182761

[22] M. Lowe, S. Tokuoka, T. Trigg, and G. Gereffi, "Lithium-ion batteries for electric vehicles", *The US Value Chain, Contributing CGGC researcher: Ansam Abayechi*, 2010.

[23] QuantumScape Corporation, *Quantumscape releases next-generation solid-state battery separator equipment "cobra"*, https://www.quantumscape.com/quantumscape-releases-next-generation-solid-state-battery-separator-equipment-cobra/, 2025.

[24] 24M Technologies, *Impervio separator*, `https://24-m.com/impervio`, 2025.

[25] S. Arora, W. Shen, and A. Kapoor, "Review of mechanical design and strategic placement technique of a robust battery pack for electric vehicles", *Renewable and Sustainable Energy Reviews*, vol. 60, pp. 1319–1331, 2016.

[26] A. H. Lutey, A. Fortunato, S. Carmignato, and M. Fiorini, "High speed pulsed laser cutting of licoo2 li-ion battery electrodes", *Optics & Laser Technology*, vol. 94, pp. 90–96, 2017.

[27] C. Angeloni, E. Liverani, A. Ascari, and A. Fortunato, "Characterization and process optimization of remote laser cutting of current collectors for battery electrode production", *Journal of Materials Processing Technology*, vol. 324, p. 118 266, 2024.

[28] R. Tao, Y. Gu, Z. Du, X. Lyu, and J. Li, "Advanced electrode processing for lithium-ion battery manufacturing", *Nature Reviews Clean Technology*, pp. 1–16, 2025.

[29] A. Schilling, J. Schmitt, F. Dietrich, and K. Dröder, "Analyzing bending stresses on lithium-ion battery cathodes induced by the assembly process", *Energy Technology*, vol. 4, no. 12, pp. 1502–1508, 2016.

[30] V. Dimatteo, A. Ascari, E. Liverani, and A. Fortunato, "Experimental investigation on the effect of spot diameter on continuous-wave laser welding of copper and aluminum thin sheets for battery manufacturing", *Optics & Laser Technology*, vol. 145, p. 107 495, 2022.

[31] E. Capello et al., *Le lavorazioni industriali mediante laser di potenza*. Libreria Clup, 2003.

[32] C. P. Grigoropoulos, *Transport in laser microfabrication: fundamentals and applications*. Cambridge University Press, 2009.

[33] H. J. Eichler, J. Eichler, and O. Lux, *Lasers: basics, advances and applications*. Springer, 2018.

[34] K. Washio, "Laser applications in the electronics and optoelectronics industry in japan", in *Laser Applications in Microelectronic and Optoelectronic Manufacturing IV*, SPIE, vol. 3618, 1999, pp. 230–239.

[35] B. N. Chichkov, C. Momma, S. Nolte, F. Von Alvensleben, and A. Tünnermann, "Femtosecond, picosecond and nanosecond laser ablation of solids", *Applied physics A*, vol. 63, pp. 109–115, 1996.

[36] R. De Loor, "Polygon scanner system for ultra short pulsed laser micro-machining applications", *Physics Procedia*, vol. 41, pp. 544–551, 2013, ISSN: 1875-3892. DOI: `10.1016/j.phpro.2013.03.114` [Online]. Available: `http://dx.doi.org/10.1016/j.phpro.2013.03.114`

[37] S. Bruening, K. Du, M. Jarczynski, G. Jenke, and A. Gillner, "Ultra-fast laser micro processing by multiple laser spots", *Procedia CIRP*, vol. 74, pp. 573–580, 2018.

[38] A. Gillner, J. Finger, P. Gretzki, M. Niessen, T. Bartels, and M. Reininghaus, "High power laser processing with ultrafast and multi-parallel beams.", *Journal of Laser Micro/Nanoengineering*, vol. 14, no. 2, 2019.

[39] W. M. Steen and J. Mazumder, *Laser material processing*. springer science & business media, 2010.

[40] K.-H. Leitz, B. Redlingshöfer, Y. Reg, A. Otto, and M. Schmidt, "Metal ablation with short and ultrashort laser pulses", *Physics Procedia*, vol. 12, pp. 230–238, 2011.

[41] X. Li and Y. Guan, "Theoretical fundamentals of short pulse laser-metal interaction: A review", *Nanotechnology and Precision Engineering*, vol. 3, no. 3, pp. 105–125, 2020.

[42] S. Nolte, F. Schrempel, and F. Dausinger, "Ultrashort pulse laser technology", *Springer Series in Optical Sciences*, vol. 195, no. 200, p. 1, 2016.

[43] Q. Lu, S. S. Mao, X. Mao, and R. E. Russo, "Delayed phase explosion during high-power nanosecond laser ablation of silicon", *Applied physics letters*, vol. 80, no. 17, pp. 3072–3074, 2002.

[44] A. Žemaitis, M. Gaidys, M. Brikas, P. Gečys, G. Račiukaitis, and M. Gedvilas, "Advanced laser scanning for highly-efficient ablation and ultrafast surface structuring: Experiment and model", *Scientific reports*, vol. 8, no. 1, pp. 1–14, 2018.

[45] D. Breitling, A. Ruf, and F. Dausinger, "Fundamental aspects in machining of metals with short and ultrashort laser pulses", in *Photon Processing in Microelectronics and Photonics III*, SPIE, vol. 5339, 2004, pp. 49–63.

[46] R. Weber and T. Graf, "The challenges of productive materials processing with ultrafast lasers", *Advanced Optical Technologies*, vol. 10, no. 4-5, pp. 239–245, 2021.

[47] A. Bogatyrev, Z. Liao, D. Axinte, and A. Norton, "Femtosecond laser ablation of zirconia-based ceramic materials: From ablation mechanism to modelling of large-scale processing", *Journal of Materials Processing Technology*, vol. 335, p. 118 668, 2025.

[48] B. Ma, X. Gao, Y. Huang, P. P. Gao, and Y. Zhang, "A review of laser welding for aluminium and copper dissimilar metals", *Optics & Laser Technology*, vol. 167, p. 109 721, 2023.

[49] S. Katayama, *Fundamentals and details of laser welding*. Springer, 2020.

[50] M. Kogel-Hollacher, "The full potential of photonics in e-mobility: An overview", *Laser User*, vol. 97, pp. 22–23, 2020.

[51] A. Sattar, D. Greenwood, M. Dowson, and P. Unadkat, "Automotive lithium ion battery recycling in the uk based on a feasibility study."", *Report Summary*, 2020.

[52] G. Chianese, P. Franciosa, J. Nolte, D. Ceglarek, and S. Patalano, "Characterization of photodiodes for detection of variations in part-to-part gap and weld penetration depth during remote laser welding of copper-to-steel battery tab connectors", *Journal of Manufacturing Science and Engineering*, vol. 144, no. 7, p. 071 004, 2022.

[53] T. Purtonen, A. Kalliosaari, and A. Salminen, "Monitoring and adaptive control of laser processes", *Physics Procedia*, vol. 56, pp. 1218–1231, 2014.

[54] D. You, X. Gao, and S. Katayama, "Review of laser welding monitoring", *Science and technology of welding and joining*, vol. 19, no. 3, pp. 181–201, 2014.

[55] W. Cai, J. Wang, P. Jiang, L. Cao, G. Mi, and Q. Zhou, "Application of sensing techniques and artificial intelligence-based methods to laser welding real-time monitoring: A critical review of recent literature", *Journal of Manufacturing systems*, vol. 57, pp. 1–18, 2020.

[56] I. Eriksson, J. Powell, and A. Kaplan, "Signal overlap in the monitoring of laser welding", *Measurement Science and Technology*, vol. 21, no. 10, p. 105 705, 2010.

[57] W. Rohringer, T. Heine, R. Sommerhuber, N. Lehmann, and B. Fischer, "Optical microphone as laser-ultrasound detector wolfgang rohringer1, thomas heine1, ryan sommerhuber1, nico lehmann2, balthasar fischer1", *DAGA Procedia*, 2028.

[58] M. Yusof, M. Ishak, and M. F. Ghazali, "Acoustic methods in real-time welding process monitoring: Application and future potential advancement", *Journal of Mechanical Engineering and Sciences*, vol. 15, no. 4, pp. 8490–8507, 2021.

[59] I. Eriksson, "High speed imaging analysis of laser welding", Ph.D. dissertation, Lulea University of Technology, 2013.

[60] A. F. Kaplan and R. S. Matti, "Absorption peaks depending on topology of the keyhole front and wavelength", *Journal of Laser Applications*, vol. 27, no. S2, 2015.

[61] D. Banat, S. Ganguly, S. Meco, and P. Harrison, "Application of high power pulsed nanosecond fibre lasers in processing ultra-thin aluminium foils", *Optics and Lasers in Engineering*, vol. 129, p. 106 075, Jun. 2020, ISSN: 0143-8166. DOI: 10.1016/j.optlaseng.2020.106075 [Online]. Available: http://dx.doi.org/10.1016/j.optlaseng.2020.106075

[62] T. Jansen, M. W. Kandula, D. Blass, S. Hartwig, W. Haselrieder, and K. Dilger, "Evaluation of the separation process for the production of electrode sheets", *Energy Technology*, vol. 8, no. 2, Jun. 2019, ISSN: 2194-4296. DOI: 10.1002/ente.201900519 [Online]. Available: http://dx.doi.org/10.1002/ente.201900519

[63] W. Schulz et al., "Dynamics of ripple formation and melt flow in laser beam cutting", *Journal of Physics D: Applied Physics*, vol. 32, no. 11, pp. 1219–1228, Jan. 1999, ISSN: 1361-6463. DOI: 10.1088/0022-3727/32/11/307 [Online]. Available: http://dx.doi.org/10.1088/0022-3727/32/11/307

[64] D. Lee and J. Mazumder, "Effects of momentum transfer on sizing of current collectors for lithium-ion batteries during laser cutting", *Optics & Laser Technology*, vol. 99, pp. 315–325, Feb. 2018, ISSN: 0030-3992. DOI: 10.1016/j.optlastec.2017.09.016 [Online]. Available: http://dx.doi.org/10.1016/j.optlastec.2017.09.016

[65] R. Weber and T. Graf, "The challenges of productive materials processing with ultrafast lasers", *Advanced Optical Technologies*, vol. 10, no. 4–5, pp. 239–245, Oct. 2021, ISSN: 2192-8584. DOI: 10.1515/aot-2021-0038 [Online]. Available: http://dx.doi.org/10.1515/aot-2021-0038

[66] A. Žemaitis, U. Gudauskytė, S. Steponavičiūtė, P. Gečys, and M. Gedvilas, "The ultrafast burst laser ablation of metals: Speed and quality come together", *Optics & Laser Technology*, vol. 180, p. 111 458, Jan. 2025, ISSN: 0030-3992. DOI: 10.1016/j.optlastec.2024.111458 [Online]. Available: http://dx.doi.org/10.1016/j.optlastec.2024.111458

[67] J. Huang, W. Shi, J. Huang, Y. Xie, Y. Ba, and K. He, "High speed pulsed laser cutting of anode material for a li-ion battery in burst mode", *Optical Materials Express*, vol. 11, no. 7, p. 2300, Jun. 2021, ISSN: 2159-3930. DOI: 10.1364/ome.425816 [Online]. Available: http://dx.doi.org/10.1364/OME.425816

[68] P. Heidari Orojloo and A. G. Demir, "Study of burst mode for enhancing the ps-laser cutting performance of lithium-ion battery electrodes", *Journal of Laser Applications*, vol. 36, no. 4, Sep. 2024, ISSN: 1938-1387. DOI: 10.2351/7.0001417 [Online]. Available: http://dx.doi.org/10.2351/7.0001417

[69] A. H. Lutey, A. Fortunato, A. Ascari, S. Carmignato, and C. Leone, "Laser cutting of lithium iron phosphate battery electrodes: Characterization of process efficiency and quality", *Optics & Laser Technology*, vol. 65, pp. 164–174, Jan. 2015, ISSN: 0030-3992. DOI: 10.1016/j.optlastec.2014.07.023 [Online]. Available: http://dx.doi.org/10.1016/j.optlastec.2014.07.023

[70] X. Gu, X. Sun, Y. Han, Q. Li, J. Liu, and X. Mei, "Femtosecond laser cutting of lifepo4 electrodes: Kerf geometry, process optimization, and electrochemical performance", *Journal of Energy Storage*, vol. 101, p. 113 859, Nov. 2024, ISSN: 2352-152X. DOI: 10.1016/j.est.2024.113859 [Online]. Available: http://dx.doi.org/10.1016/j.est.2024.113859

[71] Y. Zhang, J. Li, R. Yang, T. Liu, and Y. Yan, "Analysis of kerf quality on ultrafast laser cutting of anode material for lithium-ion battery", *Optics and Lasers in Engineering*, vol. 118, pp. 14–21, Jul. 2019, ISSN: 0143-8166. DOI: 10.1016/j.optlaseng.2019.01.013 [Online]. Available: http://dx.doi.org/10.1016/j.optlaseng.2019.01.013

[72] E. Audouard, M. Fleureau, D. Pallarès, J.-M. Romano, and F. Mermet, "Characterization of batteries materials ablation by femtosecond pulses", *Procedia CIRP*, vol. 124, pp. 57–60, 2024, ISSN: 2212-8271. DOI: 10.1016/j.procir.2024.08.070 [Online]. Available: http://dx.doi.org/10.1016/j.procir.2024.08.070

[73] D. Lee, R. Patwa, H. Herfurth, and J. Mazumder, "Parameter optimization for high speed remote laser cutting of electrodes for lithium-ion batteries", *Journal of Laser Applications*, vol. 28, no. 2, Feb. 2016, ISSN: 1938-1387. DOI: 10.2351/1.4942044 [Online]. Available: http://dx.doi.org/10.2351/1.4942044

[74] R. Fabbro, S. Slimani, F. Coste, and F. Briand, "Study of keyhole behaviour for full penetration nd–yag cw laser welding", *Journal of Physics D: Applied Physics*, vol. 38, no. 12, p. 1881, 2005.

[75] J. Kim, S. Oh, and H. Ki, "A study of keyhole geometry in laser welding of zinc-coated and uncoated steels using a coaxial observation method", *Journal of Materials Processing Technology*, vol. 225, pp. 451–462, 2015.

[76] L. Huang, X. Hua, D. Wu, L. Fang, Y. Cai, and Y. Ye, "Effect of magnesium content on keyhole-induced porosity formation and distribution in aluminum alloys laser welding", *Journal of Manufacturing Processes*, vol. 33, pp. 43–53, 2018.

[77] P. Hellwiga, K. Schrickera, and J. P. Bergmanna, "Spatter formation in high-speed laser processing of high-alloyed steel", *Lasers in Manufacturing Conference 2021*, 2021.

[78] Z. Wang and M. Gao, "Numerical simulations of oscillating laser welding: A review", *Journal of Manufacturing Processes*, vol. 119, pp. 744–757, 2024.

[79] Y. Rong, L. Wang, R. Wu, and J. Xu, "Visualization and simulation of 1700ms sheet laser welding based on three-dimensional geometries of weld pool and keyhole", *International Journal of Thermal Sciences*, vol. 171, p. 107 257, 2022.

[80] D. Ma, P. Jiang, L. Shu, and S. Geng, "Real-time porosity monitoring during laser welding of aluminum alloys based on keyhole 3d morphology characteristics", *Journal of Manufacturing Systems*, vol. 65, pp. 70–87, 2022.

[81] K. Lee, S. Kang, M. Kang, S. Yi, and C. Kim, "Estimation of al/cu laser weld penetration in photodiode signals using deep neural network classification", *Journal of Laser Applications*, vol. 33, no. 4, 2021.

[82] G. Chianese, P. Franciosa, T. Sun, D. Ceglarek, and S. Patalano, "Using photodiodes and supervised machine learning for automatic classification of weld defects in laser welding of thin foils copper-to-steel battery tabs", *Journal of Laser Applications*, vol. 34, no. 4, 2022.

[83] M. Seibold, H. Friedmann, K. Schricker, and J. P. Bergmann, "Process control by real-time pulse shaping in laser beam welding of different material combinations", *Procedia CIRP*, vol. 94, pp. 769–774, 2020.

[84] B. Fischer, "Optical microphone hears ultrasound", *Nature Photonics*, vol. 10, no. 6, pp. 356–358, 2016.

[85] M. Yusof, M. Ishak, and M. Ghazali, "Detection of irregularities on weld bead from the l-statistic analysis of the acquired sound during pulse mode laser welding process", in *IOP Conference Series: Materials Science and Engineering*, IOP Publishing, vol. 788, 2020, p. 012 015.

[86] Y. Luo, L. Zhu, J. Han, X. Xie, R. Wan, and Y. Zhu, "Study on the acoustic emission effect of plasma plume in pulsed laser welding", *Mechanical Systems and Signal Processing*, vol. 124, pp. 715–723, 2019.

[87] N. Authier, E. Touzet, F. Lücking, R. Sommerhuber, V. Bruyère, and P. Namy, "Coupled membrane free optical microphone and optical coherence tomography keyhole measurements to setup welding laser parameters", in *High-Power Laser Materials Processing: Applications, Diagnostics, and Systems IX*, SPIE, vol. 11273, 2020, pp. 41–52.

[88] L. Tomcic, A. Ederer, S. Grabmann, M. Kick, J. Kriegler, and M. F. Zaeh, "Interpreting acoustic emissions to determine the weld depth during laser beam welding", *Journal of Laser Applications*, vol. 34, no. 4, 2022.

[89] T. Weiss, J. Werner, C. Geiger, and M. F. Zaeh, "Acoustic process monitoring during the laser beam welding of stainless-steel foils using an adjustable ring mode laser beam source", *Journal of Laser Applications*, vol. 36, no. 4, Oct. 2024, ISSN: 1938-1387. DOI: 10.2351/7.0001575 [Online]. Available: http://dx.doi.org/10.2351/7.0001575

[90] T. Ji and N. Mohamad Nor, "Deep learning-empowered digital twin using acoustic signal for welding quality inspection", *Sensors*, vol. 23, no. 5, p. 2643, Feb. 2023, ISSN: 1424-8220. DOI: 10.3390/s23052643 [Online]. Available: http://dx.doi.org/10.3390/s23052643

[91] D. Basile, R. A. Botros, M. D. Maddis, V. Razza, and P. Franciosa, "Monitoring part-to-part gap and laser power effects in remote laser welding of 1050 aluminum busbar-to-terminal connections via optical microphone sensing", *Optics & Laser Technology*, vol. 192, p. 113 494, Dec. 2025, ISSN: 0030-3992. DOI: 10.1016/j.optlastec.2025.113494 [Online]. Available: http://dx.doi.org/10.1016/j.optlastec.2025.113494

Appendix A

Publications of the Author

Within this dissertation and the author's work at the University of Bologna laboratory, several scientific manuscripts were published. Documents which were embedded into Chapter 5 of this thesis are:

- P1: Alessandro Ascari, Caterina Angeloni, Erica Liverani, Alessandro Fortunato, (2023). "High Speed laser cutting of ultrathin metal foils for battery cell production", Journal of Laser Application. DOI : 10.2351/7.0001091
- P2: Caterina Angeloni, Erica Liverani, Alessandro Ascari, Alessandro Fortunato, (2023). "Characterization and process optimization of remote laser cutting of current collectors for battery electrode production", Journal of Materials Processing Technology. DOI : 10.1016/$j.jmatprotec$.2023.118266
- P3: Caterina Angeloni, Dongkyoung Lee, Alessandro Fortunato, (2025). "Femtosecond Laser Cutting of Current Collectors: A Study for High-Quality Li-Ion Battery Fabrication in Electric Vehicles", Selected Topics in Manufacturing. DOI : $10.1007/978 - 3 - 031 - 99501 - 9_5$
- P4: Erica Liverani, Alessandro Ascari, Caterina Angeloni, Michele Francioso, Lorenzo Cestone, Zha Dexiang, Alessandro Fortunato, (2024). "Remote Laser Cutting of Metal Foils for Battery Electrodes Fabrication: Modeling of the Process and Experimental Validation", ASME Conference paper.DOI : $10.1115/MSEC2024-123689$
- P5: Caterina Angeloni, Samuele Piandoro, Erica Liverani, Alessandro Fortunato, (2025). "Numerical and Experimental Study of High-Speed Laser Cutting of Copper Current Collectors: Process Optimization for Quality Assessment", Advanced Materials Technologies. DOI : 10.1002/$admt$.202401905
- P6:Caterina Angeloni, Carolina Magrini, Erica Liverani, Alessandro Fortunato, (2025). "The effect of process parameters on the high-speed cut quality of Li-ion electrodes using a single mode continuous fiber laser", Optics and Laser Technology. DOI : 10.1016/$j.optlastec$.2025.113119
- P7: Caterina Angeloni, Michele Francioso, Erica Liverani, Alessandro Ascari, Alessandro Fortunato, Luca Tomesani, (2023). "Laser welding in e-mobility: process characterization and monitoring", Laser in Manufacturing and Materials Processing. DOI : $10.1007/s40516 - 023 - 00216 - 7$

- P8: Erica Liverani, Caterina Angeloni, Alessandro Ascari, Alessandro Fortunato, (2024). "Environmental Impact, Mechanical Properties, and Productivity: Considerations on Filler Wire and Scanning Strategy in Laser Welding", Journal of Manufacturing Science and Engineering. DOI : 10.1115/1.4065560

Other scientific contributions that are not included in the thesis:

- Michele Francioso, Caterina Angeloni, Alessandro Fortunato, Erica Liverani, Alessandro Ascari, (2024). "Experimental investigation on the effect of nickel-plating thickness on continuous-wave laser welding of copper and steel tab joints for battery manufacturing", Lasers in Manufacturing and Materials Processing. DOI : $10.21203/rs.3.rs-3347882/v1$

Appendix B

Supervised Student Projects

In the course of this dissertation, several student theses and research projects were supervised by the author. All bachelor's theses (BTs) and master's theses (MTs) were conducted at the University of Bologna laboratory. Certain insights that were acquired collaboratively have been integrated into both this document and the publications outlined in Appendix A. The author expresses his sincere thanks to all students for their valuable contribution to this dissertation. The supervised theses are listed in the following Table B.1 in chronological order.

Table B.1: Student theses supervised in the course of this dissertation

Name	**Type**	**Title**	**Submission**
Alberto Stevanato	MS	Laser welding monitoring with LWM signals	Jul 2023
Saracino	BT	State-of-art of electrodes laser cutting	Jul 2023
Andrea Cestone	BT	Laser welding optimization of Al AA3003 battery case (in collaboration with GD company)	Oct 2023
Domenico Torromino	BT	Laser beam welding of Al cell casings	Dec 2023
Caterina Canelli	BT	Optimization of laser welding of Al and Cu tabs of 500 µm thick (in collaboration with FAAM)	Dec 2023
Sofia Mele	BT	Experimental investigation of different configurations in laser welding of dissimilar materials of 2mm thick	Mar 2024
Sophie Tabanelli	BT	Sustainability Manufacturing of LIBs (focus on Ferrari case study)	Jul 2024
Carolina Mazzotti	BT	Experimental analysis on laser cutting of electrodes	Jul 2024

RESEARCH ARTICLE | NOVEMBER 03 2023

High speed laser cutting of ultrathin metal foils for battery cell production

Alessandro Ascari ; Caterina Angeloni; Erica Liverani; Alessandro Fortunato

J. Laser Appl. 35, 042063 (2023)
https://doi.org/10.2351/7.0001091

Journal of Laser Applications ARTICLE pubs.aip.org/lia/jla

High speed laser cutting of ultrathin metal foils for battery cell production

Cite as: J. Laser Appl. 35, 042063 (2023); doi: 10.2351/7.0001091
Submitted: 23 June 2023 · Accepted: 5 October 2023 ·
Published Online: 3 November 2023

Alessandro Ascari, Caterina Angeloni, Erica Liverani, and Alessandro Fortunato

AFFILIATIONS

Department of Industrial Engineering, University of Bologna, Viale Risorgimento 2, 40136 Bologna, Italy

Note: Paper published as part of the special topic on Proceedings of the International Congress of Applications of Lasers & Electro-Optics 2023.

ABSTRACT

Laser-based manufacturing has become a key enabling technology in the production of batteries and battery cells for the e-mobility field. Several applications, in fact, have already been industrialized, such as laser-based welding, cutting, stripping, and cleaning. Among all those technologies, laser cutting, in particular, has to deal with several very stringent constraints: the presence of highly reflective materials (aluminum and copper), very low thicknesses (6–12 μm), on-the-fly processing, and high quality of the cutting surface. According to those considerations, the present paper deals with the application of remote cutting of 12 μm thick aluminum and 6 μm thick copper foils by means of a galvo scanner and two different fiber laser sources: single mode constant wave and nanosecond pulsed wave ones. The experimental activity is devoted to understanding the feasibility of the process and to point out the pros and cons of the two different lasers involved. The cutting edges are analyzed by means of optical and SEM microscopy, in order to characterize cutting quality. The process is also characterized in terms of maximum achievable speed in order to understand the limits of both lasers and galvo scanning systems.

Key words: laser cutting, high speed cutting, thin foils cutting, battery electrodes cutting, reflective materials cutting

I. INTRODUCTION

Transportation-related gas emissions are one of the major causes for air pollution and one of the main contributors to global warming: for that reason, the electrification of vehicles, both for private and commercial transportation, has become one of the main goals to pursue in the immediate future. A quick implementation of policies devoted to decrease the dependency of vehicles on fossil fuels could allow us to meet the target of cutting greenhouse gas emissions by at least −55% by 2030 and to achieve climate neutrality by 2050. In order to assess a true sustainability of the electrification of vehicles, particular attention has to be paid to the fabrication processes: low energy consumption, low carbon footprint, and the absence of toxic and polluting elements or by-products have become mandatory constraints to respect. Among the different technologies available on the market, laser material processing is the most utilized one in battery and electric motor manufacturing. In particular, laser welding is used for contacting the different elements composing battery cells and modules, for sealing the external battery cases, and for joining hairpins on the stators of electric motors. Laser cutting, instead, is applied for profiling the foils constituting internal electrodes and the separators of battery cells, while laser stripping and polishing are applied for removing oxides from the parts to be welded or insulation lacquer from hairpins. Laser-based processes fulfill many of the constraints underlined above: the high energy density allows us to keep power consumption low, the absence of shielding or assistance gases both in welding and cutting helps to reduce emissions, the absence of mechanical contact between the laser and the processing part determines no wear and, thus, lower particle emissions. All those characteristics, together with the intrinsic high selectivity and flexibility, determine the high quality of laser-based processes, especially when applied to manufacturing of components for electric vehicles.[1] In particular, remote cutting processes applied to ultrathin aluminum or copper foils (both coated and noncoated) is a suitable example that highlights the advantages of laser technologies applied to battery manufacturing. Li-ion cells for automotive application demand high cutting qualities in terms of burrs, spatters, and heat affected zones (HAZ). The presence of such defects, in

Journal of Laser Applications ARTICLE pubs.aip.org/lia/jla

fact, may lead to a degradation of battery performance, to a reduction of its service life, and even to dangerous behaviors of the battery itself, such as fire or explosions. High-speed remote laser cutting is one of the best candidates for achieving small HAZ and keeping burr and spatter formation to acceptable levels.[2] Furthermore, the high cutting speed achievable by modern galvo scanners, together with the relative easiness of changing the cutting path, make laser remote cutting one of the most versatile technologies for processing different shapes in high volume production.[3] Last but not least, laser cutting can be applied to a large variety of materials: thin metals,[4] polymers,[5] and fibers.[6] With particular reference to the e-mobility field, in the production of electrodes for prismatic, cylindrical, and pouch battery cells, ultrafast laser remote cutting has become a key enabling technology and many scientific contributions can be found in the literature. Lee *et al.*[7] compared cutting quality on compressed and uncompressed cathode foils when scanning speed and specific energy are varied. Berhe *et al.*[8] proposed a mathematical model for top, kerf, clearance, and burr widths and identified primary physical phenomena and variables impacting cutting efficiency. $LiFePO_4$ was cut using five different laser sources by Lutey *et al.*[9] who then used numerical methods to calculate depth of ablation as a function of process parameters. Demir and Previtali[10] compared cut quality achieved with green and infrared lasers, emphasizing that pulsed lasers induce localized heating in both cases. As mentioned before, in e-mobility applications, a main driver for judging cutting quality is related to heat affected zone. Characteristics of HAZ in relation to pulse width were examined by Schmieder,[11] who found that, if process parameters are correct, HAZ is significantly smaller than the width of ablated material during cutting. According to Lutey *et al.*,[12] HAZ is barely affected by chemical and microstructural changes if a proper cutting is set up. Pulsed laser sources are frequently used in cutting battery electrodes, and many literature references are available: nanosecond pulsed lasers are the most frequently mentioned as a mainstream solution for industrial purposes, while picosecond ones are considered as a way to further improve process quality.[13] Laser cutting in high-speed automatic production lines is also applied on the uncoated edges of the electrode foils. This application is often called "notching," as it is aimed at generating a zig-zag continuous pattern on the edges for promoting a better joining with the battery case parts. In this case, the main challenge is minimizing thermal damage of the uncoated material during cutting and achieving sharp, burr, and spatter free edges. Those characteristics have to be achieved by means of on-the-fly cutting on continuous foils that "flow" at 1–3 m/s on the automated line. This request implies relative scanning speeds between laser and foil up to 20 m/s. Currently, there are no studies conducted to assess the cutting quality of foils operating at ultrahigh speeds. Luetke *et al.*[14] investigated laser cutting of Cu and Al thin foils (6 and 12 μm thick, respectively) using two different laser beam sources: continuous wave (CW) one and nanosecond pulsed wave (PW) one. Cutting speed in this case was below 5 m/s. No more papers are available in the literature concerning much higher cutting speeds of noncoated aluminum or copper foils for battery cell production. According to this, the primary goal of the present study is to narrow that knowledge gap, proposing a comparison between CW and PW remote cutting at speeds up to more than 20 m/s. Cutting quality was assessed using optical and SEM observations.

II. EXPERIMENT

Samples of 6 μm thick pure copper and 12 μm thick pure aluminum foils were clamped and stretched on a properly designed holder that guaranteed a good flatness of the foils themselves and that no contact of the specimens with the bottom surface occurred during cutting. The material was carefully positioned in correspondence of the focal plane of the laser beam and parallel cuts, with a length of 15 mm, were made with different process parameters (Fig. 1).

A maximum of ten cuts were performed on each specimen to prevent foil deformation and warping during the process. The distance between two subsequent cuts was fixed at 5 mm to prevent heat interactions. In order to guarantee a constant cutting speed during the whole cut and to avoid the effects of acceleration and deceleration of the galvos, the cutting path was divided into three parts (as described in Ref. 15): 15 mm long initial part with no laser emission for reaching the target speed, 15 mm long central part with laser on and constant speed, and final 15 mm long part with no laser emission for decelerating the galvos. The laser systems used in the present activity were the following ones: nLight Alta 1200 W single mode [continuous wave (CW)] equipped with a Scanlab Intelliscan 20 scanner and a Quioptiq fused silica F-theta lens; IPG YLPN-2-20 × 500-300 [nanosecond pulsed wave (PW)] equipped with a Raylase Superscan II-10 scanner and a Linos F-theta lens. The characteristics of both setups are summarized in Table I.

An experimental campaign was carried out for both CW and PW setups in order to identify macrodefects and cut quality and to asses a main process window. The same parameter sets were tested on both Al and Cu metal foils. In the case of CW setup, the laser power was varied from 170 to 1000 W and cutting speed from 1 to 15 m/s. In the case of PW setup, cutting speed was varied between 0.2 and 21 m/s, while pulse duration was kept constant at 30 ns.

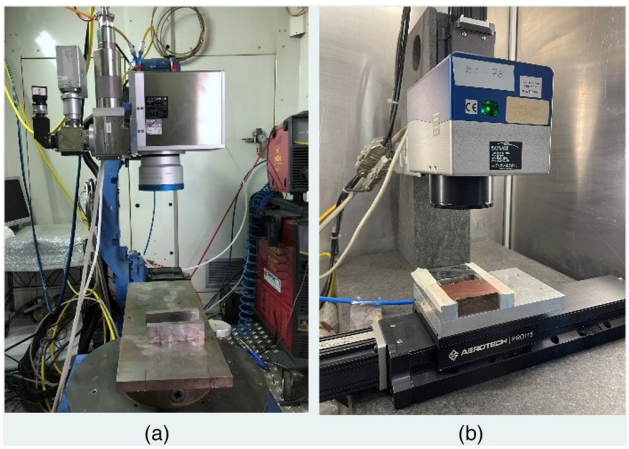

(a) (b)

FIG. 1. Experimental setups: CW (a) and PW (b).

Journal of Laser Applications ARTICLE pubs.aip.org/lia/jla

TABLE I. Detailed characteristics of laser sources and optics.

CW	Max. power (kW)	1.2
	M^2	1.2
	Collimation focal length (mm)	120
	Focalization focal length (mm)	340
	Fiber core diameter (μm)	14
	Spot diameter (μm)	40
	Scanner aperture (mm)	20
PW	Max. average power (W)	300
	M^2	1.5
	Max. peak power (kW)	10
	Max. pulse energy (mJ)	2
	Max. repetition rate (kHz)	4000
	Pulsed duration (ns)	20–500
	Collimated beam diameter (mm)	8
	Focalization focal length (mm)	100
	Spot diameter (μm)	25
	Scanner aperture (mm)	10

III. RESULTS AND DISCUSSION

The experimental campaign pointed out specific process parameter conditions that lead to good cuts and to specific macroscopic defects. In the following paragraphs, a discussion is proposed for the four cases: CW on aluminum, CW on copper, PW on aluminum, and PW on copper.

A. CW on aluminum

Figure 2 shows examples of the typical quality of CW cutting on aluminum. The presence of thin layers of resolidified metal is evident regardless of the specific parameters chosen. In case of good cut [Fig. 2(c)], the resolidified layer is straight, evenly distributed and very thin (<10 μm). This condition corresponds to an optimum specific energy of 0.33 J/cm. If this parameter goes below that threshold, discontinuous cutting or no cutting is observed. If specific energy is higher, different behaviors arise. Figure 2(a) shows that an increase of specific energy due particularly to a low speed leads to an increase in the thickness of the resolidified layer. If specific energy is higher due to both a high laser power and to a low cutting speed [Fig. 2(b)], an increase in both kerf width and resolidified layer thickness is observed. If specific energy is higher especially due to an increase in laser power, spatter occurs and the kerf tends to be less regular and straight [Fig. 2(d)]. This is due to the effect of high power density together with the turbulence caused by high speed: drops are ejected from the cutting zone and immediately resolidify making the cutting edge very irregular. The width of the area where solidified spatters are usually confined is approximately 250 μm. It is important to note that in CW cutting of aluminum, no particular dross formation is observed in the reverse side of the foil. By comparing the front and rear of cuts, it can be seen, in fact, that molten material is not ejected from the rear of the foil, but rather adheres uniformly to both sides.

B. CW on copper

Copper is a material that has been reported to be particularly sensitive to process parameter changes: slight alterations result in significant variations in cutting quality. This behavior is due to two main factors: high reflectivity toward infrared radiations and high heat conduction coefficient. This behavior is confirmed in the discussion below. Figure 3 shows examples of the typical quality of CW cutting on copper. In case of good cut [Fig. 3(b)], negligible

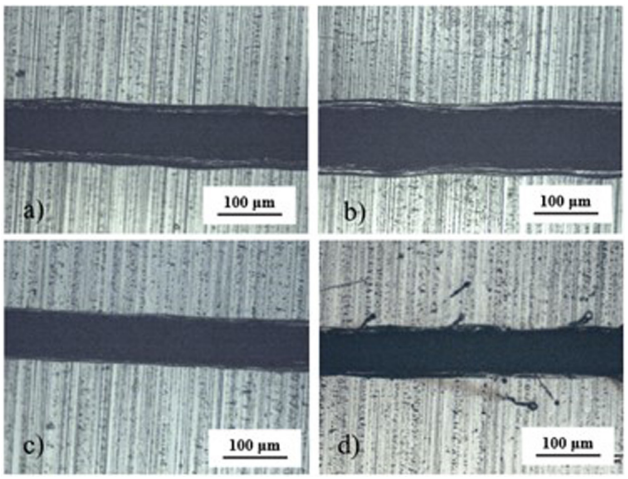

FIG. 2. Examples of CW cutting of aluminum: (a) *excessive resolidification and dross*: $P = 660$ W, speed 4 m/s; (b) *kerf too large*: $P = 1000$ W, speed = 4 m/s; (c) *good cut*: $P = 500$ W, speed =15 m/s; and (d) *spatter*: $P = 1000$ W, speed = 15 m/s.

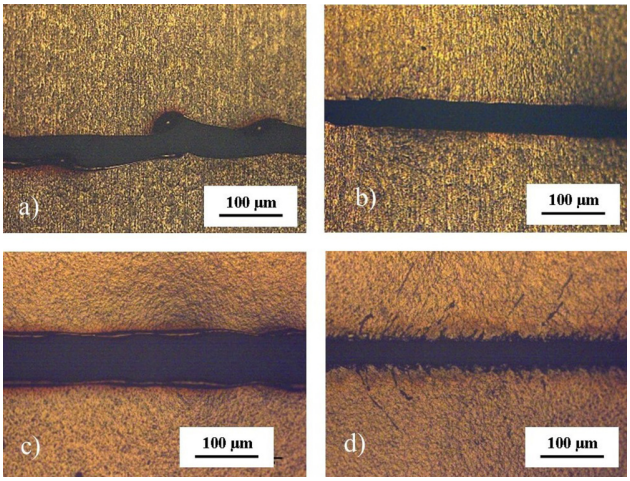

FIG. 3. Examples of CW cutting of copper: (a) *excessive resolidification and dross*: $P = 330$ W, speed = 2.6 m/s; (b) *good cut*: $P = 660$ W, speed = 15 m/s; (c) *max kerf and burns*: $P = 1000$ W, speed = 4 m/s; and (d) *spatter*: $P = 1000$ W, speed = 15 m/s.

Journal of Laser Applications ARTICLE pubs.aip.org/lia/jla

resolidification is detected and the cutting edge is rather a straight end regular. This condition corresponds to an optimum specific energy of 0.44 J/cm. This value is 30% higher than the one measured for aluminum: despite its much lower thickness, copper requires more specific energy due to its higher melting temperature and higher reflectivity. If specific energy is higher different behaviors arise also in this case. Figure 3(a) shows that an increase of specific energy due particularly to a low speed leads to an uneven heat accumulation that causes intermittent humps on the cutting edges. This is due to the high heat transfer coefficient of copper that promotes a propagation of the heating front faster than cutting speed. If specific energy is higher due to both a high laser power and to a low cutting speed [Fig. 3(c)], an increase of both kerf width and resolidified layer thickness is observed, very similar to the aluminum case, and burns tend to form. If specific energy is higher especially due to an increase in laser power, spatters occur and the kerf tends to be less regular [Fig. 3(d)]. This is due to the effect of high power density together with the turbulence caused by high speed: drops are ejected from the cutting zone and immediately resolidify making the cutting edge very irregular.

C. PW on aluminum

Figure 4 shows examples of typical quality of PW cutting on aluminum. The specimens were cut with the same pulse frequency and pulse duration and only average power was varied so that peak power P_{max} was different from trial to trial. In case of good cut [Fig. 4(b)], negligible resolidification is detected and the cutting edge is rather a straight end regular. This condition corresponds to an optimum peak power of 1.7 kW. If cutting speed decreases, more resolidified material accumulates on the cutting edges and cutting quality tends to be worse [Fig. 4(a)]. On the other hand, an increase in peak power tends to promote spatters and burns along the kerf with a dramatic decrease in the overall cutting quality [Figs. 4(c) and 4(d)].

D. PW on copper

Figure 5 shows examples of the typical quality of PW cutting on copper. The specimens were cut with the same pulse frequency and pulse duration and only average power was varied so that peak power P_{max} was different from trial to trial. In case of good cut [Fig. 5(b)], negligible resolidification is detected and the cutting edge is rather a straight end regular. This condition corresponds to an optimum peak power of 1.3 kW. If cutting speed decreases, more resolidified material accumulates on the cutting edges and cutting quality tends to be worse [Fig. 5(a)] due to the formation of evident resolidified droplets. On the other hand, an increase in peak power tends to promote spatters and burns along the kerf with a dramatic decrease of the overall cutting quality also in this case [Figs. 5(c) and 5(d)].

In particular, Fig. 5(c) also shows a change in color in correspondence with the HAZ: this is due to the oxidation of copper at high temperatures. In terms of comparison between CW and PW cutting, it can be underlined that

- PW cutting allows us to achieve higher cutting speeds due to the lower dimension and mass of the galvo mirrors.
- The kerf in PW is smaller due to the smaller spot size.
- The minimum cutting speed that gives a good cutting quality is much lower in PW applications (0.2 m/s against 2 m/s).
- The edge quality, especially at very high cutting speeds, is more regular in CW applications, as it is shown in Fig. 6.

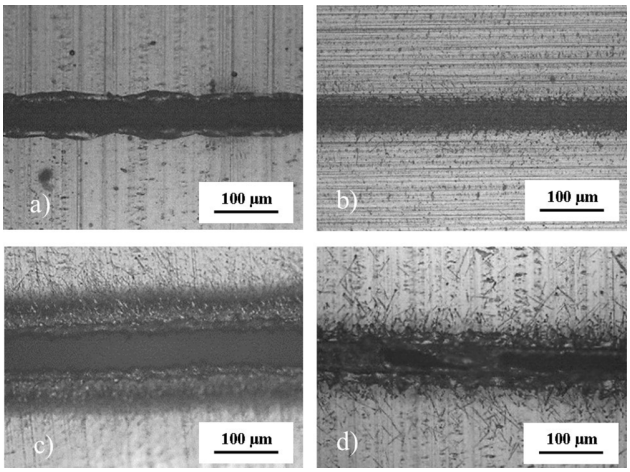

FIG. 4. Examples of PW cutting of aluminum: (a) *excessive resolidification and dross:* speed = 4 m/s, P_{max} = 1.7 kW; (b) *good cut:* speed = 21 m/s, P_{max} = 1.7 kW; (c) *burns:* speed = 8 m/s, P_{max} = 8.3 kW; and (d) *spatters:* speed = 21 m/s, P_{max} = 7.5 kW.

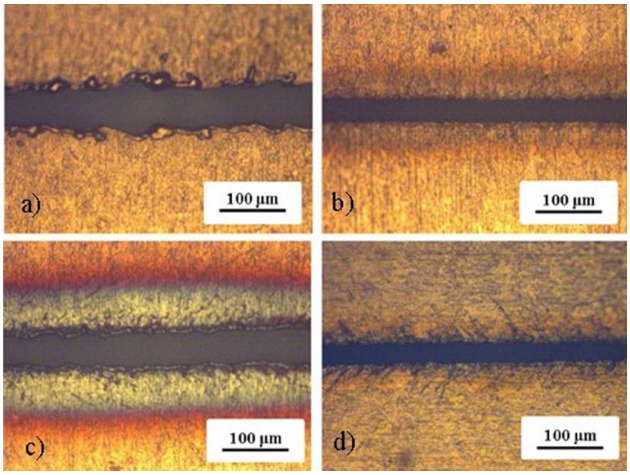

FIG. 5. Examples of PW cutting of copper: (a) *excessive resolidification and dross:* speed = 4 m/s, P_{max} = 5 kW; (*b*) *good cut:* speed = 21 m/s, P_{max} = 1.3 kW; (c) *burns:* speed = 4 m/s, P_{max} = 8.3 kW; and (d) *spatter:* speed = 21 m/s, P_{max} = 5 kW.

Journal of Laser Applications ARTICLE pubs.aip.org/lia/jla

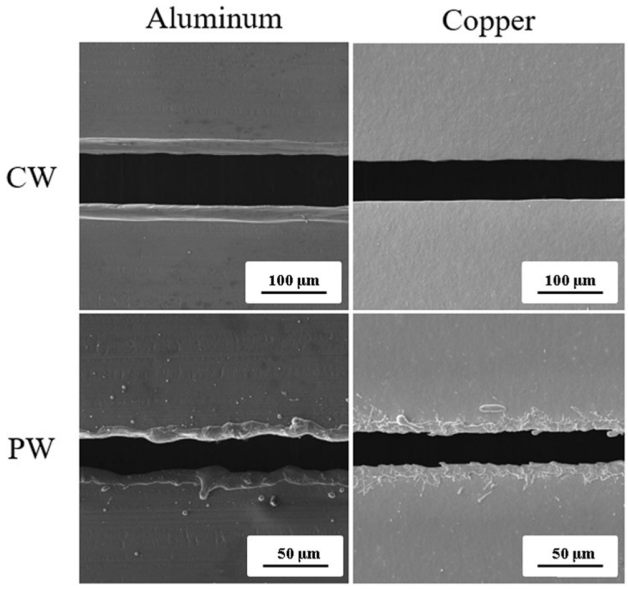

FIG. 6. SEM analysis of good cut quality samples.

IV. CONCLUSIONS

The present paper compares continuous wave and pulsed wave remote cutting of ultrathin aluminum and copper foils for battery cell production. The primary outcomes of this investigation are the following.

- In order to achieve good quality cuts, process parameters have to be carefully selected within a rather small process window.
- Good high-speed cut quality has been assessed for both CW and PW laser sources.
- CW cuts on aluminum, in contrast to the PW ones, do not produce dross.
- CW cutting does not allow us to achieve good cutting qualities on both materials if the cutting speed is below 2 m/s.
- PW laser gives better cut quality for lower speed on both materials.
- The influence of atmospheric contamination is relevant in PW cutting especially on copper.

ACKNOWLEDGMENTS

The authors would like to thank IPG Photonics Italy, Optoprim Italy, and Raylase for having supported the experimental activities with dedicated hardware setups.

AUTHOR DECLARATIONS

Conflict of Interest

The authors have no conflicts to disclose.

Author Contributions

Alessandro Ascari: Conceptualization (equal); Investigation (equal); Methodology (equal); Supervision (equal); Writing – review & editing (equal). **Caterina Angeloni:** Conceptualization (equal); Data curation (equal); Formal analysis (equal); Investigation (equal); Methodology (equal); Supervision (equal); Writing – original draft (equal). **Erica Liverani:** Conceptualization (equal); Data curation (equal); Formal analysis (equal); Supervision (equal); Validation (equal); Writing – original draft (equal); Writing – review & editing (equal). **Alessandro Fortunato:** Conceptualization (equal); Methodology (equal); Resources (equal); Supervision (equal).

REFERENCES

[1]D. Banat, S. Ganguly, S. Meco, and P. Harrison, "Application of high power pulsed nanosecond fibre lasers in processing ultra-thin aluminium foils," Opt. Lasers Eng. **129**, 106075 (2020).
[2]W. M. Steen and J. Mazumder, *Laser Material Processing*, 4th ed. (Springer, London, 2010).
[3]D. Lee, R. Patwa, H. Herfurth, and J. Mazumder, "Parameter optimization for high speed remote laser cutting of electrodes for lithium-ion batteries," J. Laser Appl. **28**, 022006 (2016).
[4]S. L. Villumsen and M. Kristiansen, "Investigation of cutting quality of remote DOE laser cutting in 0.5 mm stainless steel," Phys. Proc. **89**, 164–171 (2017).
[5]M. Y. Tabar, M. Hashemzadeh, and A. R. Rejani, "CO_2 laser cutting of reinforced polyester (CGFRP and GFRP) sheets: An experimental investigation into specific point energy, cutting volume efficiency and material removal rate (MRR)," J. Manuf. Process. **97**, 137–147 (2023).
[6]H. Liu, Y. Tang, L. Lu, Y. Xie, W. Yuan, G. Chen, J. Li, and T. Fu, "Investigation on fiber laser cutting of polyacrylonitrile-based carbon fiber tow," J. Mater. Process. Technol. **263**, 151–63 (2019).
[7]D. Lee, B. Oh, and J. Suk, "The effect of compactness on laser cutting of cathode for lithium-ion batteries using continuous fiber laser," Appl. Sci. **9**, 205 (2019).
[8]M. G. Berhe, H. G. Oh, S.-K. Park, and D. Lee, "Laser cutting of silicon anode for lithium-ion batteries," J. Mater. Res. Technol. **16**, 322–334 (2022).
[9]A. H. A. Lutey, A. Fortunato, A. Ascari, S. Carmignato, and C. Leone, "Laser cutting of lithium iron phosphate battery electrodes: Characterization of process efficiency and quality," Opt. Laser Technol. **65**, 164–174 (2015).
[10]A. G. Demir and B. Previtali, "Remote cutting of Li-ion battery electrodes with infrared and green ns-pulsed fibre lasers," Int. J. Adv. Manuf. Technol. **75**, 1557–568 (2014).
[11]B. Schmieder, "Laser cutting of graphite anodes for automotive lithium-ion secondary batteries: Investigations in the edge geometry and heat-affected zone," Proc. SPIE **8244**, 82440R (2012).
[12]A. H. A. Lutey, M. Fiorini, A. Fortunato, and A. Ascari, "Chemical and microstructural transformations in lithium iron phosphate battery electrodes following pulsed laser exposure," Appl. Surf. Sci. **322**, 85–94 (2014).
[13]Y. Zhang, J. Li, R. Yang, T. Liu, and Y. Yan, "Analysis of kerf quality on ultrafast laser cutting of anode material for lithium-ion battery," Opt. Lasers Eng. **118**, 14–21 (2019).
[14]M. Luetke, V. Franke, A. Techel, T. Himmer, U. Klotzbach, A. Wetzig, and E. Beyer, "A comparative study on cutting electrodes for batteries with lasers," Phys. Proc. **12**, 286–291 (2011).
[15]A. Ascari, E. Liverani, C. Angeloni, M. Francioso, and A. Fortunato, "High speed remote cutting of ultra-thin aluminum foils," in *Proceedings of Lasers in Manufacturing Conference 2023, Munich, Germany, 26–29 June 2023* (WLT, Hannover, Germany, 2023).

Journal of Materials Processing Tech. 324 (2024) 118266

Contents lists available at ScienceDirect

Journal of Materials Processing Tech.

journal homepage: www.elsevier.com/locate/jmatprotec

Characterization and process optimization of remote laser cutting of current collectors for battery electrode production

Caterina Angeloni, Erica Liverani *, Alessandro Ascari, Alessandro Fortunato

Department of Industrial Engineering (DIN), Alma Mater Studiorum - University of Bologna, viale Risorgimento 2, Bologna, Italy

ARTICLE INFO

Associate Editor: Hui-Ping Wang

Keywords:
Laser Cutting
Current Collectors
Battery Production
Copper Foil
Aluminum Foil

ABSTRACT

Aluminum (Al) and copper (Cu) metal foils of thickness 6–20 μm are employed as current collectors for the production of Li-ion battery cathodes and anodes. Greater demand for this product is driving up production rate requirements, especially in the field of car manufacturing. Laser-based cutting processes for trimming and cutting electrodes are considered suitable for meeting this demand as they can achieve very high throughput while maintaining process quality. In order to meet market requirements, laser manufacturers are developing new laser sources, optics, and scanning heads that will improve process productivity and quality. Establishing the relationship between the laser system and cut quality will lead to competitiveness, increased productivity, and sustainability production. This paper presents a thorough analysis of the cutting performance of pulsed and continuous-wave lasers with scanning speeds of up to 28 m/s for processing thin Al and Cu current collectors. Comparisons between process outcomes are made in terms of maximum and minimum cutting speed and power, kerf geometry, cut quality, and presence of defects. Identification of configurations leading to high and low cut quality enables detailed process parameter windows to be defined for both laser system systems employing continuous-wave and pulsed sources. By analyzing correlations between the materials, laser source, and process variables, the main outcome is that continuous-wave single-mode fiber lasers enable highest cut quality in the high-productivity regime, surpassing the current state-of-the-art in laser cutting of metal foils.

1. Introduction

Battery electrode production within the automotive industry currently includes several laser-based manufacturing processes. This is mainly due to the flexibility of laser technology, which can easily be adapted to different battery geometries, as well as its high quality, reliability, and production rate (Pfleging, 2018). The latter is one of the key factors for success of laser applications because of increasing demand from car manufacturers. For simplicity, most lithium-ion batteries have a similar design, including a metal oxide positive electrode (cathode) coated on an aluminum current collector, a carbon/graphite negative electrode (anode) coated on a copper current collector, a separator, and an electrolyte comprising lithium salt in an organic solvent. The final geometry of electrodes is obtained by cutting or trimming the current collectors both within coated and uncoated regions. Aluminum and copper current collectors are 12 μm and 6 μm thick, respectively, and can be cut with satisfactory outcomes both mechanically using knife slitting or die cutting, or thermally using a laser beam. While mechanical cutting exhibits advantages in terms of avoiding defects such as dross adhesion, melting, development of a heat affected zone or spattering, dies require frequent sharpening to prevent burrs, material attachment, and edge bending, which interrupts continuous production and lowers productivity. Laser cutting is instead a non-contact thermal cutting process that combines high production rates in terms of meters of foil cut per second, high levels of flexibility in terms of the range of patterns that can be cut, and high levels of cut quality in terms of minimizing imperfections resulting from laser-material interactions (Banat et al., 2020). There are several papers in the literature that have dealt with laser cutting of electrodes. Lee et al. (2019) evaluated cut characteristics in terms of kerf and melted width of compressed and uncompressed cathodes while varying the scanning speed and volumetric energy. Berhe et al. (2022) identified the main physical phenomena involved in laser cutting and factors affecting cutting efficiency, developing a mathematical model for top, kerf, clearance, and burr widths. Lutey et al. (2015) applied five different laser sources to cutting of $LiFePO_4$ electrodes and analyzed the ablation depth of the resulting profiles with an optical profiler. Demir and Previtali (2014) compared the cut quality achieved with green lasers and

* Correspondence to: viale Risorgimento 2, 40136 Bologna, Italy.
E-mail address: erica.liverani2@unibo.it (E. Liverani).

https://doi.org/10.1016/j.jmatprotec.2023.118266
Received 14 July 2023; Received in revised form 8 November 2023; Accepted 15 December 2023
Available online 19 December 2023

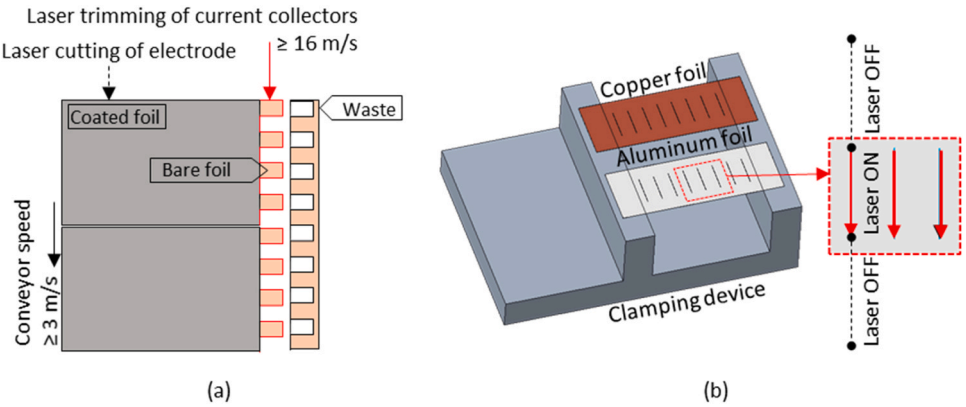

Fig. 1. Laser cutting (or trimming) path of current collectors (a) and experimental cutting setup (b).

infrared lasers, highlighting that with both solutions, pulsed lasers cause localized heating.

The size of the heat affected zone (HAZ) has a significant impact on the resulting cut quality of electrodes; therefore, several authors have addressed this aspect. Schmieder (2017) investigated the composition of the HAZ in relation to the pulse width, finding that the HAZ is substantially smaller than the actual deposition width of ablated material. Lutey et al. (2014) showed that chemical and microstructural alterations in electrode active layers are limited to the visible HAZ. Given the widespread use of pulsed lasers for electrode cutting, many studies have been conducted with this type of source. Nanosecond pulsed lasers are the most commonly cited; however shorter pulse durations have also been investigated to determine potential quality improvements. Zhang. et al. (2019) investigated the use of laser pulses of duration 250 fs – 10 ps at cutting speeds of less than 1 m/s, determining that the HAZ could not be avoided under these conditions. However, similar research on cut quality was also conducted by Baumann et al. (2019) using a continuous-wave (CW) single-mode fiber laser, with preliminary findings presented for cutting speeds of up to 10 m/s. Current collectors employ highly reflective and conductive materials, copper and aluminum, representing a significant challenge for electromobility, as illustrated by Mei et al. (2023) and Kim et al. (2022) for laser welding. However, industrial laser cutting of metallic foils is not currently done with CW green or blue lasers because of their larger focused spot size and lower beam quality when compared to CW IR lasers. On the other hand, new and interesting pulsed green lasers are currently on the market and show promise for this use, but they are expensive and have fixed duration. Luetke et al. (2011) investigated contact-free cutting of Cu and Al foils of thickness 6 and 12 μm, respectively, using two different laser sources to establish the cut quality. Both continuous-wave (CW) and nanosecond pulsed-wave (PW) lasers were exploited to determine the achievable cutting speed and quality in each case, with general fields of application described for both types of laser exposure. The cutting speed, however, was limited to less than 5 m/s in this case. To the best of the authors' knowledge, there have been no comparisons between CW and PW laser cutting of current collectors at speeds higher than 5 m/s. To meet the demands of the automotive industry, the output rates of gigafactories must be approximately one battery per second, requiring cutting speeds of at least 16 m/s. Motion systems that allow such high speeds are relatively new; therefore, the nature of laser-material interactions and the final cut quality at these speeds are currently key areas of research. Because current collectors are used to obtain an electrical connection with the battery cup after trimming and rolling of electrodes, detrimental defects are primarily associated with the edge profile. Wu at al. (2019) identified two types of hazards causing internal short circuits in Li metal batteries: 1) Physical contact between the cathode and anode due to material defects, manufacturing issues (like burrs, particles, and dust), and battery abuse conditions; 2) Contact resulting from chemical and/or electrochemical reactions. Jansen et al. (2019) linked these two factors to spatter formation. Uneven current distribution caused by spatter promotes dendrite growth across the separator, leading to micro-short circuits and early battery failure. For this reason, the main industrial requirement is to eliminate or reduce spatter as much as possible, as well as control dross formation. Dross is residual material that remains attached to the cut edge, developing as a result of insufficient vaporization of the material during the cutting process (Schulz et al., 1999). Furthermore, the kerf width must be minimized to lessen production waste during electrode cutting and trimming. Defect formation is significantly influenced by the melt pool and heat flow, as well as intensity and pressure distributions during laser cutting. Several research groups have sought to understand how these physical processes affect interaction between the laser and material. Lee (2018) described the physical mechanism of partial penetration of current collectors during laser cutting as a physical phenomenon leading to defects. Lee and Mazumder (2018) provided an interesting explanation of spatter formation, correlating this defect to the formation of a crest resulting from liquid metal flow during the cutting process. Molten material is moved from the bottom towards the sides of the keyhole, and then beyond the top surface of the foil by momentum, becoming spatter upon re-solidification. The resulting molten metal forms dross when it solidifies along the cut edge. All of these defects are strictly related to laser-material interaction phenomena and thus vary depending on the optical system and power delivery mode (PW or CW), making comparison of the two laser sources important.

The present paper therefore proposes a comprehensive comparison of CW and PW laser cutting of uncoated pure aluminum and copper current collectors, achieving industrially-relevant scanning speeds of up to 28 m/s for the first time. Results are focused on determining the effects of laser irradiance (the ratio of laser power to spot area) and fluence (the product of irradiance and interaction time) on defects that occur during remote ultra-high-speed laser cutting of aluminum and copper current collectors. Analyses with an Optical Microscope (OM) and Scanning Electron Microscope with Field Emission Gun Microscope (SEM/FEG-EDS) have been performed to characterize the cut quality and correlate these properties with the laser source and process parameters. Final results allow identification of an appropriate process parameter window for both materials and sources.

2. Materials and methods

2.1. Materials, laser sources and cutting setup

A simple metal foil geometry and linear cutting path were considered to characterize and optimize the laser trimming process used for current collectors (see Fig. 1). Strips of copper (CuAg ≥ 99.8%) and aluminium (1100 alloy, wt% Al ≥ 99.0%, Fe ≤ 0.5%, Si ≤ 0.5%, Cu ≤ 0.2% other

Table 1
Detailed characteristics of laser sources and optics.

CW	Maximum Power [kW]	1.2
	M^2	≤ 1.1
	Collimation length [mm]	120
	Focal length [mm]	340
	Fiber core diameter [μm]	14
	Spot diameter [μm]	65
	Wavelength [nm]	1064
PW	Average power [W]	300
	Max peak power [kW]	10
	Max pulse energy [mJ]	2
	Max repetition rate [kHz]	4000
	Pulsed duration [ns]	20-500
	M^2	1.5
	Collimated beam diameter [mm]	8
	Focal length [mm]	100
	Spot diameter [μm]	25
	Wavelength [nm]	1064

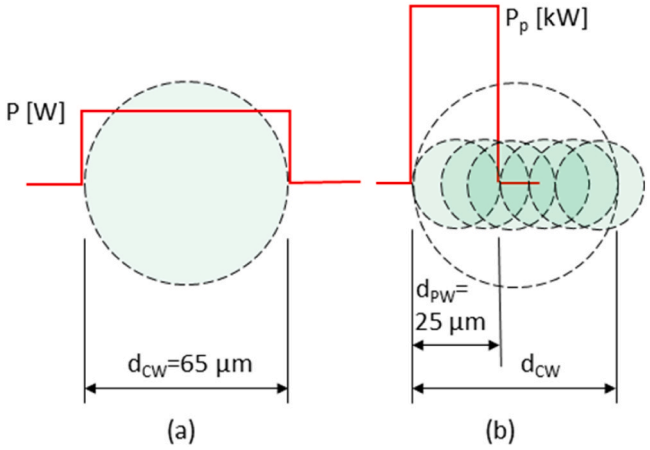

Fig. 2. Model for comparison of CW and PW lasers over the same circular area of diameter d_{CW}.

elements $\leq$ 0.05%) foil, 6 μm and 12 μm thick respectively, were cut from rolls and held under slight tension in a clamping system to keep the foils precisely positioned in the focal plane during cutting. Each strip was 20 mm × 60 mm in size, with parallel laser cuts performed over a length of 10 mm in each case. To avoid thermal interaction and local deviation of the material from the focal plane, the distance between subsequent cuts was 5 mm, while a maximum of 10 cuts were made on each strip. Laser systems employed for experiments included a continuous-wave (CW) nLight 1200 W single mode laser source (nLight, Washington, US) and a pulsed-wave (PW) IPG YLPN 300 W nanosecond ytterbium fiber laser (IPG Photonics Corporation, Massachusetts, US). These laser sources are currently the most promising for cutting current collectors because they have the power (or peak power with high frequency) to complete a cut at scanning speed up to 20 m/s. Furthermore, thanks to the high quality of the laser beam (see Table 1), very high cut quality is expected together with narrow kerf and low thermal dissipation. The CW system was equipped with a 14 μm core optical fiber for beam transportation and a Scanlab IntelliScan 20 galvanometric scanning head for beam movement, equipment with an f-theta lens with an effective focal length of 340 mm. The spot size was measured as 65 μm using a beam profiler (BeamWatch®, Ophir, Germany) in line with the standard measurement method set out in ISO 11146. For the PW system, beam movement was achieved with a Raylase Superscan II 10 equipped with an f-theta lens with a focal length of 100 mm, achieving a final spot size 25 μm.

To avoid heat accumulation within the current collectors, the laser cutting process was designed to account for galvo-mirror acceleration and deceleration, excluding these from the analysis (see Fig. 1b).

The laser beam was only turned on in the central part of the path, while the extension over which the laser beam was turned off was determined with a preliminary experimental campaign. As noted previously, both foils were held in the focal plane during all tests. Table 1 summarizes the complete characteristics of both setups.

2.2. Cutting parameters

In order to compare laser cutting under PW and CW conditions, the model for laser-material interaction displayed in Fig. 2 was adopted. Fig. 2a depicts the interaction of a CW laser beam with power P and spot diameter d_{CW}, while Fig. 2b depicts the interaction of a PW laser beam over the same area with peak power P_p and spot diameter d_{PW}.

Based on this model, the irradiance (I_{CW} and I_{PW}), fluence (F_{CW}) and equivalent fluence (F_{PW}) were calculated for PW and CW exposure in line with Eqs. 1–4.

$$I_{CW} = \frac{P}{A_{CW}} \quad \left[\frac{MW}{cm^2}\right] \tag{1}$$

$$I_{PW} = \frac{P_p}{A_{PW}} \left[\frac{MW}{cm^2}\right] \tag{2}$$

$$F_{CW} = I_{CW} \bullet \tau = I_{CW} \bullet \frac{d_{CW}}{Speed} \left[\frac{J}{cm^2}\right] \tag{3}$$

$$F_{PW} = F_{PW,p} \bullet N_p = I_{PW} \bullet t \bullet N_p = I_{PW} \bullet \tau_{EQ} \left[\frac{J}{cm^2}\right] \tag{4}$$

where A_{CW} and A_{PW} are the spot areas of the CW and PW laser beams

Table 2
Process parameters employed for CW laser cutting tests.

	P [W]	I_{CW} [MW/cm2]	Laser speed [m/s]	F_{CW} [J/cm^2]		P [W]	I_{CW} [MW/cm^2]	Laser speed [m/s]	F_{CW} [J/cm^2]
CW_A1	170	5.1	4.75	70	CW_C4	660	19.9	5.2	250
CW_A2	330	9.9	9.2		CW_C5	830	25.0	6.5	
CW_A3	500	15.1	14		CW_C6	1000	30.2	7.8	
CW_A4	660	19.9	18.5		CW_D1	170	5.1	0.95	350
CW_A5	830	25.0	23		CW_D2	330	9.9	1.85	
CW_A6	1000	30.2	28		CW_D3	500	15.1	2.8	
CW_B1	170	5.1	2.8	120	CW_D4	660	19.9	3.7	
CW_B2	330	9.9	5.4		CW_D5	830	25.0	4.6	
CW_B3	500	15.1	8.2		CW_D6	1000	30.2	5.6	
CW_B4	660	19.9	10.7		CW_E1	170	5.1	0.65	500
CW_B5	830	25.0	13.5		CW_E2	330	9.9	1.3	
CW_B6	1000	30.2	16.3		CW_E3	500	15.1	1.95	
CW_C1	170	5.1	1.35	250	CW_E4	660	19.9	2.6	
CW_C2	330	9.9	2.6		CW_E5	830	25.0	3.2	
CW_C3	500	15.1	3.9		CW_E6	1000	30.2	3.9	

Table 3
Process parameters employed for PW laser cutting tests.

	E_p [mJ]	Pulse duration [ns]	P_p [kW]	f [kHz]	I_{PW} [MW/cm^2]	Laser speed [m/s]	N_p	F_{PW} [J/cm^2]
PW_A1	0.3	240	1.3	1000	255	20.7	3.14	192.0
PW_A2	0.2	120	1.7	1500	340	20.7	4.71	
PW_A3	0.1	20	5.0	3000	1019	20.7	9.42	
PW_A4	0.15	20	7.5	2000	1529	20.7	6.28	
PW_A5	0.5	60	8.3	600	1699	20.7	1.88	
PW_B1	0.3	240	1.3	1000	255	16	4.06	248.4
PW_B2	0.2	120	1.7	1500	340	16	6.09	
PW_B3	0.1	20	5.0	3000	1019	16	12.19	
PW_B4	0.15	20	7.5	2000	1529	16	8.13	
PW_B5	0.5	60	8.3	600	1699	16	2.44	
PW_C1	0.3	240	1.3	1000	255	8	8.13	496.8
PW_C2	0.2	120	1.7	1500	340	8	12.19	
PW_C3	0.3	240	1.3	1000	255	8	8.13	
PW_C4	0.15	20	7.5	2000	1529	8	16.25	
PW_C5	0.5	60	8.3	600	1699	8	4.88	
PW_D1	0.3	240	1.3	1000	255	4	16.25	993.6
PW_D2	0.2	120	1.7	1500	340	4	24.38	
PW_D3	0.1	20	5.0	3000	1019	4	48.75	
PW_D4	0.15	20	7.5	2000	1529	4	32.50	
PW_D5	0.5	60	8.3	600	1699	4	9.75	

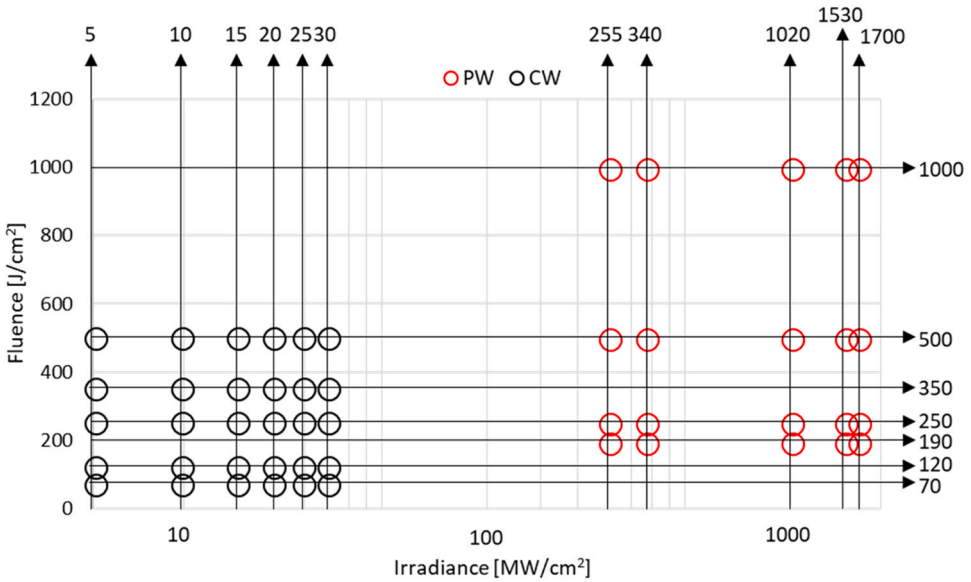

Fig. 3. Summary of laser cutting experimental campaign for PW (red dots) and CW (black dots) laser sources.

considering respective spot diameters of 65 μm and 25 μm, τ is the interaction time for CW exposure, $F_{PW,p}$ is the pulse fluence for PW exposure, and t is the pulse duration. For the purposes of comparing fluence, the number of pulses (N_p) generated by the PW laser was calculated based on Eq. 5, allowing definition of the equivalent interaction time (τ_{EQ}) based on Eq. 6.

$$N_p = \frac{d_{CW} \bullet f}{Speed} \tag{5}$$

$$\tau_{EQ} = t \bullet N_p \tag{6}$$

Detailed process parameters are reported in Tables 2 and 3 for tests conducted with the CW and PW laser sources, respectively. For CW experiments, a total of 5 fluence levels and 6 irradiance levels were employed. Due to limitations in combining process parameters for PW experiments, 4 equivalent fluence levels and 5 irradiance levels were evaluated for this type of exposure.

Two fluence levels (250 and 500 J/cm^2) coincided between the two laser sources; however, no corresponding values of irradiance could be established due to the high peak power of the PW laser source (see Fig. 3). Final process parameters were established based on the outcomes of preliminary tests, which are not the focus of this paper, with the intention of examining all physical phenomena related to laser cutting of thin films at high processing speeds.

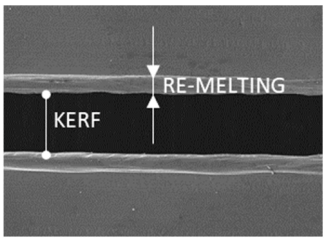

Fig. 4. Definition of kerf width and re-melting thickness.

2.3. Characterization of cut quality

Optical microscopy (OM, Nikon Optiphot-100) was performed to a

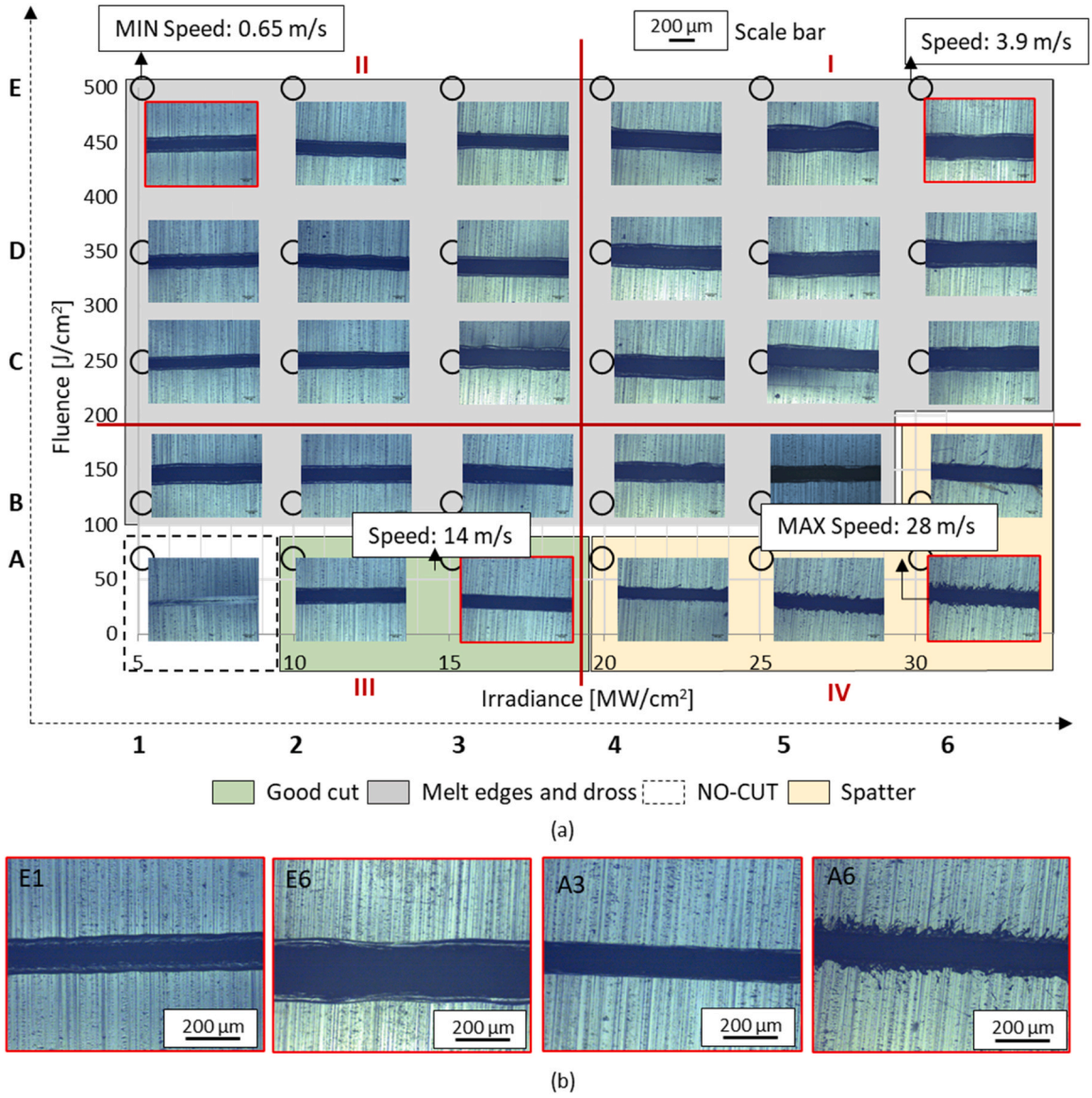

Fig. 5. OM images of CW laser cuts performed on aluminum current collectors (a) and enlargement of representative cuts (b) performed with the following process parameters: 170 W and 0.65 m/s (E1), 1000 W and 3.9 m/s (E6), 500 W and 14 m/s (A3), 1000 W and 28 m/s (A6).

provide preliminary assessment of cut quality and identify general defects for each combination of process parameters in terms of uncompleted cuts, spatter, burns, melted edges, dross, and presence of a HAZ. Furthermore, the kerf width was determined for all tests (see Fig. 4), with the mean value calculated based on 3–5 data points collected along the entire cut. SEM-FEG microscopy (Tescan Mira3 with a Schottky emitter) was then used to examine representative cuts on both the front surface (the area directly subject to laser irradiation) and the underside of each foil. Each cut was observed via SEM at the start, middle, and end of the laser path.

3. Results

3.1. Continuous-wave laser cutting

Representative images of different cut morphologies obtained on aluminum current collectors with CW laser exposure are reported in Fig. 5, considering irradiance as the driving input parameter for the various experiments. Cutting geometries were initially divided into "good cut" and "bad cut" categories, with the latter being further divided based on the primary type of defect in each case. Bad cuts were catalogued as “over-melted” when the thickness of resolidified metal was greater than 25% of the kerf width, and “sputter-cut” when the presence of sputtering was predominant (see Fig. 6). With an irradiance level of less than or equal to 5 MW/cm^2 and a fluence level of less than 100 J/cm^2, the current collectors remained uncut or partially uncut, as seen in Fig. 5a. Fluence levels greater than 100 J/cm^2 led to over-melted edges at all levels of irradiance. This region of high fluence combined with low irradiance (II quadrant) led to melted edges and dross formation (the gray area in Fig. 5a) characterized by different levels of over-melting that were considered critical or unacceptable (re-melting/kerf width ratio from 25% to 65%). The ratio of melted edge thickness to kerf width decreased from quadrant II to all other quadrants (see Fig. 4), with higher values of both parameters observed in quadrant I (high fluence and high irradiance). Finally, spatter was observed at high levels of irradiance and low fluence (IV quadrant). After identifying the regions where the main defects were located, it was clear that the best combination for achieving good cut quality was low fluence and low irradiance.

The samples highlighted by red frames (enlarged in Fig. 5b) were

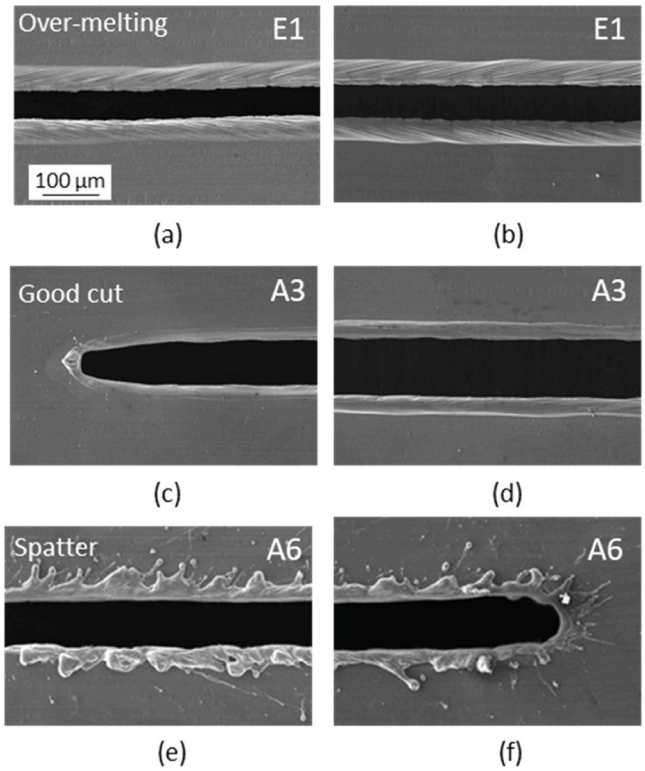

Fig. 6. SEM images (SE, 10 kV) of CW laser cuts performed on aluminum current collectors: (a,b) cut with over-melted edge (170 W, 0.65 m/s), (c,d) good cut (500 W, 14 m/s) and (e,f) spattered cut (1000 W, 28 m/s).

chosen for SEM analysis (Fig. 6) as representative of cut quality obtained in each process region. The selected cut in quadrant I was characterized by a larger kerf, that in quadrant II by a severely over-melted edge, that in quadrant III by high cut quality and that in quadrant IV by spatter. Parts a and b of Fig. 6 display the front and back sides of the cut obtained with parameter set CW_E1 (see Table 2). It is worth noting that the over-melted edges were very homogeneous on both sides, which was observed along the entire cut. No dross formation was found on aluminum current collectors using this parameter set or any other parameters employed during CW laser irradiation.

Parts a and b of Fig. 6 highlight the fact that a large quantity of molten material is not ejected from the bottom of the current collector but remains adherent to both the top and bottom surfaces. A ridge can be seen along the cut edge, with the width depending on the specific process parameters employed. In the case of CW_E1, the mean ridge width was 40 µm in the middle of the cut, while the kerf was 48 µm, yielding a ratio of 0.83. Very similar cut quality was identified for other samples within quadrant I (CW_E6). The respective images are not reported as the kerf increased to 215 µm, with the ratio between the ridge and kerf widths decreasing to 0.29. The same considerations can be made for high quality cuts (Fig. 6c and d, sample CW_A3); however, in this case, the size of the kerf and remelted width are significantly smaller, 160 µm and 45 µm respectively, with the same ratio of 0.28. By observing the final part of the cut in Fig. 6c, the melted metal generates an appendage on the cut edge, with the same phenomenon visible on the underside in the initial part of the cut. For completeness, this defect was analyzed on cuts performed with parameters similar to CW_A3, with the defect present in all cases; however, the molten droplet was identified on both surfaces without a direct correlation with the position of the start and end of the cut. It was sometimes found on the front surface at the start of the cut and other times at the end of the cut and vice versa. Images of the spattered sample (CW_A6) are shown in Fig. 6e and f. Due to melt turbulence, the profile of the melted edges was no longer uniform, with spatter ejected far from the laser path onto the surface around the cut in the middle (e) and partially at both ends (f), over a width of 250–300 µm.

Representative images of different cut morphologies obtained on copper current collectors with CW laser exposure are reported in Fig. 7.

With reference to Fig. 7a, a larger number of parameters led to no cut or a partially cut than was observed for aluminum over the same irradiance and fluence ranges. Despite the copper current collector being thinner, this result was in line with expectations due to lower optical absorptivity of copper in the near infrared. To achieve a complete cut with fluence below 100 J/cm^2, it was necessary to employ an irradiance level greater than 25 MW/cm^2. As with aluminum, high-quality cuts were achieved with process parameters near the uncut region.

It is immediately clear from Fig. 7a that copper exhibited a wider parameter range leading to high quality cuts than aluminum, suggesting a better response of copper to ultra-high-speed laser cutting. The wider range of parameters leading to good quality was due to lower levels of spattering, with defects confined to speeds greater than 25 m/s, at the operating limit of current galvanometric scanning heads. Melted edges were obtained over a similar range of process parameters to aluminum but with two important differences in relation to edge melting and the presence of burns. Edge melting was not homogeneous but was localized to very small areas, with melted droplets appearing at relatively regular intervals depending on the specific parameters employed, and dross formation resulting from localized heat accumulation rather than as a continuous ridge. Burning instead affected a broad range of parameters in quadrant I, overlapping with regions within quadrants I and II where defects relating to melting were also observed. Despite burns being more evident at higher fluences, this defect was relatively limited and only affected a relatively limited area of the surfaces under all process conditions. The samples highlighted by red frames (enlarged in Fig. 7b) were chosen for SEM analysis (Fig. 8) as representative of cut quality in each process region. Fig. 8a and b display SEM images of samples located in quadrant I (CW_E6) and quadrant II (CW_E1), respectively, both of which were affected by edge melting. The appearance of the former was similar to that observed for aluminum under the same process conditions but with some width irregularities, while the latter was characterized by melting in the form of dross, as was observed with all combinations of process parameters employing high fluence and medium or low irradiance. In both cases, no relevant difference in cut quality was observed between the front and back sides. Conversely, process parameters leading to high cut quality (B4 in Fig. 8c and d) led to a significant difference between the characteristics of the two sides. The upper side, on which laser interaction took place, was free of melting, which was instead visible on the underside in the form of a narrow homogeneous ridge similar to that observed for aluminum, with the ratio between the melt width (30 µm) and kerf (135 µm) being 0.22. Due to the formation of less molten material along the edges, the spattered sample (A6, Fig. 8e and f) also exhibited a lower quantity of ejected material. However, copper spatters reached a distance from the laser path similar to that of aluminum, with molten droplets affecting both the upper and lower surfaces of the current collector (Fig. 8c and d).

3.2. *Pulsed-wave laser cutting*

Significant differences in cut quality were observed when switching to PW laser cutting. Despite the same types of defects being observed, the impact of these defects on the quality of the resulting cuts was more evident, in particular on aluminum samples. Fig. 9 displays images of the cut quality obtained on aluminum current collectors with the parameters given in Table 3. As observed for CW cutting, high fluence caused over-melted edges at all levels of irradiance. However, the over-melting threshold increased for PW cutting, rising to above 250–500 J/cm^2. In addition, melted edges were irregular, with this discontinuity worsening as irradiance increased despite the fact that the melted region was narrower.

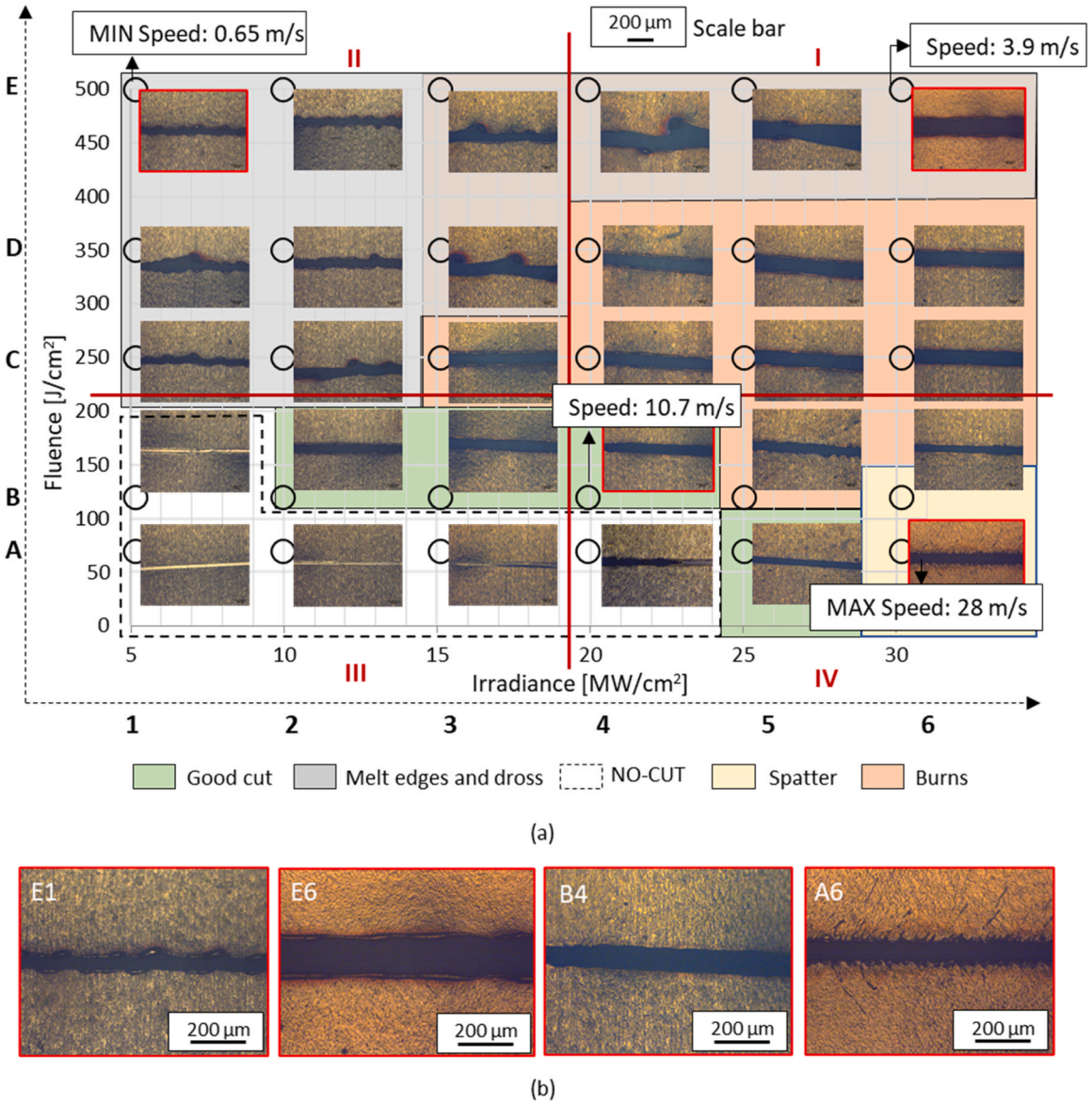

Fig. 7. OM images of CW laser cuts performed on copper current collector (a) and enlargement of representative cuts (b) performed with the following process parameters: 170 W and 0.65 m/s (E1), 1000 W and 3.9 m/s (E6), 660 W and 10.7 m/s (B4), 1000 W and 28 m/s (A6).

At the opposite end of the tested parameter window, where low fluence levels were employed, spatter and burns were instead the main types of defects observed. The latter appeared as dark regions adjacent to the cut edges, with the effect being more pronounced at higher irradiance levels. Best cut quality was obtained at a cutting speed of 16 m/s at all irradiance levels; however, upon comparison of the best cuts obtained with PW (Fig. 10c) and CW (see Fig. 8c) laser sources, worse cut quality was evident in the former case.

Following the same criteria for selection of samples for SEM analysis, representative images of the obtained cut quality in each process region are shown in Fig. 10, including samples exhibiting melting (PW_D2), burning (PW_C5), high cut quality (PW_B2) and spattering (PW_A4). No underside images are provided as these surfaces exhibited the same characteristics as the top sides. Comparison of OM and SEM images leads to the following observations:

- While edge remelting (Fig. 10a) was not as homogeneous as with CW laser cutting, this type of defect was nonetheless similar under both CW and PW conditions. Despite the smaller spot diameter employed in the PW setup, the kerf width of sample PW_D2 was comparable with that of sample CW_E1 due to twice the fluence being employed.
- The highest cut quality achieved with the PW laser (Fig. 10c) was not completely free of small, rounded droplets of material within the entire region surrounding the cut due to turbulence of the molten phase during laser exposure.
- Spatter (Fig. 10d) was abundant but more contained around the cut, up to 130 µm from the center of the cut.
- No burns were visible in SEM images, confirming that no state changes were associated with this defect.

Fig. 11 displays images of the cut quality obtained on copper current collectors with the PW laser setup. The same general considerations can be made as for aluminum in terms of defect formation. In this case, process parameters leading to good cut quality were those employing low irradiance levels, while a wider range of parameters comprising high irradiance led to the development of burns.

Finally, edge melting was less of an issue for copper, as was observed for CW cutting, suggesting that differences in this aspect were due to material properties rather than the type of laser exposure.

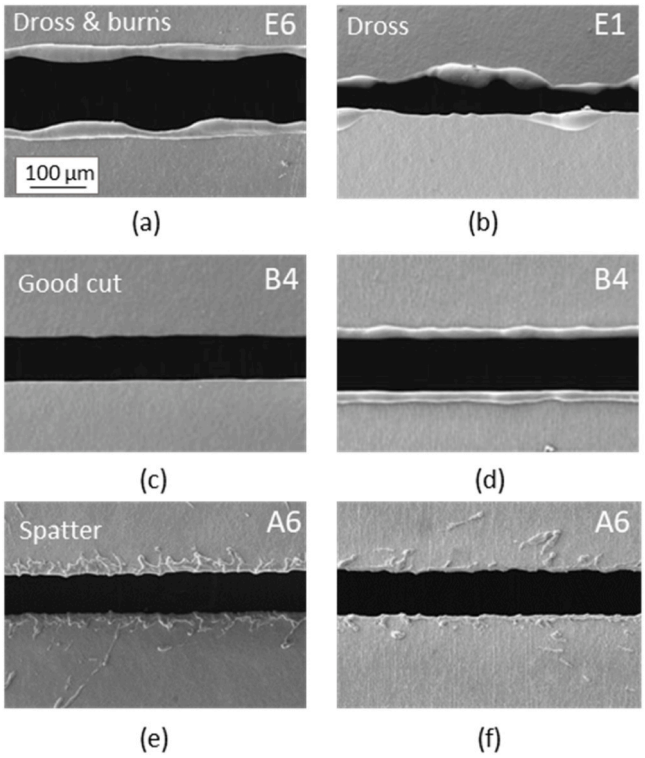

Fig. 8. SEM images (SE, 10 kV) of CW laser cuts performed on copper current collectors: (a,b) cut with dross (1000 W, 3.9 m/s) and burns (170 W, 0.65 m/s), (c,d) good cut (660 W, 10.7 m/s) and (e,f) spattered cut (1000 W and 28 m/s).

3.3. Kerf width measurements

The results of kerf width measurements were analyzed based on three levels of comparison. The first (Level 1) compared the influence of the *laser source* on the kerf width, the second (Level 2) the influence of the *material* and the third (Level 3) the influence of the *process parameters* in terms of fluence and irradiance.

The Level 1 comparison (influence of laser source) was performed by calculating the mean width and standard deviation of all cuts obtained with both laser sources. The resulting values were 36 ± 14 µm for the PW laser source and 90 ± 5.5 µm for the CW source. The Level 2 comparison (influence of material) was performed by calculating the mean width obtained using PW and CW sources for both materials. The results of this comparison are presented in Table 4.

Finally, the Level 3 comparison (influence of process parameters) was performed by calculating the mean kerf width obtained under all conditions having constant values of fluence or irradiation for each combination of laser source and material. For example, the value represented by the first bar on the left of Fig. 12a (highlighted by a single red asterisk) was obtained by averaging the measured kerf widths of samples CW_A1, CW_A2, …, CW_A6, which all employed the same fluence level of 70 J/cm^2. In the same way, the value represented by the second bar (highlighted by two red asterisks) was obtained by averaging the measured kerf widths of samples CW_B1, CW_B2, …, CW_B6. An analogous comparison in terms of irradiance is presented in Fig. 12b. The value represented by the first bar (highlighted by a single black asterisk) was obtained by averaging the measured kerf widths of samples CW_A1, CW_B1, …, CW_E1, and so on.

4. Discussion

One of the main goals of battery production is to achieve high productivity and quality, conditions that directly apply to cutting of battery current collectors. To date, a comprehensive study of feasible laser sources, optics and process parameters has yet to be presented in the literature. As a result, a thorough investigation of CW and PW laser cutting of copper and aluminum current collectors was conducted within this work. In the following section, a detailed analysis of correlations between cut quality and material, power delivery, and process parameters is presented.

4.1. Correlation between cut quality and material

By employing the same process parameters for cutting of aluminum and copper current collectors, it was possible to demonstrate that aluminum required lower levels of irradiance and fluence despite being twice as thick. This behavior was connected to the material properties of the current collectors. During laser cutting of copper, material removal took place at lower rates than for aluminum due to copper's lower mean optical absorptivity and higher thermal conductivity. Once cutting was achieved, by comparing Figs. 5 to 11, it is interesting to note the more widespread presence of burns for copper than aluminum. While aluminum was only susceptible to burns at the highest tested value of irradiance (> 1000 MW/cm^2), copper current collectors had burnt edges at low irradiance (CW mode), although this effect was more confined. By observing Figs. 9 and 11, it is possible to infer that during cutting of aluminum current collectors, highest temperatures were confined to the kerf and a very limited area in the neighboring region. This outcome was due to the physical characteristics of the materials in question, considering that the thermal conductivity of aluminum at room temperature is almost half that of copper (210 W/mK vs. 395 W/mK). However, the absence of burns was replaced by a melted edge, which was always visible along the aluminum cut edge. According to Babadjanov et al. (2023), this demonstrates that materials with high thermal conductivity melt less and burn more due to faster heat dissipation, while materials with lower thermal conductivity exhibit melted edges as a result of localized heat accumulation. Additionally, when observing CW cuts, the remelted edge was typically uniform in width and shape for aluminum but irregular for copper due to discontinuous heat accumulation (see Fig. 7), in accordance with Lee et al. (2012).

From a broader perspective, it is possible to argue that the resulting cut quality of copper depended on both irradiance and fluence (Figs. 6–10), while that of aluminum depended more on the interaction time (i.e. fluence) than on power (i.e. irradiance). In fact, by comparing results obtained for aluminum at the same fluence level, the presence of specific types of defects or good cut quality occurred at all irradiance levels, in particular for PW laser cutting.

4.2. Correlation between cut quality and process parameters

Fig. 13 provides a summary of results presented previously to assist in interpreting the correlation between process parameters and cut quality.

Four types of defects were detected, with the following correlations between defect type and irradiance and fluence levels:

1. Predominance of remelted edge at high fluence and low irradiance
2. Spatter at low fluence
3. Burns at high irradiance
4. Incomplete cutting at low fluence and low irradiance

Good cut quality was achieved with moderate fluence levels and moderate-to-low irradiance levels. High irradiance levels led to the formation of a large amount of liquid phase due to high power, resulting in two main issues: a large kerf and spatter. In particular, where high power was combined with low speed, the resulting kerf width was very large due to the larger area over which thermal conduction led the material to reach its vaporization temperature. In contrast, where high irradiance levels were connected with fast speeds, the interaction time was short and the vaporization temperature was attained over a width

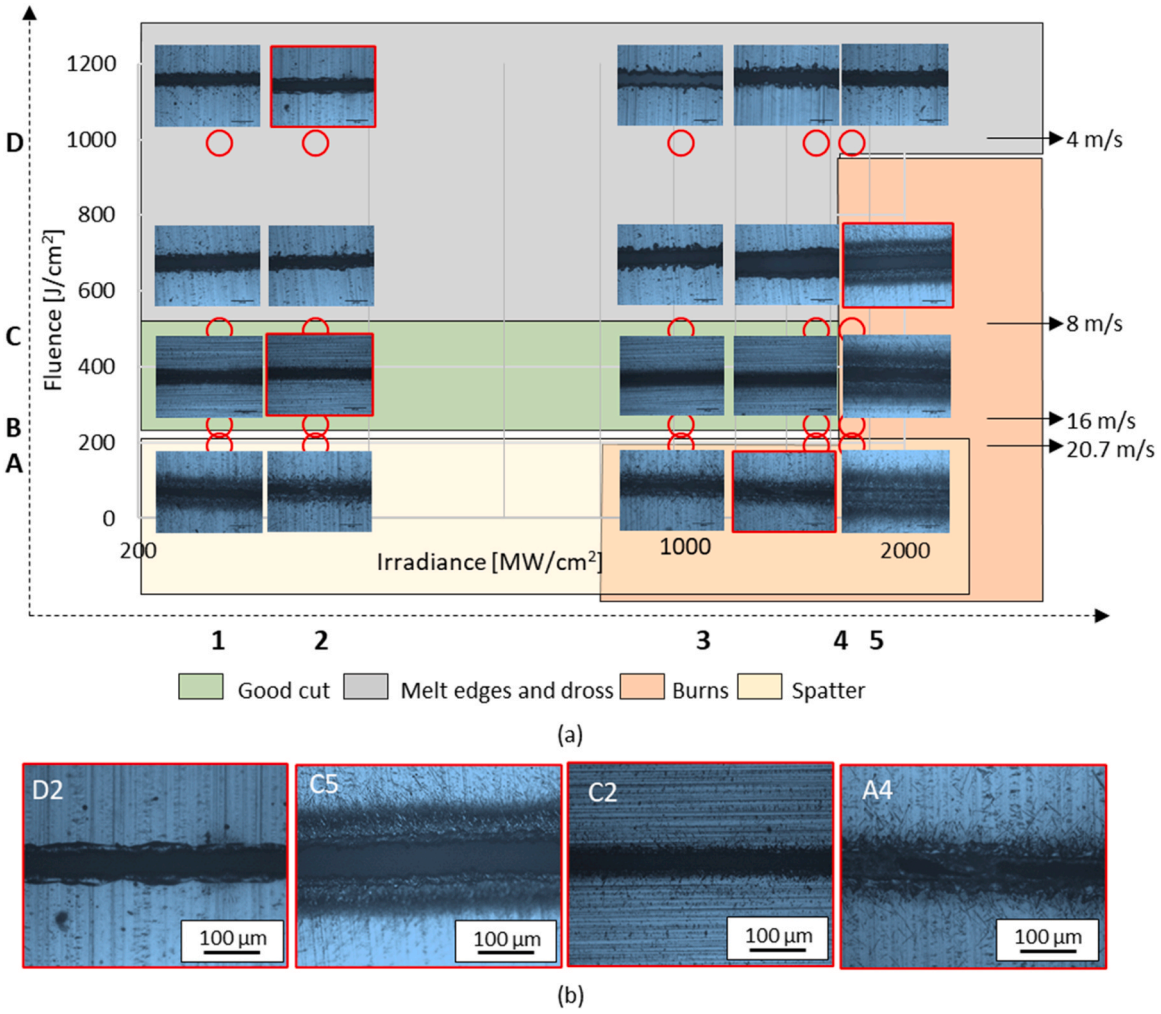

Fig. 9. OM images of PW laser cuts performed on aluminum current collector (a) and enlargement of representative cuts (b) performed with the following process parameters: 1.7 kW and 4 m/s (D2), 8.3 kW and 8 m/s (C5), 1.7 kW and 8 m/s (C2), 7.5 kW and 20.7 m/s (A4).

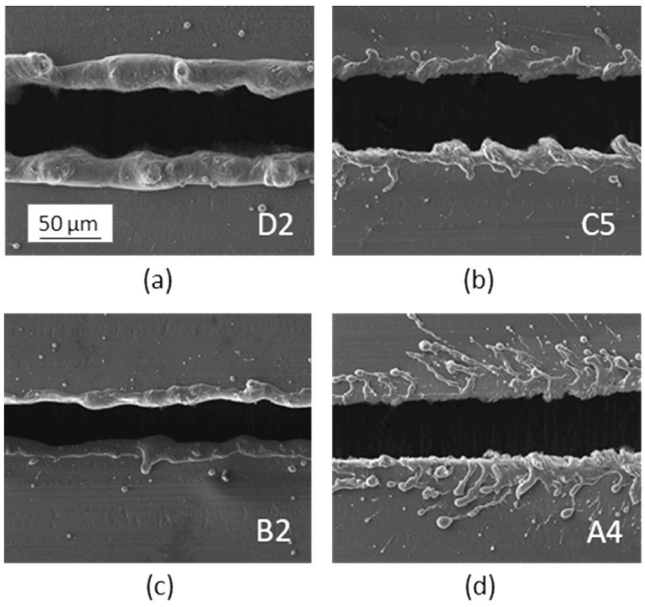

Fig. 10. SEM analysis (SE, 10 kV) of PW laser cuts performed on aluminum current collectors: (a) PW_D2, (b) PW_C5, (c) PW_B2 and (d) PW_A4 samples are shown.

that was smaller than the spot diameter, with melting of the cut edges. However, the high speed led to turbulence in the molten material, which in turn promoted spatter. For a given power, higher speeds nonetheless provided the best cutting conditions up until the onset of spatter.

Upon observation of the relationship between the cut quality of aluminum and the employed process parameters, a dependence on fluence becomes evident. Fig. 14a presents an image of a cut performed with the highest fluence, and consequently the longest interaction time, while Fig. 14b presents an image of a cut obtained with the highest irradiance and roughly half the fluence. SEM analysis shows that in the first case (PW_D2), a small kerf developed with a large extension of the heat affected zone (the white area), while in the second case (PW_C5), a large kerf developed but with a smaller HAZ. These outcomes can be explained in terms of the total heat input and peak temperature. The larger HAZ in the first case can be attributed to the larger heat input (i.e. longer interaction time), while the smaller kerf can be attributed to the lower peak temperature of D2 compared to C5 (i.e. lower peak power).

4.3. Correlation between cut quality and laser source

Although the current state-of-the-art for cutting of copper and aluminum current collectors (with or without coatings) is evolving from mechanical to pulsed laser cutting, the outcomes of this study demonstrate that the best quality is undoubtedly obtained with CW single mode lasers. Comparison of the two types of lasers requires complex assessment of laser-material interactions leading to the physical outcomes. It is

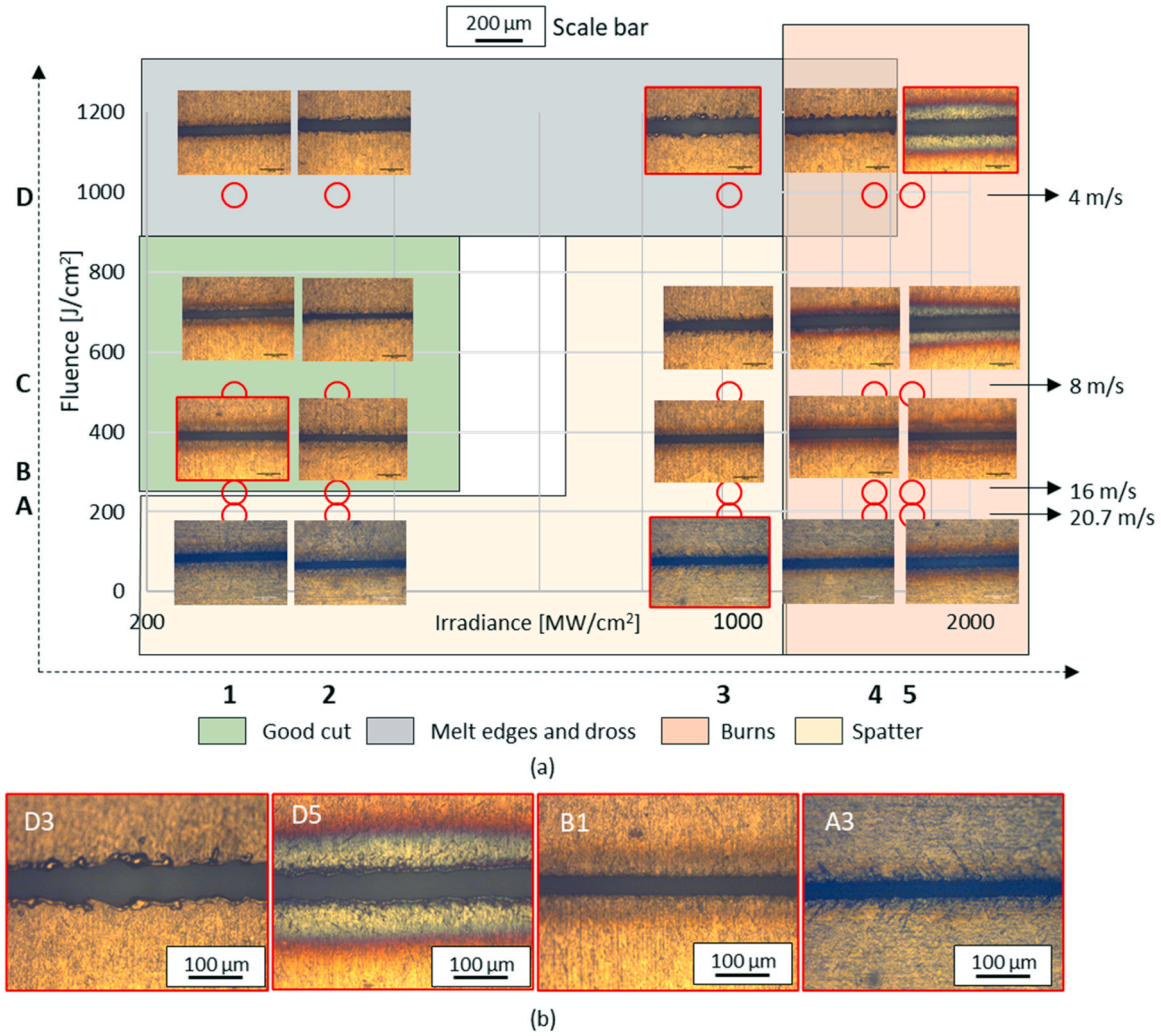

Fig. 11. OM images of PW laser cuts performed on copper current collectors (a) and enlargement of representative cuts (b) performed with the following process parameters: 5 kW and 4 m/s (D3), 8.3 kW and 4 m/s (D5), 1.3 kW and 16 m/s (B1), 5 kW and 20.7 m/s (A3).

Table 4
Influence of material (Level 2 comparison).

	ALUMINUM			COPPER		
	Mean [µm]	Std.Dev [µm]	Std.Dev/ Mean	Mean [µm]	Std.Dev [µm]	Std.Dev/ Mean
CW	**96**	23.8	0.25	**84**	28.9	0.34
PW	**35**	13.0	0.37	**36**	8.5	0.24

interesting to note that for CW laser sources, ideal cutting conditions were close to those leading to no cut, taking place at the highest tested cutting speed that could be achieved. This is consistent with literature in the field of laser cutting of sheet metal performed at lower cutting speeds (Wandera et al., 2009). The same consideration cannot be made for PW laser sources, where ideal cutting conditions were within a more central part of the process parameter window. The effect of vapor pressure in the pulsed regime goes beyond simple evaluation of phase changes (vaporization and melting) and heating by conduction. The explosive effect of vapor pressure on the molten phase requires optimization of cutting speed to be balanced with the prevention of dross at low speeds and spatter at high speeds. The final cutting quality was negatively affected by the contribution of vapor pressure across all parameters. Figs. 6 and 7 show that by using a CW source rather than a PW source, better results were obtained under all conditions, both optimal and suboptimal.

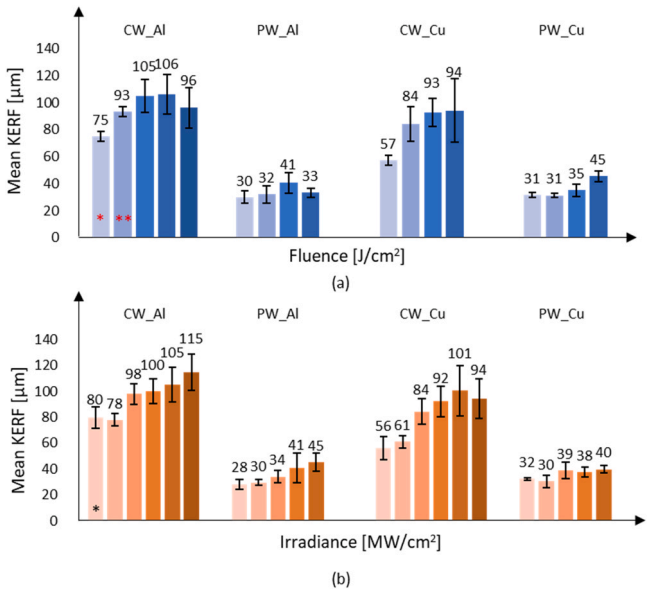

Fig. 12. Correlation between kerf width and fluence (a) or irradiance (b).

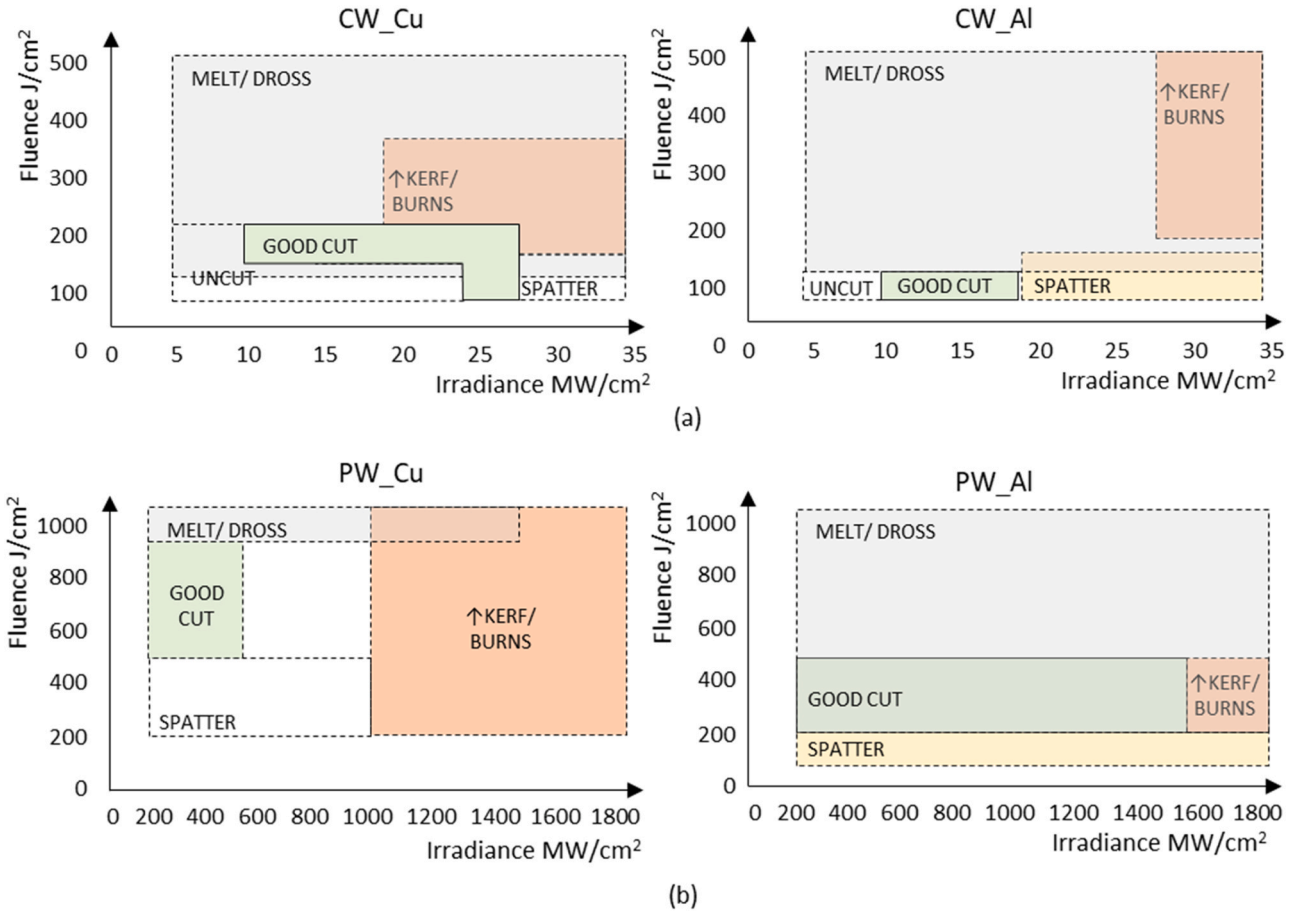

Fig. 13. Correlation between cutting parameters and defects for CW (a) and PW (b) laser sources.

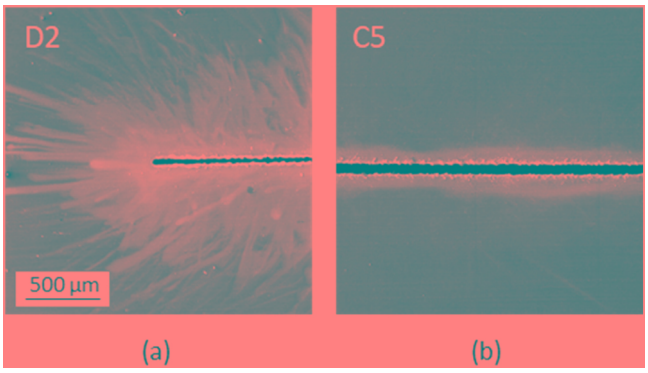

Fig. 14. Low magnification images of aluminum (a) PW_D2 (1.7 kW and 4 m/s) and (b) PW_C5 (8.3 kW and 8 m/s) samples.

4.4. Kerf width

The kerf width was generally highest in quadrant I, corresponding to high fluence and irradiance, as shown in Figs. 5, 7, 9, and 11. However, by examining the data provided in Section 3.3, more specific considerations can be made for each process variable.

Firstly, the result shows that the average kerf width obtained with the PW setup with a spot diameter of 25 µm was smaller than that obtained with the CW setup with a spot diameter of 65 µm. By comparing average values, the mean kerf width obtained with the PW source was 39.7% of that obtained with the CW source, with this value almost equal to the ratio of the two spot diameters (38.5%). This implies that the focusing system had a direct impact on the relationship between kerf width and laser setup. However, upon analysis of the standard deviation, it becomes clear that other variables such as the material and process parameters also influenced the kerf width. A value of 31% was obtained by dividing the standard deviation by the average value for both sources, proving once more that variability of the kerf width was linked to other parameters, with similar correlations for both PW and CW sources.

The effects of the most important process parameters on the kerf width were assessed by comparing data for the two tested materials. The average kerf width for copper was 88% of that obtained for aluminum with the CW laser source, while similar values were obtained for both materials with the PW laser source. As a result, the material had no effect on the obtained outcomes with the PW laser source and a moderate-to-low impact on outcomes obtained with the CW laser source. However, some additional considerations can be made by again focusing on the standard deviation.

For copper foils subject to CW laser exposure and aluminum foils subject to PW laser exposure, the ratio of the standard deviation to the mean value was higher, suggesting greater dependence on the specific process parameters employed and implying that process optimization is more difficult under these conditions. This outcome supports earlier conclusions relating to cut quality, including comparison of CW cutting results in Figs. 5 and 7. In fact, aluminum foils are typically cut with knife slitting or die cutting due to the challenging process of tuning laser parameters, whereas pulsed lasers are currently widely used for cutting of copper foils.

However, values of standard deviation in Table 4 suggest dependence of the kerf width on process parameters for all of the tested setups. As a result, further analysis of data in Fig. 12 is necessary. In order to better analyze the data presented for each comparison group, linear

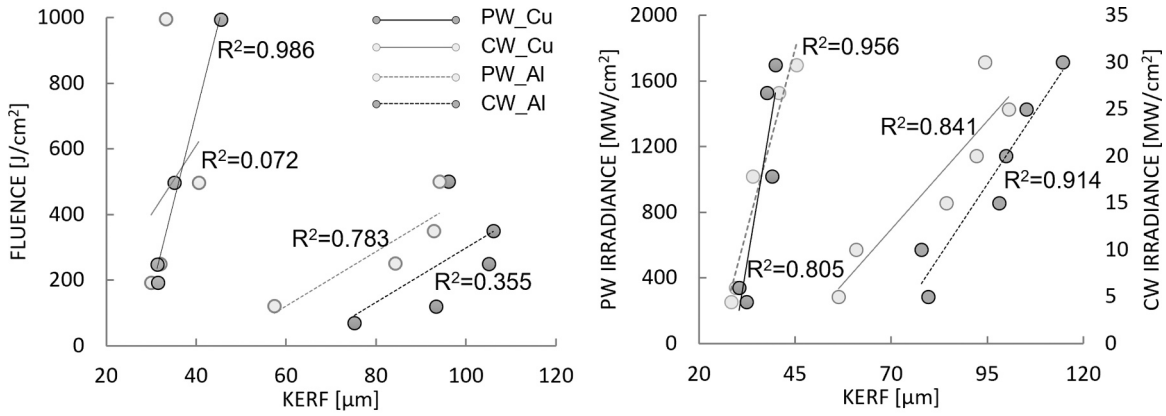

(a)

Cut condition - variable under consideration	R-squared value	Cut condition - variable under consideration	R-squared value
CW_Al - Fluence	0.355	CW_Al - Irradiance	0.914
PW_Al - Fluence	0.072	PW_Al - Irradiance	0.956
CW_Cu - Fluence	0.783	CW_Cu - Irradiance	0.841
PW_Cu - Fluence	0.986	PW_Cu - Irradiance	0.805

(b)

Fig. 15. Kerf-fluence and kerf-irradiance correlations with R-squared values. Trend lines (a) and summary of R-squared values (b).

trends were assumed. Fig. 15 displays the resulting trend lines and R-squared coefficients related to the accuracy of the regression line. These results demonstrate that the kerf width for aluminum foil was primarily correlated to the irradiance, while for copper foil it was connected to both irradiance and fluence. Considering the discussion points raised in Section 4.2, it is possible to infer that, for aluminum foil, the cut width depended on irradiance and power, while the HAZ depended on the fluence and interaction time.

5. Conclusion

State-of-the-art of laser cutting of aluminum and cooper current collectors of thickness 12 µm and 6 µm, respectively, has been presented in the context of battery electrode production. Continuous-wave and pulsed laser sources with high performance scanning heads were used for experiments, allowing investigation into how the laser source, material, and process parameters were correlated with the cut quality, kerf width and defect formation. The main outcome was that CW single mode fiber lasers enable higher cut quality under all tested conditions, surpassing the current state-of-the-art in metal foil cutting. Although both PW and CW setups led to similar process parameter windows achieving best cut quality, the CW setup achieved overall superior cut quality than the PW setup. The results showed that there were fewer or no burns, less spatter, and a more uniform kerf width geometry and re-solidified edges with a CW laser. Additionally, when comparing optimal process parameters for both setups, the quality was clearly better with the CW source. The only exception was low-speed ($\leq$ 4 m/s) cutting of copper foils. In this case, the resulting cut edge was jagged and irregular with the CW laser, whereas less significant dross and remelted edges were observed with the PW laser under low-speed cutting conditions with low irradiance ($<$ 350 MW/cm^2).

From a process parameter point of view, it was possible to achieve cutting speeds greater than 20 m/s with acceptable cut quality with both CW and PW laser sources. A maximum value of 28 m/s was attained with the CW laser source. Limitations in terms of cutting speeds greater than 28 m/s are currently related to the limitations of galvanometric scanning heads rather than available laser sources.

CRediT authorship contribution statement

Caterina Angeloni: Investigation. Writing - Review & Editing Erica Liverani: Methodology. Writing - Original Draft. Alessandro Ascari: Investigation. Alessandro Fortunato: Conceptualization. Writing - Review & Editing.

Declaration of Competing Interest

The authors declare that they have no known competing financial interests or personal relationships that could have appeared to influence the work reported in this paper.

Data Availability

Data will be made available on request.

References

Babadjanov, F., Specht, U., Lukasczyk, T., Mayer, B., 2023. Heat accumulation-induced surface structures at high degrees of laser pulse overlap on Ti6Al4V surfaces by femtosecond laser texturing. Materials 16 (6), 2498. https://doi.org/10.3390/ma16062498.

Banat, D., Ganguly, S., Meco, S., Harrison, P., 2020. Application of high power pulsed nanosecond fibre lasers in processing ultra-thin aluminium foils. Opt. Lasers Eng. 129, 106075 https://doi.org/10.1016/j.optlaseng.2020.106075.

Baumann, R., Lasagni, A.F., Herwig, P., Wetzig, A., Leyens, C., Beyer, E., 2019. Efficient separation of battery materials using remote laser cutting–high output performance, contour flexibility, and cutting edge quality. J. Laser Appl. 31, 022210 https://doi.org/10.2351/1.5096127.

Berhe, M.G., Oh, H.G., Park, S., Lee, D., 2022. Laser cutting of silicon anode for lithium-ion batteries. J. Mater. Res. Technol. 16, 322–334. https://doi.org/10.1016/j.jmrt.2021.11.135.

Jansen, T., Kandula, M.W., Blass, D., Hartwig, S., Haselrieder, W., Dilger, K., 2019. Evaluation of the separation process for the production of electrode sheets (Advances in Battery Cell Production). Energy Technol. 8 (2). https://doi.org/10.1002/ente.201900519.

Kim, H., Nam, K., Kim, Y., Ki, H., 2022. Analysis of laser-beam absorptance and keyhole behavior during laser keyhole welding of aluminum alloy using a deep-learning-based monitoring system. J. Manuf. Process. 80, 75–86. https://doi.org/10.1016/j.jmapro.2022.05.044.

Lee, D., 2018. Investigation of physical phenomena and cutting efficiency for laser cutting on anode for Li-ion batteries. Appl. Sci. 8 (2), 266. https://doi.org/10.3390/app8020266.

Lee, D., Mazumder, J., 2018. Effects of momentum transfer on sizing of current collectors for lithium-ion batteries during laser cutting. Opt. Laser Technol. 99, 315–325. https://doi.org/10.1016/j.optlastec.2017.09.016.

Lee, D., Patwa, R., Herfurth, H., Mazumder, J., 2012. Computational and experimental studies of laser cutting of the current collectors for lithium-ion batteries. J. Power Sources 210, 327–338. https://doi.org/10.1016/j.jpowsour.2012.03.030.

Lee, D., Oh, B., Suk, J., 2019. The effect of compactness on laser cutting of cathode for lithium-ion batteries using continuous fiber laser. Appl. Sci. 9 (1), 205. https://doi.org/10.3390/app9010205.

Luetke, M., Franke, V., Techel, A., Himmer, T., Klotzbach, U., Wetzig, A., Beyer, E., 2011. A comparative study on cutting electrodes for batteries with lasers. Phys. Procedia 12, 286–291. https://doi.org/10.1016/j.phpro.2011.03.135.

Lutey, A.H.A., Fiorini, M., Fortunato, A., Ascari, A., 2014. Chemical and microstructural transformations in lithium iron phosphate battery electrodes following pulsed laser exposure. Appl. Surf. Sci. 322, 85–94. https://doi.org/10.1016/j.apsusc.2014.10.069.

Lutey, A.H.A., Fortunato, A., Ascari, A., Carmignato, S., Leone, C., 2015. Laser cutting of lithium iron phosphate battery electrodes: characterization of process efficiency and quality. Opt. Laser Technol. 65, 164–174. https://doi.org/10.1016/j.optlastec.2014.07.023.

Mei, L., Lin, L., Yan, D., Xie, S., Liu, Y., Li, S., 2023. Metal spattering in laser scanning welding of T2 copper and welding quality. Opt. Lasers Eng. 161, 107392 https://doi.org/10.1016/j.optlaseng.2022.107392.

Pfleging, W., 2018. A review of laser electrode processing for development and manufacturing of lithium-ion batteries. Nanophotonics 7, 549–573. https://doi.org/10.1515/nanoph-2017-0044.

Schmieder, B., 2017. Laser cutting of graphite anodes for automotive lithium-ion secondary batteries: investigations in the edge geometry and heat affected zone. Proceding of SPIE 2012;8244:82440R-1–82440R-7.

Schulz, W., Kostrykin, V., Nießen, M., Michel, J., Petring, D., Kreutz, E.W., Poprawe, R., 1999. Dynamics of ripple formation and melt flow in laser beam cutting. J. Phys. D: Appl. Phys. 32, 1219. https://doi.org/10.1088/0022-3727/32/11/307.

Wandera, C., Salminen, A., Kujanpaa, V., 2009. Inert gas cutting of thick-section stainless steel and medium-section aluminum using a high power fiber laser. J. Laser Appl. 21, 154–171. https://doi.org/10.2351/1.3184429.

Wu, B., Yang, Y., Liu, D., Niu, C., Gross, M., Seymour, L., Lee, H., Le, P.M.L., Vo, T.D., Deng, Z.D., Dufek, E.J., Whittingham, M.S., Liu, J., Xiao, J., 2019. Good practices for rechargeable lithium metal batteries. J. Electrochem. Soc. 166 https://doi.org/10.1149/2.0691916jes.

Zhang, Y., Li, J., Rukun, Yang, Tongwei, Liu, Yiguo, Yan, 2019. Analysis of kerf quality on ultrafast laser cutting of anode material for lithium-ion battery. Opt. Lasers Eng. 118, 14–21. https://doi.org/10.1016/j.optlaseng.2019.01.013.

Femtosecond Laser Cutting of Current Collectors: A Study for High-Quality Li-Ion Battery Fabrication in Electric Vehicles

Caterina Angeloni, Dongkyoung Lee, and Alessandro Fortunato

Abstract The average power of ultrashort laser sources has steadily increased, alongside significant investments by battery companies in advanced technologies, which necessitate solutions to improve ablation efficiency and quality in laser cutting of Li-Ion electrodes. Although burst mode processing has been primarily investigated in micro-processing, its application to cutting remains rarely explored. This paper introduces a simplified efficiency model that provides, with minimal computational cost, rapid insights into process dynamics of femtosecond laser cutting of 8 μm copper and 12 μm aluminum current collectors both in the single pulse and burst mode. The model results are then compared with actual cutting quality under constant conditions of 40 W average laser power and 200 fs pulse length. Results demonstrate that burst mode triples scanning speed, albeit with heat accumulation in aluminum, while MHz processing enables scalpel-like cuts in copper with a kerf half the spot size.

Keywords Laser cutting · Zero defects · Burst mode

1 Introduction

As the dawn of third-generation electric vehicles, the competition for high-energy–density batteries is becoming increasingly intense. Next-generation vehicles must achieve a mileage of 500 km minimum on a single charge, necessitating the development of high-performance lithium-ion batteries (LIBs) with exceptional capacity, rate capability, stability and long lifespan [1]. Thus, relevant research is being conducted through material and technological innovation to improve performance and quality

C. Angeloni (✉) · A. Fortunato
Department of Industrial Engineering (DIN), University of Bologna, Bologna, Italy
e-mail: caterina.angeloni2@unibo.it

D. Lee
Department of Mechanical and Automotive Engineering, Kongju National University, Cheonan, South Korea

L. Fratini et al. (eds.), *Selected Topics in Manufacturing*, Lecture Notes in Mechanical Engineering, https://doi.org/10.1007/978-3-031-99501-9_5

along with the manufacturing costs. In this respect, current collectors (CCs) made of aluminum (Al) and copper (Cu), are critical in LIB systems as they constitute ~15–50% of the weight, hence impacting significantly the price, weight, and energy density. CCs in automotive applications are thin, 6–30 μm thick foils which undergo various manufacturing processes, starting with trimming, followed by coating, and then notching to prepare them for the assembly and welding of battery connections. Laser beam is the state-of-the-art technology for cutting metal foils, in both trimming and notching, thanks to its ability to concentrate the high energy of the beam within a small spot, its rapid processing time, its wide range window of process parameters and its contact-free process [2]. Trimming (uncoated metal foil cutting) is performed in a "roll-to-roll" configuration with web speeds of up to 3 m/s, while laser spot velocities can reach 20 m/s for complex geometries. As a thermal process, laser cutting introduces thermal defects like spatter, dross, and heat-affected zone, which must be minimized for optimal battery performance [3].

Most studies in the literature have optimized laser cutting using a Pulsed Wave (PW) nanosecond lasers in IR or green wavelength. For example, PW nanosecond laser with a 532 nm wavelength has achieved good results in terms of kerf width and speed for 10 μm copper cutting with a direct interference pattern [4].

However, high-quality continuous laser beams (CW) recently available in the market, with spot dimension of 60 μm and gaussian beam shapes are increasing their applicability in industrial environment. Lee et al. [5] developed a numerical model for CW laser cutting of CCs at speeds up to 5 m/s, while Angeloni et al. [6] drew a thorough comparison of CW and PW nanosecond lasers for high-speed cutting ($\leq$28 m/s) of Al and Cu CCs demonstrating how these are affected by laser irradiance (the ratio of laser power to spot area) and fluence (the product of irradiance and contact time). The key finding was that, in all studied settings, CW single mode fiber lasers allowed for improved cut quality, except at $\leq$4 m/s for copper foils. Even with optimized process parameters, thermal defects occur because ablation is mainly due to melt ejection and evaporation rather than direct solid–vapor transition, as in ultra-short pulsed laser systems [7].

Ultrashort pulsed lasers (pulse length <10 ps) minimize thermal effects, achieving nearly dross-free cut edges by ending pulses before thermal diffusion occurs. The problem of ultrashort laser power limitation or efficient ablation evolved gradually over time: the average power doubles every three years, with pulse repetition rates (PRRs) reaching tens of megahertz [8]. Even at such high pulse repetition rates, the resulting fluence exceeds the optimal one. A practical solution to reduce pulse energy (and fluence) without sacrificing the average power is temporal pulse division, which creates *pulse bursts*. These bursts typically feature intra-burst repetition rates in the MHz-GHz range, significantly enhancing ablation efficiency and reducing surface roughness [9]. However, the use of such techniques for cutting Li-ion battery electrodes remains limited, being applied intensively in micromachining. The primary challenges for industrial implementation up to now include relatively low processing speeds, high investment costs and the delicate requirements of the equipment and environment (e.g., a controlled atmosphere). Pico-second lasers in burst mode have improved cutting speeds of Cu CCs up to 3.8 m/s and reduced heat-affected zones

HAZ [10]. Heidari Orujo et al. [11] optimized burst fluence in 10 ps laser cutting of CCs, achieving peak speeds of 4.7 m/s and 2.1 m/s for Al and Cu, respectively. It was not observed any improvement when varying the burst shape, namely equal pulse (EP) and increasing pulse (IP). Recent studies are exploring GHz-burst mode for electrode femtosecond cutting, with Audouard et al. [12] demonstrating increased speed and metal-dependent cutting times.

To the best of author knowledge, no studies have been published on femtosecond laser cutting of Li-ion current collectors only, likely due to the challenges previously mentioned. As industries are becoming more prone to invest in advanced technologies capable of achieving dross below 1 μm when cutting in a single pass at high cutting speeds, a critical question emerges: can quality be improved without compromising power and productivity?

This study investigates femtosecond laser cutting of CCs, analyzing speed and frequency effects on the final quality. Both MHz and GHz burst mode were tested with adjustable pulse numbers (N and P indexes) from 1 to 10. Results showed that higher pulse splitting increased maximum speed. Hence, with P and N fixed at 10, five frequency levels were studied (burst fluence 0.6~2.8 J/cm^2), identifying max speed for each. As a result, ablation efficiency and quality were assessed to strike a physical explanation of the results obtained in both the single mode and burst mode (Fig. 1).

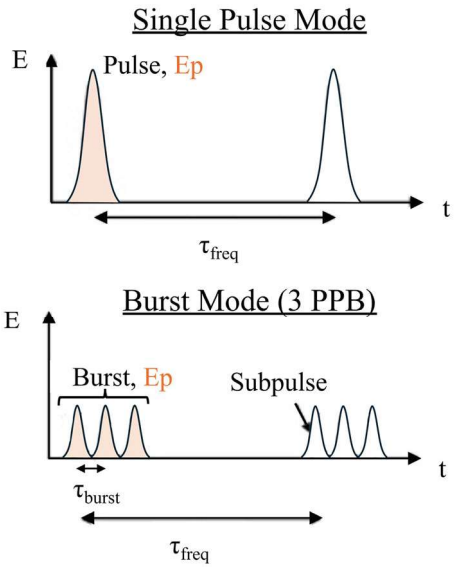

Fig. 1 Schematic representation of burst mode (PPB: pulses per burst)

2 Materials and Methods

2.1 *Materials, Laser Source and Cutting Setup*

A simple metal foil geometry and linear cutting path were considered to characterize and optimize the laser trimming process used for current collectors. Strips of copper Cu (CuAg $\geq$ 99.8%) and aluminum Al (1100 alloy, wt.% Al $\geq$ 99.0%, Fe $\leq$ 0.5%, Si $\leq$ 0.5%, Cu $\leq$ 0.2% other elements $\leq$ 0.05%) foil, 8 μm and 12 μm thick respectively, were cut from rolls and placed on a vacuum chuck shown in Fig. 2 to prevent bending and ensure the foil remained in the same focal plane during the single-pass cutting. Each strip was 20 mm × 60 mm in size, with parallel laser cuts performed over a length of 20 mm in each case. To avoid thermal interaction and local deviation of the material from the focal plane, the distance between subsequent cuts was 5 mm, while a maximum of 10 cuts were made on each strip. Since the Rayleigh distance is very small (0.69 mm), to ensure the consistency of our results, each process parameter combination was repeated three times.

Laser system employed for experiments was a solid-state laser (Carbride, Light Conversion) with a variable pulse duration in the range of 200 fs–10 ps and radiating at the light wavelength of $\lambda = 1030$ nm. It can produce a linearly polarized Gaussian beam with the diameter of 4.3 mm, pulse energies up to 400 μJ (40 W max) and repetition rates from a single pulse up to 1 MHz. During all experiments the pulse duration of 200 fs and an average power of 40 W were fixed. This laser source can work also in burst mode, as Fig. 1 explains. Two values of intra-burst repetition rate could be chosen: 66.7 MHz and 2.5 GHz for a respective τ_{burst} of 15 ns and 400 ps.

A galvanometer scanner (SG8220, Sino Galvo) and F-theta lens with a focal distance of 100 mm were used to scan and focus the laser beam into a spot of 30 μm. Figure 2 reports the specifications of the laser system. The experimental campaigns were conducted in a controlled environment: temperature was maintained between 15 °C and 30 °C, and relative humidity was kept below 80% (non-condensing).

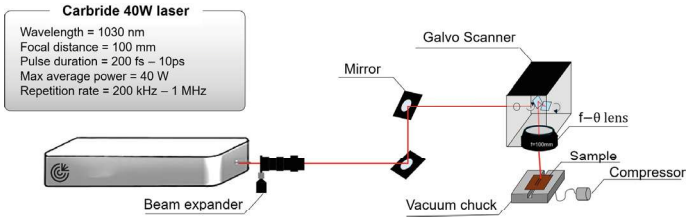

Fig. 2 Experimental set-up: ultrafast laser pulses guided via mirrors towards a galvanometer scanner and focus on the metal foil through the f-theta lens

Table 1 Process parameters for single pulse (SP) and burst mode (BM) campaigns

	Scanning speed (m/s)	Frequency (kHz)	P	N
SP	0.1–0.2–0.4–0.7–0.9	200–400–600–800–1000	1	1
BM	0.4–0.8–1.6	200–600–1000	1–10	1–10

2.2 Design of Experiments

For the Single Pulse *SP* experimental campaign, five levels of pulse fluences (5.7–28.3 J/cm^2) and five levels of speeds (0.1–0.9 m/s) were tested. The process parameters were chosen so that the no cut condition was found for both aluminum and copper. With the burst mode, thanks to the pulse splitting, the pulse fluences decreased up to 0.57 J/cm^2 ensuring the cutting condition. Maximum 40 W power and minimum 200 fs pulse length were kept constant to exploit at full potential the laser source. The burst mode *BM* campaign was conducted to evaluate the effect of intra-burst separation time, ranging from 400 ps (2.5 GHz) to 15 ns (66.7 MHz), on both quality and efficiency. Additionally, the number of pulses per burst was also varied from 1 to 10: P index for GHz mode and N for the MHz mode.

For each level of frequency, the maximum speed was found, both for BM and SP processing. Table 1 summarizes the combinations of process parameters investigated to assess fs laser cutting quality vs efficiency across SP and BM regimes. All tests were performed three times on both Aluminum and Copper.

2.3 Modeling of Ablation and Efficiency Analysis

Femtosecond laser ablation has been widely used in micromachining for its precision and minimal thermal defects by promoting direct sublimation. This results in cleaner cuts and reduced heat affected zones, making it ideal for defect-free processes such as the cutting of thin metallic foils. Hence, this study characterizes the relationship between laser pulse fluence, thermal defects, and kerf geometry to optimize ablation efficiency and resulted quality.

By adopting the approach in Ref [13] the laser beam at the entrance of the scanner is characterized by a two-dimensional Gaussian shape with a fluence distribution described by:

$$F(r) = F_{\max} e^{-\frac{2r^2}{w^2}} \left[\frac{J}{\text{cm}^2}\right] \tag{1}$$

$$F_{\max} = \frac{2E_p}{\pi w^2} \left[\frac{J}{\text{cm}^2}\right] \tag{2}$$

With $F_{\max}$ [J cm^2] being the laser peak fluence in the center, r is the radial distance from the beam center, w is the laser spot radius and $E_p[J]$ is the laser pulse energy, described as $E_p = P/f$.

In ultrashort pulse lasers not all the energy is efficiently used to remove the material, part remains in the latter as residual heat and part of the energy is emitted from the surface with the hot liquid/gaseous matter [14]. To ensure efficient material removal, laser has to work near its optimum fluence, which is a function of the material's fluence threshold. Threshold fluence F_{th} is the value of local fluence $F(r)$ after which material ablation occurs. For cutting applications, theoretical (TH) threshold fluence is determined experimentally by measuring the kerf width D, which corresponds to the spot size where the local fluence equals F_{th}. This is expressed as:

$$F_{th}^{TH} = F(D/2) = F_{\max} e^{-\frac{D^2}{2w^2}} \tag{3}$$

Energy losses after kerf formation and heat accumulation due to pulse overlapping has to be taken into account. This introduces two additional efficiency factors: thermal η_t and energy η_e efficiency. The real threshold fluence for cutting is given by:

$$F_{th}^{RE} = F_{th}^{TH} \eta_t \eta_e \tag{4}$$

The ratio between the real threshold value and its respective pulse fluence is called "cut efficiency" η_{cut} as reflects how effectively the laser energy is utilized to achieve material ablation under given process parameters.

Thermal efficiency η_t

High power and high repetition rates regimes in femtosecond laser processing lead to heat accumulation in the material, resulting in detrimental effects [15]. Thermal efficiency quantifies the extent of this thermal accumulation. The interaction between fs pulses and the metal foils is governed by two characteristic times: the pulse-to-pulse interval $\tau_{freq} = 1/f$ and the thermal relaxation time τ_{rel}. Hence, thermal efficiency is defined as:

$$\eta_t = 1 - e^{-\frac{\tau_{freq}}{\tau_{rel}}} \tag{5}$$

The thermal relaxation time quantifies the time required for heat to dissipate within the material over a specific distance, such as the laser spot radius w. Thermal relaxation time is given by:

$$\tau_{rel} = \frac{w^2}{4\alpha} \tag{6}$$

where α is the thermal diffusivity, defined as $\alpha = k/(\rho C_p)$, with k being the thermal conductivity, ρ the density and C_p the specific heat capacity. Material properties for

both Aluminum and Copper were taken from standard sources [16] and the calculated τ_{rel} are 0.577 µs and 0.489 µs, respectively.

When the time between two subsequent pulses τ_{freq} is shorter than τ_{rel}, thermal accumulation occurs, leading to localized residual heat. Typically, the residual heat generated during the ablation process by a single ultra-short laser pulse is comparably small and avoids detrimental effects on the cut edge. However, as the repetition rate increases, residual heat may not dissipate fast enough through heat conduction into the workpiece, leading to material damage around the cut edge. For the SP processing frequencies tested in this study, this condition occurs only for aluminum at the maximum frequency of 1 MHz. This corresponds to a minimum τ_{freq} of 1 µs, which is less than, yet very close to τ_{rel} for both Cu and Al. As a result, heat spreads rapidly from the region heated by the laser pulse, preventing melting in copper but not in aluminum due to its lower thermal conductivity. When BM is activated, different mechanisms of laser ablation come into play, requiring a more attentive selection of optimal laser conditions. The influence of the number of sub pulses and their time interval is described in the *Burst Mode* section.

Energy Efficiency η_e

This factor describes the fraction of energy effectively used for ablation and it is defined as:

$$\eta_e = \frac{E_{v,\min}}{E_v} \tag{7}$$

where $E_{v,\min}$ is the minimal volumetric energy density required to open the kerf. It is calculated for each level of frequency tested at its maximum speed. For higher overlapping, it is supposed that part of the beam energy doesn't contribute fully to vaporize the material, and it is therefore considered as "lost". Hence, the volumetric energy density for each combination of speed and frequency is modelled as:

$$E_v = \frac{E_p}{V}\left[\frac{\mu J}{\mu m^3}\right] \tag{8}$$

where E_p is the energy of a single laser pulse $[\mu J]$ and V is the removed material between subsequent pulses defined as:

$$V = \frac{tDv}{fN_b}\left[\mu m^3\right] \tag{9}$$

where t is the foil thickness (8 µm for copper and 12 µm for aluminum), D is the kerf width and N_b is the number of pulses within a burst.

Burst Mode

When burst mode is activated, the calculation of the ablated volume per pulse V and the total pulse energy E_v must account for the division of total pulse energy among N_b

sub-pulses within a single burst. Additionally, thermal accumulation within the burst has to be modelled. Since the time interval between consecutive sub-pulses is shorter than the material's thermal relaxation time, the energy from successive sub-pulses accumulates because the heat does not fully dissipate between them. Consequently, this thermal accumulation necessitates a reformulation of the energy distribution within a single burst, as described by:

$$F_{\max,burst} = \frac{F_{\max}}{N_b} \sum_{i=1}^{N} e^{-\left(\frac{(i-1)\tau_{burst}}{\tau_{rel}}\right)} \tag{10}$$

The first sub impulse (i = 1) contributes with its full energy, while the following ones (i > 1) overlap thermally, each with a contribution reduced by an exponential factor. In other words, sub pulses within a burst do not act independently: their energy accumulates based on residual heat from previous pulses.

When the sub-pulse separation $\tau_{burst} \ll \tau_{rel}$, the exponential decay term in the fluence summation becomes negligible and heat does not dissipate significantly, leading to a near-complete energy accumulation. In this case, the peak burst fluence $F_{\max,burst}$ closely matches the single-pulse peak fluence and remains nearly unaffected by τ_{burst}. Conversely, when $\tau_{burst} \leq \tau_{rel}$, heat dissipates efficiently between sub-pulses, reducing thermal accumulation and lowering $F_{\max,burst}$. The latter is then utilized in Eq. (3) for the subsequent determination of F_{th}^{RE}.

2.4 Sample Characterization

Digital microscopy (DM, Leica DVM6) was used to provide preliminary assessment of cut quality and to identify defects for each combination of process parameters in terms of uncompleted cuts, dross, melted edges, spatter, and presence of a HAZ (see Fig. 3). Furthermore, the kerf width was determined for all tests with the mean value calculated based on the three data points collected along the entire cut.

SEM-FEG microscopy (Tescan Mira3 with a Schottky emitter) was then used to examine the representative cuts on both the front surface (the area directly subject to laser irradiation) and the underside of each foil. Each cut was observed via SEM at the start, middle, and end of the laser path.

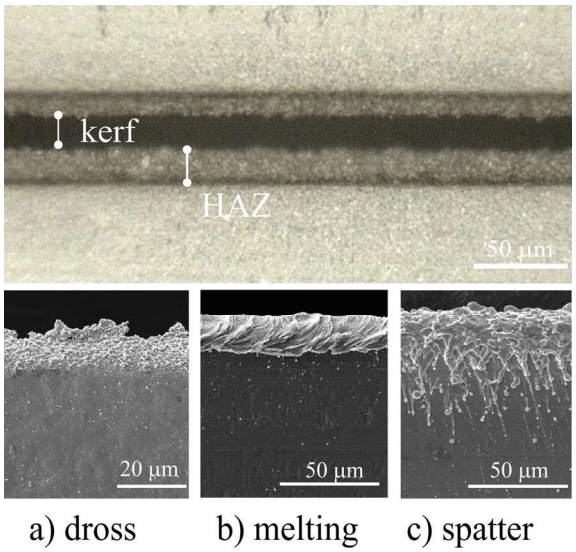

Fig. 3 Defects classification and definition of kerf and HAZ width

3 Results and Discussions

3.1 Ablation Efficiency

The influence of scanning speed v and laser pulse repetition rate *PRR* on cutting efficiency, defined as the maximum portion of energy utilized for ablation (as described in Sect. 2.3), was investigated.

Experimental results show a linear decrease in kerf width with increasing speed ($R^2 = 98\%$) and PRR ($R^2 = 80\%$). At higher speeds, maximum energy efficiency is achieved because a big portion of incident energy contributes to material removal, with minimal heat accumulation from pulse overlap. Moreover, the standard deviation of mean efficiency at each speed level decreases fivefold at lower speeds, indicating that the cutting process becomes less sensitive to frequency variations, as shown in Fig. 4.

Aluminum and copper registered a maximum efficiency of 0.79 and 0.86, respectively, at 400 kHz. As frequency increases, part of the incident energy in aluminum is retained within the material, reducing overall efficiency. Another effect of heat accumulation is the decrease in the SP threshold fluence F_{th}^{RE} at higher frequencies, leading to increased cutting speeds. For aluminum, the SP maximum cutting speed jumps from 0.6 m/s for 200 kHz $\left(F_{th}^{RE} = 14.9 J/\text{cm}^2\right)$ up to 0.8 m/s for 1000 kHz $\left(F_{th}^{RE} = 3.5 J/\text{cm}^2\right)$. This effect is less pronounced in copper, which, due to its higher thermal conductivity, is less affected by heat accumulation and the maximum cutting speed is set constant to 0.9 m/s. On average, efficiency values in copper are 24% higher than in aluminum.

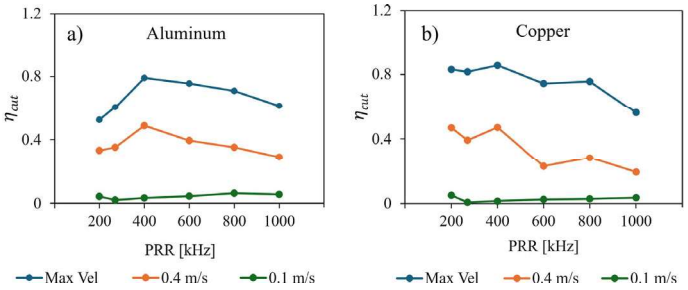

Fig. 4 Single pulse cut efficiencies for **a** aluminum and **b** copper

The concept of a progressive decrease in the ablation threshold with increasing frequency, leading to higher material absorptivity due to residual heat from previous pulses, becomes more prominent in the burst mode. Micromachining literature has long-established that dividing a pulse's energy into a series of sub-pulses (in MHz and GHz range) minimize thermal damage and mechanical stress, enabling higher processing speeds. Huang et al. [10] demonstrated that maximum speeds could be achieved with the highest degree of pulse splitting. Hence, the maximum speeds for each frequency level were identified for both materials in the MHz and GHz modes when N = 10 and P = 10. The ablation thresholds F_{th}^{RE} attained for both Al and Cu were lower for all burst regimes in comparison to the single-pulse processing.

In MHz mode, aluminum reaches 3 m/s at 600 kHz—almost four times the SP speed—while in GHz mode, it peaks at 2.3 m/s at 1000 kHz. When comparing MHz and GHz efficiencies in the BM campaign, MHz mode outperforms GHz mode efficiencies for PRR < 600 kHz across all three speed levels. However, at 1000 kHz and 1.6 m/s MHz mode reaches a no-cut condition, whereas GHz mode fails to cut at 200 kHz at the same speed. This trend highlights the interdependence of the two "duty cycles": shorter intra-pulse intervals for the GHz mode require higher pulse overlap to sustain the full cut compared to MHz mode. Despite this, both efficiencies were lower than those in the SP regime, suggesting greater residual heat accumulation, which increases with intra-burst frequency for this set of process parameters.

For copper, scanning speed climbed up to 3.4 m/s in MHz mode at 200 kHz. Interestingly, the speed increase from SP to BM in MHz mode is consistent at 3.8 times for both materials: from 0.8 to 3 m/s for Al and from 0.9 to 3.4 m/s for Cu. As shown in Fig. 5, unlike other trends, while aluminum MHz max speeds decrease beyond 600 kHz, copper follows this trend across all frequencies. Theoretically, the opposite would be expected, as higher repetition rates would produce a significant rise of temperature and then induce a lower threshold and a higher absorption of the target material [17, 18], facilitating kerf opening. At the same time, an antagonist phenomenon comes into play. Many authors [19, 20] have pointed out both plasma and particle shielding after 200 fs-laser ablation of Al and Cu for high frequencies (1 MHz). Plasma shielding is related to primary material ejection after the laser pulse,

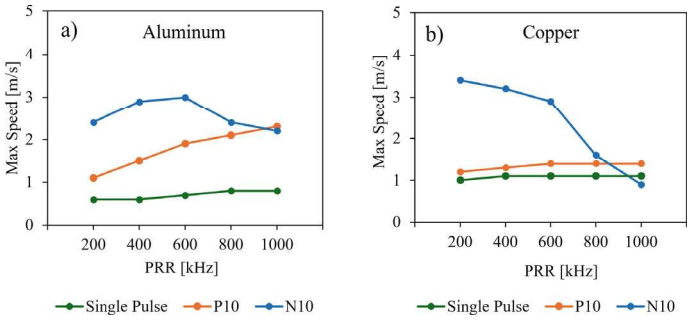

Fig. 5 Maximum scanning speed for each frequency level of **a** aluminum and **b** copper

creating a particle cloud which causes beam defocusing and prevents further heat transfer to the target material, thereby limiting the achievable cutting speeds.

3.2 Ablation Quality

In the previous section, it was observed that higher cutting speeds led to greater energy efficiency. However, cuts performed near the maximum speed in the SP mode were found to exhibit burs along the cut edge for pulse overlaps lower than 87%. In this case, heat accumulation at high PRRs positively affects quality, leading to a more consistent kerf. However, exceeding heat accumulation may cause melting along the cut edge, as shown in Fig. 6b.

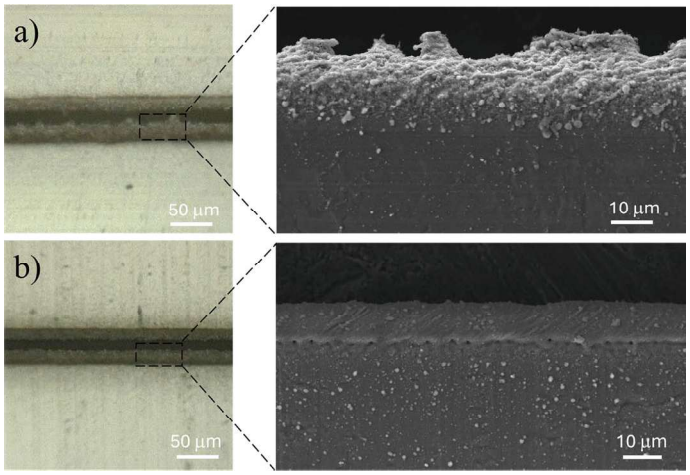

Fig. 6 Aluminum single pulse cuts at maximum speed 800 mm/s carried out at **a** 200 kHz and **b** 1000 kHz

Additionally, SP aluminum processing was accompanied by the occurrence of phase explosion, which caused micrometer liquid particles and gas mixtures to splash out. Per our observation, the greater the pulse overlap and the material removal, the higher the number of particles expelled and then redeposited near the cut edge.

When burst mode is activated, thermal effects exacerbate. Every test performed in the burst mode on aluminum involved *liquid* formation along the cut edge. Even after a fs pulse, a significative quantity of absorbed energy remains within the material, generating heat accumulation if the interval between pulses is too short for a complete heat dissipation in the bulk material. Since sub-pulses occur at intervals (τ_{burst}) shorter than the material relaxation time (τ_{rel}), part of the energy from subsequent sub-pulses accumulates heat. Vaghasiya et al. [21] demonstrated with simulations that the electron temperature increases with rising bursts pulse numbers. If heat accumulation leads to a temperature increase which exceeds the melting point T_m in the non-ablated material next to the interaction zone, the surface remains liquid between two subsequent pulses. Each new pulse then hits a still liquid surface which leads to a completely different, and in particular no longer "cold" process, which will be dominated by hydrodynamic effects and the benefit of ultrafast laser ablation is lost [15]**.** This concept is illustrated in Fig. 7a. This physical explanation is supported by two facts: first, aluminum is more prone to this phenomenon due to its lower thermal conductivity and melting point; second, increasing the number of pulses P only broadens the molten zone rather than increasing the kerf width for high PRR (explicit in Fig. 7b).

At low frequencies on aluminum, a distinct pattern is observed in both GHz and MHz modes (Fig. 7c). For even pulse numbers, the kerf width increases (reducing efficiency), but this trend is lost when increasing the PRRs or changing material. This phenomenon can be attributed to several factors related to particle plume dynamics and thermal accumulation. Žemaitis et al. [9] reported lower removal efficiencies for the second pulse due to particle shielding, indicating different plume and thermal effects when the process changes (drilling to cutting). As a result, little material is ablated by the third pulse. In copper, this even–odd dependence is absent.

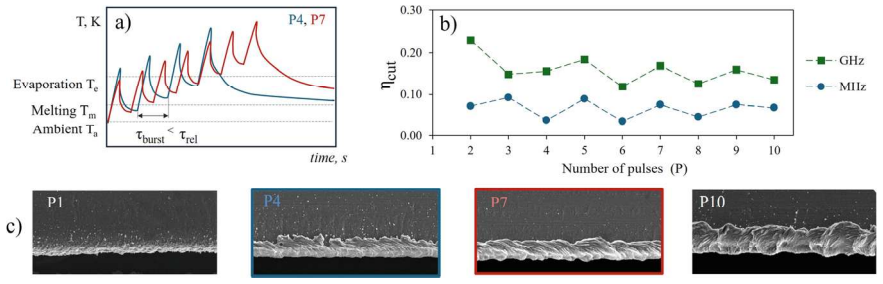

Fig. 7 Number of pulses within a burst influencing melting formation. Possible explanation in: **a** Temperature trend indicating heat accumulation. **b** Cut efficiency for aluminum in GHz and MHz modes when 200 kHz and 0.8 m/s are applied with related SEM images in (**c**)

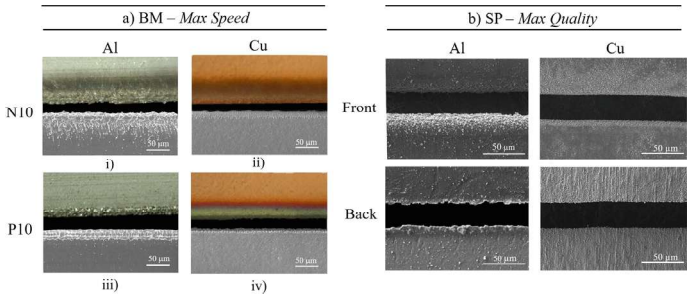

Fig. 8 **a** BM defects formation when max velocities are used for aluminum and copper causing spattering in the MHz mode for lower overlapping and F_{max} values of (i) 60%, 2.8 Jcm^2, (ii) 73%, 1.4 Jcm^2 and dross formation for aluminum at (iii) 82%, 2.8 Jcm^2 and copper along with HAZ at (iv) 97%, 0.57 Jcm^2. **b** High quality aluminum and copper SP cuts performed at 9.4 J/cm^2, O% = 95.6% and 5.7 J/cm^2, O% = 99.8%, respectively

When MHz high speeds are coupled with low PRRs (Overlapping $\leq$76%), hydrodynamic instabilities in molten aluminum cause fingers-like droplets detachment, as shown in Fig. 8a(i). Each image displays an OM view (top) and the corresponding SEM picture (bottom). In GHz cutting, fingers-like spatters are absent, and particle deposition near the molten edge is minimized across all process conditions.

In SP processing of copper, burs form at 200 kHz with high speeds, similar to aluminum but at a higher overlap threshold of 93%. While the front edge maintains good quality across different sets of parameters, the backside's quality improves while decreasing speed, with a perfect cut achieved at 0.1 m/s, as shown in Fig. 8b. Hence, the best balance of energy efficiency and quality is at 0.4 m/s.

Below 400 kHz in SP cuts, the HAZ appears along the cut edges, enlarging as PRRs decrease and is present for all GHz cuts (see Fig. 8a(iv)). Tests confirmed that Argon shielding gas prevents HAZ, confirming it results from heated foil-environment reaction.

4 Conclusions

Aluminum and Copper current collectors for secondary battery manufacturing were ablated using a femtosecond laser at PRRs = 200 kHz – 1 MHz both in the single-pulse and burst mode (MHz and GHz inter pulse frequency). A dual analysis of cut efficiency and quality was conducted, leading to the development of a simplified model that quantifies the fraction of laser energy effectively used for ablation and the portion retained in the material.

The analysis has led to the following findings:

- For aluminum in SP mode, efficiency peaked at intermediate frequencies (400–600 kHz), balancing cutting speed and defect minimization.

- Copper exhibited high-quality front edges in all conditions, though low speeds were required for a consistent kerf across the entire thickness.
- The burst mode allowed for a significant speed increase, though at the cost of increased thermal effects, particularly in aluminum. Specifically, in MHz mode, speeds up to 3.4 m/s were achieved for copper and 3 m/s for aluminum, while GHz mode showed reduced spattering but introduced a heat-affected zone.

While the proposed efficiency model is intentionally simplified, it enables efficient rapid extraction of key insights into SP experimental quality with minimal computational cost. This approach captures the main trends related to intra-burst pulse separation and repetition rate, offering a practical tool for analyzing process conditions and cut edge quality without requiring complex simulations.

References

1. Jeong H, Jang J, Jo C (2022) A review on current collector coating methods for next-generation batteries. Chem Eng J 446:136860. https://doi.org/10.1016/j.cej.2022.136860
2. Pfleging W (2018) A review of laser electrode processing for development and manufacturing of lithium-ion batteries. Nanophotonics 7:549–573. https://doi.org/10.1515/nanoph-2017-0044
3. Yuan Y, Wang H, Han X et al (2024) The local lithium plating caused by anode crack defect in Li-ion battery. Appl Energy 361:122968. https://doi.org/10.1016/j.apenergy.2024.122968
4. Baumann R, Alamri S, Aguilar-Morales AI et al (2022) Advanced remote laser cutting of battery foils using an interference approach. Mater Lett X 14:100138. https://doi.org/10.1016/j.mlblux.2022.100138
5. Lee D, Patwa R, Herfurth H, Mazumder J (2012) Computational and experimental studies of laser cutting of the current collectors for lithium-ion batteries. J Power Sources 210:327–338. https://doi.org/10.1016/j.jpowsour.2012.03.030
6. Angeloni C, Liverani E, Ascari A, Fortunato A (2024) Characterization and process optimization of remote laser cutting of current collectors for battery electrode production. J Mater Process Technol 324:118266. https://doi.org/10.1016/j.jmatprotec.2023.118266
7. Chichkov BN, Momma C, Nolte S et al (1996) Femtosecond, picosecond and nanosecond laser ablation of solids. Appl Phys A 63:109–115. https://doi.org/10.1007/BF01567637
8. Weber R, Graf T (2021) The challenges of productive materials processing with ultrafast lasers. Adv Opt Technol 10:239–245. https://doi.org/10.1515/aot-2021-0038
9. Žemaitis A, Gudauskytė U, Steponavičiūtė S et al (2025) The ultrafast burst laser ablation of metals: Speed and quality come together. Opt Laser Technol 180:111458. https://doi.org/10.1016/j.optlastec.2024.111458
10. Huang J, Shi W, Huang J et al (2021) High speed pulsed laser cutting of anode material for a Li-ion battery in burst mode. Opt Mater Express 11:2300. https://doi.org/10.1364/OME.425816
11. Heidari Orojloo P, Demir AG (2024) Study of burst mode for enhancing the ps-laser cutting performance of lithium-ion battery electrodes. J Laser Appl 36:042013. https://doi.org/10.2351/7.0001417
12. Audouarda E, Pallarèsb D, Romanob J-M, et al. Characterization of batteries materials ablation by femtosecond pulses
13. Žemaitis A, Gaidys M, Brikas M et al (2018) Advanced laser scanning for highly-efficient ablation and ultrafast surface structuring: experiment and model. Sci Rep 8:17376. https://doi.org/10.1038/s41598-018-35604-z
14. Breitling D, Ruf A, Dausinger F (2004) Fundamental aspects in machining of metals with short and ultrashort laser pulses. In: Herman PR, Fieret J, Pique A, et al (eds). San Jose, Ca, p 49

15. Weber R, Graf T, Berger P et al (2014) Heat accumulation during pulsed laser materials processing. Opt Express 22:11312. https://doi.org/10.1364/OE.22.011312
16. Incropera FP, DeWitt DP, Bergman TL, Lavine AS (2007) Fundamentals of heat and mass transfer, 6th edn. Wiley, Hoboken, NJ
17. Joerg S (2012) Characterisation of interaction phenomena in high repetition rate femtosecond laser ablation of metals. https://doi.org/10.13140/2.1.2575.5841
18. Schille J, Schneider L, Loeschner U, et al (2011) Micro processing of metals using a high repetition rate femtosecond laser: from laser process parameter study to machining examples. In: International congress on applications of lasers & electro-optics. Laser Institute of America, Orlando, Florida, USA, pp 773–782
19. König J, Nolte S, Tünnermann A (2005) Plasma evolution during metal ablation with ultrashort laser pulses. Opt Express 13:10597. https://doi.org/10.1364/OPEX.13.010597
20. Ancona A, Döring S, Jauregui C et al (2009) Femtosecond and picosecond laser drilling of metals at high repetition rates and average powers. Opt Lett 34:3304. https://doi.org/10.1364/OL.34.003304
21. Vaghasiya H, Krause S, Miclea P-T (2023) Fundamental study of a femtosecond laser ablation mechanism in gold and the impact of the GHz repetition rate and number of pulses on ablation volume. Opt Mater Express 13:982. https://doi.org/10.1364/OME.474452

Proceedings of the ASME 2024 19th International Manufacturing Science and Engineering Conference
MSEC2024
June 17-21, 2024, Knoxville, Tennessee

MSEC2024-123689

REMOTE LASER CUTTING OF METAL FOILS FOR BATTERY ELECTRODES FABRICATION: MODELLING OF THE PROCESS AND EXPERIMENTAL VALIDATION

Erica Liverani
Department of Industrial Engineering, University of Bologna, Bologna, Italy

Alessandro Ascari
Department of Industrial Engineering, University of Bologna, Bologna, Italy

Caterina Angeloni
Department of Industrial Engineering, University of Bologna, Bologna, Italy

Michele Francioso
Department of Industrial Engineering, University of Bologna, Bologna, Italy

Lorenzo Cestone
Department of Industrial Engineering, University of Bologna, Bologna, Italy

Zha Dexiang
Department of Industrial Engineering, University of Bologna, Bologna, Italy

Alessandro Fortunato
Department of Industrial Engineering, University of Bologna, Bologna, Italy

ABSTRACT

A significant socioeconomic shift is arising from the world's and Europe's direction towards a radical change in transportation with an increasing demand for electric vehicles. In this context, the definition and the optimization of the processes involved in battery production and assembly are currently under development, and the electrode production steps are key topics. Cutting and trimming of electrodes are two of these relevant processes and the cut quality of the cutting edges is considered the main quality criterion for the success of the process. This high quality is continuously in pursuit of new productivity demands and flexibility requests from Gigafactories, so new technological solutions must be introduced. According to this perspective, laser-based manufacturing is currently the best viable option, making these processes the new standard for producing electric vehicles. Competitiveness, higher productivity, and sustainable production will result from establishing the link between the laser system and cut quality. Following the previous considerations, this paper presents an experimental investigation and a process modeling of remote ablation trimming performed with a single-fiber laser. CUT/NO-CUT threshold was defined for copper and aluminum current collectors, respectively 6 µm and 12 µm in thickness, as well as the process conditions that return spatter, dross and burns. These defects were correlated to specific areas of the CUT process windows with proper differentiation between Al and Cu foils.

The presented thermal-based model identifies cutting condition and dross formation and a good accuracy in kerf width prediction was confirmed, which is crucial for reducing resource consumption. The final results allow for the identification of an appropriate process parameter window for both materials.

Keywords: Laser cutting, Battery fabrication, Copper current collectors, Aluminum current collectors

• INTRODUCTION

Current state-of-the-art identifies laser material processing (LMP) as the heart of EVs manufacturing. In EVs, LMP technologies are used for battery fabrication in electrodes cutting/welding and can-to-cap welding, processing internal tabs, sealing individual cells and modules, and fabricating structural enclosures.

Focusing on the topic of laser processing for electrode production, currently most lithium-ion batteries have a similar design, which consists of an electrolyte that contains lithium salt in an organic solvent, a separator, a metal oxide positive electrode (cathode) coated on an aluminum current collector, and a carbon/graphite negative electrode (anode) coated on a copper current collector. Cutting or trimming the current collectors in both coated and uncoated regions yield the final electrode geometry. Aluminum and copper current collectors can be cut both mechanically, using knife slitting or die cutting, or thermally using a laser beam. Defects like dross adhesion, melting, the formation of a heat-affected zone, and spattering can be avoided with mechanical cutting, but dies need to be sharpened frequently to avoid burrs, material attachment, and edge bending, which reduces productivity and interrupts continuous production. As an alternative, laser cutting is a non-contact thermal cutting method that combines high production

rates (measured in meters of foil cut per second), high levels of flexibility (determined by the range of patterns that can be cut), and high levels of cut quality (measured in terms of minimizing imperfections resulting from laser-material interactions) [1]. Advances in laser sources and new generation scanning optics have the potential to offer enhanced utilization of materials, improved process efficiency (competitive process speed) and product quality, allowing high quality and high production rate, aiming at satisfying the high demand of the EVs coming from the market. However, the complete exploitation of new laser sources and optics devices need to be fully understood and verified in real industrial laser manufacturing processes involved the battery fabrication. There are several papers in the literature that have dealt with laser cutting of electrodes with the main focus on the final quality of the cut. Several authors evaluated cut characteristics in terms of kerf and melted width [2,3], however most of them refer to coated anode/cathode cutting using pulsed lasers [4-7], while for continuous laser there is a lack of knowledge and few papers have been published [8]. Other authors have dealt with the topic by focusing on the analysis of the heat-affected zone [9].

Because current collectors are used to obtain an electrical connection with the battery cup after trimming and rolling of electrodes, detrimental defects are primarily associated with the edge profile. Two types of detrimental problems can cause internal short circuits in Li metal batteries [10]: 1) Physical contact between the cathode and anode due to material defects, manufacturing issues (like burrs, particles, and dust), and battery abuse conditions; 2) Contact resulting from chemical and/or electrochemical reactions. In literature, these two factors are linked to spatter formation [11]. For this reason, the main industrial requirement is to eliminate or reduce spatter as much as possible, as well as control dross formation.

Following the market demand, electrodes move on conveyors of automatic lines at 1-3 m/s which leads to scanning speed, between laser and substrate, up to 20 m/s. These ultra-fast cutting speeds can be reached using high-brightness laser sources, delivered via single-mode fiber, coupled to highly dynamic scanning optics with f-theta focusing lenses. Working area depends on the focal length but it is limited to 180 x 180 mm to guarantee small laser spot and a remote ablation cutting.

Nevertheless, scanning speed higher than 10 m/s are really demanding for current scanning (usually reachable only working in positioning speed) and correct laser intensity have to be selected in order to minimize defects. Therefore, there is a lack of scientific reports addressing performances and specific defects in ultra-fast (>10 m/s) of un-coated Cu and Al thin foils cutting with continuous (CW) lasers. In particular, when processing high reflectivity metals such as aluminium and copper, high quality process window is very narrow: high power combined with low velocity leads to drops and burns, high power with higher velocity do not present drops but maintain burns until optimum speed, while low power combined with high velocity leads to un-cutting conditions. Following the previous considerations, a process modelling of remote ablation cutting was developed with the following aims:

i) prediction of cutting/no cutting process parameters.
ii) Prediction of process parameters with high quality cut.
iii) Prediction of kerf dimensions.

Estimating the kerf width, the minimum material consumption can also be determined, favouring the minimum waste of raw materials and the process sustainability. The proposed model is developed in COMSOL Multyphisics ® and the laser beam dimension and intensity were simulated using the actual spot geometry and power distribution measured by means of Ophir-Spiricon BeamWatch and characterizing the actual optical path. The absorption coefficient of both Cu and Al was numerically evaluated by experiments comparison. Validation of the model is also presented together with the high accuracy in predicting a reliable optimal process window (highest cutting speed with the fewest defects) in case of Cu and Al electrode ultra-fast remote laser cutting.

2. MATERIALS, PROCESS SETUP AND MODELLING

2.1 Laser system and optics

The hardware equipment exploited herein is based on a nLight CW 1200 W single-mode laser source equipped with a feeding fiber core of 14 μm. The galvo scanner is a Scanlab IntelliScan 20 with a F-Theta lens characterized by a 340 mm effective focal length. The actual spot measured by means of Ophir's BeamWatch is 65 μm.

2.2 Materials and samples

Strips of high purity copper (CuAg ≥ 99.8 %) and aluminium (1100 alloy, wt% Al ≥ 99.0%, Fe ≤ 0.5%, Si ≤ 0.5%, Cu ≤ 0.2% other elements ≤ 0.05%) foils measuring 150x200 mm^2 and respectively 6 and 12 μm thick, have been obtained from rolls and gripped into a clamping system. Parallel laser cuts of 100 mm in length were performed with the material precisely positioned in the focal plane. The distance between subsequent cuts was 15 mm in order to avoid thermal interactions. A preliminary experimental campaign was carried out for the evaluation of the real absorption coefficients (Ca) for Al and Cu foils. In this preliminary campaign, laser speed was varied from 1 m/s to 20m/s. Following the evaluation of the absorption coefficients, a more extensive experimental campaign was performed with the aim of determining defects, cutting-edge quality and kerf dimensions and verifying the accuracy of the process modelling proposed. Table 1 summarizes the cuts performed. The number on the bracket represents the power step: i.e. 50-300 (25) means that cutting tests were performed in the range between 50 W and 300 W with a power step of 20 W.

Laser power was therefore varied from 50 to 1200 W (Irradiance from 1.5 to 36 MW/cm^2), which, combined with speed from 1 to 20 m/s, returned Energy densities from 4.9 to 2350 J/cm^2.

TABLE 1: CUTTING SPEED AND LASER POWER USED FOR EXPERIMENTAL EVALUATION AND MODEL VALIDATION.

Speed [m/s]	Cu laser power [W]	Al laser power [W]
1, 2, 3, 4	50-300 (25) 300-1200 (50)	50-300 (25) 300-1200 (50)
6, 8	200-450 (25) 450-1200 (50)	200-450 (25) 450-1200 (50)
10, 12	350-550 (25) 550-1200 (50)	350-550 (25) 550-1200 (50)
16, 20	500-600 (50)	500-600 (50)

2.3 Characterization

The metal foils were separated from the clamping device after the cut, and the full cut occurring and its quality were evaluated using an optical microscope (OM, Nikon Optiphot-100). The first and last parts of the cut were excluded from the analysis because they were obtained with the laser during the acceleration and deceleration phases. The nominal speed achievement for correctly excluding the aforementioned parts was identified using the laser source in the pulsed regime with defined frequency and path length.
Finally, a Scanning Electrone Microscope SEM-FEG (Tescan Mira3 with a Schottky emitter) was used to analyse representative cuts and defects.

2.4 Process modelling

The proposed process simulation is a thermal model and comprises the evaluation of the temperature distribution due to the laser interaction without any implicit phase change. This simplification is possible due to the ablative nature of the cutting and the high speeds that reduce the heat input effects far from the cutting edge. Calculation of the time-dependent temperature field is performed, based on the measured intensity of the incident laser beam (section 2.1) and copper and aluminium state-of-the-art properties [12,13]. The energy amount delivered and absorbed during the cutting was determined using the laser-materials Ca. According to the literature, copper and aluminium absorptivity were initially set to 0.05 (absorptivity for solid conditions) and were then increased in accordance with experimental evidence by tuned real and predicted cuts with the aim of determining a Ca coefficient of ablation cutting for Cu and Al. A simulation domain of 2.5x1x0.06 mm3 respectively in x, y and z directions was considered, and discretised by using tetrahedral mesh elements. The simulation domain was defined, with a preliminary simulation campaign, as the minimum domain where the workspace dimension did not influence the temperature calculation. Considering the foil thickness used, a maximum element size of 3 µm was set in the entire domain and a mesh refinement was carried out along with the cutting line and in a mid-plane probe (Figure 1).

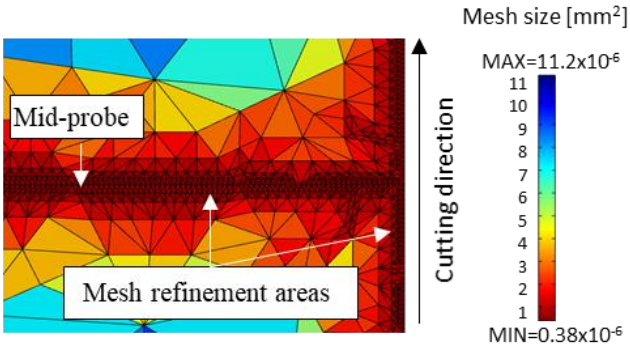

FIGURE 1: DOMAIN DISCRETISATION FOR HIGH RESOLUTION AND HIGH ACCURACY SIMULATION. MESH DIMENSION MAPS ARE REPORTED FOR HIGHLIGHT THE REFINEMENT

The simulation is carried out considering a Gaussian energy source moving on the foil surface, with the thermal field calculated by means of numerical resolution of the Fourier equation. The first interesting result of the model is the prediction of the two temperatures vs. time reported in Figure 2. Those temperatures represent the temperature evolution, calculated during the laser-material interaction, on the surface (black continuous line) and at the bottom (red dotted line) of the foil, and both points are along the laser axis (z axis in Figure 2) where, due to the gaussian intensity distribution, the temperature is the highest.

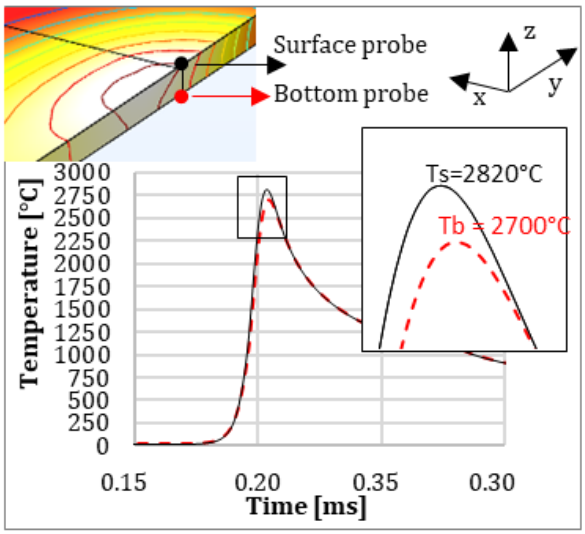

FIGURE 2: SURFACE AND BOTTOM TEMPERATURE EVOLUTION IN THE CASE OF 275 W AND 6 m/s LASER PROCESS PARAMETERS FOR PURE Cu FOIL.

Based on the temperature prediction, the cut happens if the maximum peak temperature of both curves exceeds the boiling temperature of the foil material. The peak temperatures of the curves refer to the maximum temperature calculated when the laser directly impacts the probe.

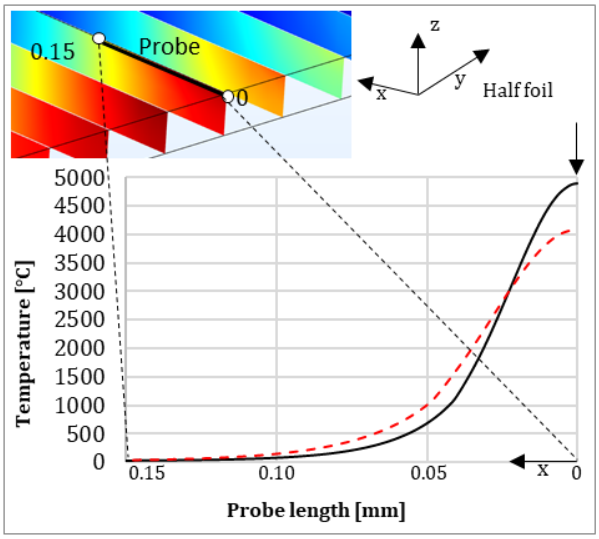

FIGURE 3: TRANSVERSAL TEMPERATURE DISTRIBUTION IN THE CASE OF 800 W AND 10 m/s LASER PROCESS PARAMETERS FOR PURE Cu FOIL.

Once the laser has passed the probe, the heat propagates inside the foil in x direction and the temperature increases. The kerf was therefore defined as the width (in the x direction) of the portion of volume that exceeded the boiling temperature along the entire thickness of the foil In Figure 3 the thermal field evolution after t0.01=0.01 ms is reported (red dotted line) and compared with the maximum temperature (black continuous line) calculated when the probe is directly irradiated from the laser (t0). From this comparison it is underlined that it is necessary to evaluate the kerf with a time-dependent model. In fact, exceeding the vaporization temperature occurs both through direct interaction with the laser and through heat dissipation after the passage of the laser, albeit with a reduced relevance of this second phenomenon on the total kerf.

The model validation has been carried out according to the following steps, for all the process parameters investigated in the experiments:

- Prediction and comparison of cut/no cut accuracy.
- Accuracy in the prediction of ~~the~~ defects.
- Accuracy of the kerf dimensions.

3. EXPERIMENTAL RESULTS

3.1 CUT/NO-CUT threshold evaluation

CUT/NO-CUT conditions were defined for every combination power-velocity-material reported in Table 1 and the threshold between these two conditions was used in the model for Ca evaluation via parametric simulations (see Section 4). The threshold line is defined by one point for each considered laser speed, and it indicates the first power at which cutting is permitted. The threshold can be shown as a linear trend line with an R-squared close to 1, as shown in Figure 4 (black dotted line). Two areas are defined experimentally by this line: the CUT and NO-CUT process areas. All low- and high-quality cuts are included in the CUT area, whereas incomplete cuts are included in the NO-CUT area. Despite the higher thickness, aluminium foils require less power to be cut with respect to copper foils at the same speed.

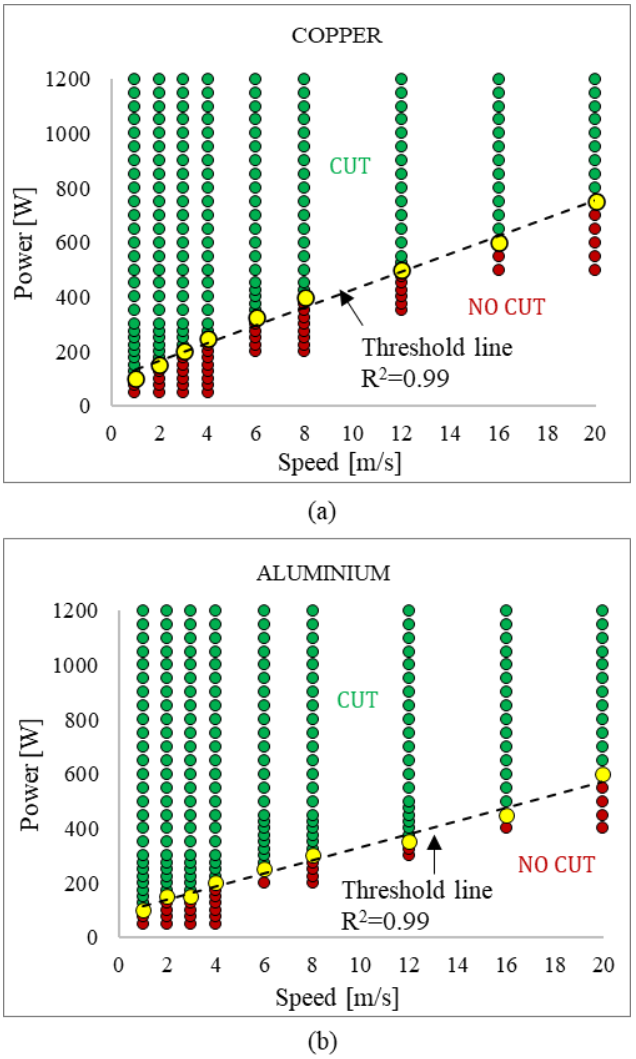

FIGURE 4: PARAMETER WINDOW FOR ULTRA-FAST REMOTE CUTTING OF COPPER (A) AND ALLUMINIUM (B) FOILS.

Table 2 summarizes the results obtained in terms of experimental data for threshold line calculation.

TABLE 2: ABLATIVE CUTTING EXPERIMENTAL RESULTS FOR CUT (Y)/NO CUT (N) THRESHOLD EVALUATION.

	COPPER		ALLUMINUM	
v [m/s]	P [W]	Cut	P [W]	Cut
1	70	N	70	N
1	100	Y	100	Y
2	125	N	125	N
2	150	Y	150	Y
3	175	N	125	N
3	200	Y	150	Y
4	225	N	175	N
4	250	Y	200	Y
6	300	N	225	N
6	325	Y	250	Y
8	375	N	275	N
8	400	Y	300	Y
12	475	N	300	N
12	500	Y	350	Y
16	550	N	400	N
16	600	Y	450	Y
20	700	N	550	N
20	750	Y	600	Y

3.2 Cut quality experimental analysis

Following the results presented in Section 3.1, the subsequent experimental tests were carried out to identify, within the operative cutting window, the onset of poor-quality cuts and to measure kerf dimension.

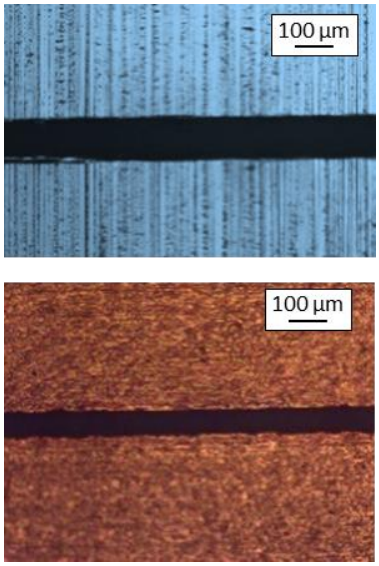

FIGURE 5: HIGH QUALITY CUTTING CONDITION FOR ALUMINUM (A) AND COPPER (B) FOILS.

The term "poor quality cut" refers to a cut where the metal foils' edges exhibit burns, spatter and/or dross simultaneously. Because the battery cup is connected electrically through current collectors, defects in the cut's edge could be detrimental, making the electrode useless owing to the likelihood of short circuits and an increase in electrical resistance Therefore, it is crucial to identify in which area of the operative windows, described in Figure 4, these defects occur and improve the model for the prediction of these conditions. Figure 5 displays two micrographs of aluminium cut at 400 W and 10 m/s and copper cut at 500 W and 10 m/s as reference examples of high-quality cutting.

Following these first results the subsequent experimental tests were carried out to identify, within the operative cutting window, the onset of poor-quality cuts and to measure kerf dimension.

Figures 6b, 6d and 6e refer to cutting defects on copper foils, while Figures 6a and 6c. Arrows are used to indicate burns, dross and spatter, which represent the two unacceptable defects for electrodes in battery fabrication.

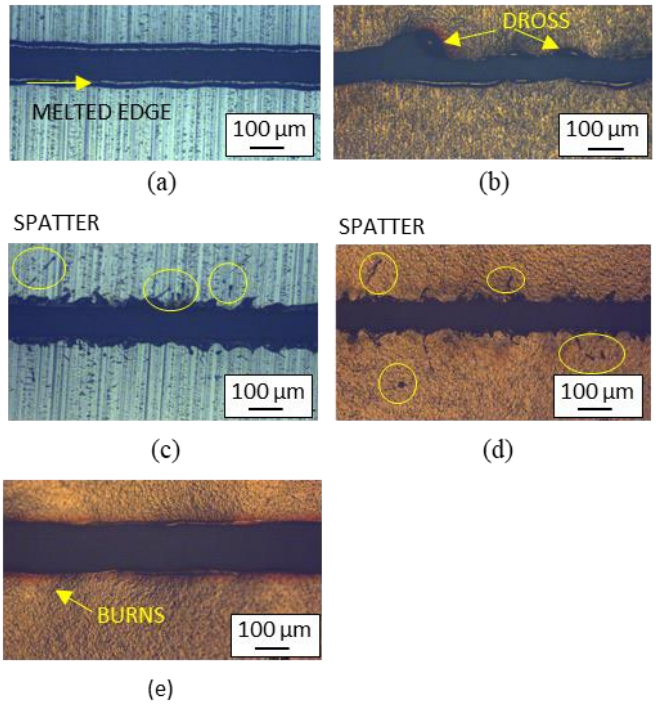

FIGURE 6: DEFECTS IN THIN FOIL CUTS.

Undesired melted edge and dross formation happen when cutting is performed with too low speeds and irradiance. In the range of parameters investigated in this study, big dross was revealed only for cuts performed on copper at speeds less than 4 m/s (Figure 6b), while relevant melted edge occurred on alluminium samples up to combination of irradiance and energy density respectively equal to 10 MW/cm2 and 120 J/cm2 (Figure 6a). At the opposite, spatter occurs at high speed for both materials with a threshold value of 12 m/s for alluminium (Figure 6c) and 20 m/s for copper (Figure 6d). Finally, slight burns are

visible in copper foils (Figure 6e) if irradiance and energy density are both higher respectively then 25 MW/cm2 (>830 W) and 120 J/cm2, but the very small width interested by overheating make this condition negligible for continuous laser cutting.

Representative samples of each cut type described above were chosen for SEM analysis (Figure 7), excluding cuts with burns, which can only be seen under an optical microscope.

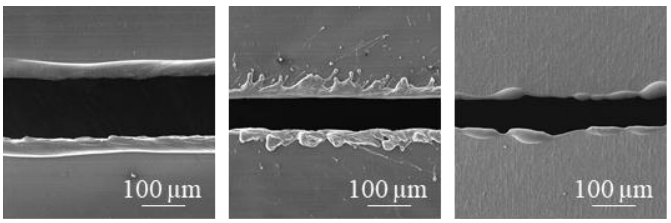

FIGURE 7: SEM IMAGES OF CW LASER CUTS PERFORMED ON ALUMINUM FOIL WITH 1000 W, 4 m/s (a), 1000 W, 20 m/s (b) AND ON COPPER FOIL WITH 175 W AND 1 m/s (c).

In conclusion, moderate to high speed and moderate-to-low irradiance levels produced good cut quality. Due to high power (and high irradiance), a significant amount of liquid phase formed, which can cause two major problems: spatter and a big kerf. Specifically, when the interaction time was short (high speed) the turbulence of the molten material encouraged spatter formation. Conversely, at lower speeds, melting becomes more relevant than vaporization, promoting dross and bumps. Higher speeds nevertheless provide the finest cutting conditions for a given power up until the spatter starts.

3.3 Kerf measurements

The kerf width of relevant cuts was measured, and the data obtained as mean value of several measurements along the cut are shown in Table 3. At 2 m/s no kerf value was defined for copper foils due to excessive dross formation. The highest values were identified for high-power and low-speed process parameters, as expected.

TABLE 3: KERF MEASUREMENTS

		Cu		Al
v [m/s]	P [W]	Kerf [µm]	P [W]	Kerf [µm]
2	/		200	55
2			1200	147
4	250	78	300	86
4	1000	125	1000	170
6	300	58	500	108
6	1200	144	1200	173
8	400	58	500	108
8	800	63	800	118
12	500	44	500	102
12	1200	93	1200	130
20	800	38	800	70
20	1200	55	1200	78

4. MODEL VALIDATION AND DISCUSSION

4.1 Evaluation of the coefficient of absorptivity of ablative cutting

For all experimental cutting conditions, a thermal simulation was conducted to determine the minimum Ca value necessary to surpass the boiling temperature (2570°C for copper and 2467°C for aluminum) at both the surface and bottom of the foil. The minimum Ca variation considered is 0.005.
Tables 3 and 4 present the calculated temperatures on the surface (Ts) and bottom (Tb) of copper and aluminum foils, respectively. Based on these results, average Ca values of 0.19 for copper and 0.31 for aluminum foil were established for interaction with the infrared single-mode laser.

TABLE 4: TEMPERATURE PREDICTION WITH THE ABSORPTIVITY COEFFICIENTS Ca FOR COPPER

COPPER				
v [m/s]	P[W]	T_s[°C]	T_b[°C]	Ca
2	150	2570	2470	0.19
2	175	3050	2950	
4	250	2500	2400	0.19
4	275	2820	2700	
8	400	2480	2350	0.19
8	450	2980	2840	
16	550	2580	2390	0.19
16	600	2975	2820	
20	700	2630	2500	0.19
20	750	2750	2590	

TABLE 4: TEMPERATURE PREDICTION WITH THE ABSORPTIVITY COEFFICIENTS Ca FOR ALUMINIUM

ALLUMINUM				
v [m/s]	P[W]	T_s[°C]	T_b[°C]	Ca
2	125	1720	1630	0.32
2	150	2550	2475	
4	225	2640	2480	0.31
4	250	2985	2810	
8	375	2615	2415	0.31
8	400	2820	2600	
16	550	2600	2360	0.315
16	600	2755	2500	
20	650	2610	2325	0.31
20	750	2850	2540	

Using these Ca, simulations of all the cuttings listed in Table 1 were performed to identify good-cut quality regions and poor-cut quality regions by comparison to the experimental results.

Finally, kerfs obtained with the simulation were compared to the real kerf for model validation.

4.2 CUT/NO-CUT region and defects prediction

The CUT/NO-CUT regions were determined by calculating the temperatures across the foils for all cutting instances listed in Table 1. Cutting was assumed to occur when the boiling temperature was reached at the bottom of the foils.

A maximum error of 12 % was obtained for aluminium foil cut at 2 m/s.

Regarding the capacity in predicting defects (dross and burns at low speed), the accuracy of the model is presented showing the temperatures calculated in two conditions: i) a good quality cut obtained at 2 m/s and 250 W and ii) a cut with dross and burns obtained at 2 m/s and 350 W (see Figure 8). For good quality cuts (Figure 8a), the boiling temperature has the first intersection with the maximum temperature along x direction (instant t_0). This situation physically corresponds to the complete vaporization of the target material directly irradiated from the laser with minimum/null heat conduction into the foils. Conversely, in the process condition where the defects occur (Figure 8b), the first temperature distribution curve intersected from the boiling temperature is a lower isothermal (after 0.01 ms from the direct illumination of laser in the case in Figure 8b) which means that a certain heat was conducted into the foils and defects were observed on the foils.

Considering this simulation result, it follows that the necessary condition for a good quality cut is that the maximum temperature isotherm intersects the straight line relating to the boiling temperature inside the theoretical cutting kerf. If this situation is not verified, the amount of energy supplied by the laser beam would be transmitted, by conduction, inside the foil causing dross or dross and burns simultaneously.

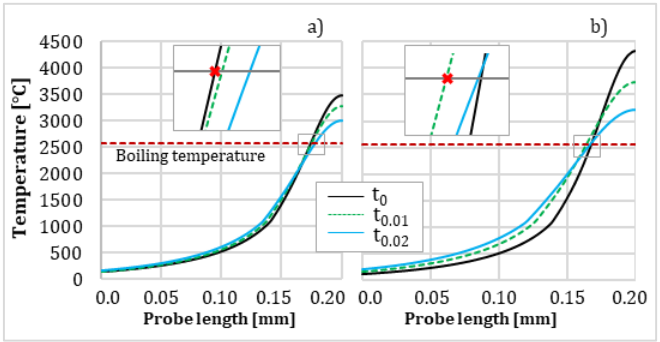

FIGURE 8: TEMPERATURE DISTRIBUTION AND INTERSECTION WITH BOILING TEMPERATURE FOR HIGH QUALITY CUT (A) AND CUT WITH DROSS AND BURNS (B).

4.3 Kerf prediction

The accuracy of the model in predicting kerf dimension, under different process parameters, was presented by comparing theoretical and experimental upper and lower kerf dimension as in Figure 9. Following the previous results, it can be concluded that the accuracy in the prediction of kerf dimension is very good because of an average error lower than 10% in the comparisons. Similar results were obtained with aluminum. Finally, it is worth noting the importance in predicting kerf dimensions, in good cut quality area, due to its impact on resource consumption. As an example, if we consider 24h activities, for an automated line for battery production, with a cutting speed of 20 m/s, a reduction of 10 mm of the kerf width leads to about 3.4 kilograms of copper saved per year.

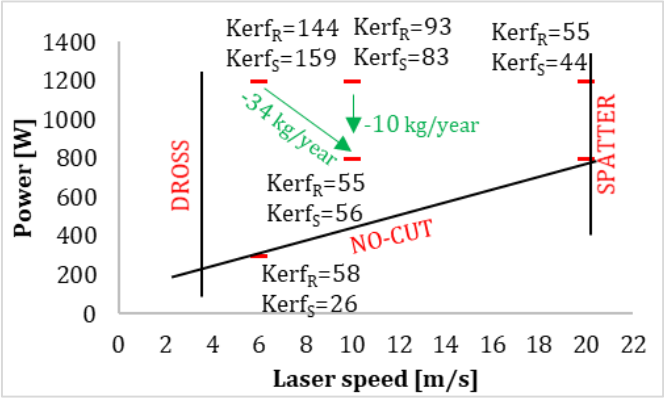

FIGURE 9: KERF EXPERIMENTAL MEASUREMENTS ($KERF_R$) AND MODEL PREDICTION ($KERF_S$) IN CASE OF Cu FOILS.

5. CONCLUSIONS

In this paper a simplified model for the prediction of the optimal process parameters, in case of ultra-high-speed cutting of aluminum and copper foils for the manufacture of automotive batteries, is presented. The main results obtained are summarize in the following points:

- The absorptivity coefficients for Al and Cu that best fit the experiments, in case of ablation cutting with high-quality near IR laser, are 0.31 for Al and 0.19 for Cu.
- When processing thin foils with high laser reflectivity and high thermal conductivity such as Al and Cu the optimal process parameters window must be determined avoiding thermal defects such as dross (observed in Cu for low velocity) and burns (observed for both Cu and Al for high power and high velocity).
- Bottleneck for cutting at speed higher than 20 m/s are due to scanners.
- Two main defects were identified in ultra-high speed of foils: dross and spatter respectively in case of low speed (< 3m/s for copper) and high speed (12 m/s for aluminum and 20 m/s for copper)
- The proposed model predicts, with high accuracy and with low computational time, the process parameters which give good quality cut (no burns and drops).
- The model predicts with a maximum error of about 10% the kerf dimensions in both cases allowing to select process parameters which give good quality cut with minimum waste of raw materials.

REFERENCES

[1] Banat, D., Ganguly, S., Meco, S., Harrison, P., 2020. Application of high power pulsed nanosecond fibre lasers in processing ultra-thin aluminium foils. Optics and Lasers in Engineering. 129. 106075, 10.1016/j.optlaseng.2020.106075

[2] Lee, D., Oh., B., Suk, J., 2019. The Effect of Compactness on Laser Cutting of Cathode for Lithium-Ion Batteries Using Continuous Fiber Laser. Applied Sciences. 9(1), 205. https://doi.org/10.3390/app9010205

[3] Berhe, M.G., Oh, H.G., Park, S., Lee, D., 2022. Laser cutting of silicon anode for lithium-ion batteries. Journal of Materials Research and Technology. 16, 322-334. 10.1016/j.jmrt.2021.11.135.

[4] Lutey, A.H.A., Fortunato, A., Ascari, A., Carmignato, S., Leone, C., 2015, Laser cutting of lithium iron phosphate battery electrodes: Characterization of process efficiency and quality, Optics and Laser Technology, 65:164-174.

[5] Zhang, Y., Li, J., Yang, R., Liu, R., Yan, Y., Analysis of kerf quality on ultrafast laser cutting of anode material for lithium-ion battery, 2019, Optics and Laser in Engineering, 118: 14-21.

[6] Bauman, R., Alamri, S., Aguilar-Morales, A.I., Lasagni, A.F., Kunze, T., Advanced remote laser cutting of battery foils using an interference approach, 2022, Materials Letters, X14: 1001138

[7] Luetke, M., Franke, V., Techel, A., Himmer, T., Klotzbach, U., Wetzing, A., Beyer, E., A Comparative Study on Cutting Electrodes for Batteries with Lasers, 2011, Physics Procedia, 12: 286-291

[8] Baumann, R., Lasagni, A.F., Herwig, P., Wetzig, A., Leyens, C., Beyer, E., 2019. Efficient separation of battery materials using remote laser cutting–high output performance, contour flexibility, and cutting edge quality. Journal of Laser Applications, 31, 022210. https://doi.org/10.2351/1.5096127

[9] Schmieder, B., 2017. Laser cutting of graphite anodes for automotive lithium-ion secondary batteries: investigations in the edge geometry and heat affected zone. Proceding of SPIE 2012;8244:82440R-1–82440R-7

[10] Wu, B., Yang, Y., Liu, D., Niu, C., Gross, M., Seymour, L., Lee, H., Le, P.M.L., Vo, T.D., Deng, Z.D., Dufek, E.J., Whittingham, M.S., Liu, J., Xiao, J., 2019. Good Practices for Rechargeable Lithium Metal Batteries. J. Electrochem. Soc. 166. 10.1149/2.0691916jes

[11] Jansen, T., Kandula M.W., Blass, D., Hartwig, S., Haselrieder, W., Dilger, K., 2019. Evaluation of the Separation Process for the Production of Electrode Sheets. Energy Technology. 8(2): Advances in Battery Cell Production. 10.1002/ente.201900519

[12] Baba, Y., Inoue, T., Sugioka, K., Kobatake, H., Fukuyama, H., Kubo, M., Tsukada, T. Thermal conductivity measurement of molten copper using an electromagnetic levitator superimposed with a static magnetic field, 2012, Measurement Science and Technology, 23: 045103.

[13] Ho, C.Y., Powell, R.W., Liley, P.E. Thermal Conductivity of the Elements: A Comprehensive Review the American Chemical Society and the American Institute of Physics for the National Bureau of Standards, 1974, West Lafayette, Indiana

Erica Liverani is an Assistant Professor at the University of Bologna. He obtained his PhD at the same university in 2017 with a thesis on optimization of the Additive Manufacturing Process (Laser Powder Bed Fusion Process) for biomedical applications. Erica's current topics include laser materials processing with a particular focus on laser cutting and laser welding, laser manufacturing through Additive Manufacturing (AM) and modeling of laser-matter interactions. She is author of 58 publications on international journal and conference proceeding with a number of citation greater than 1400.

108
ADVANCED MATERIALS TECHNOLOGIES
www.advmattechnol.de

Numerical and Experimental Study of High-Speed Laser Cutting of Copper Current Collectors: Process Optimization for Quality Assessment

Caterina Angeloni, Samuele Piandoro, Erica Liverani, and Alessandro Fortunato*

Ensuring high-edge quality in battery current collectors is crucial for improving battery performance and preventing potential safety issues. Defects such as uneven cuts, spatter, and excessive remelted zones can negatively impact the current collectors' electrical conductivity and mechanical integrity. Laser cutting offers advantages over mechanical methods by enabling faster processing, higher precision, and greater energy concentration. This study models and predicts defect occurrence under varying process parameters, focusing on the interaction between a single-mode continuous-wave (CW) laser and a copper current collector foil. Key factors influencing edge profile defects and cutting quality are investigated through experimental analysis and numerical simulation. A Computational Fluid Dynamics (CFD) model based on the volume of fluid method identifies parameters affecting the physical phenomena and optimal cutting conditions. Model validation is achieved by comparing experimental results across a range of process parameters associated with distinct defect formation modes. This model enables the prediction of defect types across a wide spectrum of laser speeds (2–25 m s^{-1}), power levels (200–1000 W), and foil thicknesses (8–16 µm). Findings serve as a guideline for selecting process parameters when using current collectors of varying materials and thicknesses.

1. Introduction

The production and assembly of lithium-ion batteries are constantly evolving to meet increasing requirements for productivity and quality. The sizing of electrodes with good edge and surface quality is one of these manufacturing challenges. This process involves trimming the current collectors and notching the electrodes for subsequent assembly and welding of the battery connections. Current collectors are thin, conductive metal foils (typically copper and aluminum) that facilitate the transfer of electrical current within the battery, while electrodes are the coated layers that store and release energy during charge and discharge cycles.[1]

Laser beam cutting is a state-of-the-art technology for cutting metal foils in both the aforementioned processes. Its ability to concentrate the high energy of the beam within a small spot, combined with fast processing times and a contact-free approach, makes it more viable compared to traditional mechanical methods.[2,3] Mechanical cutting techniques, such as die cutting and rotary knife slitting, require precise and relatively expensive tooling that wears over time. This leads to poor cut edge quality, downtime for tool repair and change, and unstable process due to tool wear. As a result, mechanical cutting methods often have longer production times and higher costs compared to laser cutting. In contrast, laser cutting, being a contactless process, eliminates tool wear and associated downtime, thereby improving overall efficiency.[3] However, as a thermal process, laser cutting of thin current collectors is inherently associated with thermal defects on the edge profile, such as spatter deposition, dross, and heat-affected zones that can negatively affect battery performance. The first industrial request is to eliminate, or strongly reduce, spatter and control dross formation. Dross formation is undesirable from a technical point of view because particles may detach from the main body and mix with the electrode slurry. If a metal particle, accidentally deposited on the electrode, has a diameter bigger than the separator (>12 µm) it may pierce it and during the winding process the battery will be discarded.[4] Even particles smaller than the separator are problematic, as they create a preferential pathway for metallic deposition on the anode. When they come into contact with lithium ions during a charging cycle, uneven deposits can form, leading to dendrite growth. During the various charge/discharge cycles of the battery, these dendrites grow until they pierce the separator, causing a short circuit that can lead to premature battery failure or even an explosion.[5,6]

The nature of these defects depends on the laser-material interaction and, consequently, on the selected laser source continuous-wave (CW) or pulsed-wave (PW), the material used,

C. Angeloni, S. Piandoro, E. Liverani, A. Fortunato
Department of Industrial Engineering (DIN), viale Risorgimento 2
Alma Mater Studiorum - University of Bologna
Bologna 40136, Italy
E-mail: caterina.angeloni2@unibo.it

The ORCID identification number(s) for the author(s) of this article can be found under https://doi.org/10.1002/admt.202401905

DOI: 10.1002/admt.202401905

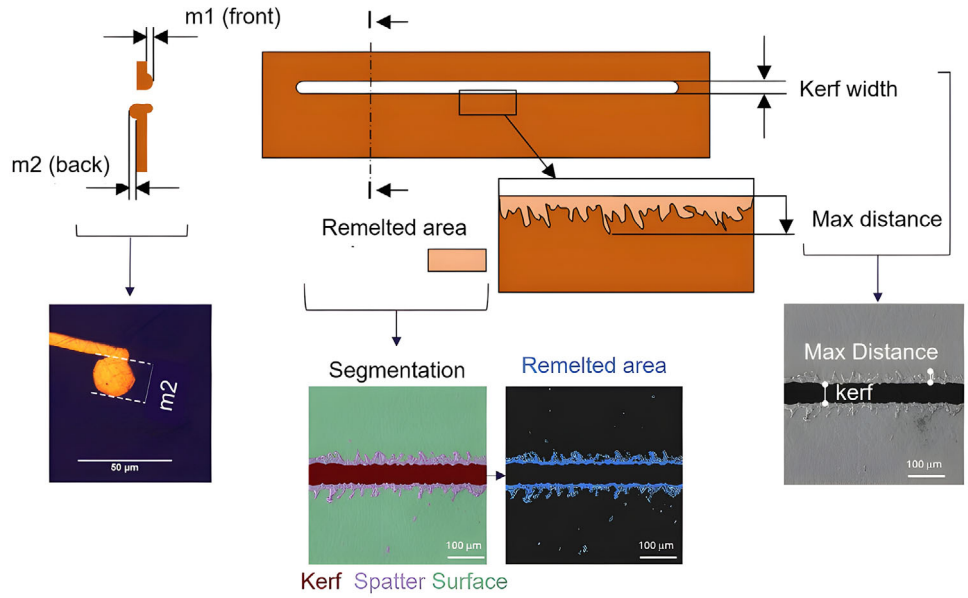

Figure 1. Defects analysis and measured parameters: m_1 and m_2 for dross thickness, kerf width, remelted area, and maximum distance for spatter identification.

in terms of metal purity, foil thickness, and the specific trimming path. Unlike laser cutting of thicker sheets, where defect formation results from a complex balance of forces, in thin foils the process is primarily driven by recoil pressure from near-instant material vaporization. This recoil pressure can cause molten material to either adhere to the cut edge, forming rough dross or burr,[7] or gain sufficient momentum to break free from the weld pool as spatter.[8] The escape threshold for droplet ejection depends on local values of surface tension, geometry, viscosity, and gravity and is described by the Weber number (We).[9] In cases where We $\ll$2, droplet formation occurs, while We $\gg$2 leads to a free-stream flow, where the molten material separates from the surface as a continuous jet rather than forming discrete droplets.[7,10] This behavior explains why changes in thickness, material composition, and process parameters can lead to different spatter patterns. Yule and Dunkley[11] further describe how laminar flows in liquid films break into droplets when Reynolds numbers are below 1000.

To minimize thermal effects and improve cutting quality many studies have been conducted using PW ultrashort laser beams. Hartmann et al.[12] employed a PW picosecond laser to fabricate high-quality hole arrays on 15 µm thick aluminum foil, achieving precise cuts with minimal thermal influence. Similarly, Zhu et al.[13] investigated the drilling of sub-10 µm holes in various metals with thicknesses ranging from 1.5 to 50 µm using a PW femtosecond laser. The study aimed to analyze the effects of laser parameters and material properties and ultimately proposed a simple model to predict the ablation rate for a range of metals. However, such ultra-short, PW lasers are not widely used in industry because of their limitations such as low productivity, high-cost investment, and difficulties in the system handling. Therefore, research has increasingly focused on commercial PW nanosecond and CW lasers to address these limitations in metal foil cutting. In a previous study conducted by Angeloni et al.,[14] the authors drew a comparison of cutting quality using CW and PW sources. A correlation has been established between cut quality, process parameters, and laser source used, and the main outcome was that CW single-mode fiber lasers enable higher cut quality.

Numerous models[7,15–18] have been developed to describe melt flow dynamics and kerf evolution during CW laser cutting, primarily focusing on thick sheets. These studies provide insights into how processing parameters influence melt behavior and the resulting cut quality. For example, Yilbas and Aleem[17] proposed a model to predict the size of ejected melt droplets based on melt flow dynamics and laser parameters during CO_2 laser cutting with assistance gas. While such models have been valuable for understanding laser cutting of high-thickness materials, they fall short when addressing the unique challenges of thin foil processing, particularly for current collectors and electrodes. In this context, Lee et al.[19] is, to the authors' knowledge, the only existing application of a numerical model for laser cutting of current collectors and electrodes. In their work (extended in Ref. [20]) they applied a 3D-Self consistent mathematical model developed by Ki et al.[21] using the set level method to study the penetration time, depth, and thresholds of pure copper and aluminum foils, with thicknesses of 10 and 15 µm respectively. They also correlated spatter and dross appearance to the formation of a crest of molten material, which, when expelled from the keyhole, either solidifies as dross or becomes spatter. Therefore, such unwanted defects can be prevented by controlling the magnitude of the melt pool flow through laser parameters. Their study, however, was limited to relatively low speed and power, reaching a maximum of 5 m s^{-1} and 300 W.

In this research, we developed a Computational Fluid Dynamics (CFD) framework for laser-material interaction simulations using the well-known volume of fluid method. In this context, the present paper aims to develop a model for the prediction of physical phenomena and defects occurring during laser cutting of copper current collectors. The model was tuned and

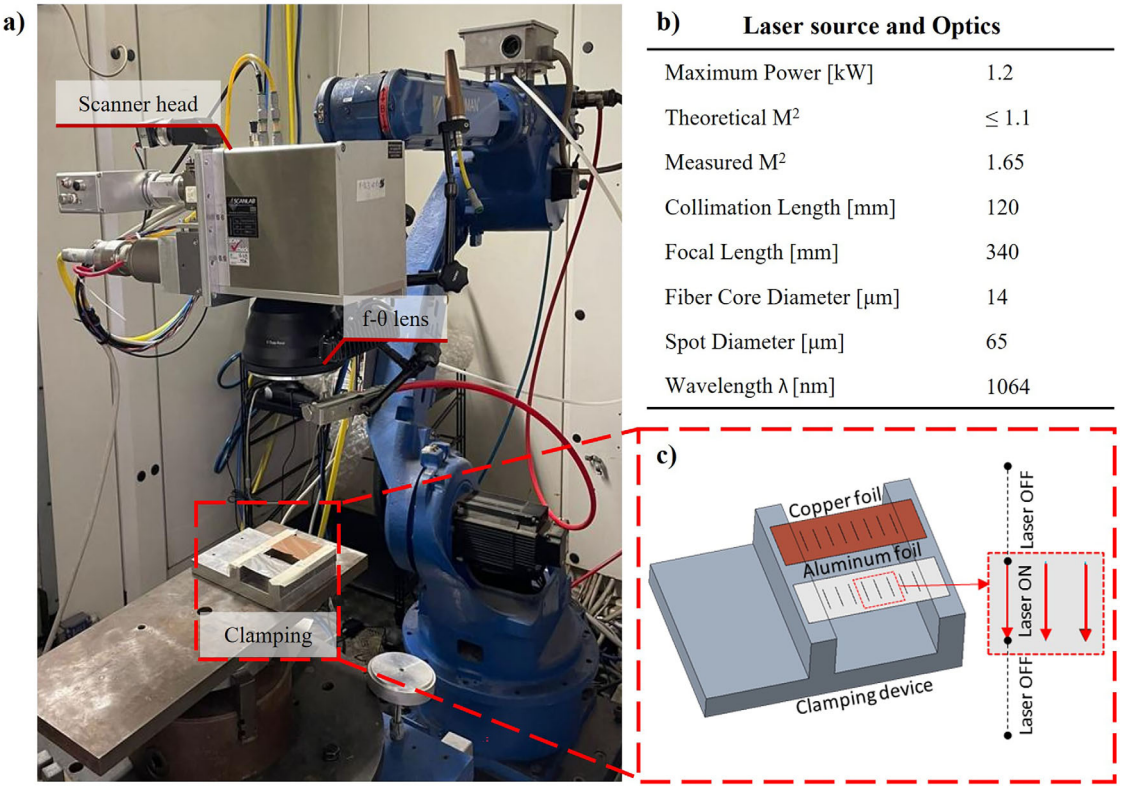

Figure 2. Laser Source and Optics Set-up.

validated against multiple experimental results using different process parameters, demonstrating its ability to predict defect formation under various laser-material interactions. It was then used to analyze and compare the outcomes of laser cutting on copper current collectors of different thicknesses using a wide range of process parameters. As a result, a power-speed graph shows the optimal cut area identified for medium-to-high speeds and a laser-material physical explanation has been proposed to explain the different cut qualities, both for the 8 and 16 µm foils.

2. Experimental Procedure

2.1. Material, Laser Source, and Cutting Set-Up

A simple metal foil geometry and linear cutting path were considered to characterize and optimize the laser trimming process used for current collectors (see **Figure 1**).

Current collectors of pure copper 8 µm thick were cut from rolls and kept in a clamping system to maintain the foils stretched out in the focal plane. Linear and parallel laser cuts 20 mm in length were performed considering a distance between adjacent cuts of 5 mm. The laser system is shown in **Figure 2a**, where a CW nLight 1200 W single-mode laser source (nLight, Washington, US) was employed. The laser system was equipped with a 14 µm optical fiber and a scanning head (Scanlab IntelliScan 20) equipped with a 340 mm f-theta lens for beam movement. The theoretical spot size was calculated as $d_{spot} = d_{fc} \cdot \frac{F_f}{F_c}$, where d_{fc} is the diameter of the beam when it exits the fiber (14 µm), and F_f and F_c are the collimation and focal lengths, respectively. To compare the theoretical spot size of 40 µm with the real one, a beam profiler (BeamWatch, Ophir, Germany) was used in accordance with the standard measurement method established in ISO 11146, and it was found to be 65 µm. Using the same equipment, the BPP was measured as 0.56 [mm·rad] from which the real beam quality factor was calculated as $M^2 = \frac{BPP \cdot \pi}{\lambda}$ accounting for 1.65. The parameter M^2 represents the degree of variation of the beam from an ideal Gaussian profile ($M^2 = 1$).

To avoid heat accumulation within the current collectors, the laser cutting process was designed to account for galvo-mirror acceleration and deceleration, excluding these from the analysis (see Figure 2c). The laser beam was only turned on in the central part of the path, while the extension over which the laser beam was turned off was determined with a preliminary experimental campaign. As noted previously, both foils were held in the focal plane during all tests. All the technical specifications are reported in Figure 2b.

The process parameters selected for experimental analysis, model tuning, and sequential model validation are reported in **Table 1**. They were defined following a previous study[14] and each cut was chosen to highlight a specific defect (cuts A, C, D in Table 1) or an optimized result (B). In particular, the following defects were looked for: i) spatter, ii) bubble-shape recast on the cut edge, and iii) burn cut with extremely wide kerf. Cuts A, B, and C were used for model tuning (see Section 3.3), while Cut D and Cut E were chosen for model validation. The irradiance

Table 1. Process parameters employed for laser cutting tests.

	P [W]	Laser Speed [m s^{-1}]	I [MW cm^{-2}]	F [J cm^{-1}]	Model
A	200	2	6.0	195.9	Tuning
B	600	10	18.1	117.5	Tuning
C	1000	25	30.1	78.4	Tuning
D	1000	2	30.1	979.4	Validation
E	200	5	6.0	78.4	Validation

(I) and the fluence (F), reported in Table 1, were calculated as follows:

$$I = \frac{P}{A_{spot}}\left[\frac{\mathrm{MW}}{\mathrm{cm}^2}\right] \tag{1}$$

$$F = I \cdot \tau = I\frac{d_{spot}}{Speed}\left[\frac{\mathrm{J}}{\mathrm{cm}^2}\right] \tag{2}$$

Where τ is the interaction time and d_{spot} is the spot diameter.

2.2. Characterization of Cut Quality

Optical microscopy (OM, Nikon Optiphot-100) and SEM-FEG microscopy (SEM, Tescan Mira3 with a Schottky emitter) were used for cutting quality evaluation. Defects classification and quantification were carried out considering the cut edge geometry. Four parameters were analyzed, as summarized in Figure 1: i) dross thickness (front m_1 and back m_2), ii) remelted area, iii) spatter max distance, and iv) kerf width. Dross thickness represents the amount of resolidified material accumulated along the laser beam axis. The remelted area quantifies the portion of the molten material that did not exit the kerf but instead splashed on the surface (blue area in Figure 1). Spatter max distance measures how far ejected molten droplets travel from the cut edge before solidifying. The kerf width reflects the amount of material removed by the laser, directly reflecting the extent of ablation. OM was initially used to provide a preliminary assessment of cut quality. Hence, high-quality images for spatter quantification and kerf measurements were carried out with SEM on the same surfaces. Two different methods were used to quantify the remelted area after experimental and simulation cuts. The experimental images were processed with Trainable Weka Segmentation, a Fiji plugin.[22] The Fast Random Forrest machine learning algorithm was applied as the classifier to be trained on one SEM image given as input. Three classes were therefore selected for input labeling: kerf, surface, and remelted area. Once the model was confirmed to make accurate predictions, the area with an 80–100% probability of belonging to the spatter class was measured (Figure 1). Instead, simulated cut images were processed by applying the Threshold Color function in ImageJ.[23] The area obtained was then doubled since the cutting process was supposed to be symmetric. The simulation results were then compared with the experimental measurements. The spatter maximum distance was defined as the greatest distance measured from the cut edge to the furthest melted metal finger lying on the copper foil. Data was collected through SEM image analysis, with three SEM images acquired from the front and three from the back of the cut. For each image analyzed, three measurements were taken, and the maximum value, along with the standard deviation of these measurements, was calculated. The same images were used for average kerf width comparisons, both on the top and back of the surface, and the mean value was calculated considering five measurements for each picture. After non-destructive cut analysis, the current collectors were sectioned and embedded in resins for dross height measurements (m_1 and m_2 in Figure 1). After polishing the samples twenty measurements were taken for each cut type (A, B, C, D) at both sides, for a total of 160 measurements. Hence, it was possible to calculate the mean dross thickness in the middle section of the cut and the respective standard deviation (see Figure 6).

3. Numerical Investigation

The commercial CFD software FLOW-3D (v12.0 Update 3) with the laser module FLOW-3D WELD (release 7 Update 3) was employed for the simulation of the laser cut process. Material properties for pure copper were obtained from the literature.[24] Constant values were summarized in **Table 2**, while all the temperature-dependent properties, including the laser absorption rate[25] are plotted in **Figure 3** with a red dashed line representing the melting temperature.

3.1. CFD Model

Based on the finite volume method, FLOW-3D implements the most advanced Volume of Fluid algorithm, called TruVoF©, to track all the interfaces between different fluids or phases. By modeling the material as a fluid region, it is possible to track the dynamics of the melting front interface generated during the laser interaction. Like the original VoF method, the TruVoF© calculates a scalar function F_i (x,y,z,t) defined as the ratio of the volume occupied by the fluid or phase i and the total volume of the grid cell. The function follows the conservation equation:

$$\frac{\partial F_i}{\partial t} + u\frac{\partial F_i}{\partial x} + v\frac{\partial F_i}{\partial y} + w\frac{\partial F_i}{\partial z} = 0 \tag{3}$$

Within each grid cell, the sum of all the F_i must equal 1. In the laser cutting model proposed, the fluids considered are only the metal and surrounding air which reduces the model to:

$$\begin{cases} F = 0 & \text{Air} \\ 0 < F < 1 & \text{Air and metal interface} \\ F = 1 & \text{Metal} \end{cases} \tag{4}$$

Table 2. Pure copper properties.

Property	Value
Solidus temperature	1357.45 K
Liquidus temperature	1357.85 K
Boiling temperature	2835 K
Latent heat of fusion	2.087e + 05 J kg^{-1}
Latent heat of vaporization	5.23e + 06 J kg^{-1}
Vapor specific heat ratio	1.6

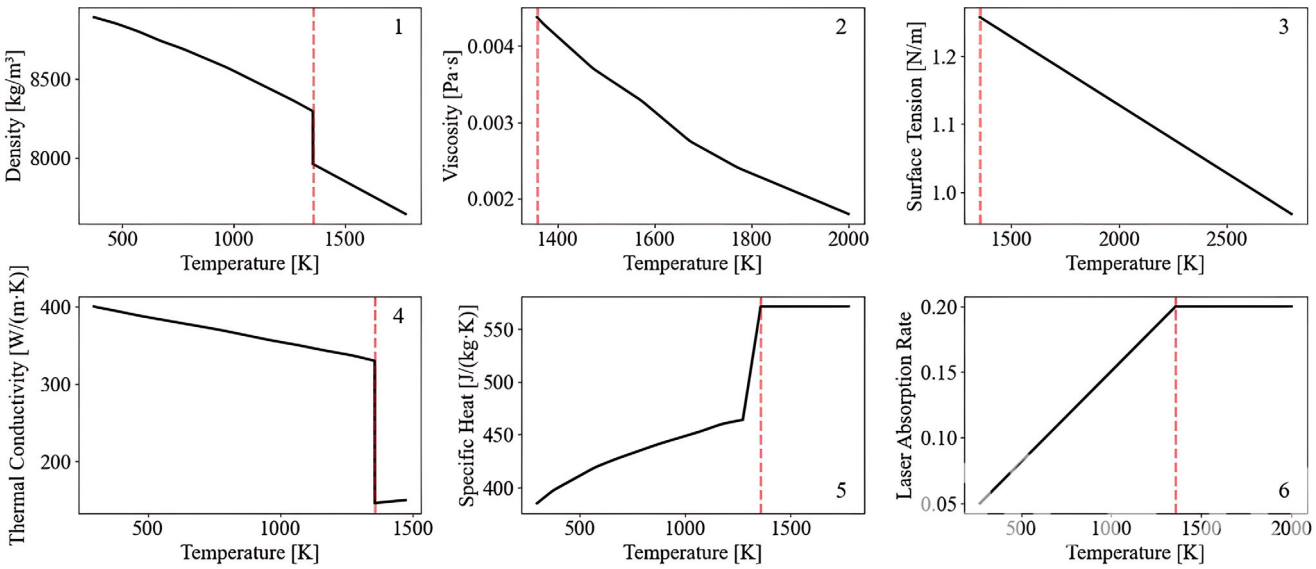

Figure 3. Temperature-dependent properties of pure copper used for simulations.

The air region was considered a void area, with uniform pressure and temperature fields, reducing the computational time. The following physical phenomena were considered in the laser cutting model: viscous flow, heat transfer, energy conservation, phase change with evaporation and solidification, volumetric thermal expansion, surface tension with Marangoni forces, multiple laser reflections with temperature-dependent absorption, and gravity. The viscous flow follows the non-stationary mass and momentum conservation (Equation 5 and Equation 6) for a laminar flow.

$$\frac{\partial \rho}{\partial t} + \nabla \cdot (\rho \mathbf{u}) = 0 \tag{5}$$

$$\rho \frac{D\mathbf{u}}{Dt} = \rho\left(\frac{\partial \mathbf{u}}{\partial t} + (\mathbf{u} \cdot \nabla)\mathbf{u}\right) = -\nabla p + \nabla \cdot \left\{\mu\left[\nabla \mathbf{u} + (\nabla \mathbf{u})^T - \frac{2}{3}(\nabla \cdot \mathbf{u})\mathbf{I}\right]\right\} + \mathbf{f} \tag{6}$$

Where ρ is the density, $\mathbf{u}$ the velocity vector (u, v, w), p the pressure, μ the dynamic viscosity and $\mathbf{f}$ is the sum of all external body forces (for example the gravity). As previously mentioned, the metal region is modeled as a fluid and to account for the differences in behavior between the solid and liquid phases, a viscosity near infinity was defined for the solid phase. ($T < T_{solidus}$: $\mathbf{u} = \mathbf{0}$) Energy conservation is solved using the following equation:

$$\frac{\partial \rho e}{\partial t} + \nabla \cdot (\rho e \mathbf{u}) = -\nabla \mathbf{q} - p \cdot \nabla \cdot \mathbf{u} \tag{7}$$

Where e is the internal energy per unit mass and $\mathbf{q}$ is the conductive heat flux vector. The laser-cutting process of such thin foils is mainly driven by the evaporation of material. Hence, particular attention must be given to the evaporation and recoil pressure model. The evaporation is modeled as a mass transfer from the fluid type to the void type, proportional to the difference between the saturation pressure and the void external pressure:

$$Q_{eva} = \frac{\alpha}{\sqrt{2\pi RT}}(P_{sat} - P_{vap}) \tag{8}$$

Where R is the gas constant (8.314 $\frac{J}{K \cdot mol}$) and α a dimensionless coefficient called accommodation. The saturation vapor pressure is given by the Clapeyron equation:

$$P_{sat} = P_v \, exp\left\{\frac{1}{(\gamma - 1)\frac{c_v}{\Delta H_v}}\left(\frac{1}{T_v} - \frac{1}{T}\right)\right\} \tag{9}$$

Where P_v and T_v identify a point in the saturated curve, γ is the vapor's specific heat ratio, c_v is the vapor's specific heat at constant volume, and ΔH_v is the latent heat of vaporization. Finally, the recoil pressure P_{recoil}, which exerts a force on the material surfaces through the term $\mathbf{f}$ in Equation (6), is derived from the saturated vapor pressure using an empirical equation.[26]

$$P_{recoil} = P1 \, exp^{\left\{P2\left(1 - \frac{T_v}{T}\right)\right\}} \tag{10}$$

The two parameters, $P1$ and $P2$, must be calibrated through experimental results. During the laser-material interaction, the incident beam is discretized into a finite number of rays originating from the focal point and propagating in the laser beam irradiation direction (z-axis). The number of rays propagated through the domain depends on the cell size. Therefore, a small cell size is required to ensure a sufficient number of rays, enabling an accurate representation of the laser beam and its interaction with the material. Upon contact with the surface, a ray with direction

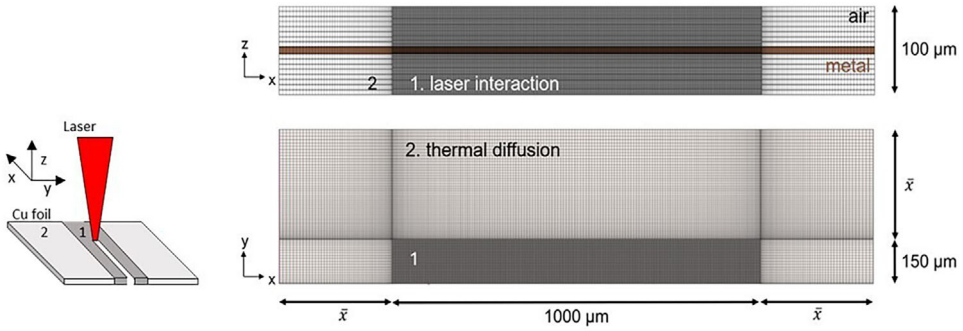

Figure 4. Computational domain.

I transfers a portion of its energy proportional to the material's absorption rate and is reflected toward the opposite side with direction **R** calculated as:[27]

$$\mathbf{R} = \mathbf{I} - 2(\mathbf{I} \cdot \hat{n})\hat{n} \tag{11}$$

Where $\hat{n}$ is the material surface normal vector calculated as $\nabla F/|\nabla F|$. The reflections stop either when the ray energy is below a threshold, or the ray exits the computational domain. The last force considered is the Marangoni force acting on the melting metal. As a result of temperature variations, a surface tension gradient is formed at the liquid–solid interface, producing a force S_M directed along the normal direction of the interface and equal to:

$$S_M = \nabla_t \sigma \tag{12}$$

Where ∇_t indicates the gradient evaluated along the tangent direction of the melting interface. The plasma plume that rises for the material evaporation was not directly considered in the investigation except for the definition of the laser absorption rate as used in previous works.[28,29] Lastly, an automatic time-step control is employed to stabilize the simulation while keeping the time step as large as possible. The time step is dynamically adjusted based on several conditions related to the primary physics models, including fluid advection, pressure at the free surface, heat transfer, and surface tension. These conditions ensure that fluid does not cross more than one computational cell per time step and that pressure and temperature residuals are sufficiently minimized within each time step.

3.2. Simulation Domain

Experimental cuts are not always symmetric in the x-axis direction, as highlighted in Figures 6 and 7), however, both their edge geometry follows a consistent trend. Since the model aim to predict the overall quality, only one cut edge is sufficient to assess the final quality trend. Therefore, only half of the domain was considered (see **Figure 4**), reducing the total number of cells and the computational time. Spatial discretization was performed using a staggered Cartesian grid and the domain was divided into two parts: a main region in which the laser-current collector interaction occurs and needs a finer discretization and a thermal diffusion region that considers the heat transfer in the material. The dimension of the main region is 1 mm × 0.15 mm × 0.1 mm on the x, y, and z-axis respectively. These dimensions were defined considering the minimum cutting length necessary to achieve a stationary condition (x direction), the maximum expected kerf width (y direction), and dross height (z direction). The size of the thermal diffusion region in the x and y directions was calculated using Equation (13)

$$\bar{x} = 2\sqrt{2\frac{k}{\rho c_p} t_{end}} \tag{13}$$

Where t_{end} is the simulation end time calculated as the ratio between the main region x length and the laser velocity. While the size in z was kept fixed. Looking at the Cartesian coordinates of Figure 4, the following constraints were defined: symmetry of one zx surface, constant atmospheric pressure (101325 Pa) in both xy surfaces, and fixed walls on the remaining sides.

A mesh convergence study was carried out to find the optimal cell dimension for the main region. It was found that a minimum of 5 cells in thickness for the 8 μm foil were required for capturing the spatter and the melting behavior for high velocity. For this reason, the domain was discretized into a mesh of fixed

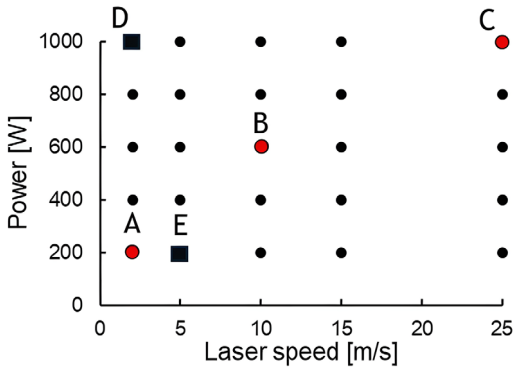

Figure 5. Simulated cut conditions. The red dots and back squares correspond, respectively, to the cut parameters used for model tuning and validation.

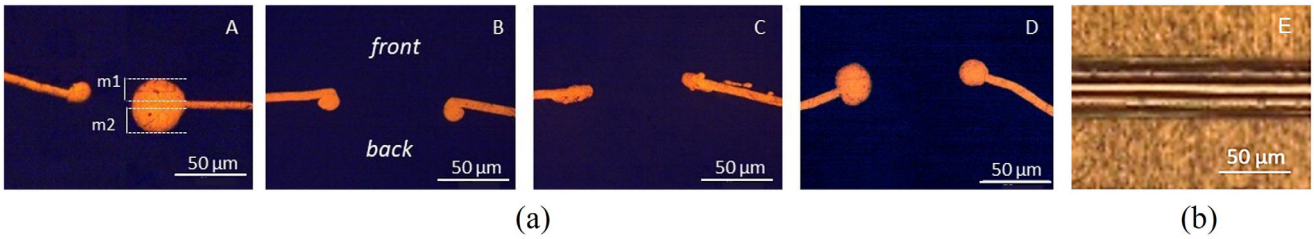

Figure 6. Characterization of edge profile of cuts a) A (2 m s^{-1}, 200 W), B (10 m s^{-1}, 600 W), C (25 m s^{-1}, 1000 W), and D (2 m s^{-1}, 1000 W) and b) E (5 m s^{-1}, 200 W).

rectangular cells with a minimum dimension equal to 1.4 µm. The thermal diffusion cell size was four times the main one and, therefore, 5 µm. The total number of cells inside the computation domain was close to 6 million, with a simulation time that ranges from 4 h for the 25 m s^{-1} simulation to almost 14 h for the 2 m s^{-1}.

3.3. Modeled Cut Conditions

The developed model aims to simulate the effects of laser cutting on copper current collectors across a broad range of process parameters, with laser power ranging from 200 W to 1000 W and cutting speeds from 2 m s^{-1} up to 25 m s^{-1}. To calibrate the CFD model, three sets of process parameters were selected based on their ability to produce distinctly different edge geometries, according to the experimental plan described in Section 2.1. These selected conditions are marked as large red dots in **Figure 5**: 2 m s^{-1} at 200 W (point A), 10 m s^{-1} at 600 W (point B), 25 m s^{-1}at 1000 W (point C). The model was subsequently validated using samples processed under parameter conditions at the boundaries of the operating window. Specifically, Point D represents the condition with maximum power and minimum speed, while point E corresponds to the lowest power and the first speed at which cutting no longer occurs. The numerical results were compared with experimental data for these reference cuts marked with black squares (Point D and E in Figure 5), as reported in Table 1. Once the model was confirmed to make accurate predictions, a wider range of process parameters, identified as black points in Figure 5, were used as input for the simulation. Five levels of laser speed and power were studied. This allowed for the investigation of the influence of speed, power, and foil thickness over a broad window of possible conditions.

The same process parameters have been selected for evaluating the effect of cutting by increasing the current collector thickness from 8 to 16 µm.

4. Results

4.1. Experimental Cut Analysis

Defect formation is significantly influenced by the melt pool and heat flows, as well as the intensity and pressure distributions during the laser cutting. Hence, the five sets of process parameters mentioned above were used to investigate the characteristics of full penetration cutting for copper current collectors. In the E condition, the power-velocity couple fails to achieve the melting and vaporization temperature necessary for the cut (see **Figure** 6b). As a result, no further experimental analyses were carried out and the model's predictive capability was evaluated based on the consistency of the "cut"/"no-cut" result. The quality of each cut was quantified and compared in terms of the front (m_1) and the back (m_2) dross height on the cut edge profile, kerf width, and by evaluating the remelted area and the spatter maximum distance. An example of edge profile measurements of cuts is reported in Figure 6, while all data are reported in **Table** 3.

At high speeds (cuts B and C), the kerf remains consistent along the cutting edge, while lower speeds cause irregularities in kerf width if combined with low power (A), as indicated by the high standard deviation. Furthermore, in that process condition, the dross solidifies into bubble-like formations along the edge (see **Figure** 7a), which results in a high standard deviation also for m_1. This variation is reduced when power is increased up to 1000 W (set D, Figure 7d). Differently, cut B exhibits nearly zero dross height at the front (Figure 7b) and a dross height of approximately 15 µm at the back of the cut.

Dross formation and remelted area (see **Table** 4) highlight the effect of process parameters on melted and ablated material portions. The largest remelted area is observed in sample A, likely due to its combination of the lowest speed (2 m s^{-1}) and power (200 W), which benefits melting over vaporization. At the same speed, increasing power leads to less molten material and more metal ablation, placing sample D second in the remelted area. The smallest remelted layer is observed in sample B.

Table 3. Process parameters employed for CW cutting of copper foils and their relative cut characterization measurements.

	P [W]	Laser speed [ms^{-1}]	I [$MWcm^{-2}$]	F [Jcm^{-2}]	kerf mean [µm]	kerf std [µm]	m_1 mean [µm]	m_1 std [µm]	m_2 mean [µm]	m_2 std [µm]
A	200	2	6.0	195.9	131	53	4.7	7.0	12.5	6.0
B	600	10	18.1	117.5	70	4	0.1	0.1	14.4	5.0
C	1000	25	30.1	78.4	53	5	3.0	1.8	5.7	4.4
D	1000	2	30.1	979.4	83	4	5.1	3.1	6.9	3.8

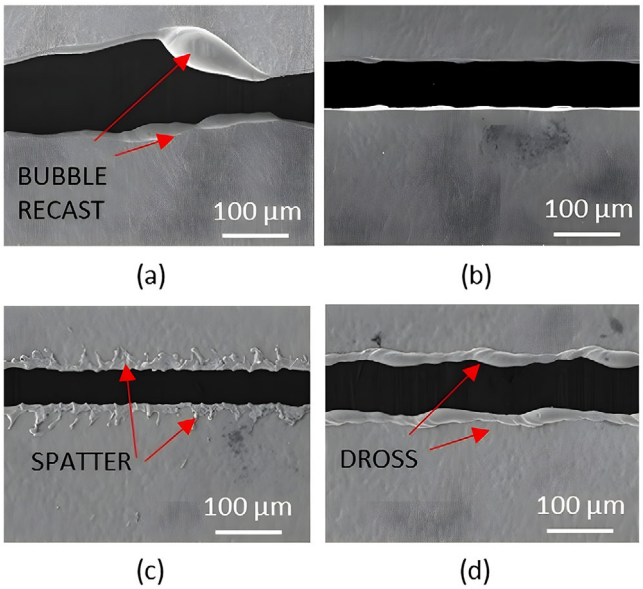

Figure 7. SEM images of cuts a) A (2 m s^{-1}, 200 W), b) B (10 m s^{-1}, 600 W), c) C (25 m s^{-1}, 1000 W), and d) D (2 m s^{-1}, 1000 W) with the typical defects highlighted.

Intermediate speed and power settings favor the accumulation of melted material on the back side of the foil (see m_1 and m_2 in Table 3) facilitating the expulsion of a part of melted metal. In sample C the melted material is more widely spread across the surface, with a low value of dross height. However, the metal droplets escaping from the molten pool (Figure 7c) must be considered and the maximum distance of the melted material from both the front and back of the cut edge becomes the most significant parameter. Table 4 shows the measurement results highlighting the effect of high speed on spattering phenomena (cut C). The high values resulting in sample A are due to the large diameter of the resolidified metal droplets, which is doubled with respect to cut C.

4.2. Model Tuning and Validation

The CFD model was tuned using the results of cuts A, B, and C described in Section 4.1. As stated in Section 3.1, the process is primarily driven by evaporation, and a single set of recoil pressure parameters $P1$ and $P2$ failed to reach a satisfactory match with the experimental data. Therefore, an independent tuning of each cut was performed, and then empirical equations between $P1$ and $P2$ and the process parameters, in terms of fluence and irradiance, were defined. The reliability of this relation was then validated with cuts D and E.

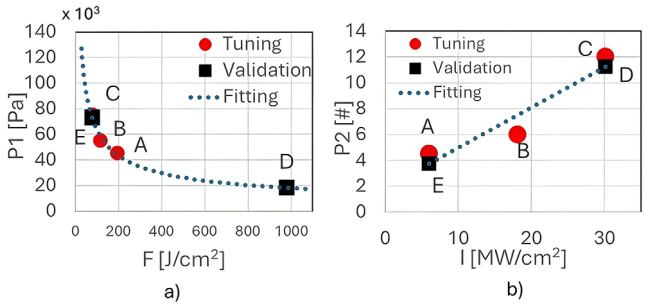

Figure 8. Evaporation parameters $P1$ and $P2$ tuning (red dots A, B, C) and validation (black squares D, E).

Specifically, a power law trend between parameter $P1$ and fluence was identified (**Figure 8a**) and the following equation used for subsequent simulation:

$$y = 14.4 \cdot 10^7 \, x^{-1.18} \qquad R^2 = 0.96 \tag{14}$$

On the other hand, parameter $P2$ was adjusted linearly with Irradiance. As the irradiance increases, $P2$ also increases following Equation:

$$y = 0.358x + 0.068 \qquad R^2 = 0.99 \tag{15}$$

Both trends have a coefficient of determination greater than 0.96. The fitting approach of P2 was evaluated not only based on the coefficient of determination R^2 but also using the MAPE and RRMSE indices, which provide a more detailed evaluation of absolute and relative errors. While a quadratic model results in a lower MAPE of 0.2% compared to 7% for the linear model, the improvement falls within the range of experimental and numerical uncertainties. To ensure interpretability and avoid overfitting, we adopted the linear model as a more generalizable representation of the underlying phenomenon. The resulting values $P1$ and $P2$ were then used in the tuning and validation stage and a qualitative comparison between the different cut-edge profiles is shown in **Figure 9**. For each image, the top half part corresponds to the simulated result, while the bottom half is the corresponding SEM picture. Both front and back were evaluated. The red surface shown in the simulated part represents the material that resolidified after melting.

A quantitative evaluation followed, and the data matching between the model and experiments was carried out by measuring the height of the dross, the spattered area, the maximum

Table 4. Remelted area and spatter maximum distance from the cut edge measurements.

	Remelted area front [µm²]	Remelted area back [µm²]	Spatter maximum distance front [µm]	Spatter maximum distance back [µm]
A	30	26	139	85
B	Negligible	21	4	20
C	21	16	50	60
D	24	22	27	36

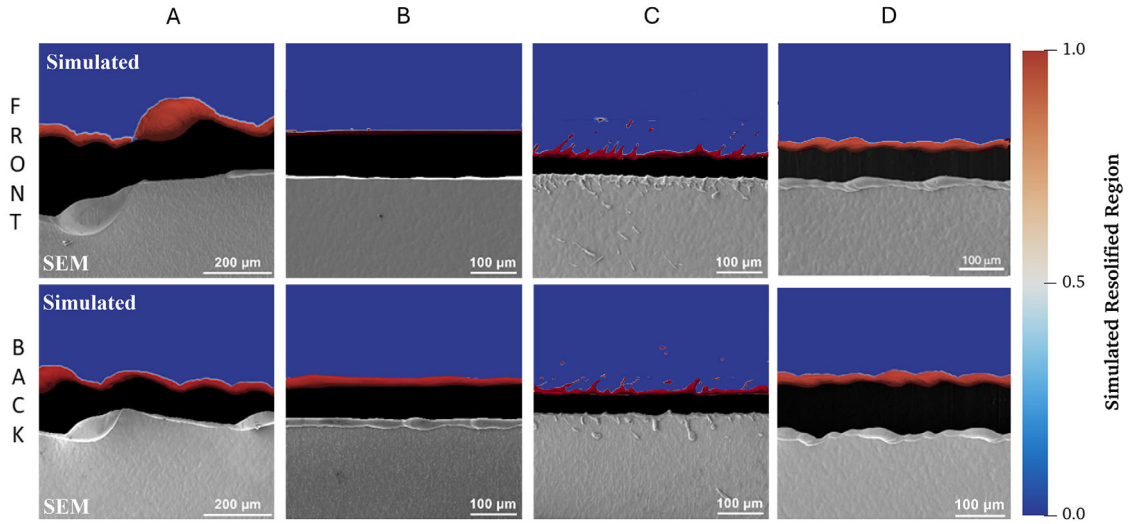

Figure 9. Comparison between simulated and experimental laser cuts when A, B, C, and D parameters were applied for tuning and validation.

spatter distance, and the kerf width, as illustrated for the experimental cuts.

The simulation results, represented by the gray bars in **Figure 10**, were obtained by considering five positions along the entire cutting length. A generally good agreement with the experimental data emerged, both in terms of average values and their respective standard deviations. The standard deviation provides insight into how the cutting trend evolves along its entire length. It is worth noticing that the results obtained for cut D, used to validate the model, show good performance. More specific consideration can be carried out by introducing specific measurable metrics. The errors were thus quantified using two unit-free metrics: the Relative Root Mean Square Error (*RRMSE*) and the Mean Absolute Percentage Error (*MAPE*).[30] The *RRMSE* is calculated by taking the square root of the ratio between the mean squared difference between experimental (*EXP*) and simulated (*SIM*) values, normalized by the same simulated value, as shown in the formula:

$$RRMSE = \sqrt{\frac{(EXP - SIM)^2}{SIM^2}} * 100 \tag{16}$$

The *MAPE*, on the other hand, quantifies the average of the absolute percentage differences between the experimental and simulated values, expressed as a percentage:

$$MAPE = |\frac{EXP - SIM}{EXP}| * 100 \tag{17}$$

Both metrics provide interpretable thinking regarding the quality of prediction even when different measurement techniques are involved. These calculations were applied across multiple parameters, such as m_1, m_2, Kerf, remelted area (front and back), and maximum spatter distance (front and back), for the different cuts (A, B, C, D) and the data are reported in **Table 5**.

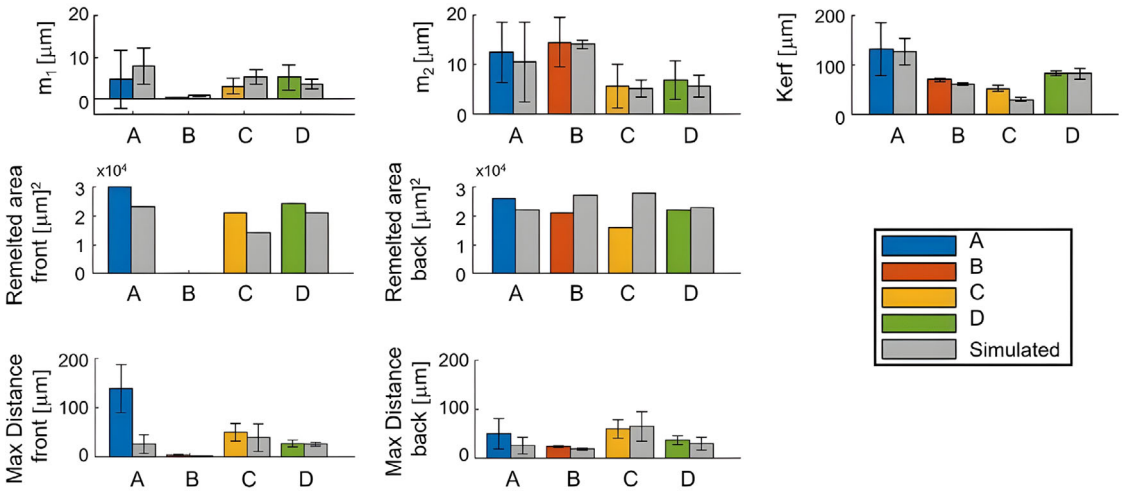

Figure 10. Comparison between experimental and simulated cut by kerf, dross measurements, and spatter area and distance.

Table 5. *RRMSE* and *MAPE* metrics to quantify the discrepancy between simulated and experimental results.

	RRMSE				*MAPE*			
Cut	A	B	C	D	A	B	C	D
m_1	38	#	6	26	61	#	7	35
m_2	14	5	23	10	12	5	30	12
Kerf width	7	2	2	1	7	2	2	1
Remelted area front	32	61	54	15	24	158	35	13
Remelted area back	16	22	43	3	14	28	75	3
Max spatter distance front	223	0	17	0	69	0	0	0
Max spatter distance back	108	23	14	3	52	30	17	3

The classification of errors into "good" or "poor" predictions follows established thresholds from the literature:[31]

- *RRMSE* and *MAPE* < 10%: Very good agreement (green boxes in Table 5)
- *RRMSE* and *MAPE* between 10% and 20%: Good agreement (green boxes in Table 5)
- *RRMSE* between 20% and 30% and *MAPE* between 20% and 50%: Acceptable agreement (orange boxes in Table 5)
- *RRMSE* > 30% and *MAPE* > 50%: Poor agreement (white boxes in Table 5)

The obtained results highlight a close overlap between simulation and experimental results of the kerf, with *RRMSE* and *MAPE* values consistently low for all samples (1–7%) and dross height in the backside. A good alignment is found on all phenomena that concern the backside (m_2, remelted and spatter distance), while the remelted area in the front side shows a poorer agreement with experimental measurements, in particular for cut B. However, the disagreement is partially due to the main drawback of *MAPE*, which is scale-sensitive, leading to extreme values when the actual value is very small (i.e. m_1 error for cut B), and it penalizes negative errors more heavily (when the predicted value exceeds the actual). This occurs, for instance, in sample A when measuring m_1 or in sample B when measuring the remelted area at the front; in both cases, the error should ideally be halved. The max spatter distance for cut A, both front and back, shows very high values due to the high experimental measurements of the big diameter of the remelted metal droplets, which occur less frequently in simulations.

4.3. Cut Quality Prediction

Once the robustness of the model in accurately predicting the laser-current collector interaction was established, the influence of power, speed, and foil thickness on defect formation was investigated. The kerf, m_1 and m_2 average and standard deviation measurements of every set of process parameters simulated are reported in **Table 6**.

Thanks to the model, it was possible to fill the graph shown in **Figure 11**. The process window is divided into five main regions indicating the prevailing condition for each cut: No Cut, Recast, Dross, Good, and Spatter areas. The defect classification was defined by two main parameters: the kerf coefficient of variation (CV_{kerf}), defined as the ratio of the standard deviation to the mean, and the normalized dross height (*NDH*) calculated as the ratio between m_1 (or m_2) and the thickness of the metal foil. The CV_{kerf} is a dimensionless number representing the relative variability of the kerf measurements in relation to its mean.

First, the dross region is defined when both m_1 and m_2 have high values:

$$Dross\ Area \Leftrightarrow NDH_{m_1} > 10\% \ \wedge NDH_{m_2} \geq 50\% \tag{18}$$

Specifically, this means that the dross height has to be at least 10% and 50% of the foil thickness to be classified as "Dross." Inside the dross area, two sub-regions can be identified: "Spatter" or "Recast" area collocated at the two extreme opposite angles of the graph. When both low speed and low power are applied (i.e., 2 m s^{-1} and 200W), the kerf becomes unstable, and the dross turns into a bubble-shaped recast. Hence, this sub-region is called "Recast" and it is characterized by a significant kerf variability and by a high standard deviation for either m_1 or m_2:

$$Recast\ Area \Leftrightarrow \begin{cases} CV_{kerf} \geq 30\% & kerf\ inconsistency \\ CV_{m_1} \vee CV_{m_2} \geq 50\% & bubble-shaped\ recast \end{cases} \tag{19}$$

At speeds higher than 19 m s^{-1}, spatters are formed, mainly at the back, if the melt profile along the entire cut length is highly irregular, in other terms with the highest standard deviation:

$$Spatter\ area \Leftrightarrow STD_{Max\ Spatter\ Distance} > 40\% \tag{20}$$

At higher speed and power levels (≥1000 W), more droplets are ejected from the front as well. Between the Not Cut and the Dross region lies the good cut area, characterized by near-zero front dross, a regular kerf, and a melted area only close to the cutting edge, specifically:

$$Good\ area \Leftrightarrow \begin{cases} NDH_{m_1} \leq 10\% \\ CV_{kerf} \leq 5\% \\ STD_{Max\ Spatter\ Distance} < 10\% \end{cases} \tag{21}$$

In this range of process parameters, the effect of power is quite evident: starting from a good cut condition, for example from cut B with increasing the power to 1000 W alters the cut edge geometry, leading to dross formation also in the front surface.

4.4. Influence of Foil Thickness

Finally, the effect of doubling the foil thickness from 8 to 16 µm was also investigated. The average measurements of kerf, m_1 and m_2, as well as their respective standard deviations, all obtained only from simulations, are reported in **Table 7**. These results allowed to fill the area graph in **Figure 12**, following the equations described in Section 4.3.

With an increase in thickness, even if the inequalities for the defect's definition remain valid, some observations about the defect morphology need to be explicitly noted. First, the no-cut region expands significantly as expected, indicating that thicker

Table 6. Simulation measurements of 8 µm foil laser cutting.

P [W]	v [m s^{-1}]	kerf mean [µm]	kerf std [µm]	m_1 mean [µm]	m_1 std [µm]	m_2 mean [µm]	m_2 std [µm]	Classified Area
200	2	122.4	35.2	7.6	5.8	11.0	7.6	Recast
400	2	109.5	32.2	7.7	4.2	11.2	7.6	Recast
600	2	105.4	33.8	3.0	2.1	11.0	9.4	Recast
800	2	87.3	8.5	3.4	0.7	6.2	2.1	Dross
1000	2	82.3	4.3	6.9	2.9	7.7	2.3	Dross
200	5	–	–	–	–	–	–	No Cut
400	5	86.9	10.8	8.1	2.0	8.8	4.0	Dross
600	5	81.4	4.4	6.9	2.9	11.2	3.7	Dross
800	5	82.8	4.5	6.3	2.9	9.3	1.4	Dross
1000	5	80.2	4.5	5.3	2.1	11.6	3.9	Dross
200	10	–	–	–	–	–	–	No Cut
400	10	–	–	–	–	–	–	No Cut
600	10	68.9	2.3	0.0	0.0	15.1	1.5	Good
800	10	69.4	3.7	0.2	0.0	14.8	2.1	Good
1000	10	64.6	3.3	9.7	1.0	16.2	2.1	Dross
200	15	–	–	–	–	–	–	No Cut
400	15	–	–	–	–	–	–	No Cut
600	15	66.5	2.7	0.4	0.3	14.7	1.1	Good
800	15	62.8	2.9	0.6	0.5	15.5	1.6	Good
1000	15	58.0	2.2	4.7	0.9	13.6	2.8	Dross
200	25	–	–	–	–	–	–	No Cut
400	25	–	–	–	–	–	–	No Cut
600	25	–	–	–	–	–	–	No Cut
800	25	59.8	3.4	6.7	0.6	7.2	0.5	Spatter
1000	25	54.0	1.6	3.2	0.9	7.4	3.1	Spatter

foils require higher power densities to achieve full penetration and complete cutting. The recast region disappears and the Good area is narrowed in length.

As foil thickness doubles, the Dross region becomes fragmented: at 5 m s^{-1}, one portion appears after the no-cut region and another after the good region. The dross height is more pronounced in thicker materials due to the larger volume of molten material that can adhere to the bottom edge of the cut. Lower speeds exacerbate this issue as they allow more time for the molten material to cling and solidify, forming dross.

The Good region shifts toward slightly lower levels of speed, suggesting more precise control over process parameters is necessary to maintain cut quality with increased thickness. The good cut condition continues to apply (600 W and 10 m s^{-1}), with an increase in the m_2 dross height from 15 to 25 µm. The shrinkage of the Good cut window with increasing foil thickness might be associated with thermal dissipation. When a laser beam interacts with a material, energy is initially absorbed within a surface layer. For thinner foils (8 µm) the absorbed energy is concentrated over a very small thickness, resulting in a high energy density that promotes rapid vaporization while limiting heat transfer to surrounding areas. However, if the foil thickness doubles, the energy is distributed over a larger volume, reducing the energy density and requiring a longer interaction time to reach vaporization temperatures. Additionally, thicker foils have a longer thermal diffusion path, causing heat to take more time to dissipate laterally.

The Spatter area becomes much more prominent, covering the largest portion of the graph, right after the No Cut region. In fact, spatters are more likely to occur at lower speeds: from 19 m s^{-1} with the 8 µm foil, down to 10 m s^{-1} when the foil thickness is doubled. This is likely due to the higher volume of molten material generated when cutting thicker foils, which causes more molten droplets to escape from the molten pool. The remelted area confirms this, 3.6 larger compared to the same process parameters used on 8 µm foils.

5. Discussion

The main goal of laser notching for current collectors is to achieve high cutting speeds combined with high cut edge quality. This often requires numerous experimental campaigns to identify the optimal process parameters. The proposed CFD model allows for predicting the behavior of CW laser cutting of thin foils with varying thicknesses, offering insights into the correlation between cut quality and process parameters, as well as spatter formation.

The formation of defects in the cutting process can be attributed to the varying amounts of evaporated over melted material and the latter dynamics governed by the recoil pressure forced. The recoil pressure (P_{recoil}) was extracted from the simulation results at each time step and averaged throughout the cutting length. At low power and low speed (cut A), the recoil pressure is

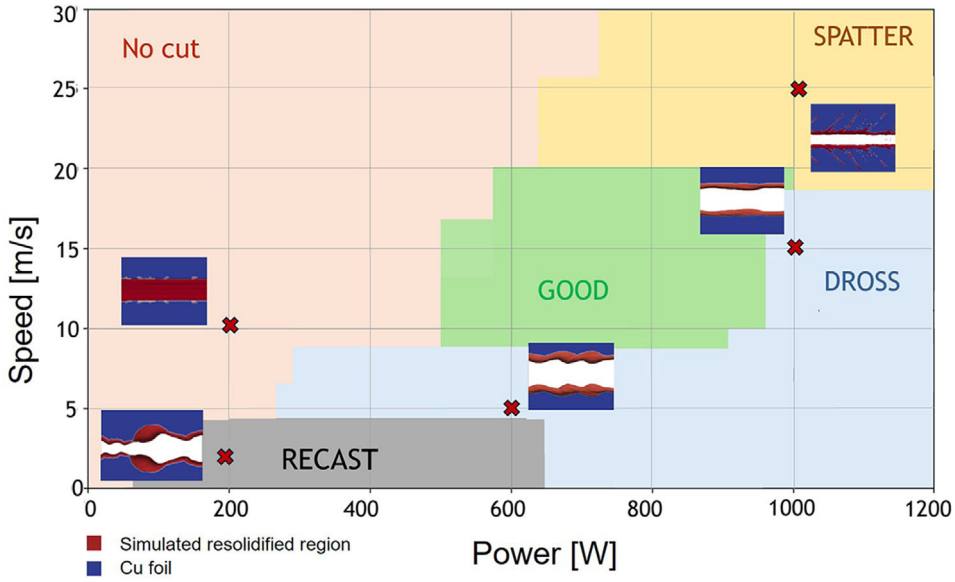

Figure 11. Quality prediction of 8 µm foil laser cutting within a wide range of process parameters.

at its lowest, with a P_{recoil} of 8×10^4 Pa. While it was sufficient to induce material evaporation and enable cutting, this condition favors melting over evaporation. The weak force exerted on the molten pool results in a minimal downward kinetic energy, leading to the accumulation of molten material along the cutting path. This material re-solidifies into bubble-shaped recast, producing an inconsistent kerf. As shown in Figure 11, the kerf width in the recast region ranges from 75 to 130 µm, with a standard deviation over 15 times higher than that of cuts in the Good region (35.2 µm for cut A versus 2.3 µm for cut B). The reason why it accumulates as not as an uniform dross layer can be also related to its high surface tension (1.3 N m^{-1}[32]) and viscosity (4 mPa s, near the melting point[33]). These properties contribute to the retention of molten material at the kerf edges rather than its expulsion, further facilitating recast formation.

By increasing power while maintaining the same speed, the recoil pressure rises ($P_{recoil} = 1.15 \times 10^5$ Pa), enhancing material evaporation and preventing excessive melt accumulation, resulting in a more uniform kerf.

Higher recoil pressure values lead to optimal conditions ($P_{recoil} = 1.5 \times 10^5$ Pa), as they push the molten material downward, where it solidifies (m_2 up to 15.5 µm), resulting in a defect-free cutting front ($m_1 < 0.6$ µm).

At even higher power and speed combinations (lowest fluence conditions), the recoil pressure reaches its peak at $P_{recoil} = 4.8 \times 10^5$ Pa, leading to a stable kerf but also imparting excessive kinetic energy to the molten pool. This condition favors evaporation rather than melting, as highlighted in Figure 6a for cut C which shows less molten material formed along the edges, with the back height dross accounting for a maximum of 7.4 µm. However, with this value of recoil pressure exerted within the kerf, molten material can be ejected onto the front and back surfaces as irregular spatters. This phenomenon aligns with findings in laser welding research,[8] where spatters occur when local melt volumes gain sufficient momentum perpendicular to the melt surface. The vertical drag force of the vapor jet plays a critical role, as spatters form when the vertical momentum of the melt surpasses surface tension forces. Materials that fail to escape the melt pool re-solidify into rims or droplet fingers near or far from the cut edge. The latter defect is important to be quantified as melted droplets ejected far from the edge profile can potentially be incorporated into the electrode slurry, harming battery functionality. Compared to good cut conditions, spatter formation occurs when lower fluence and shorter dwell times are applied. This is demonstrated by the recoil pressure formula in Equation (11), where lower fluence values ($P1$) and higher irradiances ($P2$) result in elevated vapor temperatures and increased recoil pressure.

In order to strike a "spatter condition," the Weber number is introduced. This dimensionless parameter describes the competition between kinetic energy and surface tension[9] and is defined as:

$$We = \frac{\rho r V^2}{\sigma} \tag{22}$$

where ρ is the density of liquid Cu (7900 kg m^{-3}),[33] V is the velocity magnitude of the melt droplet (15 m s^{-1}), r is the local curvature radius (3 µm), and σ is the surface tension of liquid Cu (1.3 N m^{-1}).[33] The speed and radius values of the metal droplet were obtained by averaging measurements taken at five different time steps during the simulation of the cut. The corresponding average Weber number is 3.87 (>2), indicating sufficient kinetic energy to overcome surface tension forces. For thicker foils, the threshold speed for spatter formation decreases (below 10 m s^{-1}), as larger droplets (greater than 3.5 µm in diameter) are formed. This results in a lower Weber number of approximately 2.63 (>2).

6. Conclusion

Thanks to the developed CFD model it has been possible to thoroughly predict the behavior of CW laser cutting quality of thin copper foils with different thicknesses, which are used as current collectors of the lithium-ion battery electrodes. After tuning

Table 7. Simulation measurements of 16 µm foil laser cutting.

P [W]	v [m s^{-1}]	kerf mean [µm]	kerf std [µm]	m_1 mean [µm]	m_1 std [µm]	m_2 mean [µm]	m_2 std [µm]	Classified Area
200	2	–	–	–	–	–	–	No Cut
400	2	71.5	9.7	6.2	3.5	17.9	5.2	Dross
600	2	69.6	4.0	5.4	2.2	18.5	1.8	Dross
800	2	68.3	3.4	5.6	1.6	18.9	1.1	Dross
1000	2	67.8	2.1	6.9	0.9	22.1	3.2	Dross
200	5	–	–	–	–	–	–	No Cut
400	5	70.4	1.8	5.7	1.5	21.6	2.7	Dross
600	5	68.2	2.0	0.3	0.2	29.3	3.2	Good
800	5	65.3	2.9	1.9	1.4	27.4	8.4	Good
1000	5	64.5	1.2	7.1	2.5	19.8	2.5	Dross
200	10	–	–	–	–	–	–	No Cut
400	10	–	–	–	–	–	–	No Cut
600	10	67.9	2.2	0.1	0.1	25.2	4.9	Good
800	10	64.0	2.3	7.4	1.9	15.2	2.7	Dross
1000	10	61.7	4.0	7.6	2.3	16.4	4.6	Spatter
200	15	–	–	–	–	–	–	No Cut
400	15	–	–	–	–	–	–	No Cut
600	15	–	–	–	–	–	–	No Cut
800	15	61.1	1.8	5.8	2.2	18.6	1.5	Dross
1000	15	59.7	1.0	6.4	1.4	20.1	1.4	Spatter
200	25	–	–	–	–	–	–	No Cut
400	25	–	–	–	–	–	–	No Cut
600	25	–	–	–	–	–	–	No Cut
800	25	–	–	–	–	–	–	No Cut
1000	25	53.6	2.5	4.2	1.7	13.9	3.5	Spatter

and validating the model with experimental results it was possible to investigate the influence of laser power and speed in kerf dimension, dross height, and spatter. The threshold laser parameters for cutting with good quality, as well as the parameters that lead to defect formation, have been assessed. Experimental results revealed the presence of spatters, dross, and bubble-shaped recast defects, which the CFD model accurately predicted. This allowed for the identification of reliable equations that pinpointed the work regions where these defects occur as when current collectors thickness and process parameters change. The physical

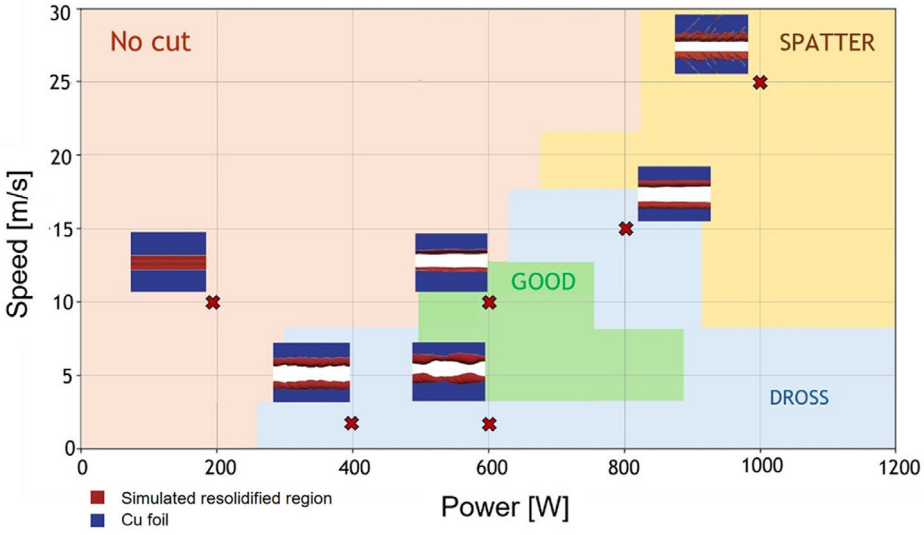

Figure 12. Quality prediction of a 16 µm foil laser cutting.

phenomena responsible for defects occurrence were jointly identified. This study could be utilized as a guideline for achieving optimal cutting conditions when input specifications undergo slight variations, such as changes in material characteristics, spot dimensions, speed, and thickness. Utilizing this approach can save time and resources by reducing the need for extensive experimental campaigns.

Acknowledgements

Open access publishing facilitated by Universita degli Studi di Bologna, as part of the Wiley - CRUI-CARE agreement.

Conflict of Interest

The authors declare no conflict of interest.

Author Contributions

C.A. and S.P. wrote the manuscript. C.A. conducted the experimental campaign, performed measurements, and carried out data analysis and interpretation. S.P. developed the numerical approach, conducted the numerical investigation, and collected numerical data. C.A. and S.P. contributed to data analysis and interpretation. E.L. and A.F. supervised the study, with E.L. designing the overall study and contributing to data analysis and interpretation, while A.F. contributed to the experimental design.

Data Availability Statement

The data that support the findings of this study are available from the corresponding author upon reasonable request.

Keywords

copper foil, current collector, laser cutting, numerical optimization, numerical simulation

Received: November 13, 2024
Revised: March 17, 2025
Published online: April 7, 2025

[1] P. Zhu, D. Gastol, J. Marshall, R. Sommerville, V. Goodship, E. Kendrick, *J. Power Sources* **2021**, *485*, 229321.
[2] W. Pfleging, *Nanophotonics* **2018**, *7*, 549.
[3] M. Luetke, V. Franke, A. Techel, T. Himmer, U. Klotzbach, A. Wetzig, E. Beyer, *Physics Procedia* **2011**, *12*, 286.
[4] J. Grabow, J. Klink, R. Benger, I. Hauer, H.-P. Beck, *Batteries* **2022**, *9*, 9.
[5] Y. Yuan, H. Wang, X. Han, Y. Pan, Y. Sun, X. Kong, L. Lu, M. Ouyang, *Appl. Energy* **2024**, *361*, 122968.
[6] J. Garche, C. K. Dyer, *Encyclopedia of electrochemical power sources*, Academic Press: Imprint of Elsevier, **2009**.
[7] W. Schulz, V. Kostrykin, M. Nießen, J. Michel, D. Petring, E. W. Kreutz, R. Poprawe, *J. Phys. D: Appl. Phys.* **1999**, *32*, 1219.
[8] A. F. H. Kaplan, J. Powell, *J. Laser Appl.* **2011**, *23*, 032005.
[9] S. P. Lin, R. D. Reitz, *Annu. Rev. Fluid Mech.* **1998**, *30*, 85.
[10] W. G. Pritchard, P. Saavedra, L. R. Scott, S. J. Tavener, In A. Friedman, W. Miller, R. A. Brown, S. H. Davis, editors, *Free Boundaries in Viscous Flows*, Springer New York, New York, NY **1994**, vol. *61*, pp. 29–48.
[11] A. Yule, J. Dunkley, *Atomization of Melts: for Powder Production and Spray Deposition*, Oxford University Press, **1994**.
[12] C. Hartmann, *J. Laser Micro/Nanoeng.* **2013**, *8*, 266.
[13] X. Zhu, D. Villeneuve, A. Naumov, S. Nikumb, P. Corkum, *Appl. Surf. Sci.* **1999**, *152*, 138.
[14] C. Angeloni, E. Liverani, A. Ascari, A. Fortunato, *J. Mater. Process. Technol.* **2024**, *324*, 118266.
[15] N. K. Makashev, E. S. Asmolov, V. V. Blinkov, A. Y. Boris, O. G. Buzykin, A. V. Burmistrov, M. R. Gryaznov, V. A. Makarov, *Sov. J. Quantum Electron.* **1992**, *22*, 847.
[16] S. Stoyanov, D. Petring, F. Piedboeuf, M. Lopes, F. Schneider, *J. Laser Appl.* **2023**, *35*, 042028.
[17] B. S. Yilbas, B. J. A. Aleem, *J. Phys. D: Appl. Phys.* **2006**, *39*, 1451.
[18] L. Yu, *J. Mater. Process. Technol.* **1997**, *63*, 637.
[19] D. Lee, R. Patwa, H. Herfurth, J. Mazumder, *J. Power Sources* **2012**, *210*, 327.
[20] D. Lee, R. Patwa, H. Herfurth, J. Mazumder, *J. Laser Appl.* **2016**, *28*, 032010.
[21] H. Ki, P. S. Mohanty, J. Mazumder, *J. Phys. D: Appl. Phys.* **2001**, *34*, 364.
[22] J. Schindelin, I. Arganda-Carreras, E. Frise, V. Kaynig, M. Longair, T. Pietzsch, S. Preibisch, C. Rueden, S. Saalfeld, B. Schmid, J.-Y. Tinevez, D. J. White, V. Hartenstein, K. Eliceiri, P. Tomancak, A. Cardona, *Nat. Methods* **2012**, *9*, 676.
[23] C. A. Schneider, W. S. Rasband, K. W. Eliceiri, *Nat. Methods* **2012**, *9*, 671.
[24] D. Lee, J. Mazumder, *Data in Brief* **2018**, *17*, 6.
[25] W. Huang, H. Wang, T. Rinker, W. Tan, *Mater. Des.* **2020**, *195*, 109056.
[26] V. Semak, A. Matsunawa, *J. Phys. D: Appl. Phys.* **1997**, *30*, 2541.
[27] J.-H. Cho, S.-J. Na, *J. Phys. D Appl. Phys.* **2006**, *39*, 5372.
[28] R. Lin, H. ping Wang, F. Lu, J. Solomon, B. E. Carlson, *Int. J. Heat Mass Transfer* **2017**, *108*, 244.
[29] G. Chianese, Q. Hayat, S. Jabar, P. Franciosa, D. Ceglarek, S. Patalano, *J. Mater. Process. Technol.* **2023**, *322*, 118202.
[30] M. Szudarek, A. Piechna, P. Prusiński, L. Rudniak, *Energies* **2022**, *15*, 6549.
[31] Padhma, A comprehensive introduction to evaluating regression models, **2024**, https://www.analyticsvidhya.com/blog/2021/10/evaluation-metric-for-regression-models/.
[32] B. B. Alchagirov, A. M. Chochaeva, A. G. Mozgovoi, M. N. Arnol'dov, V. B. Bekulov, K. B. Khokonov, *High Temp.* **2003**, *41*, 755.
[33] M. J. Assael, A. E. Kalyva, K. D. Antoniadis, R. Michael Banish, I. Egry, J. Wu, E. Kaschnitz, W. A. Wakeham, *J. Phys. Chem. Ref. Data* **2010**, *39*, 033105.

Optics & Laser Technology 189 (2025) 113119

Contents lists available at ScienceDirect

Optics and Laser Technology

journal homepage: www.elsevier.com/locate/optlastec

The effect of process parameters on the high-speed cut quality of Li-ion electrodes using a single mode continuous fiber laser☆

Caterina Angeloni *, Carolina Magrini, Erica Liverani, Alessandro Fortunato

Department of Industrial Engineering (DIN), Alma Mater Studiorum – University of Bologna, viale Risorgimento 2, Bologna, Italy

ARTICLE INFO

Keywords:
Laser cutting
Continuousfiber laser
Battery electrodes
Graphite anode
Lithium iron phosphate
High quality
High speed

ABSTRACT

Coated Al and Cu current collectors are employed in the production of Li-ion batteries (LIBs) serving as cathodes and anodes, respectively. The increasing demand and the need for net zero-defect cutting quality are driving industrial production towards fast and reliable technologies. Laser cutting of LIB electrodes is an efficient and cost-effective alternative to conventional mechanical methods, enabling high accuracy and less damaged active material while maintaining high processing speeds. Thanks to remote laser technology flexibility, several combinations of process parameters, electrode material, and thicknesses of the electrode sandwich have been studied. This material variety discussed in the literature reflects the need of the industry to exploit different solutions. Currently, electrode cutting mainly involves the application of short pulse nanosecond (ns) fiber laser. However, the fast-advancing technology of laser manufacturing (including laser sources, optics and scanning heads) allows for new opportunities to improve process productivity and quality. This study evaluates the interaction between a single mode (SM) continuous wave (CW) source and LIB electrodes, exploring the effects of laser power and scanning speed (up to 11 m/s) on thermal defects. These include clearance width and heat affected zone (HAZ) for the anode, as well as HAZ width and the quantity of spherical defects detached from the aluminum foil for the cathode. This investigation identified a significant reduction of defects for both materials when higher speeds are set. Specifically, high-quality cuts were achieved at 5.5 m/s for the anode and 4.4 m/s for the cathode, with a clearance width kept below 20 μm and HAZ under 30 μm.

1. Introduction

Lithium-ion batteries (LIBs) are secondary rechargeable batteries representing a highly widespread technology implemented in hybrid electric vehicles, electronic devices, energy storage and home appliances [1]. The increasing demand for LIBs is attributed to a high energy density, low self-discharge and good energy to weight ratio[2,3]. The manufacturing of LIBs is mainly divided into three steps: electrode production, cell assembly and electrochemical deposition for safe battery usage[4], where an efficient preparation of electrodes can ensure less material waste and lower costs of the production line. In other words, the production of LIBs electrodes should aim to net-zero defects.

The fast-advancing technology of laser material processing (LMP) is an efficient, flexible, contact-free process that is implemented in the electrode manufacturing industry for several steps, including drying of active materials, cutting of electrodes and welding [5–8]. In fact, LMP exhibits several advantages in comparison to mechanical processing. This is because it is a wear-free process with low thermal impact, leading to a small heat affected zone (HAZ) as well as reducing the energy cost and increasing production speed [2,7–9].

In recent years, the scientific community has driven its attention towards finding optimal laser parameters to obtain electrode cutting of high quality[10]. However, the sandwich-like structure of electrodes makes LMP challenging. Specifically, the anode is made of Cu-foil with a layer of graphite on both sides, while the cathode is made of Al-foil sandwiched between two layers of active material, which can include $LiCoO_2$, lithium nickel manganese cobalt (NMC) or $LiFePO_4$ (LFP). The state-of-the-art for the ideal parameter window mostly focuses on applying short pulse nanosecond fiber laser and subsequently analyse the effect of laser parameters on kerf geometry, defect formation and HAZ size. Nanosecond pulsed lasers can achieve high beam qualities and reduce HAZ size thanks to the low thermal contribution at high processing speeds. The short interaction time can prevent the conduction of heat across the material with a discontinuous energy input [11]

☆ This article is part of a special issue entitled: 'LaserEMobility' published in Optics and Laser Technology.

* Corresponding author.
E-mail address: caterina.angeloni2@unibo.it (C. Angeloni).

https://doi.org/10.1016/j.optlastec.2025.113119
Received 17 January 2025; Received in revised form 4 April 2025; Accepted 20 April 2025
Available online 9 May 2025

maintaining high velocity, which made nanosecond lasers the leading technology for years. However, the constant evolution of laser sources, optics and scanning systems has opened a new research field of laser cutting where quality can be further improved and processing speed further increased. In particular, the most recent literature focuses on two technologies: ultra-short, pulsed lasers to maximise cut quality and single-mode (SM) continuous wave (CW) lasers to guarantee maximum production and reduce HAZ size (when compared to multi-mode CW lasers).

Though nanosecond pulsed lasers allow for a low thermal contribution, this technology can also lead to superheating of the material surface when the pulse rate is high and result in material ablation creating a clearance width [6]. Gu *et al.*[10] investigated femtosecond laser cutting of LFP, showing that high power leads to significant decline in battery performance by creating delamination and substantial remelting in the HAZ. Zhang *et al.*[12] conducted a study on graphite anode showing that both HAZ size and delamination width increase with laser power and pulse width. The corresponding Raman analysis revealed that the ordered graphite structure is partially damaged near the kerf edge, limited to the coloured changed zone. In other words, transitioning from a primarily conduction-based process (with continuous wave lasers) to the application of ultrashort pulses leads to material removal through ablation, occurring within picosecond to femtosecond timescales. It is therefore crucial to adjust the peak fluence to ensure sufficient material removal while preventing heat dissipation into surrounding material, which could cause defects such as the heat-affected zone (HAZ) and burrs[4]. Laser source manufacturers have introduced an innovative burst mode feature, allowing control over pulse energy. Heidari *et al.*[4] found that increasing the number of pulses per burst and frequency lowers the peak fluence of each pulse, making it easier to fine-tune the optimal peak fluence and achieving higher processing speeds. Audouard *et al.*[13] applied GHz-burst mode for anode cutting and stated that the cutting time is mainly driven by the metal collector of the electrode (Cu-foil for anode, Al-foil for cathode).

Despite the notable results regarding cut quality of ultrafast lasers, the need for increased production and lower cost of laser sources of the LIBs industry has attracted attention towards SM-CW lasers as they can achieve higher processing velocities. With maximum speed of 5 m/s and maximum power of 450 W, experimental studies using SM-CW remote lasers were conducted on both anode and $LiCoO_2$ cathode[14]. A relatively wide parameter window for good cut was defined for both anode and cathode by focusing on the relationship between line energy and kerf width. For the graphite anode, a clearance width of 25 μm to 27 μm was found and determined not significant with respect to battery performance. From a computational perspective, Lee *et al.* conducted simulations of SM-CW laser on both anode and NMC cathode, showing that penetration depth and absorptivity change significantly when the laser beam reaches the metal current collectors. This is mainly due to pool flow patterns, temperature distribution, material properties and composition changes at the interfaces [2]. Lee *et al.* also conducted a study focusing on SM-CW laser cutting of compressed and uncompressed LFP cathodes up to 5 m/s, measuring absorption coefficients of graphite and copper. Because of the lower melting point and favourable gasification, the graphite undergoes a significant delamination, leading to a decrease in active material and battery capacity [15]. In other words, the different melting point between current collector and active material causes a higher heat conduction on the active material as more time is needed to cut the metal foil, leading to a grater energy transfer. To assess the more efficient laser source on cutting of current collectors, a recent study made a comparison of cut quality of Cu- and Al- foils between nanosecond pulsed lasers and SM-CW laser. The investigation revealed that the SM-CW laser obtains better cut quality, with fewer burns, less spatter and an increased quality of kerf geometry when high speeds are set [16].

This study aims to be an extension of the previous one, investigating the interaction of electrodes with high-quality, high-power CW laser source and high-speed scanning system. In fact, the current state-of-the-art lacks an investigation on the effect of SM-CW fiber laser on high-speed electrode cutting, which this paper aims to provide by applying speed up to 11 m/s and power up to 1140 W. The effect of laser parameters of a SM-CW laser was investigated on both graphite anode and LFP cathode to demonstrate the true potential of this technology by enabling rapid processing without sacrificing edge quality, obtaining fine cuts at $>$ 5 m/s and 1 kW. Correlations between irradiance and fluence are determined with respect to HAZ width for both cathode and anode, clearance width with respect to anode and quantification of spherical droplets with respect to LFP cathode.

2. Experimental set up

2.1. Materials, laser sources and cutting set-up

Commercial LFP cathode and graphite anode films were tested. A lithium-ion battery anode material made of copper foil with equal-thickness graphite layers coated on both sides was provided. The copper foil measured 8 μm in thickness, whereas each graphite layer was 66 μm. Graphite is composed of active graphite powder (90 %), carbon black (7 %), sodium carboxymethyl cellulose CMC (2 %), polymer binder (1 %). The composition of the given LFP sample was estimated through thermal-gravimetric analysis (TGA) with TA instrument TGA Q50, resulting in LFP (93.88 %), polyvinylidene fluoride PVDF + carbon black (6,12 %).

Layer thicknesses were measured with SEM-FEG microscopy (SEM, Tescan Mira3 with a Schottky emitter) by positioning the anode sample orthogonal to the plane. The Al-foil measured 14 μm and each LFP layer 80 μm. Additionally, the element composition of LFP remelted on the section was investigated by energy-dispersive X-ray spectroscopy (EDS) analysis, using a silicon drift detector (SSD). SEM accelerating voltage was set at 12 kV with a working distance of 14 mm, a current of 200/250 pA and the count rates for EDS at 3000 cps.

All the pictures were acquired with the SE (Secondary Electrons) detector, the anode samples also with the BSE detector (Backscattered electrons). BSE images show high sensitivity to differences in atomic number; the higher the atomic number, the brighter the material appears in the image. Hence, copper was bright light and graphite dark black (see Fig. 1), and it was therefore easier to quantify the clearance width with image processing in all anode samples.

An n-light Corona fiber laser source with emission wavelength of 1064 nm, maximum output power of 1.2 kW was applied for the experiments. A 2D galvo scanner system (Scanlab Intelliscan 20) was employed to move the laser beam with speed reaching up to 11 m/s. The scanner was equipped with a 163 mm focal length f-theta focusing lens achieving a 22 μm diameter spot on electrode surface. The electrode film was prepared in 3.0x3.5 mm size and held onto a vacuum chuck to remain flat and in tension without incurring defocusing issues. At the top plate of the fixture, where the electrode lies, a narrow groove was machined less than 5 mm in width. This groove allows material to escape from the cutting kerf, preventing it from reattaching at the back. The cut length was 10 mm. A clean ambient environment with constant temperature was provided for the experiments. No shielding gas was applied. The cutting was performed with suitable exhaust systems in a clean and dust-free environment.

2.2. Cutting parameters

The laser power ranges from 190 to 1140 W and the laser speed from 0.3 to 11 m/s. The different combinations of power and speed were chosen with the aim of evaluating the effect of irradiance and fluence. Irradiance I was determined as the ratio of laser power to the spot area, while fluence F was calculated as the product of Irradiance and the interaction time. The interaction time represents the duration for which the laser beam remains within a spot diameter of 22 μm (spot size) and it

Table 1
Parameters for anode and cathode continuous wave remote laser cutting (P, power; I, Irradiance and F, fluence).

	P (W)	I (MW/cm^2)	Speed (m/s)	F (J/cm^2)		P (W)	I (MW/cm^2)	Speed (m/s)	F (J/cm^2)
A1	190	50	1.83	600	D1	760	200	7.33	600
A2			1.10	1000	D2			4.40	1000
A3			0.73	1500	D3			2.93	1500
A4			0.55	2000	D4			2.20	2000
A5			0.44	2500	D5			1.76	2500
A6			0.37	3000	D6			1.47	3000
A7			0.31	3500	D7			1.26	3500
B1	380	100	3.67	600	E1	950	250	9.17	600
B2			2.20	1000	E2			5.50	1000
B3			1.47	1500	E3			3.67	1500
B4			1.10	2000	E4			2.75	2000
B5			0.88	2500	E5			2.20	2500
B6			0.73	3000	E6			1.83	3000
B7			0.63	3500	E7			1.57	3500
C1	570	150	5.50	600	F1	1140	300	11.00	600
C2			3.30	1000	F2			6.60	1000
C3			2.20	1500	F3			4.40	1500
C4			1.65	2000	F4			3.30	2000
C5			1.32	2500	F5			2.64	2500
C6			1.10	3000	F6			2.20	3000
C7			0.94	3500	F7			1.89	3500

is calculated as spot/speed. Six levels of irradiance and seven levels of fluence were chosen, with a range of 50–300 MW/cm^2 and 600–3500 J/cm^2 respectively. Detailed process parameters are summarized in Table 1.

2.3. Characterization of cut quality

Three main situations occurred for each electrode material: partial/no cut, presence of defects, good cut. To evaluate the cutting quality of each experiment, digital microscopy (DM, Keyence VHX-7000) and SEM-FEG microscopy were used. Defects were classified for each material as shown in Fig. 1. The defects considered on the anode were the HAZ width and max clearance/burr area. The defects considered on LFP cathode were the HAZ width, the quantity of spherical defects detached from the aluminum foil and the resulting diameter. Only the spherical droplets on the front side were counted.

More specifically, DM was used to provide a preliminary assessment of cut quality and measurements of HAZ width. The HAZ was measured manually as the distance from the cut edge to the color transition boundary of the unaffected area on both cathode and anode. To ensure consistency, measurements were conducted with the same lighting and imaging settings in the DM. For each sample three orthogonal measurements of the bottom-edge of each cut across each sample were taken and an average HAZ width was calculated, as shown in Fig. 1. Measuring HAZ width is crucial to minimizing thermal damage to the electrode, as excessive heating can degrade the active layer, affect electrochemical stability, and cause non-uniform current distribution, leading to increased internal resistance and reduced battery lifespan [10].

High-quality images for clearance quantification were carried out with SEM on the same surfaces for anode. One representative image was analysed for each cut. A high contrast was set (BSE channel) to identify the non-coated copper in white, as opposed to the black graphite. A MATLAB script was used to process multiple grayscale images to calculate and highlight white pixel areas. Each image was binarized using a threshold to distinguish white regions (set to 0.5) and then converted to microns based on a set scale factor. This led to an automated quantification of clearance area, which allowed for the calculation of the average clearance width.

The classification of spherical defects on cathode material was conducted based on the number of droplets on the bottom-edge of each cut, deposited on the LFP active material, as they detached from the Al-current collector, as shown in Fig. 1. The importance of such quantification method is because detached droplets (DDs) could create

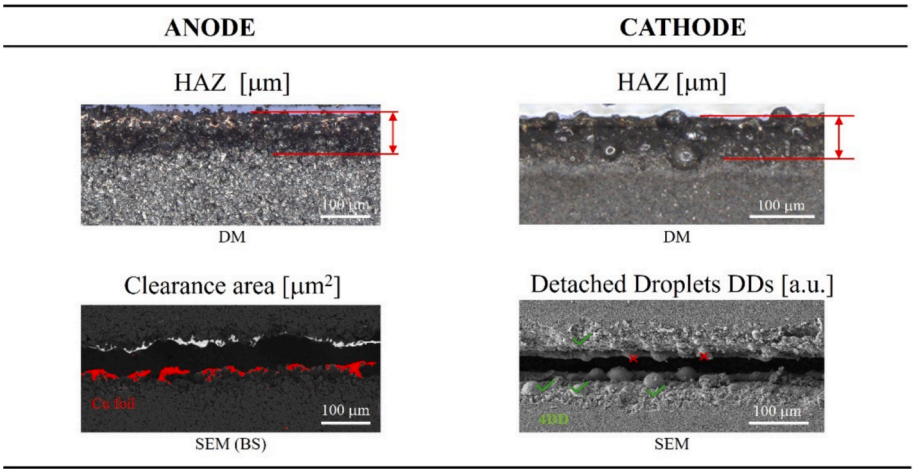

Fig. 1. Characterisation of defects created by CW laser cutting of graphite anode and LFP cathode. Digital Microscopy (DM) images show HAZ quantification for both electrodes; scanning electron microscope (SEM) images show clearance area for anode and detached droplets (DDs) for cathode.

Table 2
Classification of each cut performed with SM-CW laser cutting of graphite anode and LFP cathode. SEM images are categorised according to three classes of partial/not cut, good cut and the defect of anode and cathode, with respective parameter exposure.

Class	Partial/no cut	Good cut	Defects
Exemplary class image of anode	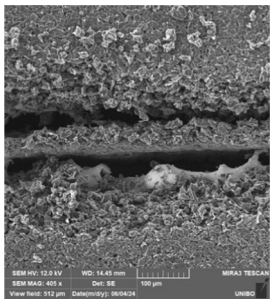	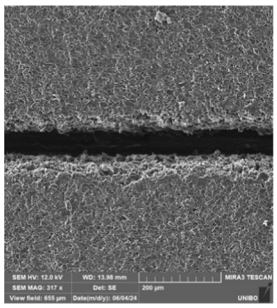	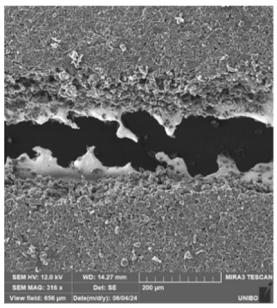
Parameters Description	A1 Full penetration is fragmented, with segment of graphite.	E3 Linear edges with full laser penetration.	A7 Presence of clearance, Cu-foil is exposed in the shape of jagged burrs.
Exemplary image of cathode	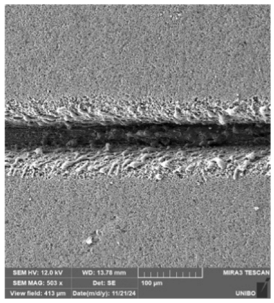	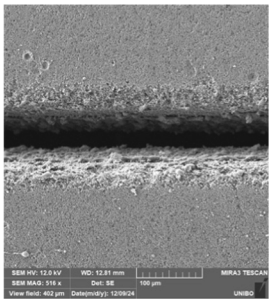	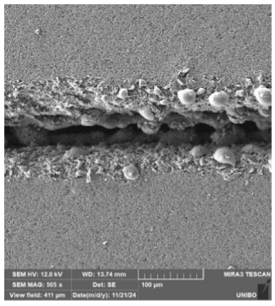
Parameters Description	D1 Only partial penetration across entire cut.	E2 Linear edges with full laser penetration.	C7 Formation of large spherical droplets, detached from Al-foil.

conductive bridges between the metal current collector and the active material, increasing the risk of internal short circuits. Additionally, oxidation and contamination of spatter may further degrade the electrochemical stability of the electrode [10,17]. The quantity of spherical defects on the cathode was calculated through four high-quality images obtained at the SEM, to assess the relevance of the formed droplets based on 3D vision and deeper understanding for droplet characterization. Some EDS analyses were also performed. To analyse the same point on each cut, each image was taken 3 mm from the beginning of the cut with x250 mag. Subsequently, three images with x500 mag were taken moving towards the opposite end of the cut. The size of DDs was taken from a single representative SEM picture of each cut. Overall, four images were acquired for each cut at the front for a total of 336 pics (considering 84 samples). Additionally, two images for the good cut and defects category were investigated at the back and at the section to assess the presence of a clearance width and DDs. Hence, 8 pics for anode and 8 pics for the cathode were added to the analysis. For a total of 352 SEM pictures.

3. Results

The images obtained from DM and SEM of each cut were divided into three categories: firstly partial/no cut, secondly good cut when edges were found smooth and absent of defects and lastly, the cuts that present a high threshold of defects, as shown in Table 2, for both anode and cathode. The following section will firstly analyse the graphite anode with respect to clearance and HAZ width, followed by the characterisation of the LFP cathode with respect to the formation of detached droplets and HAZ width.

Overall, 42 different sets of parameters were tested on each material. For preliminary considerations, Table 3 shows the quantity of performed cuts belonging to each category. It can be noted how the graphite anode exhibited 45 % more experiments that did not achieve full penetration. This is attributed to the higher melting point of Cu (1083 °C) compared to Al (661 °C) [18], along with its higher thermal conductivity, which reflects the relevance of the current collector. For the *good cut* category, four cut samples were selected for the cathode and only three for the anode, highlighting a more complex SM-CW laser cutting optimization for the latter.

3.1. Anode cutting

In this section, the cutting samples are evaluated in terms of fluence and irradiance to characterize the highest quality achievable and to analyse the influence of process parameters on the typical rising defects: HAZ and delamination width.

3.1.1. Clearance width

During laser cutting of anodes, delamination occurs at the cut edge. This phenomenon is primarily influenced by the differing thermal and optical properties of the anode's components. The copper foil, due to its lower absorptivity and higher thermal conductivity, exhibits higher ablation thresholds and lower material removal rates compared to graphite. The portion of absorbed energy exceeding the ablation threshold of copper is used for material removal, while the residual heat diffuses across the copper's surface due to its high thermal conductivity. Because of the lower ablation threshold of graphite, the residual heat can then be absorbed by graphite layers, resulting in their ablation creating clearance width. This phenomenon explanation is demonstrated by our experimental results: on the backside of good cut sample in Fig. 2 no copper foil is visible and only a small amount is observable on the front side due to direct interaction with the laser beam. No

Table 3
Total class assignment with respect to anode and cathode.

	Anode		Cathode	
	Total	**Parameters**	**Total**	**Parameters**
Partial/ no cut	9	A1, A2, B1, C1, D1, D2, D3, E1, F1	5	B1, C1, D1, E1, F1
Good cut	3	C4, E2, E3	4	D2, E2, E3, F2
Defects	30	A3-A7, B2-B7, C2, C3, C5-C7, D3-D7, E4-E7, F2-F7	33	A1-A7, B2-B7, C2-C7, D3-D7, E4-E7, F3-F7

degradation is caused by heat conduction, as observed instead in the "bad cut".

The *no-cut* conditions were found for each level of power at their maximum speed, which corresponds to a fluence of 600 J/cm^2. Increasing fluence up to 2000 J/cm^2 resulted in optimal cutting, with some samples exhibiting a delamination width under 25 µm. These results align with existing studies, such as Lee *et al.* [19] which demonstrate that higher speeds result in lower delamination width due to reduced energy absorption and shorter interaction times.

Minimum delamination widths of 17 µm (upper layer) and 8 µm (lower layer) were achieved at irradiance levels of 250 MW/cm^2 and fluence of 1000 J/cm^2. These values are comparable to those reported in other studies, as summarized in Table 4. Specifically, Lee *et al.* [14] have obtained the smallest clearance width of 25 µm with the highest speed of 5 m/s. This investigation therefore provides an improvement of 32 % on the clearance width with a 10 % increase in speed.

When high fluence and low irradiance (low speed and low power) are set, thermal effects exacerbate, increasing delamination width. When a threshold of F > 2000 J/cm^2 deterioration of edge consistency arises, and delamination width increases until the current collector forms *jagged burrs*, highlighted by the black bubbles at the top left in Fig. 3**a**. These observations corroborate findings from our previous study [16], which showed that when cutting bare foils with excessive energy input at low speeds causes significant melting, resulting in bubble-shaped recasts along the cut edge and poor kerf quality.

Conversely, high irradiance combined with high speeds minimized thermal diffusion but increase turbulence at the cut edge, contributing to spatter formation. This interaction causes molten copper to spatter upward, depositing onto the upper graphite layer, as evidenced by the spatter diameters ranging between 2–5 µm observed in SEM images in Fig. 2. Spatters were found exclusively in the cutting section.

Table 4
Anode Delamination width comparisons across literature.

Reference	Clearance width	Process Parameters	Set up
this paper	17 µm	950 W, 5.5 m/s	CW
[20]	40 µm	300 W, 0.25 m/s	CW
[14]	25 µm	450 W, 5 m/s	CW
[12]	27 µm	250 fs, 20 W, 0.050 m/s	PW
[5]	35 µm	10 ps, 32.4 W, 0.2 m/s, N = 10	PW-burst

3.1.2. *Heat-affected zone (HAZ)*

The size of visible color-changed zone can be easily measured by the DM. However, further examination with SEM revealed that color-changed zone is not a typical HAZ as material is not burnt, but rather crumbled. This suggests that a higher HAZ indicates partial damage to the ordered graphite structure due to excessive heat input.

HAZ size increased significantly with higher power and lower speeds. A threshold irradiance value of 150 MW/cm^2 was identified, beyond which HAZ sizes peaked, as shown in Fig. 3**d**. The lower layer consistently showed smaller HAZ sizes compared to the upper surface, likely due to reduced thermal exposure as the beam moved through the material.

The optimal process parameters for graphite anode cutting were identified within the range of I ≤ 150 MW/cm^2 and F ≤ 2000 J/cm^2. This parameter window achieved minimal defects, with delamination widths as low as 17 µm and HAZ sizes up to 30 µm. High speeds and moderate power settings were critical in minimizing thermal conduction and achieving fine cuts.

While ultrafast lasers achieve excellent quality, the results demonstrate that SM-CW lasers, when optimized, offer a cost-effective alternative with comparable quality at significantly higher processing speeds. Adjustments in beam focus and speed can mitigate spatter formation, particularly in multi-layer configurations where molten material interacts with adjacent layers.

3.2. *Cathode cutting*

This section analyses the cut samples of LFP cathode to determine the highest cut quality. This is achieved by characterising detached spherical droplets (DDs) and HAZ width in correlation with irradiance and fluence.

3.2.1. *Spherical defects*

The laser interaction with LFP cathode leads to the formation of spherical droplets on both the current collector and the active material

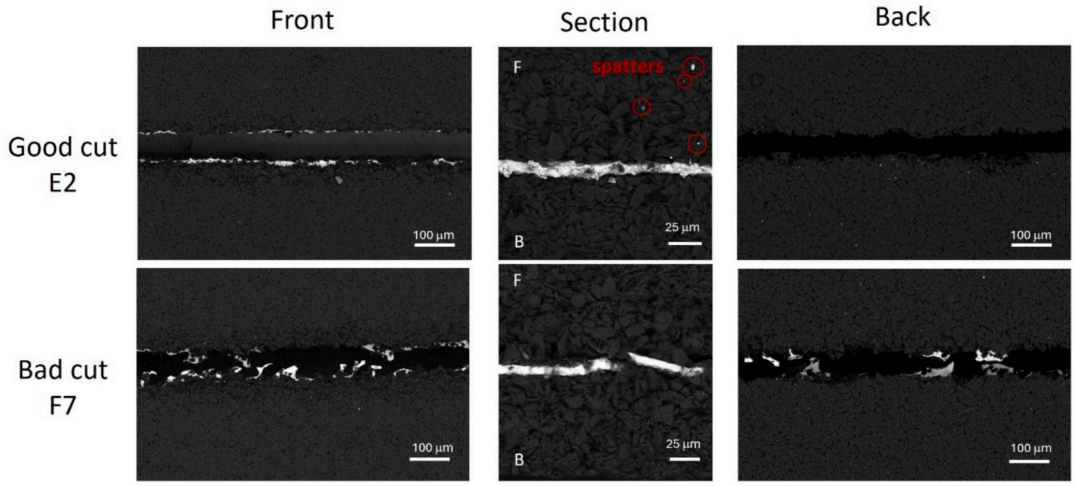

Fig. 2. Top, section and back SEM images of anode cut samples following exposure at 950 W – 5.5 m/s (Good cut) and 1140 W – 1.9 m/s (Bad cut). Spatters can be noticed in the upper layer of graphite (front F) in the good cut conditions.

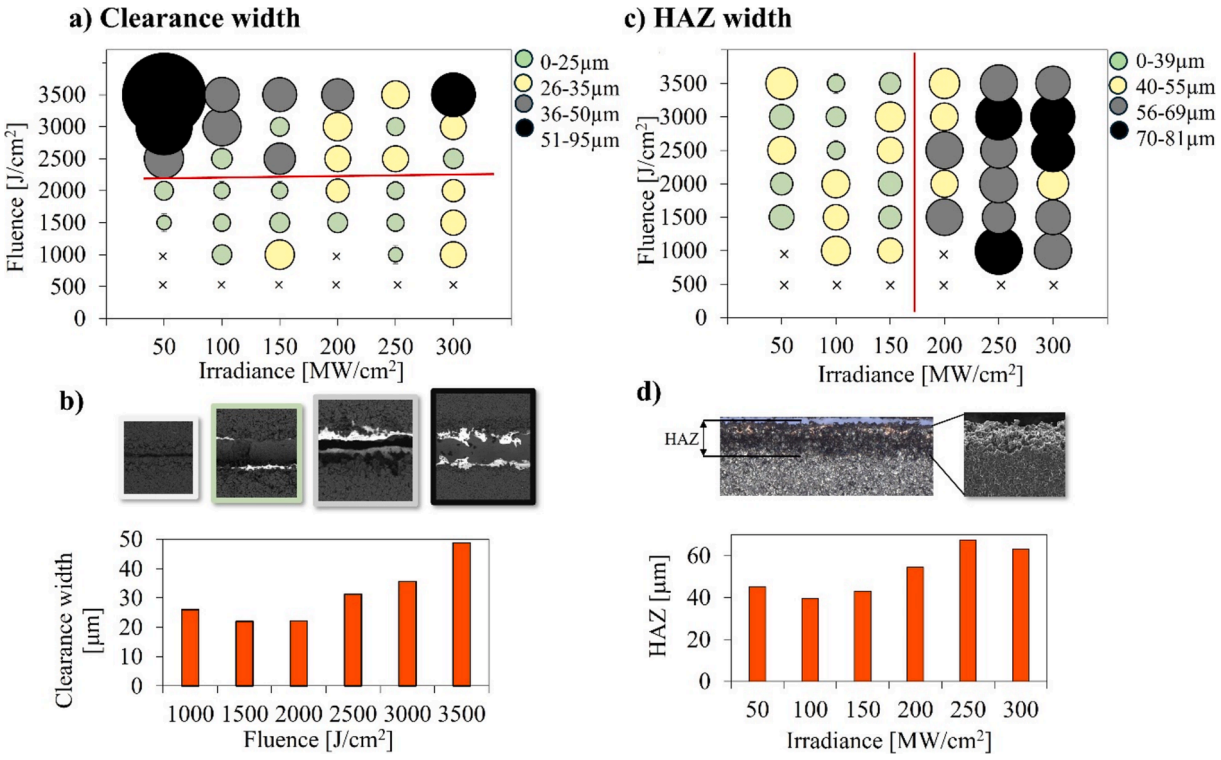

Fig. 3. a) Bubble graph of clearance width for anode cut samples. b) Correlation of clearance width with fluence. c) Bubble graph of HAZ width for anode cut samples d) Correlation of average HAZ width with irradiance.

coating. These droplets are hypothesized to follow a similar mechanism of formation to that of spatters, previously characterised by Angeloni *et al.* [16], with the significant difference of creating sphere shaped droplets of remelted material, detached from the current collectors. Such detached droplets (DDs) decrease cut quality and battery performance. The formation is attributed to the thermal conduction of heat across the electrode material. Specifically, by analysing the front, section and back of samples shown in Fig. 4, it is evident that heat is the main cause of DDs formation. In fact, it can be observed that the front-side of the cut presents a higher number of DDs compared to the back side. This is further confirmed by the section profiles shown in Fig. 4, where spatter formation leading to DDs is mostly present on the cathode interface that directly interacts with the laser source.

Though LFP is the most stable cathode material commercially used in LIBs production, the reaction with Al-current collector at very high temperatures and pressure, leads to the evaporation of some material, while a portion undergoes remelting in the shape of droplets. Energy dispersive spectroscopy (EDS) analyses were performed on the section profiles of cut samples, reported in Fig. 5, to qualitatively assess the composition of the remelted material in comparison to unaffected active material. Specifically, the SEM section view in Fig. 5a shows that the affected material exhibits lower carbon percentage and higher percentages of phosphorous and iron. This agrees with Raman analyses conducted by Lutey *et al.* [21], where they compared the structural changes on unaffected LFP with affected LFP in the form of spherical defects. Results showed a reduction or complete absence of carbon bands in the remelted spherical defects as well as a sharpening of the olivine peak (crystal structure of LFP). The affected material is therefore subject to remelting with fast recrystallisation, leading to lattice structure and composition changes in the remelt. EDS analyses also show that the remelted material is significant to the point of resolidifying over the cut portion of Al-foil, forming an inhomogeneous LFP layer, as shown in Fig. 5b where 88 % aluminium was detected across one of the cracks present in the remelt layer. In fact, it is hypothesized the remelted material over the Al-foil is prone to cracking because of fast recrystallisation, high cooling speed and very low thickness. These cracks can result

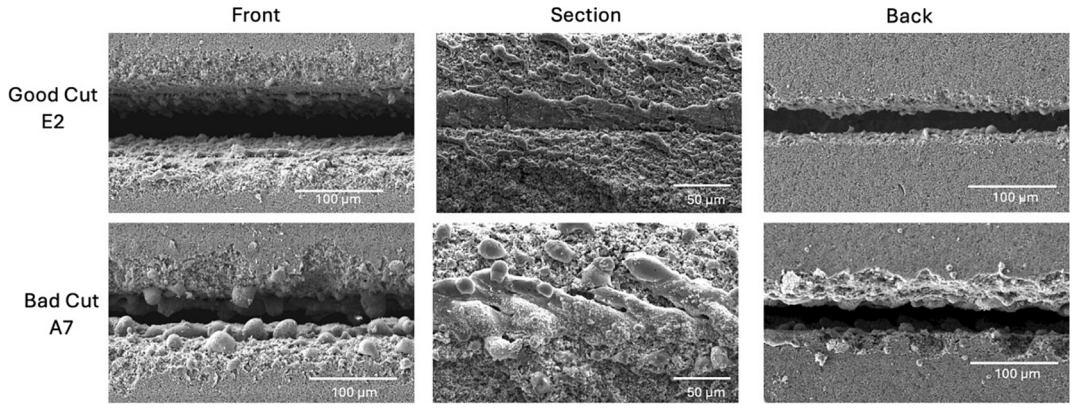

Fig. 4. Front, section and back SEM images of cathode cut samples, following exposure at 950 W- 5.50 m/s (good cut) and 190 W-0.31 m/s (bad cut).

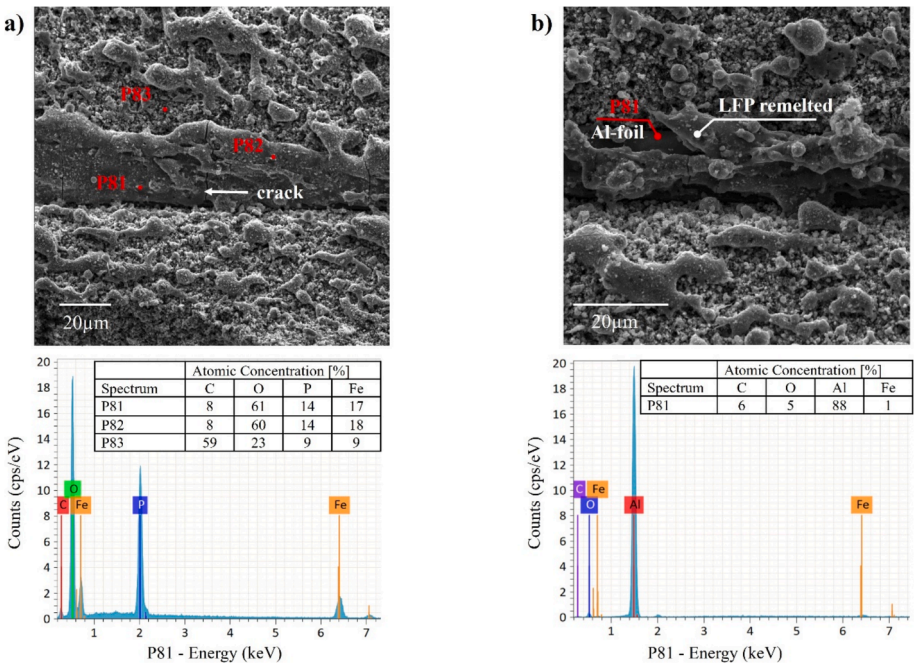

Fig. 5. EDS analysis of section profile of cut sample A7 showing a) remelted LFP layer and b) Al-foil underneath remelted active material.

in detachment of remelt-LFP leading to short circuits as well as decreased conductivity upon activation of the battery cell.

The numerical estimation of DDs created by SM-CW laser cutting on LFP cathode is shown in Fig. 6**a** where each colour represents a quantity in arbitrary units. DDs are counted from SEM images at x250 mag. The × symbol represents experiments classified as partial/no cut. In fact, the optimal cuts with one or no DDs were found between 1000 and 2000 J/cm^2, attributed to the lower energy transfer to both the active material and Al-foil, which limits the melting and subsequent solidification of the material. Specifically, *good cut* quality was found with parameters B2-B4, C1-C2, C4, D2, E2-E3, F2-F4 (Fig. 6**a**).

Being the first in the literature with a numerical estimation of spherical defects, no direct comparison with other laser sources is possible. However, the analysis reveals that the higher the fluence, the higher number of DDs are formed with a larger diameter on average, as shown in Fig. 6**b**. Specifically, minimum diameter sizes (in the range of 10.7 µm–16.4 µm) were found for high irradiances ranging between 200 to 300 MW/cm^2 and low fluences of 1000 to 1500 J/cm^2, with a minimum diameter of 10.7 µm for sample E2 (I = 250 MW/cm^2 and F = 1000 J/cm^2). This is in accordance with Baumann *et al.* study [22] who evaluated that higher scan velocities result in lower quantity of spatter. Conversely, the higher values of particle diameters (in the range of 27.9 µm – 35.1 µm) are found at low irradiances of 50–150 MW/cm^2 and high fluences of 3000 to 3500 J/cm^2, peaking at 35.1 µm for sample A7 (I =

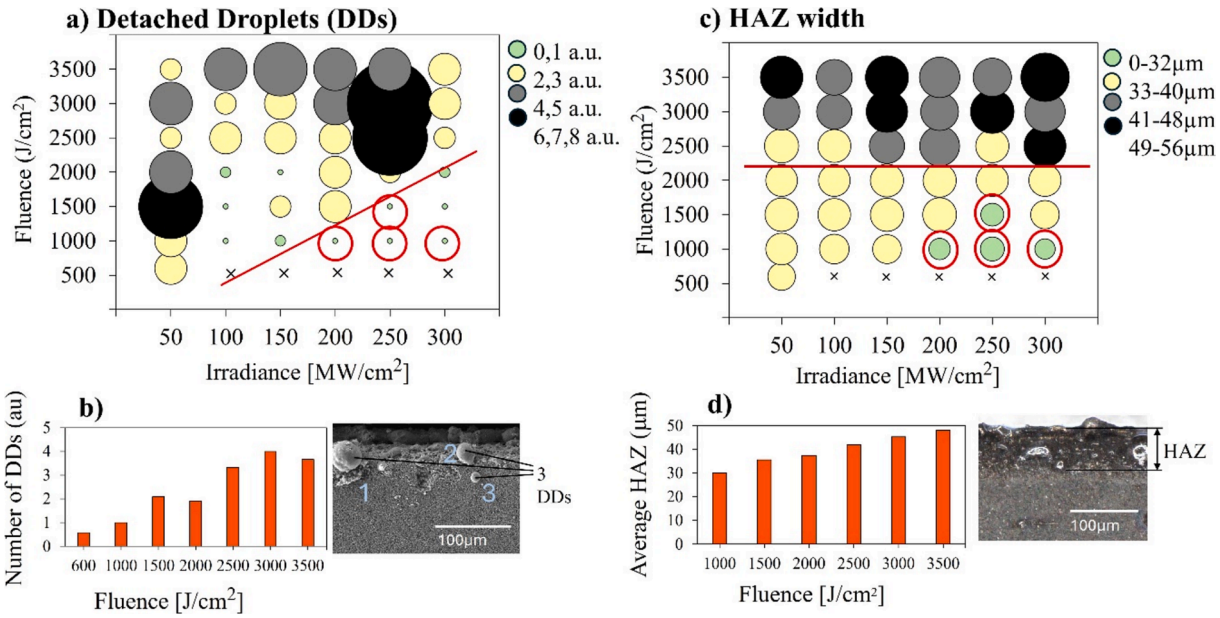

Fig. 6. a) Bubble graph of DDs for cathode cut samples. b) Correlation of DDs with fluence. c) Bubble graph of HAZ width for cathode cut samples d) Correlation of average HAZ width with fluence.

50 MW/cm^2 and F = 3500 J /cm^2). Therefore, the quantification of DDs revealed a direct relationship between number and size of DDs, where the formation of more DDs is associated with a larger diameter and vice versa.

3.2.2. Heat affected zone (HAZ)

The colour-changed zone or HAZ was easily measured from DM images. Thanks to SEM analysis, a similar crumbling phenomenon to that of the anode was also observed on cathode active material. The effect of irradiance and fluence on HAZ width on LFP cathode is shown in Fig. 6**c**, where each colour represents a width range of HAZ. The "×" symbol represents experiments classified as partial/no cut.

It can be observed from Fig. 6**d** that thermal degradation increases with fluence. The HAZ measurements in Fig. 6**c** confirm that interaction time is the dominant factor in quality deterioration, as the HAZ becomes excessively large for all irradiance levels at Fluences $\geq$ 2500 J/cm^{-2}. These results suggest that while irradiance variations showed negligible impact on HAZ growth, the process achieves optimal results at higher speeds, where shorter interaction times mitigate thermal damage.

The analysis showed that HAZ sizes are of medium size with respect to fluence up to 2000 J/cm, to then reach a *threshold* and exhibit a width of more than 40 μm width. The minimum HAZ width was 24 μm and it was achieved for irradiance level of 300 MW/cm^2 and fluence of 1000 J/cm^2. The optimal parameter window with respect to HAZ width is determined to be between 4.40 m/s at 760 W, 3.67–5.50 m/s at 950 W and 6.60 m/s at 1140 W, as highlighted by the red circles in Fig. 6**c**. Existing literature on LFP cathode found good quality at 250 W, 3.5–5 m/s with SM-CW laser [14]. In this study, good cut quality was determined for high speeds and power, with maximum speed of 6.60 m/s and 1140 W, with minimised defects including spherical defects and HAZ. Therefore, the use of SM-CW laser proves to be efficient at high speeds and power for LFP cutting, leading to an optimised production.

4. Conclusions

The analysis conducted in this study has proved significant quality enhancement when high-quality continuous wave laser beams are applied to cut commercial electrodes. For the graphite anodes, a minimum clearance width of 17 μm was found at 950 W and 5.5 m/s, significantly improving the current state-of-art by minimizing heat affected zones and material evaporation providing a 32 % improvement on the clearance width with a 10 % increase in speed. HAZ width on the graphite anode exhibited a strong relationship with irradiance, increasing with higher power and lower speeds due to greater heat accumulation. On the other hand, cathode HAZ width exhibited a linear correlation with fluence, with lower speeds causing more material crumbling. An experimental systematic method was successfully presented to estimate spherical droplet formation (DDs) on the cathode. The analysis of spherical droplets (DDs) detached from the current collector led to a new insight with respect to laser speed: DDs formation is promoted by low velocities and low power. Therefore, optimal cutting of the LFP cathode was achieved at high power and speeds above 5 m/s, with a maximum speed of 6.6 m/s representing a 32 % increase in processing efficiency compared to the current state-of-the-art, enabled by increased beam quality and higher power.

CRediT authorship contribution statement

Caterina Angeloni: Writing – original draft, Investigation, Data curation. **Carolina Magrini:** Writing – original draft, Investigation, Data curation. **Erica Liverani:** Writing – review & editing, Methodology, Data curation, Conceptualization. **Alessandro Fortunato:** Supervision, Resources.

Declaration of competing interest

The authors declare that they have no known competing financial interests or personal relationships that could have appeared to influence the work reported in this paper.

Acknowledgments

This research did not receive any specific grant from funding agencies in the public, commercial, or non-profit sectors.

Data availability

Data will be made available on request.

References

[1] M.G. Berhe, H.G. Oh, S.-K. Park, D. Lee, Laser cutting of silicon anode for lithium-ion batteries, J. Mater. Res. Technol. 16 (2022) 322–334, https://doi.org/10.1016/j.jmrt.2021.11.135.
[2] D. Lee, R. Patwa, H. Herfurth, J. Mazumder, Computational and experimental studies of laser cutting of the current collectors for lithium-ion batteries, J. Power Sources 210 (2012) 327–338, https://doi.org/10.1016/j.jpowsour.2012.03.030.
[3] J. Suk, D.Y. Kim, D.W. Kim, Y. Kang, Electrodeposited 3D porous silicon/copper films with excellent stability and high rate performance for lithium-ion batteries, J. Mater. Chem. A 2 (2014) 2478, https://doi.org/10.1039/c3ta14645f.
[4] P. Heidari Orojloo, A.G. Demir, Study of burst mode for enhancing the ps-laser cutting performance of lithium-ion battery electrodes, J. Laser Appl. 36 (2024) 042013, https://doi.org/10.2351/7.0001417.
[5] A.H.A. Lutey, A. Fortunato, S. Carmignato, M. Fiorini, High speed pulsed laser cutting of LiCoO 2 Li-ion battery electrodes, Opt. Laser Technol. 94 (2017) 90–96, https://doi.org/10.1016/j.optlastec.2017.03.022.
[6] A.H.A. Lutey, A. Fortunato, A. Ascari, S. Carmignato, C. Leone, Laser cutting of lithium iron phosphate battery electrodes: Characterization of process efficiency and quality, Opt. Laser Technol. 65 (2015) 164–174, https://doi.org/10.1016/j.optlastec.2014.07.023.
[7] M. Luetke, V. Franke, A. Techel, T. Himmer, U. Klotzbach, A. Wetzig, E. Beyer, A Comparative Study on Cutting Electrodes for Batteries with Lasers, Phys. Procedia 12 (2011) 286–291, https://doi.org/10.1016/j.phpro.2011.03.135.
[8] M.R. Kronthaler, F. Schloegl, J. Kurfer, R. Wiedenmann, M.F. Zaeh, G. Reinhart, Laser Cutting in the Production of Lithium Ion Cells, Phys. Procedia 39 (2012) 213–224, https://doi.org/10.1016/j.phpro.2012.10.032.
[9] J. Kriegler, T.M. Duy Nguyen, L. Tomcic, L. Hille, S. Grabmann, E.I. Jaimez-Farnham, M.F. Zaeh, Processing of lithium metal for the production of post-lithium-ion batteries using a pulsed nanosecond fiber laser, Results Mater. 15 (2022) 100305, https://doi.org/10.1016/j.rinma.2022.100305.
[10] X. Gu, X. Sun, Y. Han, Q. Li, J. Liu, X. Mei, Femtosecond laser cutting of LiFePO4 electrodes: Kerf geometry, process optimization, and electrochemical performance, J. Storage Mater. 101 (2024) 113859, https://doi.org/10.1016/j.est.2024.113859.
[11] T. Jansen, M.W. Kandula, D. Blass, S. Hartwig, W. Haselrieder, K. Dilger, Evaluation of the Separation Process for the Production of Electrode Sheets, Energ. Technol. 8 (2020) 1900519, https://doi.org/10.1002/ente.201900519.
[12] Y. Zhang, J. Li, R. Yang, T. Liu, Y. Yan, Analysis of kerf quality on ultrafast laser cutting of anode material for lithium-ion battery, Opt. Lasers Eng. 118 (2019) 14–21, https://doi.org/10.1016/j.optlaseng.2019.01.013.
[13] E. Audouarda, D. Pallarèsb, J.-M. Romanob, F. Mermet, M. Fleureaua, Characterization of batteries materials ablation by femtosecond pulses, (n.d.).
[14] D. Lee, R. Patwa, H. Herfurth, J. Mazumder, Parameter optimization for high speed remote laser cutting of electrodes for lithium-ion batteries, J. Laser Appl. 28 (2016) 022006, https://doi.org/10.2351/1.4942044.
[15] D. Lee, B. Oh, J. Suk, The Effect of Compactness on Laser Cutting of Cathode for Lithium-Ion Batteries Using Continuous Fiber Laser, Appl. Sci. 9 (2019) 205, https://doi.org/10.3390/app9010205.
[16] C. Angeloni, E. Liverani, A. Ascari, A. Fortunato, Characterization and process optimization of remote laser cutting of current collectors for battery electrode production, J. Mater. Process. Technol. 324 (2024) 118266, https://doi.org/10.1016/j.jmatprotec.2023.118266.
[17] T. Jansen, M. Kandula, S. Hartwig, L. Hoffmann, W. Haselrieder, K. Dilger, Influence of Laser-Generated Cutting Edges on the Electrical Performance of Large Lithium-Ion Pouch Cells, Batteries 5 (2019) 73, https://doi.org/10.3390/batteries5040073.
[18] C. Zhou, L. Jiang, Z. Gu, C. Wang, L. He, L. Huang, Z. Li, K. Li, Flexible core–shell structured Al-Cu alloy phase change materials for heat management, Chem. Eng. J. 471 (2023) 144610, https://doi.org/10.1016/j.cej.2023.144610.
[19] D. Lee, Investigation of Physical Phenomena and Cutting Efficiency for Laser Cutting on Anode for Li-Ion Batteries, Appl. Sci. 8 (2018) 266, https://doi.org/10.3390/app8020266.

[20] J. Kriegler, M. Binzer, M.F. Zaeh, Process strategies for laser cutting of electrodes in lithium-ion battery production, J. Laser Appl. 33 (2021) 012006, https://doi.org/10.2351/7.0000335.
[21] A.H.A. Lutey, M. Fiorini, A. Fortunato, A. Ascari, Chemical and microstructural transformations in lithium iron phosphate battery electrodes following pulsed laser exposure, Appl. Surf. Sci. 322 (2014) 85–94, https://doi.org/10.1016/j.apsusc.2014.10.069.
[22] R. Baumann, A.F. Lasagni, P. Herwig, A. Wetzig, C. Leyens, E. Beyer, Efficient separation of battery materials using remote laser cutting–high output performance, contour flexibility, and cutting edge quality, J. Laser Appl. 31 (2019) 022210, https://doi.org/10.2351/1.5096127.

Lasers in Manufacturing and Materials Processing (2024) 11:3–24
https://doi.org/10.1007/s40516-023-00216-7

RESEARCH

Laser welding in e-mobility: process characterization and monitoring

Caterina Angeloni[1] · Michele Francioso[1] · Erica Liverani[1] · Alessandro Ascari[1] · Alessandro Fortunato[1] · Luca Tomesani[1]

Accepted: 13 June 2023 / Published online: 15 July 2023

Abstract

The global automotive industry is shifting to e-mobility, where the main challenge is addressed to battery's mass-production. To keep up with the market demand, high speed production rates and quality products must be accomplished. Since laser welding of dissimilar thins sheets has earned rising demand for battery electrodes connections, a defect-free welding process has to be performed on behalf of a closed-loop monitoring system that updates corrective and/or preventive actions in order to obtain a reliable, "zero waste, zero stop" process. However, nowadays photodiode systems do not allow real-time modification of the parameters, they only tell, at the end of the process, if any signal has gone out of threshold. The objective of this paper is to find correlations between the data collected by the monitoring system with the typical process characteristics of laser welding. Materials investigated are pure copper 300 μm and aluminum 400 μm, processed by means of different sources, length tracks, wavelengths and scanning heads. In this contribution, a Precitec system has been implemented as a possible economical and industrial-oriented solution.

The experimental data was analyzed offline and the relationships between technological and signals outputs were evaluated by means of statistical analysis with MATLAB for both Al-Cu and Cu-Al configuration. Findings plotted stable signals if high speeds were set. Results further suggested the power to be the most influent variable for the closed-loop monitoring system and the dependance on the first material irradiated and the laser source used to define the threshold value for the control of the welding process.

Keywords Quality control · Photodiodes · Monitoring system · Laser welding · E-mobility

✉ Caterina Angeloni
caterina.angeloni2@unibo.it

[1] Department of Industrial Engineering (DIN), University of Bologna, Viale del Risorgimento 2, 40136 Bologna, Italy

Introduction

Nowadays it is well known that the future of Mobility is Electric, ranking first among the solutions in the automotive field to address the reduction of emissions into the environment. European Parliament states that by 2035, all new cars manufactured for the EU market should produce *zero-emissions*[1]. However, switching to electric mobility represents for many companies a fundamental revamp of production technology. The electrical energy storage system is the most critical feature since the battery is the most expensive and the heaviest component inside the electric vehicle. Many companies operating in this field are adopting lithium-ion batteries because of their advantages in terms of high energy density, making them easier and faster to charge and long-lasting. There are three battery geometries for automotive applications: cylindrical, prismatic and pouch. These geometries are assembled into modules which are put together into a battery pack. The number of modules and, consequently, batteries are chosen depending on the power/energy that must be supplied by the vehicle[2].The pouch cells that contain the battery are equipped with two contact tabs made of copper and aluminum for anode and cathode. When more cells are mounted in a battery pack, electrical connections are needed between these contact tabs in order to get a serial connection of the cells[3]. Welding processes are suitable to create such contacts characterized by high strength and low electrical resistance.

In this context, laser is becoming a fundamental tool thanks to its flexibility in terms of automation and control, therefore can be easily inserted into industrial production. In particular laser-welding is widespread thanks to its production speeds and accuracy, which are the highest in the entire panorama of technologies. Automated production itself calls for a high number of welds and a wide range of differences in terms of materials, thickness and welding units involved in the process.

Lap- or butt-joint welding of dissimilar highly reflective metals, such as aluminum and copper, has been widely investigated, as shown by Katayama et al.[4]. The latter discern thoroughly more than one-hundred papers on laser welding of thin metal sheets. It is therefore well known how to weld a proper seam in hybrid configurations. The challenge today is when it comes to high production rates and high demand of quality required by a zero-defect process. Industrial production speeds can reach up to 5–10 batteries/sec and the assembly of a single battery pack can contain up to 20,000 welds [5]. It is estimated that each Gigafactory produces 6% circa of defected cells and battery modules [6]. Since most of the materials (electrodes, cell separators, electrolytes) are not fully recyclable and the whole disposal process is pricy, the quality target of the process has been set to 99.7%[6]. This highlights the central role of a monitoring system that gathers information from the process, improving the understanding of the detecting phenomena. It uses the collected data to create quality control methods and adaptive, closed loop control of the process[7]. Hence, as the number of destructive samples inspections are minimized, the implementation of a monitoring system can be seen as a product certification.

A lot of studies of online quality control have been carried out aiming at reducing or eliminating product quality defects and process errors. Nowadays

monitoring systems range from simple systems using single sensors to more sophisticated systems which utilize a great deal of sensors and detection methods, as shown by Katayama et al.[8] and Cai et al.[9]. The latter reviewed three-hundred-ish papers describing the typical sensors used for laser welding and adaptive control: it ranges from photodiodes, visual sensor, spectrometer, acoustical sensor, pyrometer, plasma charge sensor to the application of artificial intelligence algorithms. It states that, to date, it is consolidated that the geometry of the melt pool exerts a major influence on the weld. That's why researchers are now assessing imaging as a tool in monitoring and predicting weld's quality. Moreover, machine learning (ML) models have been exploited since they are able to learn the error between the predicted value and the real value. Especially, deep learning is the present research highlight [9].

To date, a wide range of ML algorithms have been applied for the classification of selected defects. For example, Schimdt et al. [10] found that FRESH algorithm well classifies a spatter and a no spatter weld based on photodiode data gathered in-process. Lee et al. [11] demonstrated the feasibility and applicability of neural network classification to classify Al/Cu laser weld penetration as unsatisfactory, transient, or good in photodiode signals.

Blug et al. implemented a closed-loop system based on the observation of the penetration depth of keyhole welding processes on aluminum foils. A stochastic approach was implemented for the relation between laser power and the probability to detect full penetration hole. A CNN based system called Q-eye developed by Anafocus was used to execute the algorithms for the detection of the full penetration hole. The optics units were mounted to the coaxial process window of the welding head in order to create the thermal image in the spectral range of 820 to 980 nm. A 20 m cable connects the camera with the CNN control unit, which contains the interface to the laser control unit on the one hand and the PC on the other hand. The latter runs the control software which functions as the user interface. The results show that the standard deviation of the laser power was in the order of 2% [12].

Ascari et al. [13] proposed a method to ascertain the laser weld depth of battery connector tabs (Al e Cu thin foils) using *optical coherence tomography* (OCT) equipment. An adjustable ring mode (ARM) laser integrating OCT technology with two beams was exploited: one pointing at the bottom of the keyhole and the other one referring at the sample's surface. They used the "Keyhole Mapping" approach, which identifies the optimum positioning of the OCT measuring ray. Considerations on both the measurement's accuracy and the keyhole stability were made. It was demonstrated that ARM laser returns a more stable process as it reduced the fluctuations of the opening of the keyhole and it improved the measurement accuracy by the 50%.

Recently, part of the research focuses on the implementation of *deep learning* and *digital twin algorithms*. Good results were achieved by Franciosa et al. studies [14]. It presents a digital twin framework for assembly systems combining sensors with deep learning and CAE simulations. This study developed a closed-loop in-process control using a fully digital developed remote welding process for aluminum doors for e-mobility applications. It can identify the main causes of quality defects and suggest corrective actions for automatic defects mitigation.

The above studies are based mostly on deep-learning methods that can achieve only one prediction task. As laser welding is a complex phenomenon that is influenced by multiple parameters, multiple tasks have to be accomplished, as the work of Kim et al. shows [15]. Another study carried out by Franciosa et al. [16] developed a method for closed-loop in-process quality control in battery assembly lines. It is based on a holistic approach exploiting the potential use of *light-based technology*. The authors exploit both in and off-process methodologies to monitor the process: SEM scanning (off-process) to correlate grain structure with the material strength status, CT scanning (off-process), Optical measure (off-process) to evaluate weld penetration depth and weld interface width, Laser radiation (in-process) to measure weld depth penetration through OCT technology, thermal radiation (in-process) inspected with a IR camera. The closed-loop system is based on the development of a low fidelity artificial intelligence model, which identifies critical patterns in data flows that are then improved by implementing Multiphysics simulations.

Seibold et al. [17] realized a process control by real-time pulse shaping where the power is adjusted in each pulse. Al-Cu thin foils were welded, and it was found out that the steps of the welding process can be captured and recognized by using photodiodes with band-pass filters.

Currently, there is little research on effective closed-loop industrial solution that can be implemented in an industrial environment: most of the technologies cited previously involved an equipment that is complicated, bulky and pricy, making them suitable just for experimental studies. Only a simple and flexible monitoring system can cope with rapid product variety in terms of materials and geometries that can be processed.

In this direction, this paper considers a low-level system which includes photodiodes sensors PD (Laser Welding Monitor LWM 4.0). A *low-level* system is a *ready to use* industrial system: a PD can be defined as a commercial sensor that can perform direct measurements and be easily integrated into different setups and detect different wavelengths ranges. This kind of monitoring systems for mass production integrated in the production line nowadays do not allow a real-time modification of the process parameters, they only state, at the end of the process, if any signal values have gone out of range, which has been established previously during high-quality welding.

In literature it is described which parameters have the major influence on the process quality in laser welding but there is a consistent lack of information on the correlation between physical phenomena and sensor response. Big Consistently, the aim of this paper is to investigate the in-process signals measured by photodiodes and the level of correlation between the three signals in order to improve our understanding of the feedback they provide, both individually and together. To accomplish this, experimental tests on Cu and Al thin plate were performed by varying laser power, welding speed and the length of the trace while monitoring the signals of the three photodiodes. The experimental data was evaluated offline and analyzed to evaluate the relationships between technological and signals outputs.

Table 1 Physical properties of aluminum and copper [19]

	Copper	Aluminum
Density [g/cm^3]	8.9	2.71
Melting temperature [°C]	1083	660
Thermal conductivity [W/ (m ·K)]	390	226
Thermal expansion coefficient [°C^{-1}]	17 ·10^-6	24 ·10^-6
Specific heat capacity [J/ (kg K)]	385	880

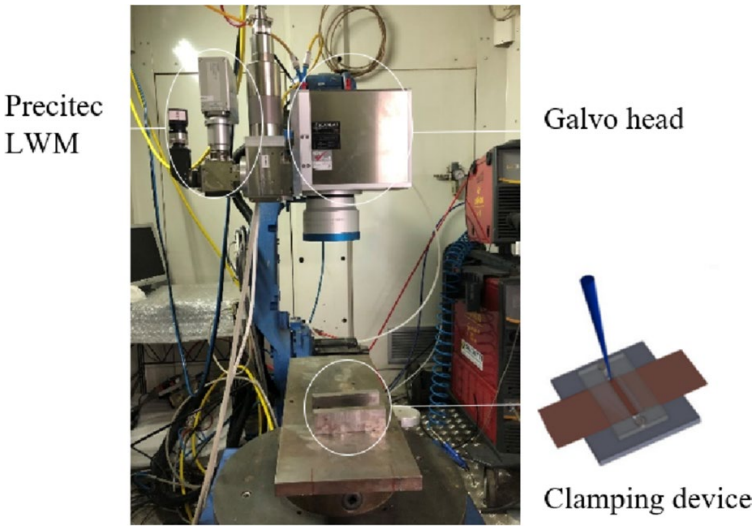

Fig. 1 Laser system set-up. Galvo head, Precitec monitoring system and clamping device position are highlight with white circles

Materials and Method

The welding experiments were carried out using pure copper (Cu > 99.6%, 0.3 mm thick), coated with a thin nickel layer in order to improve optical absorptivity of the laser radiation [18] and to avoid surface oxidation, and commercially pure aluminum AA1060 (99.4% Al, 0.25% Si e 0.35% Fe, 0.4 mm thick). The physical properties of both materials are shown in Table 1. Welds were performed on samples in a lap-joint configuration. For all the tested process parameters, both Al-Cu (aluminum on top) and Cu-Al (copper on top) configurations were examined in order to understand the importance of laser absorption and melt pool dynamics during re-solidification. For the purpose of keeping the adhesion between the two sheets during the process, a clamping device was used. As Fig. 1 shows, the clamp consists of two plates in which the two metal sheets are pressed together by means of two screws positioned at the two ends of the slot. The upper smaller plate consists of a slot which facilitates in accommodating the laser beam during laser welding and both ends of the same plate are screwed to the lower plate to hold the sheets together.

Methodology

Laser welding equipment and Optical Setup

Two near-infrared fiber laser sources were selected for the experiments. A single mode and a multimode laser source delivered by feeding fiber with core diameter respectively of 49 and 68 µm were used in a continuous (CW) mode for weld tests. The multimode source was a nLight Alta 3KW, while the single mode source was a nLight CFL-1200. The characteristics of both laser sources and optical systems are shown in Table 2. The motions of the laser beam to perform linear weldings were achieved by a galvo scanning head for both configurations to maximize the laser speed, while the initial displacement of each weld was carried out by (ROBOT Motoman HP-20 six axes). The Precitec monitoring system, fully described in the following 'Process Monitoring' section, was mounted on the scanning head, as Fig. 1 shows.

The full experimental campaign is described in Table 2. After defining a feasibility window, the effects of power and welding speed on the weld bead geometry were assessed. Only the first test was conducted with the multimode laser source, while the single mode laser source was implemented in the second and third trial. Each of the three tests includes nine weld beads and was repeated twice, for a total of 54 weldings for each configuration. If a signal value was found to be very far from repetition, a third test would have been carried out, which was then not necessary. The results reported in the Result section are the average of the two tests. All experiments were performed without shielding gas and without filler wire for reducing external influences on monitoring signals. In order to avoid surface contamination, samples' surface was cleaned before welding.

The two different F-Theta lenses installed in the galvo scan head lead to different spot dimensions. A 19% larger spot results from multimode laser configuration, therefore higher laser power and slower speeds are needed to get roughly the same energy density, defined as the product between power density and interaction time [J/cm3]. See Table 1.

Table 2 Multimode and Single mode Laser source properties

Laser source			**Optical Path**		
Specific	**Value**		**Specific**	**Value**	
	Multi mode	Single mode		Multi mode	Single mode
Beam's wavelength [nm]	1064	1064	Collimation length [mm]	120	120
Operative Method	CW	CW	Focal length galvo [mm]	163	420
Max Laser Power [W]	3000	1200	Fiber diameter [µm]	50	14
BPP [mm·mrad]	2	0.4	spot [µm]	68	49

In the third test, only the length of the linear weld track was increased from 48 to 100 mm to discern the influence the influence of weld-path on weld-bead geometry and measured signals. A comparison was then made with the previous tests.

At the end of the experimental campaign, the welds were sectioned in the middle of the bead and were prepared for metallurgical analysis by using standard criteria for sample preparation. Cross sections of the weld joints were mounted in resin and then polished with SiC paper grit from 800 to 2500 followed by 1 µm alumina suspension. The metallurgical specimens were etched with Keller's reagent (1 ml HF, 1.5 ml HCL, 2.5 ml HNO3 and 95 ml H2O) with an etching time of 20 s for preliminary observation**.** Micrographs and weld bead measurements were taken with a ZEISS Axio Vert.AlM for a visual correspondence of the results obtained.

Process monitoring

The Precitec monitoring system used (LWM 4.0; Precitec GmbH, Germany) assures non-destructive online control in real time. As Fig. 1 shows, the system is mounted on the camera flange located on the laser head. Hence, the internal optical path in the welding head is used, meaning that the sensors are always coaxially aligned to the welding spot and preserved from contamination. The system contains 3 photodiodes which detect the luminous intensity of three radiations emitted over three wavelength ranges. These detectors collect plasma signal (PS), temperature signal (TS) and back-reflection signal (BS) at a maximum sampling rate of 1 kHz.

- The plasma sensor documents the UV light (< 400 nm) and luminous radiation VIS (450 nm – 580 nm) from the plasma plume by recording and analyzing the amplitude. The plasma control variable itself indicates the amount of metal vapor ionized during the keyhole formation process [20].
- Back-reflection is that fraction of the laser beam which is not absorbed by the material and therefore emits at the same wavelength as the laser. The sensor record optical emission with wavelength within the following range:1020 nm – 1090 nm). It is consolidated that the BS is directly correlated with the keyhole geometry, thus providing information about the penetration depth [21].
- The temperature detector captures radiation in the near infrared NIR (1100 nm – 1800 nm) and gives information on the thermal condition of the irradiated surface. Hence, the TS enables the identification of lack of fusion.

Both hardware and software gains were set to clamp the signals in the range [0,10] V.

The system stores all the process signals in the SQL-Database, which is used to manage the Measurements and Configurations. The Control Module happens to be the core connection between the database, one or more View modules and possible external units connected by the customer. The View Module in the software guarantees a visualization of the processed signals. All the measurements were then selected and exported as.txt files, which were then given as an input for a short MATLAB script whose purpose was to graph the data and perform statistical

analyses. The statistical features extracted from each raw signal of a weld are the mean value (T_m, P_m, B_m) and the standard deviation (T_std, P_std, B_std). The average between the two repetitions is then stored in one datapoint. As a result, every point in the dataset, which is obtained with different combination of parameters, contains a six-tuple of signal features (T_m, P_m, B_m,. T_std, P_std, B_std). The standard deviation is proportional to the uncontrolled process changes, whereas the mean value is correlated with the amount of energy of the radiation emitted. The script was then readapted to all tests carried out in the experimental campaign, the results of which were then compared.

Results and Discussion

With the aim of developing better in-process monitoring, this paper focuses on finding correlations between the data detected by the monitoring system with the typical welding process characteristics.

Welding characterization

From a first rough analysis of the weld's micrographs, it is clear that the process parameters utilized result in a wide range of outcomes, from unsuccessful joining to full cutting of the specimen. A high-quality weld should not have variations in the weld profile and the weld penetration depth should be such as to ensure the connection without leading to overpenetration: excessive weld penetration depth raises the possibility of damaging nearby components (such as electrodes), leading to future gas leaks that might cause a thermal runway.

The micrographs reported in Fig. 2 point out the different characteristics of the weld bead morphology of Al-Cu and Cu-Al configurations when a

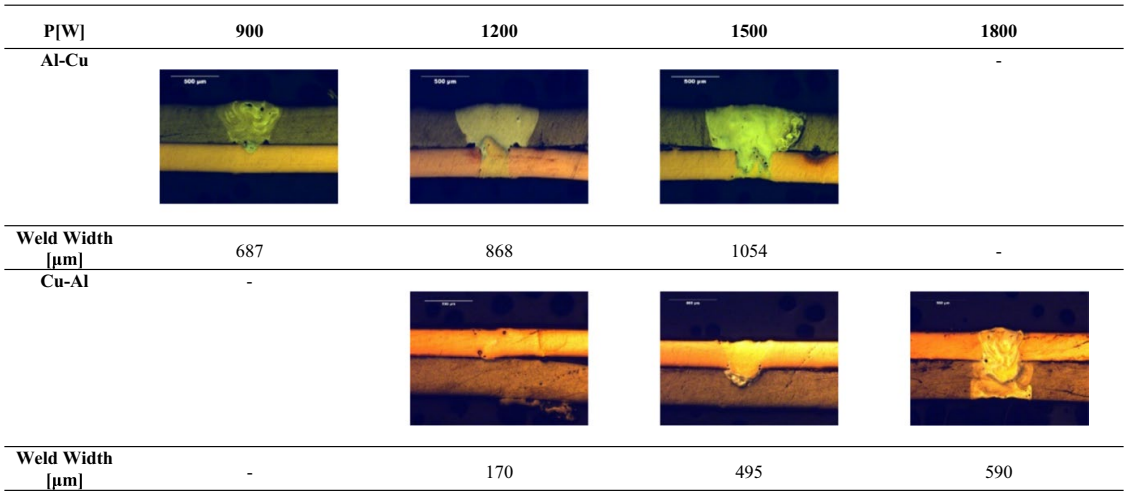

Fig. 2 Corresponding micrographs and weld bead width taken at the middle of trace when the *multimode* source is exploited at 200 mm/s speed

multimode source is exploited. The following considerations are valid for single source tests also. When the laser beam interacts with aluminum first, its weld bead tends to be larger at the top and narrower at the bottom. While if the first interaction is with the copper, the situation is the opposite. The Table 3 showing the weld dimensions performed with various parameters illustrates the previously mentioned trend. This behavior is due to the different physical properties of the two metals involved in the process, in terms of heat conduction coefficient and melting temperature (see Table 1). When the aluminum is at the top side, the laser beam melts, at first, the material that has the lower temperature melting point and then the copper that is situated at the interface between the two sheets. Copper has a much higher melting point and a higher thermal conductivity than aluminum, that's why it melts to a much lower extent.

When copper is at the top side, heat is transferred very quickly at the interface with aluminum which, because of the lower melting temperature, melts abruptly and, if the energy is excessive, tends to favor a complete penetration of the specimen [19].

From Table 4 it can be stated that it is generally true that the multimode weld lengths are larger than the single mode ones. As the power is raised, the width of the weld likewise grows.

The higher thermal conductivity and melting point of copper, together with the larger spot size, have resulted in the need for higher specific energies to melt the copper layer: a complete penetration of the weld is reached at 1800W when a multimode source is used, while 1000 W for the single mode.

From the observation of the sample morphology of both configurations, two opposed types of defects are emphasized when the maximum and lowest energy densities are applied. Figure 3 shows that if the material receives either too much or too little energy, there are two possible defects. In the first case, the excessive energy leads the melt pool of the keyhole to be unstable and to have tumultuous motions with the formation of bubbles and intermetallics which make the joint brittle. In contrast, the joint is not formed if the material does not absorb enough energy.

Table 3 Process parameters investigated

			Power [W]	**Speed [mm/s]**	**Weld length [mm]**
Multi mode	Test 1	Al-Cu	900–1200-1500	100–200-300	48
		Cu-Al	1200–1500-1800	100–200-300	48
Single mode	Test 2	Al-Cu	800–1000-1200	120–240-360–480	48
		Cu-Al	800–1000-1200	200–300-400–500	48
	Test 3	Al-Cu	800–1000-1200	120–240-360–480	100
		Cu-Al	800–1000-1200	200–300-400–500	100

Table 4 Multimode and single mode weld length

MULTIMODE									
Al—Cu	P[W]				**Cu—Al**	P[W]			
	900	1200	1500	200 [mm/s]		1200	1500	1800	200 [mm/s]
Weld length [µm]	685	870	990		Weld length [µm]	170	595	500	
Interface length [µm]	180	315	470		Interface length [µm]	145	330	415	
Depth penetration [µm]	85	300	300		Depth penetration [µm]	25	50	400	
Aspect ratio [µm]	0,12	0,35	0,30		Aspect ratio [µm]	0,15	0,08	0,80	
SINGLE MODE									
Al—Cu	P[W]				**Cu—Al**	P[W]			
	800	1000	1200	240 [mm/s]		800	1000	1200	200 [mm/s]
Weld length [µm]	700	670	595		Weld length [µm]	315	420	320	
Interface length [µm]	220	300	190		Interface length [µm]	0	250	260	
Depth penetration [µm]	145	300	300		Depth penetration [µm]	0	300	300	
Aspect ratio [µm]	0,21	0,45	0,51		Aspect ratio [µm]	0,00	0,71	0,93	

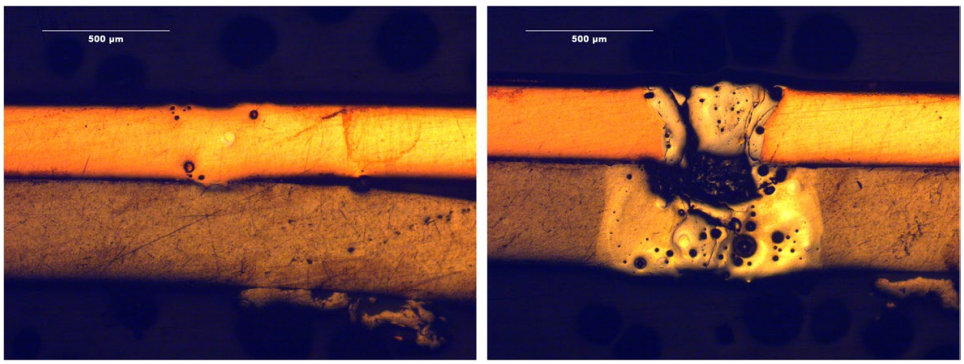

Fig. 3 Cross sections of Cu-Al samples when the lowest and excessive energy density is applied

Plasma and Temperature

In the first place, the welds performed with the multimode fiber source were initially analyzed and the results of test 1 were compared with each other. Al-Cu configuration was analyzed in the first place. PS and TS monitored during the laser welding process are reported in Fig. 4. If speed is fixed (v = 100 mm/s), there is a linear correspondence between the two signals and power: if power steps up from 900W (blue line) to 1500W (yellow line), PS and TS increase also. It can be noticed that the trend of PS along the trace over time mirrors that of the temperature: a

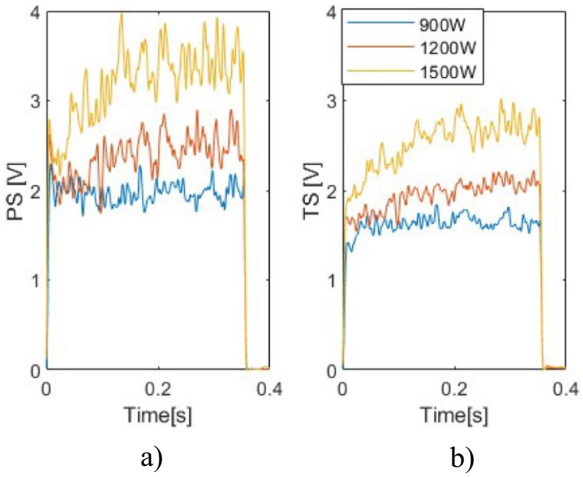

Fig. 4 **A**)Plasma and **b**) Temperature vs time as power ranges from 900 to 1500W for fixed velocity of 100 mm/s. Current data refers to Al-Cu configuration

progressively increasing value can be noticed, which gets steeper as the laser power applied grows. For example, the increase of PS along the trace changes from 3.24% for lower power to 28% for 1500W.

This similarity between the two signals can be related to the fact that the temperature measured on the surface directly affects aluminum's vaporization and its alloy elements leading to the opening or closing of the keyhole. This observation agrees with the findings of Franciosa [6] and Eriksson et al. [22] who state that temperature and plasma signals are strongly correlated with Pearson's correlation coefficient above 94%. This suggests that the plasma plume emits not only in the UV/visible spectrum but also contributes to thermal radiation in the IR, it is therefore necessary to remove the PS from the TS.

The graph in Fig. 5 describes the effect of *speed* on the process: within the process parameters window analyzed, the trend of the signals becomes more stable (less oscillating) for high-speed values up to assuming an almost constant trend (like for v = 300 mm/s). This effect is more evident for higher power (1500W), as it is highlighted in Fig. 5 by the yellow squares. From a process point of view, this data behavior could be explained as follows: for low speeds, during the laser-aluminum interaction, the component increases its temperature moment by moment since not all the heat can be dissipated by conduction. Therefore, it is logical to think that, by heating continuously, the characteristics

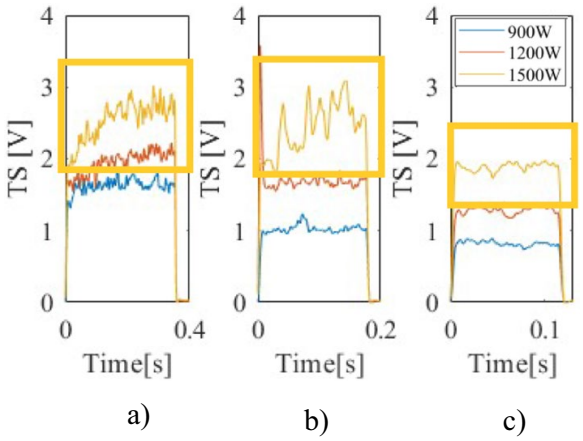

Fig. 5 Influence of speed on the welding process in test 1: for higher values of speed which ranges from **a**) 100 mm/s **b**) 200 mm/s to **c**) 300 mm/s, the standard deviation of the signal decreases

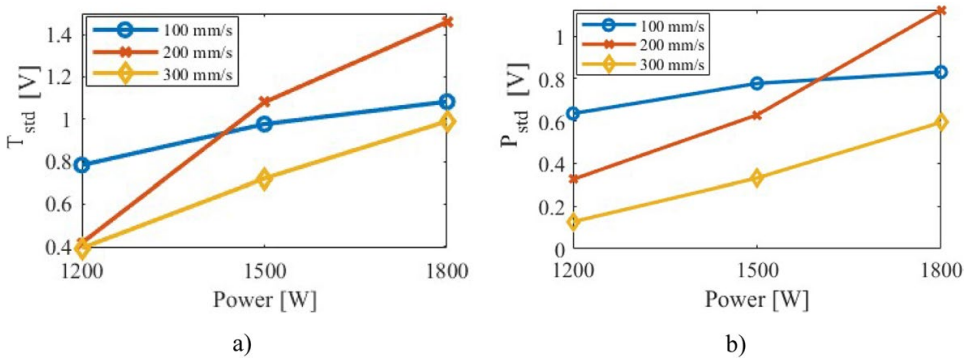

Fig. 6 **A**) Temperature and **b**) Plasma signals standard deviation for test 1 Cu-Al. As laser power increases and speed is diminished, an increasing trend can be noticed, leading to keyhole instability

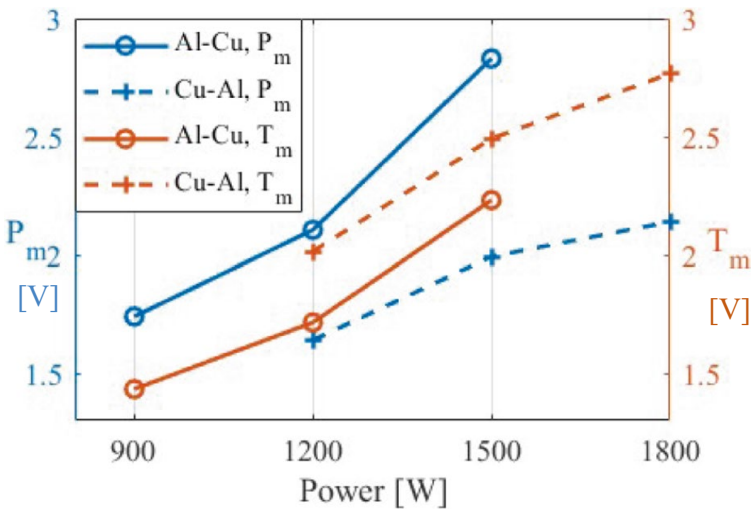

Fig. 7 Mean values of PS [V] when a multimode source is exploited and speed is fixed at 200 mm/s for both Al-Cu and Cu-Al configurations

of the joint vary from the beginning to the end of the weld bead. This problem of heat accumulation during welding is emphasized for low speeds that lead to a longer interaction time and the amount of heat absorbed by the material increases with it. In the graphs in Fig. 5 this behavior is very evident: as the speed increases from 100 mm/s (a) to 300 mm/s (c) the signals are much less oscillating and more centered on the average value, which, presumably, is equivalent to a more homogeneous, sound weld bead along the track. To sum up, BS and TS standard deviation (T_{std},P_{std}) increases as laser power increases and decreases for higher speeds, which comes to a higher energy density on the material. This feature is found to be more relevant for the Cu-Al configuration, hence the Fig. 6 is reported. This means that the more energy density is applied, the more the signal oscillates, hence the more unstable the keyhole gets. As previously anticipated, the mean value and the standard deviation of PS and TS were calculated for every test over the entire measurement signal of the weld.

The increasing linear relationship is consistent not only for T_{std} and P_{std}, but also for PS. The average between the two repetitions gives the final values P_ m and T_ m. The resulting values are plotted in Fig. 7 when a multimode laser source was exploited. Both Al-Cu and Cu-Al configuration values are reported.

There is clear evidence of a linear relationship between power and monitoring signals. A similar trend was identified also for weld-bead width. Overpenetration is esteemed from 1200 W, thus a mean value of PS and TS should stay below 2 V, according to Fig. 7. The same graph has been made for the single mode, but P_m and T_m values are so small (under 1 V) that is hard to state which is the optimal value for a good-quality weld.

Another thing that can be noticed is that the average amount of metallic vapor produced during the interaction between the laser beam and the aluminum is way higher than that found for welding the copper first: in Fig. 7 Al-Cu P_m curve assumes plasma values ranging in an interval that is higher than the Cu-Al P_m. This happens because aluminum has a lower phase transition temperature than copper and therefore vaporizes before. The width variation can then be monitored by the signal values of either plasma or thermal radiation during welding.

It is consequently confirmed that the control of the laser power based on thermal radiation values can minimize the variation in the bead width.

In the section "welding characterization", the defective joints obtained for high and low energy densities were observed. When the materials absorb more energy, the photodiodes recorded a higher radiation intensity for signals TS, PS and a lower intensity for BS, as expected. By looking at the average values of the three signals acquired for three different energy values (maximum, minimum, and optimal), we are able to determine an ideal working window. Large energy density Es in the TS and PS signals exhibit a greater standard deviation, which denotes weaker weldability stability. (Fig. 8).

These results for the single mode tests were not as straightforward, this is why results are not reported.

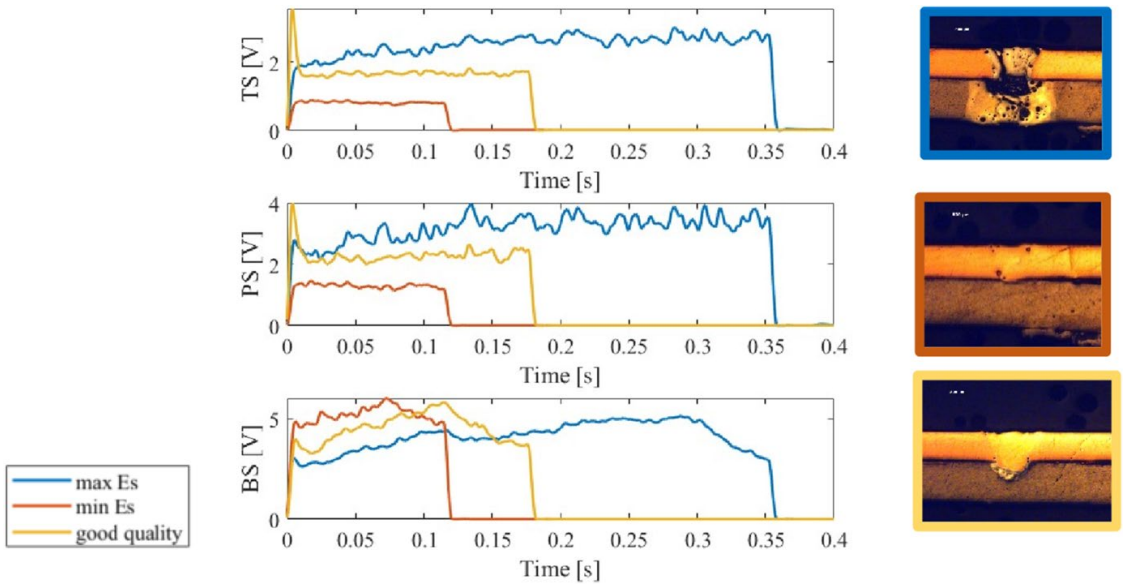

Fig. 8 Weld defects when either too much **a**) or too less **b**) energy is absorbed by the materials. Micrographs of Cu-Al configuration when a multimode laser source is exploited at max Es calculated at 1200 W 100 mm/s and min Es calculated at 1200 W and 200 mm/s

Back-Reflection

In the following paragraph BS is analyzed in test 1 Al-Cu. A comparison is then made with the data obtained in test 3 to comment the influence of the welding length. For tests 2 and 3 similar results were obtained, therefore the discussion can be extended for all Al-Cu tests. For the Cu-Al configuration such a marked trend was not evident: as the power and speed change, the signals mean values were almost steady, as Fig. 9 states. In general, it is well known that material absorptivity decreases with an increase in the welding speed [4]. As the welding speed increases, the molten pool becomes smaller, and the melt zone in front of the keyhole is also narrower (or thinner). That is, at higher welding speeds, a part of the laser beam is irradiated on the thin melt zone and solid metal surface; consequently, the laser back reflection increases, and the ratio of a laser beam absorbed into the keyhole decreases. The histogram in Fig. 9 testimony the latter consideration: increasing speed, the back reflection signal increases.

The BS itself is characterized by a fast peak near the central area followed by a fast drop, decreasing towards the end of the track. The bell-shaped pattern is probably due to the fact that the sensor, remaining integral with the laser head during the whole welding process (as a galvo head is expected to work), is able to collect all the radiations only in the configuration in which the laser head is positioned at the center of the trace and the beam is perpendicular to the surface. In all other welding positions, the inclination of the laser beam towards the surface increases and makes a good percentage of the light radiation going out from the sensor's reading range. For this reason, to make comparison analysis, the maximum value is considered, which is the peak point of the hilly trend. In support of this assumption, test 3 was carried out, where only the length of the track was changed. It was found that the bell-shaped trend is more marked: the sensor will receive very weak light radiation from the points furthest from the center of the weld bead because of the greater inclination. By making the weld bead longer, the surface temperature of the aluminum and the plasma detected decreases, if compared with the previous tests. (Fig. 10).

Looking at test 1, a comparison between BS collected during Al-Cu and Cu-Al configuration was carried out. It is clear that BS on copper is always greater because

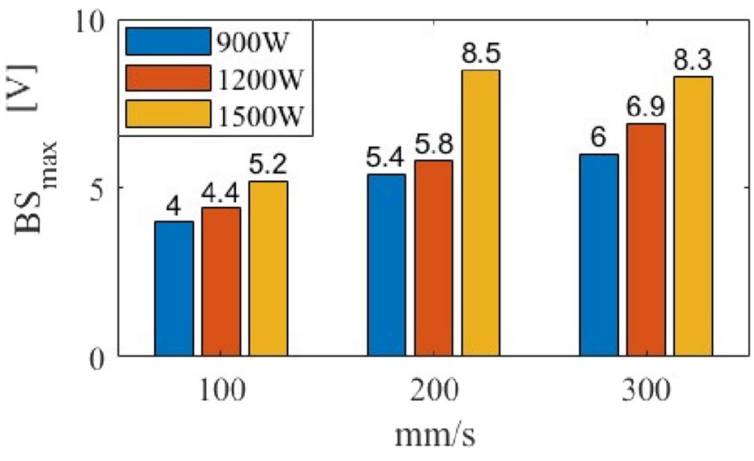

Fig. 9 Peak values of the Back reflection-time signal at varying power and laser speed for test 1 Al-Cu. It can be noticed that as the speed increases also BS increases as a smaller amount of laser beam is absorbed because of the narrower weld bead formed

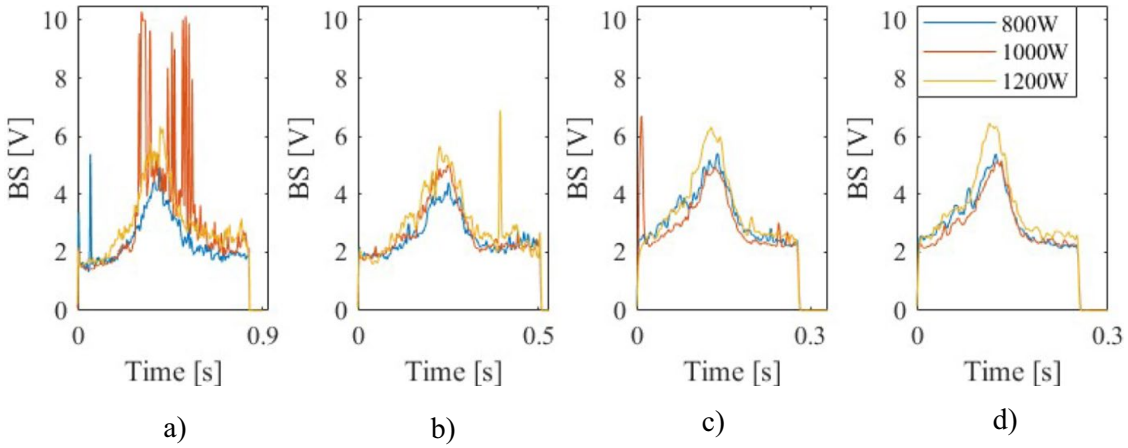

Fig. 10 Hilly trend of the BS-time at varying power and speed that ranges from a) 120 mm/s to d) 480 mm/s (on the right) for test 3. The bell-shaped trend in longer weld beads is more marked: the sensor will receive very weak light radiation from the points furthest from the center of the weld bead because of the greater inclination of the laser beam

it has a lower absorption coefficient than aluminum. Table 5. shows the percentage increase in the back reflection value B_m between the Al-Cu and Cu-Al configuration. B_m is the average between the two repetitions performed for test 1. The percentage increase formula that has been used is the following: (new value – old value) / old value *100%, where the new and old value refer, respectively, to B_m calculated for Cu-Al and Al-Cu configuration. Comparisons between all speeds (100 mm/s, 200 mm/s, 300 mm/s) and powers (900 W, 1200 W, 1500 W) parameters tested are also reported.

Table 5. Percentage increase values from Al-Cu to Cu-Al configuration in the operating window considered

	Speed [mm/s] →		
Power [W] ↓			
	106%	165%	170%
	65%	154%	133%
	133%	82%	96%

Statistical Analysis

In order to hold together the results from the whole experimental campaign, the spot dimension has to be taken into account as single and multimode sources were exploited. For every set of parameters, the mean value and the standard deviation were calculated for each weld bead and plotted against energy density.

As Fig. 12 states, TS can be modelled with a linear regression with good accuracy. In fact, the statistical analysis obtained with MATLAB shows a very low p-value

and an R^2 very close to unity ($R^2 = 90\%$), suggesting that the linear model used for temperature variable interpolates the data very well. However, this correlation is not true for back reflection and plasma variables, whose intensity depends on the laser source exploited for the experiment, as Fig. 13 and 14 point out. Hence, two different models must be implemented to describe the welding process carried out with two different sources. In order to monitor the stability of the process, the standard deviation of plasma (PS_{std}), temperature (TS_{std}) and back-reflection (B_{std}) versus Energy density Es were plotted. In this account, some considerations were raised: the TS_{std} graph in Fig. 11 a) shows clearly three patterns for both multi and single mode sources. These linear patterns were analyzed, especially for the multimode tests where it was more evident that the separate trends, with three points each, were characterized by equal speed. The histogram in Fig. 11 b) shows how the TS_{std}, which is directly correlated to process stability, depends more on power than speed: keeping the process at a constant speed, it becomes more instable as the power increases, and not vice versa. Consequently, it is possible to suggest changing the *power* as the variable input in the closed-loop system if any signal exceeds the threshold.

The same studies were made on Cu-Al configurations and the same results were observed.

Conclusions

This study clearly demonstrated that signal monitoring and control must be customized and readapted according to the spot of the laser beam and the material irradiated. Like the average amount of metal vapor produced during the interaction between the laser beam and *aluminum* is much higher than that detected for *copper* welding because aluminum has lower phase transition temperatures than copper and therefore vaporizes first. However, some considerations apply for all tests: power has

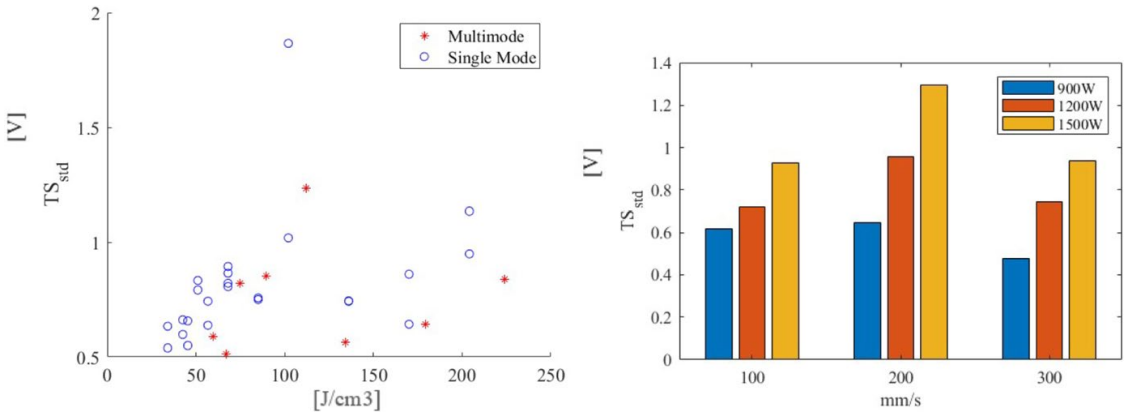

Fig. 11 A) TS_{std} against energy density Es for single and multimode sources. Three linear trends can be noticed with three scatter points each in every of which the speed is kept constant and the Power is increased. This consideration is validated by the histography in b) where for every speed, for an increased value of power, the process becomes more instable (standard deviation values increase)

proven to be the most influential parameter in every configuration of parameters, it could be then used as the feedback system's control variable. To sum up, the following results were obtained:

- The plasma trend mirrors that of the temperature: the temperature directly influences the vaporization of the aluminum and its alloying elements leading to the opening or closing of the keyhole. This suggests that the plasma plume emits not only in the UV/visible spectrum but also contributes to thermal radiation in the IR.
- There is an increasing linear relationship between plasma and power for the multimode source tests, a constant trend for the single mode ones. Observing the micrographs, the variation of the weld seam's width seems to follow the same tendency varying the power with the other parameters in play being equal.
- With the same power density as E_s the plasma values obtained in the multimode tests are greater than those obtained for the single mode tests for the Al-Cu configuration. This increased value is probably due to the greater width of the bead (the sensor detects more radiation).
- Within the window of process parameters analyzed, if high speeds were set, the trend of the signals stabilizes (less oscillating) until it assumes an almost constant trend. Hence, the standard deviation of the signal disclosed an explicit correlation with the stability of the process. This consideration is valid within the considered operative window. It is possible that the signal turns to be unstable if the speed is increased more.
- The back-reflection varies with a bell-shaped trend: the sensor is able to detect all radiations only in the configuration in which the laser head is located in the center of the trace and the light beam is perpendicular to the surface. In all other positions, a good percentage of the light radiation goes out of the reading range of the sensor. This behavior only affects the signals but not the weld quality itself.
- Windows of good weldability can be identified by comparing the cross-section's quality with the related signals.

Future work

Based on these observations, future technological implementations might follow:

It is conceptually possible to exploit plasma as an input to regulate the power with feedback control to keep the temperatures constant during the process.
If the consideration that was made on the back-reflection signal is true, it therefore makes this signal of little use for the analysis of the single trace but can only be evaluated in a comparative way with a pre-acquired signal on a bead, whose properties are considered acceptable.
The takeaway from the comparison between Al-Cu and Cu-Al configurations is that any threshold value for the bead control strictly depends on the first material irradiated.

During the analysis of the dataset, the width of the bead emerged to be a relevant parameter for the control of the opening/closing of the keyhole. This observation led us to consider the implementation of a camera system on the laser head capable of measuring the variations in shape and size of the keyhole as a possible evolution of this research. In this way, the correlation between the data detected by the sensors and the welding behavior observed by the high-speed imaging shall provide greater precision in welding control, guaranteeing the required quality. It is essential to have a larger dataset available in order to apply Machine Learning and Artificial Intelligence techniques to be able to link the behavior of one or more sensors and match it to a specific real defect and ultimately, prevent it through feedback control. That is to say, humanizing the whole laser welding monitoring process (acquiring signals, analyze them and making monitoring targets) [9].

Appendix

Al – Cu

The following Figure shows the output of the linear regression returned by Matlab with the corresponding R^2 and p-value. The p-value of the variable Es is very low 4.59e-17, which means that it is statistically significant in the model.

The R^2 is equal to 90%. It can therefore be stated that the linear model applied interpolates the data well. The linear regression model is the following: $T_m = -0.022436 + 0.0086192$ Es.

This graph highlights that for higher Es values the average temperature values are more spread out than those for low energy densities.

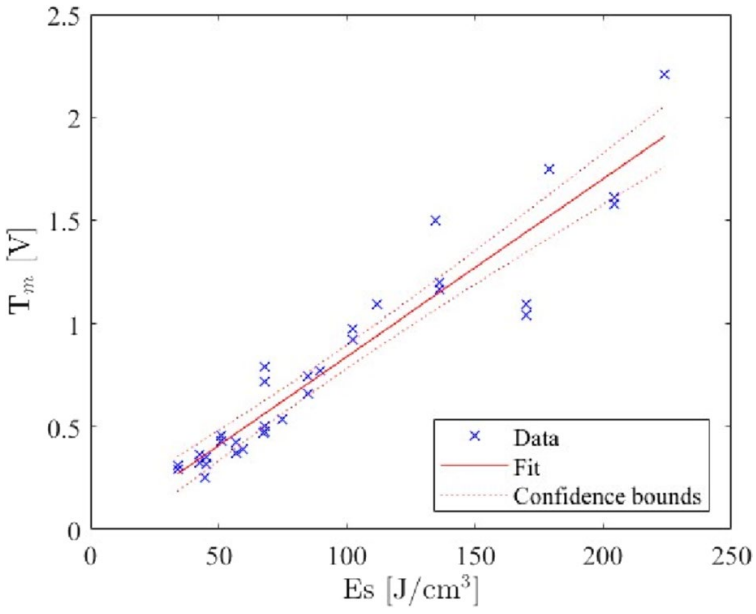

Fig. 12 Linear regression for TS Al-Cu with a $R^2 = 90\%$

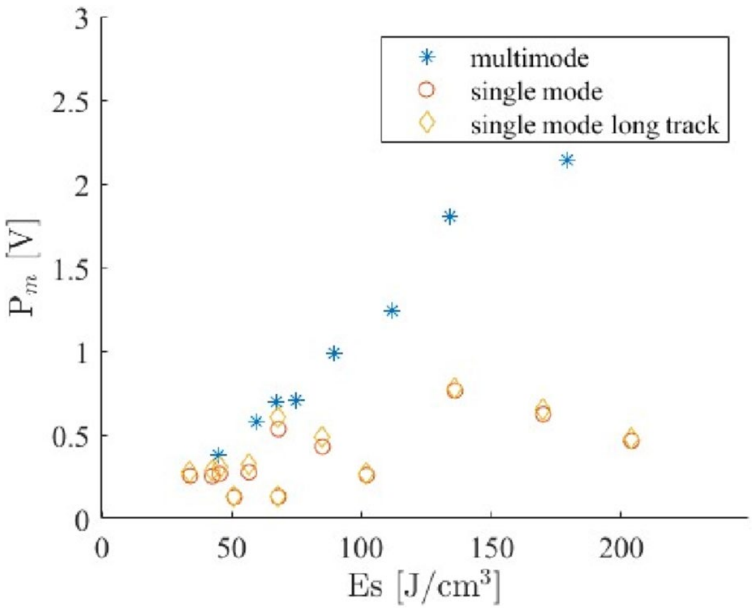

Fig. 13 Plasma values for both single mode and multimode sources

The average plasma signals of the two repetition P_m was calculated for every test and plotted against energy density Es. If a multimode source is exploited, the intensity of plasma radiation recorded grows with power density (E_s). On the other hand, if a single source is exploited, the variation of P_m against Es is not significant.

Unlike copper, aluminum seems to have a back reflection that increases with power: each source is split into three groups (three speeds) of three points each, representing the increase in power. As seen in Fig. 16, B_m on copper remains constant while Es varies. Furthermore, if copper is irradiated first, in the multimode case, B_m has higher values than for a single mode with the same Es. If Aluminum is

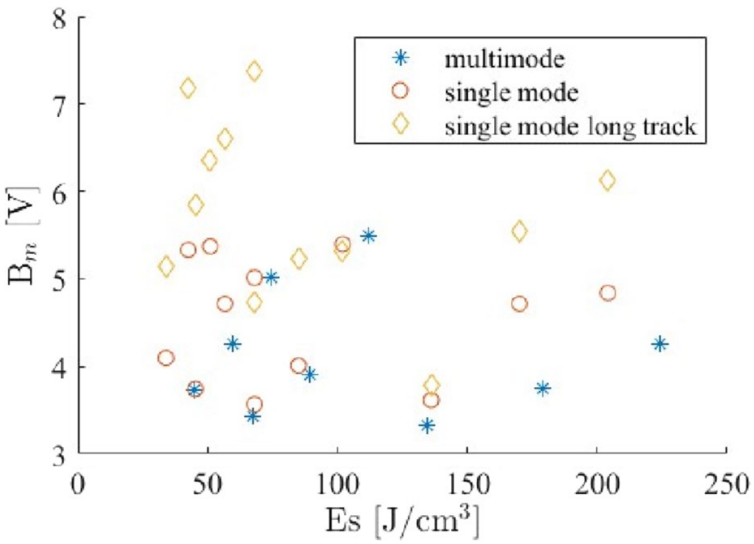

Fig. 14 B_m values plotted against energy density Es for Al-Cu configuration

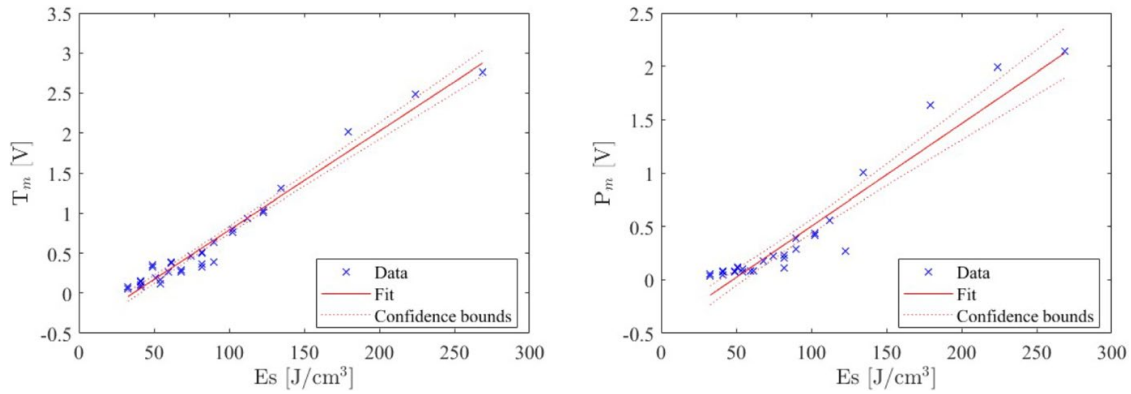

a) b)

Fig. 15 Linear regression for TS and PS Cu-Al with a $R^2 = 97\%$ and $R^2 = 90\%$ respectively

at the top, this claim is untrue: B_m values remain pretty much alike, as Fig. 14 states. The length of the weld track is shown in this graph as yellow diamond dots.

Figures 15 a) and b) show the output of the linear regression returned by Matlab of T_m and P_m.

Both p-values of the variable Es shown in Table 5. are very low.

The R^2 are close to unity, hence the linear model interpolates the data very well.

Figure 16 plots B_m values plotted against Es when copper is irradiated first. It is evident that the Multimode source has a way higher Back reflection than the single mode. It is very clear also that Es is not a very much influent parameter when a single mode source is exploited since the scatter points are at the same level when Es changes.

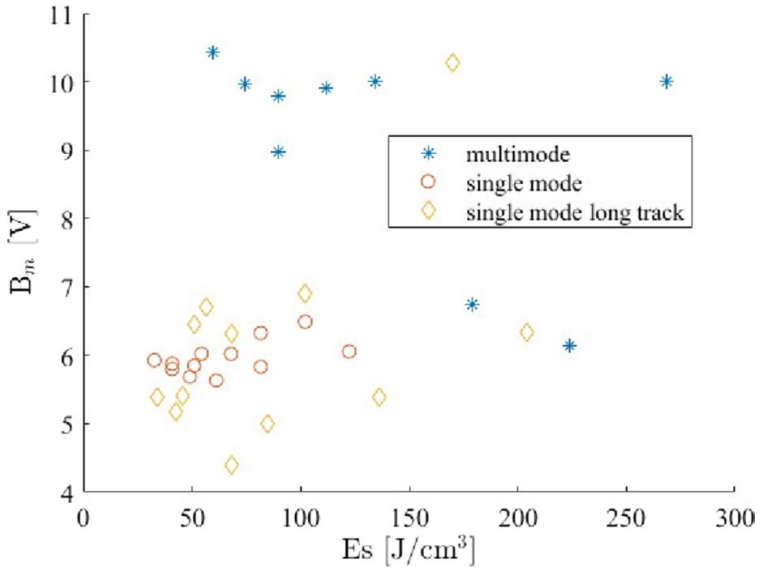

Fig. 16 B_m values plotted against energy density Es for Cu-Al configuration

Table 6. Estimated coefficients for T_m and P_m linear regression

Cu—Al	
Linear regression model	$\mathbf{T_m} = -0.44845 + 0.0123$ Es
R-squared	0.968
p-value	7.84e-25
Cu—Al	
Linear regression model	$\mathbf{P_m} = -0.45964 + 0.0096151$ Es
R-squared	0.894
p-value	1.12e-16

Authors' Contributions **Angeloni Caterina:** Investigation, Data curation, Measurement and writing**. Erica Liverani and Alessandro Ascari:** Conceptualization, Methodology, Supervision, Laser Processing. **Alessandro Fortunato:** Resources. **Luca Tomesani**: Supervision. **Michele Francioso**: Investigation.

Funding Open access funding provided by Alma Mater Studiorum - Università di Bologna within the CRUI-CARE Agreement.

Data Availability The datasets generated during and/or analyzed during the current study are available from the corresponding author on reasonable request.

Declarations

Competing Interests The authors declare no competing interests.

Competing Interest The authors have no relevant financial or non-financial interests to disclose.

References

1. Deal confirms zero-emissions target for new cars and vans in 2035, "https://www.europarl.europa.eu/news/en/press-room/20221024IPR45734/deal-confirms-zero-emissions-target-for-new-cars-and-vans-in-2035," [Online]
2. Ascari, A., Fortunato, A.: Laser dissimilar welding of highly reflective materials for E-Mobility applications. In: Joining Processes for Dissimilar and Advanced Materials. pp. 579–645. Elsevier (2022)
3. Wunderling, C., Bernauer, C., Geiger, C., Goetz, K., Grabmann, S., Hille, L., Hofer, A., Kick, M.K., Kriegler, J., Mayr, L., Schmoeller, M., Stadter, C., Tomcic, L., Weiss, T., Zapata, A., Zaeh, M.F.: Solutions of laser material processing for electric mobility – evaluation of the Technology Readiness Level.
4. Katayama, S.: Fundamentals and Details of Laser Welding. Springer Singapore, Singapore (2020)

5. Kogel-Hollacher, M.: The full potential of photonics in e-mobility: an overview. The Laser User Magazine. (2020)
6. Chianese, G., Franciosa, P., Nolte, J., Ceglarek, D., Patalano, S.: Characterization of Photodiodes for Detection of Variations in Part-to-Part Gap and Weld Penetration Depth During Remote Laser Welding of Copper-to-Steel Battery Tab Connectors. J. Manuf. Sci. Eng. **144**, 071004 (2022). https://doi.org/10.1115/1.4052725
7. Purtonen, T., Kalliosaari, A., Salminen, A.: Monitoring and Adaptive Control of Laser Processes. Phys. Procedia **56**, 1218–1231 (2014). https://doi.org/10.1016/j.phpro.2014.08.038
8. You, D.Y., Gao, X.D., Katayama, S.: Review of laser welding monitoring. Sci. Technol. Weld. Joining **19**, 181–201 (2014). https://doi.org/10.1179/1362171813Y.0000000180
9. Cai, W., Wang, J., Jiang, P., Cao, L., Mi, G., Zhou, Q.: Application of sensing techniques and artificial intelligence-based methods to laser welding real-time monitoring: A critical review of recent literature. J. Manuf. Syst. **57**, 1–18 (2020). https://doi.org/10.1016/j.jmsy.2020.07.021
10. Will, T., Schwarzkopf, K., Hölbling, C., Müller, L., Schmidt, M.: Feature extraction based on scalable hypothesis tests from photodiode data in laser welding processes. Procedia CIRP. **111**, 527–531 (2022). https://doi.org/10.1016/j.procir.2022.08.084
11. Lee, K., Kang, S., Kang, M., Yi, S., Kim, C.: Estimation of Al/Cu laser weld penetration in photodiode signals using deep neural network classification. J. Laser App. **33**, 042009 (2021). https://doi.org/10.2351/7.0000506
12. Blug, A., Carl, D., Höfler, H., Abt, F., Heider, A., Weber, R., Nicolosi, L., Tetzlaff, R.: Closed-loop Control of Laser Power using the Full Penetration Hole Image Feature in Aluminum Welding Processes. Phys. Procedia **12**, 720–729 (2011). https://doi.org/10.1016/j.phpro.2011.03.090
13. Sokolov, M., Franciosa, P., Sun, T., Ceglarek, D., Dimatteo, V., Ascari, A., Fortunato, A., Nagel, F.: Applying optical coherence tomography for weld depth monitoring in remote laser welding of automotive battery tab connectors. J. Laser App. **33**, 012028 (2021). https://doi.org/10.2351/7.0000336
14. Franciosa, P., Sokolov, M., Sinha, S., Sun, T., Ceglarek, D.: Deep learning enhanced digital twin for Closed-Loop In-Process quality improvement. CIRP Ann. **69**, 369–372 (2020). https://doi.org/10.1016/j.cirp.2020.04.110
15. Kim, H., Nam, K., Oh, S., Ki, H.: Deep-learning-based real-time monitoring of full-penetration laser keyhole welding by using the synchronized coaxial observation method. J. Manuf. Process. **68**, 1018–1030 (2021). https://doi.org/10.1016/j.jmapro.2021.06.029
16. Franciosa, P., Sun, T., Ceglarek, D., Gerbino, S., Lanzotti, A.: Multi-wave light technology enabling closed-loop in-process quality control for automotive battery assembly with remote laser welding. In: Negahdaripour, S., Stella, E., Ceglarek, D., and Möller, C. (eds.) Multimodal Sensing: Technologies and Applications. p. 9. SPIE, Munich, Germany (2019)
17. Seibold, M., Friedmann, H., Schricker, K., Bergmann, J.P.: Process control by real-time pulse shaping in laser beam welding of different material combinations. Procedia CIRP. **94**, 769–774 (2020). https://doi.org/10.1016/j.procir.2020.09.137
18. Dimatteo, V., Ascari, A., Fortunato, A.: Continuous laser welding with spatial beam oscillation of dissimilar thin sheet materials (Al-Cu and Cu-Al): Process optimization and characterization. J. Manuf. Process. **44**, 158–165 (2019). https://doi.org/10.1016/j.jmapro.2019.06.002
19. Fortunato, A., Ascari, A.: Laser Welding of Thin Copper and Aluminum Sheets: Feasibility and Challenges in Continuous-Wave Welding of Dissimilar Metals. Lasers Manuf. Mater. Process. **6**, 136–157 (2019). https://doi.org/10.1007/s40516-019-00085-z
20. Precitec: LWM Expert Training Book.
21. Andreev, A.: Smart Laser Welding Heads Provide Excellent Quality: Concerted Functionality enables High Productivity and efficiency. LTJ. **6**, 20–22 (2009). https://doi.org/10.1002/latj.200990068
22. Eriksson, I., Powell, J., Kaplan, A.F.H.: Signal overlap in the monitoring of laser welding. Meas. Sci. Technol. **21**, 105705 (2010). https://doi.org/10.1088/0957-0233/21/10/105705
23. Olsson, R., Eriksson, I., Powell, J., Kaplan, A.F.H.: Advances in pulsed laser weld monitoring by the statistical analysis of reflected light. Opt. Lasers Eng. **49**, 1352–1359 (2011). https://doi.org/10.1016/j.optlaseng.2011.05.010

ASME Journal of Manufacturing Science and Engineering
Online journal at:
https://asmedigitalcollection.asme.org/manufacturingscience

Environmental Impact, Mechanical Properties, and Productivity: Considerations on Filler Wire and Scanning Strategy in Laser Welding

Erica Liverani[1]
Department of Industrial Engineering (DIN),
Alma Mater Studiorum—University of Bologna,
Viale Risorgimento 2,
Bologna 40136, Italy
e-mail: erica.liverani2@unibo.it

Caterina Angeloni
Department of Industrial Engineering (DIN),
Alma Mater Studiorum—University of Bologna,
Viale Risorgimento 2,
Bologna 40136, Italy
e-mail: caterina.angeloni2@unibo.it

Alessandro Ascari
Department of Industrial Engineering (DIN),
Alma Mater Studiorum—University of Bologna,
Viale Risorgimento 2,
Bologna 40136, Italy
e-mail: a.ascari@unibo.it

Alessandro Fortunato
Department of Industrial Engineering (DIN),
Alma Mater Studiorum—University of Bologna,
Viale Risorgimento 2,
Bologna 40136, Italy
e-mail: alessandro.fortunato@unibo.it

Sustainability, as well as high-quality outcomes, pose significant challenges within the context of current manufacturing cycles, in alignment with European strategies aimed at decarbonization. This framework encourages a systematic evaluation of manufacturing processes in terms of their performance and carbon footprint. One sector where this is particularly relevant is the production of batteries for electric mobility, thanks to its exponential growth. Out of all the processes involved, laser welding stands out as being a critical step since it offers potential energy savings through optimization. With the dual goals of achieving mechanical strength and environmental sustainability, this study investigates alternative solutions for laser welding of aluminum sheets. Different laser welding configurations are tested to evaluate the effect of process setups on weld quality and carbon emissions across different productivity scenarios. The key findings can be summarized as follows: (1) the selection of welding setup significantly influences both quality and sustainability requirements; (2) the optimal conditions for meeting strength requirements may diverge from those aimed at minimizing environmental impact; (3) the choice of the final solution is influenced by the specific industrial scenario. The study specifically demonstrated that aluminum alloys can be welded with higher quality (porosity below 1% and equivalent ultimate strength up to 204 MPa) when filler wire is introduced alongside an active wobbling scanning strategy. Conversely, filler wire can be omitted in scenarios prioritizing high-productivity and low-carbon emissions, such as when employing a linear scanning strategy, resulting in a reduction of equivalent carbon emissions by up to 140%.
[DOI: 10.1115/1.4065560]

Keywords: laser welding, filler wire, aluminum welding, beam oscillation, carbon emission, laser processes, sustainable manufacturing

1 Introduction

Nowadays one of the main issues discussed is the environmental impact of global industrialization and the excessive use of fossil fuels, leading to increased greenhouse gas emissions and rising global temperatures. According to the International Energy Agency (IEA), global CO_2 emissions from energy combustion and industrial processes reached a record of 36.8 Gt CO_2 in 2022, a 1.5-fold increase compared to 2000 [1]. The manufacturing sector is responsible for 5% of global CO_2 emissions, where electricity usage accounts for 35% of total energy consumption in 2021 [2]. In order to meet the net-zero emissions target by 2023, 80% of the total investment goes toward expanding the mass manufacturing capacity of renewable technologies such as wind systems and electric vehicle batteries [2]. The installed production capacity for batteries has seen a robust annual increase of 72% [2], however, the energy conversion efficiency needs to be improved, as the production of a single kilowatt-hour (kWh) battery requires an energy input ranging between 40 kWh and 60 kWh. This data highlights the need to intervene at various stages of the lithium-ion battery life cycle in order to mitigate the environmental impact, from battery manufacturing to mineral extraction and shipping. Optimizing the production process to achieve defect-free production is a feasible solution [3]. Goffin et al. [4] stated that parameter selection in welding alone can produce an electrical energy saving of 60%. In this scenario, the paper highlights the importance of improving the energy efficiency of manufacturing processes. Specifically in large-scale automotive industries, fiber laser welding (FLW) plays a crucial role in joining thin components for battery pack parts thanks to its high precision achievable, resulting in minimal bead sizes and, notably, rapid production speeds [5]. In battery pack assembly, aluminum alloys are preferred for their cost-effectiveness

[1]Corresponding author.
Manuscript received December 21, 2023; final manuscript received May 13, 2024; published online June 17, 2024. Assoc. Editor: Vincent Wagner.

and favorable strength-to-weight ratio and advances in hybrid materials and processes, such as combining rolled aluminum with cast alloys, are explored to enhance geometric flexibility and optimize battery pack performance (i.e., optimized cooling for efficiency improving). However, welding parts that use hybrid processes such as die casting and sheet forming pose several challenges. The presence of dissolved gas in the solidified structure of die-cast components facilitated pores formation, while alloys used for sheet forming commonly suffer from hot cracking [6,7]. Thus, FLW still has issues when working with aluminum alloys. Inadequate welding parameters and processes, unreliable welding monitoring, material inhomogeneities, and incorrect alignment or setup all contribute to defects in the manufacturing and assembly of battery packs. As a result, eliminating defects in battery production entirely is challenging, and although their occurrence is believed to be low, the total number of welds required for a battery pack or module multiplies this number [8]. Even though achieving defect-free production in a real-world scenario remains a significant concern, it is crucial to investigate the relationship between bead performance and energy consumption and to ensure a high-quality joint and enhanced sustainability.

2 Background

The issue outlined and introduced in the previous section has been addressed by various authors in recent years. Several methodologies have been employed to analyze different primary goals. Life cycle assessment, an ISO-standardized methodology [9], is commonly used to evaluate the environmental impacts associated with manufacturing processes. This method can be classified as a problem-oriented approach and different aspects of welding have been evaluated, such as the impact of material selection [10], the choice of the welding process [11], and the end-point impact (IMPACT 2002+) [12]. Recently, Xydea et al. [13] proposed a holistic method for comparing different welding techniques, considering three different levels of analysis: process, machine, and system level. Of all the processes examined, the machine level, which accounts for the carbon emissions of auxiliary equipment, was found to be the most carbon-intensive. Similar conclusions are obtained from other authors. Generally, arc welding technologies that utilize a consumable electrode are more efficient and ought to be given preference. Recently, Wei et al. [14] proved that laser welding with a hot wire was more energy efficient. Feng et al. [15] proposed a method to quantify energy in assembly processes by defining energy efficiency and consumption of laser arc-hybrid welding as metrics.

Other authors [16,17] proposed an integrated decision-making model to minimize carbon emissions and processing time during cell-to-cell welding. However, since these methods do not consider the relationships that exist between product quality, feasibility, and carbon emissions, they cannot be applied as decision-making techniques.

A multi-objective approach must be applied to achieve the required quality while using the least amount of energy. In literature, engineering modeling is utilized to link the quality of welds with their environmental impact [18]. This involves employing metamodeling techniques, which are also referred to as machine learning or approximation modeling [19,20]. In order to determine the relationship between energy consumption and bead geometry in fiber laser welding, Wu et al. [21] built a data-driven ensemble metamodel. Next, they used a non-dominated sorting genetic algorithm to determine the ideal process parameters, resulting in the lowest possible total energy consumption and the highest possible depth-to-width ratio of the welding bead. A fitness-sharing genetic algorithm was introduced by Yan et al. [22] to optimize processing parameters for arc welding energy conservation. However, gene expression algorithms frequently experience early convergence, and produce unsatisfactory solutions due to their restricted local search capabilities [23,24]. To accurately depict the environment impact and evaluate process parameters, a methodical study that considers all energy sources and material usage must be built. Huang et al. [25] established a comprehensive parameter decision model and found that the major carbon footprint is associated not with the laser source itself but with the auxiliary equipment and the cooling system. Wu et al.'s study [21] calculated the carbon emissions from three common welding methods: laser welding, arc welding, and laser arc-hybrid welding—as well as their impact on processing performance and environmental sustainability. Tensile test results were evaluated, and factors including bead shape, microhardness, and microstructure in aluminum alloy joints were taken into account.

Additionally, an energy estimation model was developed to quantify the laser energy consumption, factoring in components such as the laser source, robot arm, cooling system, arc welding system, and wire feeder system. The findings show that laser power and processing time are the dominant factors affecting energy consumption.

In this context, this research aims to overcome these challenges to elaborate the multi-characteristic of the laser welding cell and carry out the integrated decision-making of welding parameters and sequences for minimizing the carbon emission and processing time.

Following these results, this paper wants to quantify and compare the carbon emissions of different laser welding setups. Hence, the first part of the paper focuses on the analysis of bead quality in terms of morphology (aspect ratio), porosity, and tensile-shear strength. Four laser system setups are analyzed combining welds with wobbling and filler wire. For each group, optimal parameters were assessed. The second part of the paper wants to make a step forward, applying a parametric model that calculates for each group the environmental impact, in terms of equivalent carbon emissions. The most influential factors on the environmental impacts, such as welding conditions, process parameters, and industrial scenarios are discussed. Finally, a classification of process priority criteria is assessed throughout the quantification of quality (in terms of porosity), sustainability (in terms of $CO_{2,eq}$ emissions), and industrial productivity tradeoff.

Results highlight that welding with filler wire and wobbling motion is the best option for achieving the lowest porosity and maximum mechanical strength, whereas linear welding without wire is the most sustainable solution for reducing carbon footprint. Among these two scenarios, the productivity results as the tradeoff criteria for defining the optimal welding setup.

3 Materials and Methods

3.1 Laser Welding. The proposed activities are carried out with the aim of comparing different laser welding methods for weld bead optimization with different criteria priorities: (i) weld bead quality, (ii) process environmental impact, and (iii) process productivity, and the overall methodology adopted is shown in Fig. 1. The left side of Fig. 1 depicts the energy and material consumption as inputs in the system for the quantification of equivalent carbon emissions. At the top is the welding process evaluated for defining joint quality and energy utilization. The key outcomes of the tradeoff analysis between quality (Sec. 4.1) and sustainability (Sec. 4.2) are presented on the right.

In this context, four laser welding approaches are selected for comparison, including the use of filler wire and the scanning strategy (wobbling or linear). The choice of these welding conditions was based on the literature analysis [7,26] and the available industrial laser systems.[2] For this comparison, a strategic but difficult-to-optimize weld configuration is selected. Two sheets of different aluminum alloys (AA6082 and AlSi10Mg) produced with two different processes (hot-rolling and additive manufacturing) are welded in a lap-joint configuration. Rolled $50 \times 50 \times$

[2] https://www.ipgphotonics.com/en

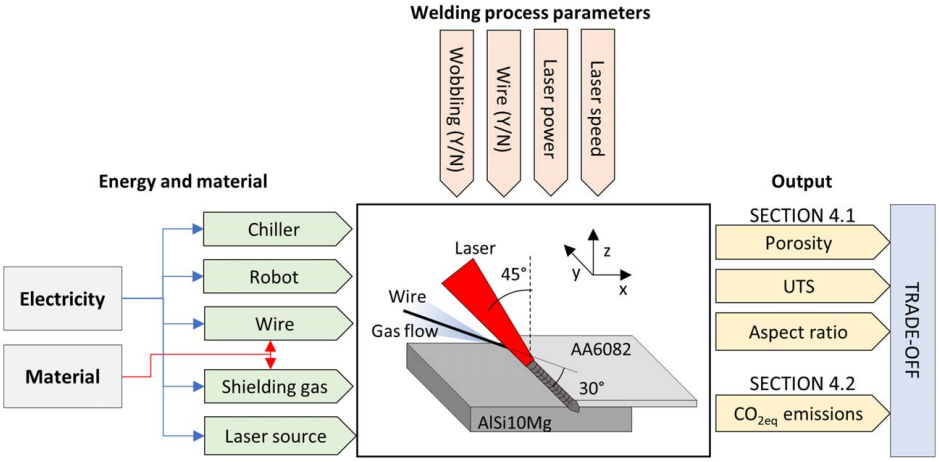

Fig. 1 Methodology adopted for the laser welding process optimization following quality and sustainability criteria

Table 1 Characteristics of laser equipment

Maximum power	6 kW
Beam parameter product (BPP)	4 mm
Collimation focal length	200 mm
Focalization focal length	300 mm
Magnification factor	1.5
Fiber core diameter	100 μm
Spot diameter	150 μm
Maximum wobbling frequency	350 Hz

1.5 mm AA6082 (wt%: Cr ≤ 0.25%, Fe ≤ 0.5%, Mg 0.6–1.2%, Mn 0.4–1%, Si 0.7–1.3%, other elements < 0.2%, Al balance) sheet is placed on top while 50 × 50 × 4 mm AlSi10Mg (wt%: Si 9–11%, Mg 0.25–0.55%, Fe ≤ 0.25%, other elements <0.2%, Al balance) sheet on the bottom (Fig. 1). In all configurations, laser beam moves in the y-direction with a 45 deg inclination with respect to z in x–z plane in order to achieve the welding in the corner. In the setups for which the use of filler material is planned, the wire guiding nozzle is placed ahead of the laser scanner with a 30 deg inclination (with respect to y in y–z plane) and the filler edge is directly below the beam. A Mg-rich AA5356 wire with a diameter of 1.2 mm is chosen for this experimental campaign.

The laser system employed for welding included an IPG YLS-6000 fiber source equipped with D50 two-axis scanning optics (refer to Table 1 for comprehensive specifications). The wire feed system is based on a Fronius KD7000 push–pull system, boasting a maximum feed rate of 10 m/min. The laser head is moved by a Yaskawa-Motoman HP-20 six-axis anthropomorphic robot.

In order to ensure that samples are in the correct position and a zero gap is obtained, a clamping device is designed and placed beneath the scanning optics.

The range of process parameters used comes from the previous experimental campaign [7], considering the combination of process parameters that enable the achievement of Irradiances (ratio between laser power and spot area) higher than 10 MW/cm^2 and energy densities (product of irradiance and interaction time) in the order of 10^4–10^5 J/cm^2 required for welding of thick highly reflective plates. Table 2 provides a summary, with the following parameters varied for optimization: laser motion, laser power, welding speed, and wire speed. A frequency of 200 Hz and an amplitude of 2 mm is employed when the wobbling approach is applied. Each test is performed with a shielding gas mixture consisting of 15% He and 85% Ar at a flowrate of 30 l/min.

3.2 Power Emission Monitoring. Following the conclusion of the welding tests used for the geometric, microstructural, and strength characterization tests, additional tests are conducted to simulate current operating conditions. Real-time current signals from all equipment units are obtained using a current clamp, which is connected to an oscilloscope. The recorded signals in millivolts are then converted into current values by Eq. (1). The current consumption of different components, such as the wire feeder, laser source, robot, laser chiller, laser head chiller, is calculated under both non-operational (standby time) and operational (processing time) conditions.

The laser and robot systems operate as balanced and unbalanced three-phase systems, respectively, while the chillers function on a single-phase system. A PYTHON script is used to convert the voltage data into power and then into carbon equivalent consumption, as described below. A graphical procedure scheme is shown in Fig. 2.

To calculate the effective current value, the voltage signal is converted using the formula

$$I = \frac{\text{voltage signal(mV)}}{S} \tag{1}$$

Table 2 Welding process parameters divided into four categories: welding without filler wire and linear motion (group A), welding with filler wire and linear motion (group B), welding without filler wire and wobbling (group C), and welding with filler wire and wobbling (group D)

Test	Wobbling	Filler wire	Laser power (kW)	Welding speed (mm/s)	Wire speed (m/min)
A (1–18)	N	N	2–3 every 0.2	25; 30; 35	—
B (1–18)	N	Y			1.5; 1.8; 2.1
C (1–18)	Y	N			—
D (1–18)	Y	Y			1.5; 1.8; 2.1

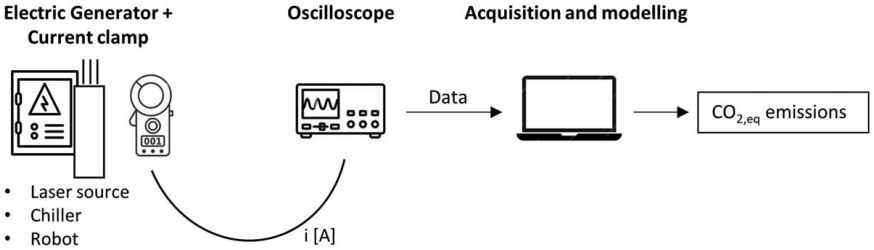

Fig. 2 Signal acquisition and processing method for the evaluation of $CO_{2,eq}$ emissions

where S represents the sensitivity of the amperometry clamp, set as 10 mV/A. The root mean square method is employed to compute the effective current signal in the system [27]

$$I_{\mathrm{RMS}} = \sqrt{\frac{1}{N} * \sum_{i=1}^{N} I_i^2} = I_\phi \tag{2}$$

Here I_i is the current value at each point of the signal, and N is the total number of points in the signal. The total active (real) power in the chiller's *single-phase system* $P_{s,\mathrm{tot}}$ is calculated as follows:

$$P_{s,\mathrm{tot}} = P_\phi = V_\phi * I_\phi * \cos\theta \tag{3}$$

where V_ϕ represents the phase voltage (230 V), I_ϕ is the current of the phase, and θ denotes the phase difference between voltage and current.

In the case of the *three-phase symmetric and balanced* system, characterized by equal line currents ($I_{\phi 1} = I_{\phi 2} = I_{\phi 3} = I_L$), the total active power $P_{t,\mathrm{tot}}$ is the sum of each phase's active power

$$P_{t,\mathrm{tot}} = 3P_\phi = 3V_\phi * I_L * \cos\theta \tag{4}$$

To express $P_{t,\mathrm{tot}}$ in terms of line voltage ($V_L = 400$ V) and line current, the equation is

$$P_{t,\mathrm{tot}} = \sqrt{3} * V_L * I_L * \cos\theta \tag{5}$$

A power factor $\cos\theta$ is close to 1 indicating good energy efficiency in the system. The power factor $\cos(\vartheta)$ can be calculated using real power (RP) (40 kW) and imaginary power (IP) (6 kVAr)

$$\cos(\vartheta) = \frac{\mathrm{RP}}{\sqrt{\mathrm{RP}^2 + \mathrm{IP}^2}} = 0.98 \tag{6}$$

The values of RP and IP were taken from the electric panel while the laser system was working.

In the case of a *three-phase unbalanced system*, where the current values in the three conductors of robot system differed, the following consideration is made:

$$P_{t,\mathrm{tot}} = P_{\phi 1} + P_{\phi 2} + P_{\phi 3} = \sum_{i=1}^{3} V_\phi * I_{\phi i} * \cos\theta \tag{7}$$

where V_ϕ is 230 V (legal standard CEI 8–9) and $I_{\phi i}$ is the current for each phase.

Using Eqs. (3), (5), and (7), the power absorbed by each component is assessed with varying power and speed, as detailed in Table 2.

3.3 Weld Bead Characterization. Following the experimental tests, middle cross sections of the welded samples are prepared by hot mounting samples in resin and polishing the final surface with 800–2500 grit SiC followed by 1–0.05 μm alumina in suspension. Samples for microstructural analysis are then etched with Keller's reagent (1 ml HF, 1.5 ml HCL, 2.5 ml HNO_3, and 95 ml H_2O) for 20 s to prepare them for initial examination. The primary geometric characteristics of the weld bead are assessed using optical microscopy (Nikon Optiphot-100), with the average porosity determined via image processing using IMAGEJ open-access software. Mechanical characterization is performed after contouring the welded samples to achieve a total length of 80 mm, overlap of 10 mm, and width of 25 mm. Room temperature tensile-shear tests are carried out using a hydraulic testing machine (Italsigma S.r.l, Forlì, Italy) with a 20 kN load cell. The strain rate is set to 2.8×10^{-4} s^{-1} and fixed using a constant cross-head separation rate of 1 mm/min.

3.4 Carbon Emission Model. The equivalent carbon emission of laser welding is calculated with the main scope of highlighting the difference due to the adopted welding strategy. Other papers describe the method for carbon emission calculation [21,28] in laser welding, so a summary of this model is here described with the appropriate specifications relating to the welding strategy. The proposed model follows a hierarchical scheme, and at the top position, there is the total equivalent carbon emission ($\mathrm{CE_{eq}}$) calculated by summing the contribution of carbon emission due to direct energy consumption (CE_e) and the material consumption (CE_m) (Eq. (8)).

$$\mathrm{CE_{eq}} = \mathrm{CE}_e + \mathrm{CE}_m \tag{8}$$

3.4.1 Energy Consumption Contribution. Starting from the analysis of CE_e, contributions are considered from all the involved items. In all the laser welding setups mentioned, including the laser source (l), chillers (c), and robot (r), their respective contributions were assessed, along with the energy consumption of the wire feeder when the filler wire is active. Therefore, for tests belonging to groups A and C, CE_e is calculated with Eq. (9), while groups B and D require Eq. (10).

$$\mathrm{CE}_{e(A,C)} = \mathrm{CE}_{e-l} + \mathrm{CE}_{e-c} + \mathrm{CE}_{e-r} \tag{9}$$

$$\mathrm{CE}_{e(B,D)} = \mathrm{CE}_{e-l} + \mathrm{CE}_{e-c} + \mathrm{CE}_{e-r} + \mathrm{CE}_{e-w} \tag{10}$$

The energy contribution of each system is then detailed. Starting from laser beam generation, the required energy differs between the standby state ($\mathrm{CE}^s_{e\text{-}l}$), when the pumping system is active and the laser is ready, but it is not emitting and the welding phase $\mathrm{CE}^p_{e\text{-}l}$. Equation (11) describes as the authors evaluate those two energy states.

$$\mathrm{CE}_{e-l} = \mathrm{CE}^s_{e-l} + \mathrm{CE}^p_{e-l} = \alpha_e(P^s_l \cdot t^s_l + P^p_l \cdot t^p_l) \tag{11}$$

P^s_l and P^p_l are the laser mean active powers calculated, respectively, during the standby and welding state. The power of standby status P^s_l is constant, while the power of processing status P^p_l depends on welding laser power. t^s_l and t^p_l denote the standby duration and processing time, respectively. Consistently with the respective powers, the value of t^s_l was kept constant across all processes (set to 1 min). In contrast, t^p_l is contingent on process parameters, particularly the welding speed, as illustrated in Eq. (12).

$$t^p_l = \frac{WL}{v_l} \tag{12}$$

Table 3 Relevant coefficients of carbon emission

α_e	0.267 $kgCO_{2eq}/kWh$	[29]
α_{gas}	0.611 $kgCO_{2eq}/m^3$	[30]
α_w	15.1 $kgCO_{2eq}/kg$	[31]

Table 4 Welding process parameters selected for tensile-shear tests

Group	Wobbling	Filler wire	Laser power (kW)	Welding speed (mm/s)	Wire speed (m/min)
A	N	N	2	35	—
B	N	Y	2.2	35	2.1
C	Y	N	2	25	—
D	Y	Y	2.2	25	1.5

where WL is the weld length and v_l is the laser scanning speed.

Finally, α_e is the coefficient of carbon emission for electricity consumption and it is reported in Table 3. The analysis of both the laser head chiller and laser source chiller employed an identical methodology.

The chiller serves the crucial function of maintaining the designated components at a prescribed temperature range. During welding, the pump periodically activates, and the chiller remains on standby during non-operational intervals. The duration and the frequency pump activation of the cooling system are dictated by the process chain. By aligning the operational periods of the laser with those of the chillers, a simplified condition is considered. Based on this consideration, the energy consumption of each chiller can be calculated using Eq. (13).

$$CE_{e-c} = \alpha_e(P_c^s \cdot t_l^s + P_c^p \cdot t_l^p) \tag{13}$$

where P_c^s and P_c^p are the chiller mean powers calculated, respectively, during the standby state and welding.

The robot's energy consumption is the final contribution that is present in all laser welding scenarios. According to earlier considerations, the power for this motion system must be measured when it is in the running ($P_r^{p)}$ and standby states ($P_r^{s)}$, with the resulting carbon emission calculated using Eq. (14*a*).

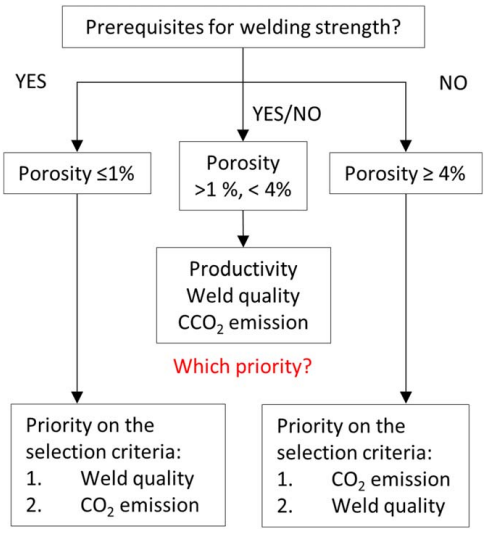

Fig. 3 Priority of the selection criteria as the requirements and industrial scenario change

Table 5 Active powers measured during welding process

Welding power (kW) / Active power	2	2.2	2.4	2.6	2.8	3
P_l^p	7.82	9.06	9.89	10.41	11.30	12.56
P_c^p				2.76		
P_r^p				0.48		
P_w^p				0.28		
P_l^s				1.30		
P_c^s				0.72		
P_r^s				0.48		

$$CE_{e-r} = \alpha_e(P_r^s \cdot t_r^s + P_r^p \cdot t_r^p) \tag{14a}$$

The duration of the robot's standby and moving states is denoted as t_r^s and t_r^p. These durations differ from the laser and chiller ones because, before laser emission, the robot reaches the initial welding position from a safety position, which is different from the previous one. Due to the negligible difference in consumption of the robot between the operating phase and the standby phase, this variance was neglected and Eq. (14*b*) was simplified as follows:

$$CE_{e-r} = \alpha_e \cdot P_r \cdot (t_r^p + t_r^s) \tag{14b}$$

Moreover, for groups B and D, the contribution of wire feeder ($CE_{e\text{-wire}}$) is considered. Due to the low current value request from this equipment, no specific measures are carried out and a maximum value of 6 A is included in the calculations, resulting in a constant power emission (P_w^p in Table 5). The final contribution is formulated as follows:

$$CE_{e-w} = \alpha_e(P_w^p \cdot t_w^p) \tag{15}$$

where t_w^p is equal to t_l^p.

3.4.2 Material Consumption Contribution. The calculation of emissions resulting from material usage (CE_m) takes into account the *wire* for groups B and D as well as shielding gas for all setups.

The application of shielding gas during welding is needed to wipe away the generated plasma, mitigating the oxidation of the weld seam. As a result, this procedure guarantees the achievement of a high-quality weld bead. The gas usage is found to have a minimal contribution to the overall quantity of carbon emissions in accordance with Eq. (16)

$$CE_{m-g} = \alpha_{gas}(Q_{gas} \cdot t_l) \tag{16}$$

where α_{gas} and Q_{gas} are, respectively, the coefficient of carbon emission for shielding gas consumption (see Table 3) and the flow rate. The welding and gas supply times coincide.

Regarding the influence of wire consumption on carbon emission outcomes, the impact can be quantified through Eq. (17)

$$CE_{m-w} = \alpha_w(v_w \cdot t_l^p \cdot \pi \cdot r_w^2 \cdot \rho_w) \tag{17}$$

where α_w is the coefficient of carbon emission associated with wire consumption (refer to Table 3), v_w is the wire feeding rate, t_l^p is the welding time (the feeding wire time is approximately equivalent to the duration of processing status), r_w is the radius of the wire, and ρ_w represents the metal density of the wire. The values of the wire's radius and density are constant and equal to 0.6 mm and 2.64 g/cm^3, respectively.

3.5 Evaluation Criteria and Tradeoff. The tradeoff between welding strength and process carbon emissions during laser welding is assessed using the straightforward graph in Fig. 3. To begin the

analysis, it's crucial to grasp the prerequisites that need to be met. If ensuring mechanical resistance (minimizing defects) is paramount, porosity becomes the primary selection criterion. Consequently, two distinct and opposing scenarios emerge:

(i) Strict prerequisites: This implies high-quality weld beads with porosities less than 1%.
(ii) No prerequisites: Porosity levels higher than 4% are acceptable because there are no strength requirements.

While the first scenario prioritizes welding quality, the second scenario focuses more emphasis on process sustainability.

The specific industrial scenario defines which of these approaches should be prioritized if there are not prerequisites, making the tradeoff between these criteria even more relevant. In this scenario, *industrial productivity* plays the main role. It is measured as the ratio between the standy time ($t_I^s = t^s$) to the production time ($t_I^p = t^p$).

This ratio helps classify industrial scenarios as either highly productive ($t^p >> t^s$) or low productive ($t^s \geq t^p$). In light of the resulting values, a definitive priority selection criterion is established.

4 Results

4.1 Welding Process Optimization. The welding quality is assessed in the four conditions (A, B, C, D) by a first evaluation of the weld bead porosity. A preliminary screening process is conducted by analyzing the graph in Fig. 4. The porosity percentage was categorized into four classes, aligning with the ISO 13919-1 standard: (1) 0–2%, (2) 2.1–4%, (3) 4.1–6%, and (4) >6%. The number of joints belonging to each class (in percentage terms) is used to define the bar's height. For example, group A has 5.6% of specimens tested with less than 2% porosity. It is clear that all samples welded without filler wire and with wobbling motion (group C) show medium or high levels of porosities, with nearly 80% of the samples falling into class 4.

Conversely, joints carried out with filler wire and wobbling motion (group D) demonstrate that 45% of process conditions result in very low porosity (porosity <4%). Finally, groups A and B exhibit a narrow operating window yielding excellent qualities.

However, despite the relevance of these results, other aspects should be contemplated, such as the bead's quality and process speed. Figure 5 illustrates micrographs of the optimal weld beads obtained for each condition. To attain the best possible weld quality with the least amount of pore formation, low energy input, or lower power, must be set.

The application of linear motion, applied in groups A and B, speeds up the welding process and minimizes porosity in the weld. Even more pronounced is the influence of laser motion on

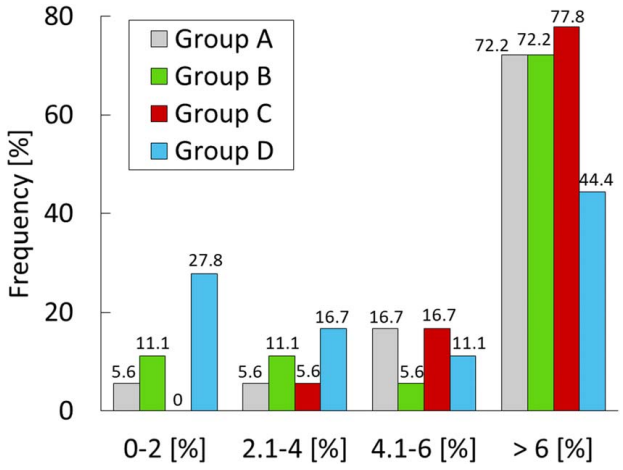

Fig. 4 Frequency of sample identification based on porosity class in the four analyzed process conditions (groups A, B, C, D)

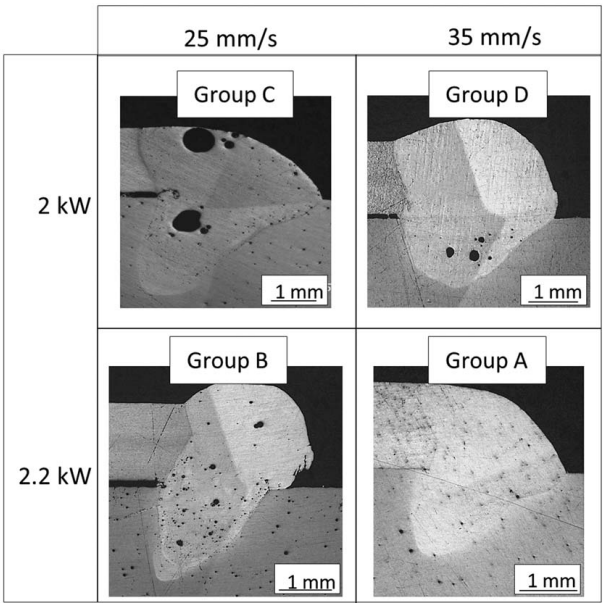

Fig. 5 Lower-class porosity weald beads for each condition: group (A) 2 kW, 35 mm/s; (B) 2.2 kW, 35 mm/s; (C) 2 kW, 25 mm/s; and (D) 2.2 kW, 25 mm/s

weld bead geometry, as wobbling results in a reduced aspect ratio (weld depth/weld width = D/W). Comparing the samples of groups B and D (with wire), the mean aspect ratio is 0.83 (max = 1.09, min = 0.67) with linear motion and 0.45 (max = 0.55, min = 0.34) with wobbling. Direct interaction between the laser beam and sheets (groups A and C) also allows a wider melt pool to be achieved with linear motion. With beam wobbling, the resulting mean weld aspect ratio is 0.57 (max = 0.64, min = 0.48), while linear motion leads to mean value of 0.42.

These findings confirm that wobbling has a great impact on the weld bead's morphology, with this effect being more significant in welding with filler wire. Moreover, the employment of wobbling without filler wire increases turbulence in the melt pool, which raises porosity without providing any advantages that would justify its use. Regarding the relationship between weld bead morphology and process variables, lower welding speeds and higher powers lead to larger widths in all tested conditions. Following the investigation of the weld bead micrographs, tensile-shear tests were performed on samples, one for each group, that had been welded using the most effective process parameters (summarized in Table 4). The aim was to measure the maximum failure load and equivalent ultimate strength allowing these values to be correlated with the process parameters and the process emissions.

Preliminary tests manifest the lowest values of strength for group C, hence those samples were not included in the mechanical characterization process. Tensile-shear test findings agreed well with the weald bead characterization data. With a mean failure load of 5.9 kN and a standard deviation of 0.37, the samples from group D demonstrated the maximum strength. Following in descending order of strength values, group A samples could withstand loads of up to 5.3 kN with a standard deviation of 0.18. Follow the samples of group B, which exhibited a mean failure load of 4.8 kN (standard deviation of 0.14). Similar considerations can be made in relation to the equivalent ultimate strength. Figure 6 presents the equivalent ultimate strength (US) of the same four samples, where it can be seen that similar values are achieved in each case. Group D samples exhibit a higher mean value of US by a factor of 1.07 compared to group B samples, which achieve the lowest mean value.

4.2 Carbon Emission Analysis. The active powers calculated with the method described in Sec. 3.2 are reported in Table 5. Laser

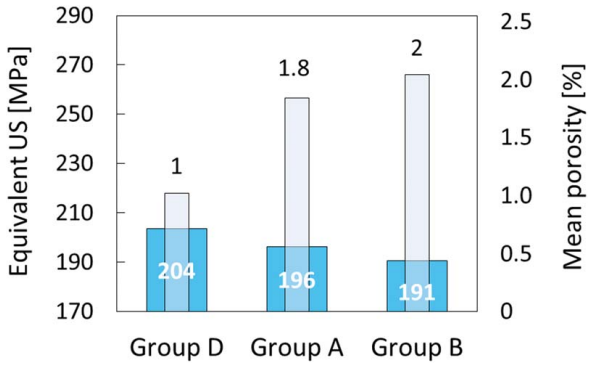

Fig. 6 Results of tensile-shear tests in terms of equivalent ultimate strength

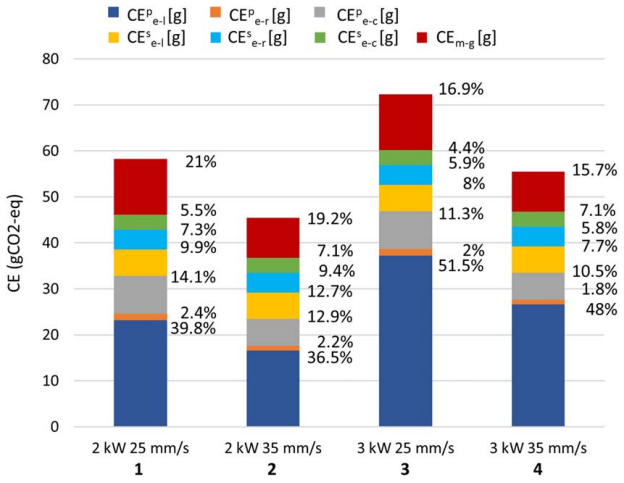

Fig. 7 Equivalent carbon emissions for different process parameters in welding without filler wire

active power, in operative condition, depends on the selected welding laser power, while the other assessed active powers remain constant. It's also important to highlight that the robot's active power always assumes similar fixed value, whether it's in standby or operational mode.

The power consumption of the chiller unit encompasses both the refrigeration of the laser source and the chiller for the laser head. Utilizing active power values, the equivalent carbon emissions were calculated for each equipment across process conditions. These values are influenced by the welding length and laser scanning speed during operational phases and the standby time during equipment idle periods. CO_2 emissions from gas assistance make an exception: they are associated with process duration, laser speed, and weld length (WL) even if they are classified as non-operational. While standby time and WL are dependent on the specific industrial scenario, the laser speed value comes from the optimization process previously stated. In summary, three main factors are considered: (i) welding condition, (ii) process parameters, and (iii) industrial scenario.

4.2.1 Influence of Process Parameters on CE_{eq}. In this subsection, the effect of power and speed was mainly considered, without taking into account the actual optimized parameters which will be the subject of analysis and comparison in Sec. 4.3. Table 6 summarizes the calculated values for welding without filler wire for the overall range of power and speed, considering a unit welding length (1 m) and a unit standby time (1 min). The impact of process parameters on total carbon emissions (CE_{eq}) can be elucidated by referencing the data in Table 6 and examining the corresponding graph in Fig. 7. The effect of power is represented by the comparison of bars 1 and 3 (or 2 and 4), obtained, respectively, using the minimum (2 kW) and the maximum (3 kW) power. Welding power has a direct influence only on the emissions resulting from the use of the laser, both in operational and non-operational conditions. The absolute values of equivalent carbon emissions CE_{eq} remain constant for all other components within the system. However, this leads to a reconfiguration in the relative percentage contributions to the total value. Specifically, as laser power increases, laser consumption becomes predominant, constituting over 50% of the total emissions. Analyzing the impact of laser speed (bars 1 and 2 or 3 and 4), each component displays variability in emission contribution during the welding phase while maintaining a similar weight of each equipment.

From a comprehensive perspective on CE_{eq}, the maximum expected difference between the selected process parameters—thus from delivering the minimum energy (2 kW, 35 mm/s) and the maximum energy (3 kW, 25 mm/s)—amounts to 26.9 g. This

Table 6 Carbon emissions calculations for various parameters in welding without filler wire

P_l (kW)	v_l (mm/s)	$CE^p_{e\text{-}l}$ (g)	$CE^p_{e\text{-}r}$ (g)	$CE^p_{e\text{-}w}$ (g)	$CE^p_{e\text{-}c}$ (g)	$CE^s_{e\text{-}l}$ (g)	$CE^s_{e\text{-}r}$ (g)	$CE_{m.w}$ (g)	$CE^s_{e\text{-}c}$ (g)	$CE_{m.g}$ (g)
2	25	23.20	1.42	8.19	32.81				12.22	57.29
	30	19.33	1.18	6.82	27.34				10.18	50.79
	35	16.57	1.02	5.85	23.44				8.73	45.43
2.2	25	26.88	1.42	8.19	36.49				12.22	61.97
	30	22.40	1.18	6.82	30.41				10.18	53.85
	35	19.20	1.02	5.85	26.06				8.73	48.05
2.4	25	29.34	1.42	8.19	38.95				12.22	64.43
	30	24.45	1.18	6.82	32.46				10.18	55.91
	35	20.96	1.02	5.85	27.82	5.79	4.27	3.20	8.73	49.81
2.6	25	30.88	1.42	8.19	40.50				12.22	65.98
	30	25.74	1.18	6.82	33.75				10.18	57.19
	35	22.06	1.02	5.85	28.93				8.73	50.92
2.8	25	33.52	1.42	8.19	43.14				12.22	68.62
	30	27.94	1.18	6.82	35.95				10.18	59.39
	35	23.95	1.02	5.85	30.81				8.73	52.80
3	25	37.26	1.42	8.19	46.87				12.22	72.35
	30	31.05	1.18	6.82	39.06				10.18	62.51
	35	26.62	1.02	5.85	33.48				8.73	55.47

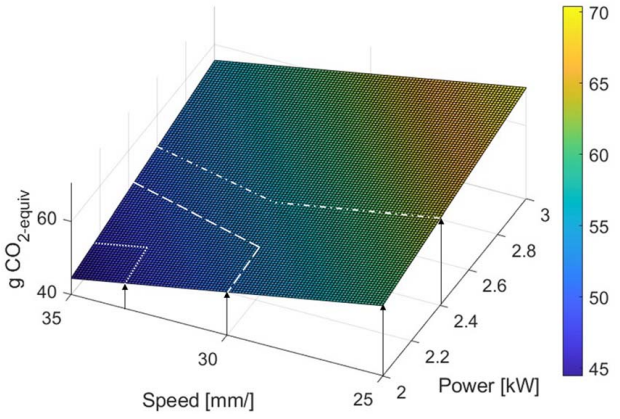

Fig. 8 Influence of laser speed and power when welding without filler wire. Welding speed exerts the most significant influence.

signifies a 59.4% increase from the first set of parameters to the second. The proportions of carbon emissions depicted in Fig. 7 facilitate the identification of the extent of influence of power and speed on the laser generation system (laser source), chillers, robot, and shielding gas. The motion system and chillers in standby status are solely influenced by laser speed (i.e., the welding time), and the associated range of variation is negligible, as mentioned earlier. The robot maintains low emissions even during welding, contributing less than 10%, whereas chiller consumptions become more significant when the pump and compressor are active (operative state).

Notably, the combined carbon emissions from the laser and shielding gas constitute up to 68%. Analyzing the variation in the average CE_{eq} response for input variables at different levels, it can be asserted that welding speed exerts the most substantial impact (refer also to Fig. 8).

Specifically, the difference between the average CE values obtained at 2 kW and 3 kW is 11.9 gCO2eq, while the disparity between the mean CE values calculated at 25 mm/s and 35 mm/s is 14.9 gCO_2eq. Figure 8 shows also the process parameters effect on the specific welding condition. Identifying a working area in which resulting welds are characterized by porosity less than 4% (areas outlined by dotted line for A welds, dashed line for B, and dash-dot line for D), the graph highlights as this area increases from B set to D set. However, considering the higher quality level of each condition the carbon emission increases in the same direction (maximum value for D setup and minimum for A setup). Everything stated so far can also be extended to the case of welding with filler material. Table 7 and Fig. 9 show the calculation performed for these welding conditions.

The considerations previously discussed regarding process parameters remain applicable even in welding with filler material. However, the introduction of wire, which involves significant material consumption, alters the order of importance for energy consumption. In this welding condition, the CE_{eq} is predominantly influenced by the wire, accounting for up to 50%, whereas the energy consumption of beam generation becomes less significant. The value $CE_{m\text{-wire}}$ in gCO_{2eq} is correlated with the welding length, and as a result, it remains constant for all the process conditions in this scenario. Further discussions on this matter will be provided in Sec. 4.2.3.

4.2.2 Influence of Welding Condition on CE_{eq}. This section shows and compares the CE_{eq} values calculated using the optimized process parameters listed in Table 4. Figure 10 shows the carbon emissions for each group's optimum weld. The comparison of bar heights shows how employing filler wire has a negative effect on the process' sustainability, with total CEs rising by as much as 140%.

Specifically, as detailed in Sec.4.1, if filler wire is used, the wobbling motion emerges as the most effective technological choice, exhibiting very low porosity and a smaller aspect ratio. These conditions in group D, however, have the most significant environmental impact. Groups A and C are almost equivalent in terms of carbon emission. Despite the comparable emissions, the low-quality weald beads obtained for group C do not make it a viable alternative.

From Fig. 10, it is also possible to establish an order of influence among the factors involved: filler wire emerges as the most influential variable, followed by laser speed. Laser speed is related to the scanning strategy because optimized welding with wobbling requires lower laser speed and, consequently, longer welding time. Due to the minimal impact of power on equipment other than the laser source and the extremely low variability of these parameters between optimal conditions, laser power is consequently ranked third in terms of influence.

Table 7 Carbon emissions calculations for various parameters in welding with filler wire

P_l (kW)	$v_l - v_f$ (mm/s−m/min)	$CE^p_{e\text{-}l}$ (g)	$CE^p_{e\text{-}r}$ (g)	$CE^p_{e\text{-}w}$ (g)	$CE^p_{e\text{-}c}$ (g)	$CE^s_{e\text{-}l}$ (g)	$CE^s_{e\text{-}r}$ (g)	$CE_{m.w}$ (g)	$CE^s_{e\text{-}c}$ (g)	$CE_{m.g}$ (g)	CE_{eq} (g)
2.0	25–1.5	23.20	1.42	0.82	8.19					12.22	105.22
	30–1.8	19.33	1.19	0.68	6.82					10.18	97.58
	35–2.1	16.57	1.02	0.58	5.85					8.73	92.12
2.2	25–1.5	26.88	1.42	0.82	8.19					12.22	108.90
	30–1.8	22.40	1.19	0.68	6.82					10.18	100.65
	35–2.1	19.20	1.02	0.58	5.85					8.73	94.75
2.4	25–1.5	29.34	1.42	0.82	8.19					12.22	111.36
	30–1.8	24.45	1.19	0.68	6.82					10.18	102.70
	35–2.1	20.96	1.02	0.58	5.85	5.79	4.27	46.11	3.20	8.73	96.51
2.6	25–1.5	30.88	1.42	0.82	8.19					12.22	112.91
	30–1.8	25.74	1.19	0.68	6.82					10.18	103.98
	35–2.1	22.06	1.02	0.58	5.85					8.73	97.61
2.8	25–1.5	33.52	1.42	0.82	8.19					12.22	115.55
	30–1.8	27.94	1.19	0.68	6.82					10.18	106.18
	35–2.1	23.95	1.02	0.58	5.85					8.73	99.50
3.0	25–1.5	37.26	1.42	0.82	8.19					12.22	119.28
	30–1.8	31.05	1.19	0.68	6.82					10.18	109.30
	35–2.1	26.62	1.02	0.58	5.85					8.73	102.17

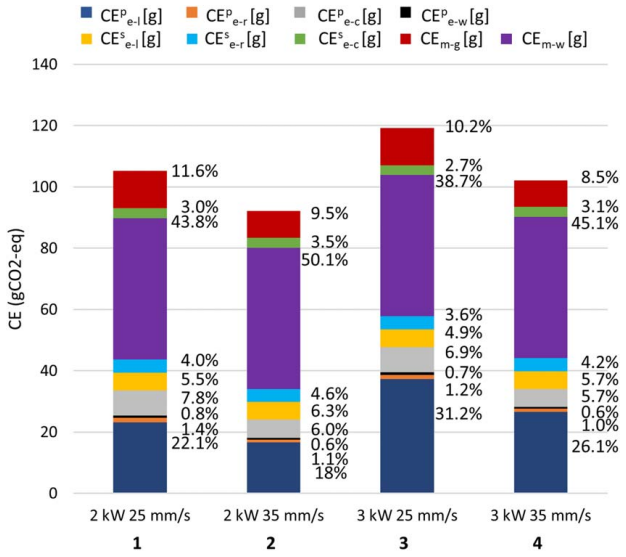

Fig. 9 Equivalent carbon emissions for various process parameters in welding with filler wire

4.2.3 Influence of the Industrial Scenario on CE_{eq}. To further examine the calculated data of CE, some consideration about the effect of specific products and industrial scenarios can be made, without claiming to analyze in detail a specific case study but drawing general considerations. As mentioned before, the laser-material interaction phase (or operational phase) is defined as the duration of laser beam emission for allow sheets welding($t_l^p = t^p$). However, the duration of the whole process consists of two parts: the interaction phase (t_l^p=t^p) and the standby phase (t_l^s=t^s), during which some complementary operations can be performed. For example, this stage encompasses the movement of the components out of the assembly line and the arrival of the new parts to be welded.

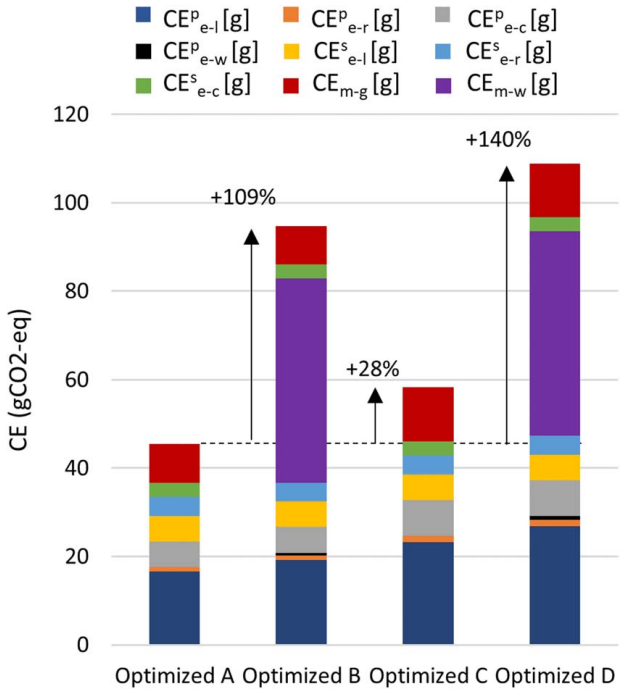

Fig. 10 Influence of factors involved in calculating equivalent carbon emission of the optimized welding conditions. The use of filler wire is ranked first, with an increase of 109% for group B and of 140% for group D, followed by laser speed, which shows a +28% increase in group C.

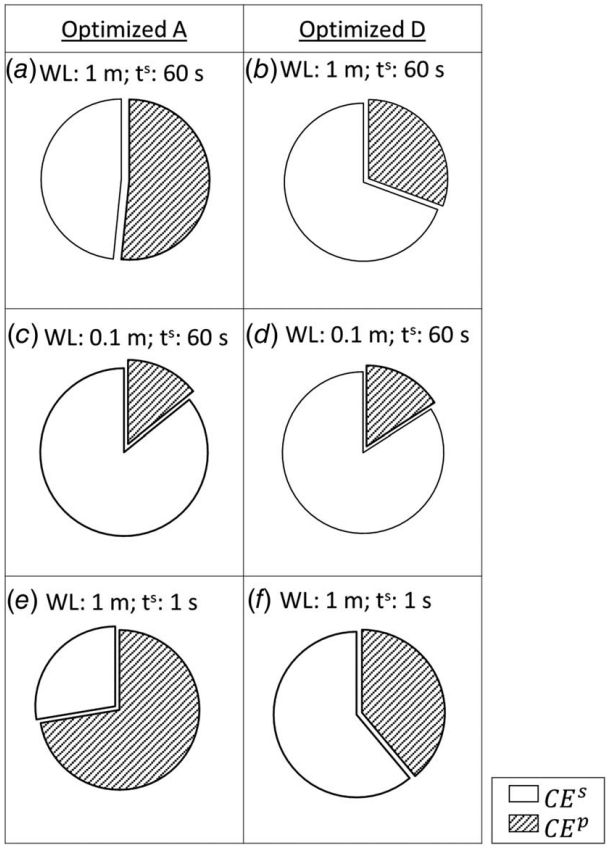

Fig. 11 Contribution of CE in operational and standby phases

The relevance of equipment consumption in these two phases is strictly correlated to the welding length and the standby time and the correlation is highlighted in Fig. 11. Two welding conditions were selected for this comparison: welding performed with the optimized parameters defined for group A (No wobbling, no wire) and group D (wobbling and wire), respectively shown on the left and right sides of Fig. 11. Then the equivalent CE proportion between non-operational (^{s}phase) and operational (^{P}phase) phases was respectively white and marked with black lines for the three combinations of welding length WL and standby time: (i) WL: 1 m, t^s: 1 min (Figs. 11(*a*) and 11(*b*)), (ii) WL: 0.1 m, t^s: 1 min (Figs. 11(*c*) and 11(*d*)), and (iii) WL: 1 m, t^s: 1 s (Figs. 11(*e*) and 11(*f*)).

By reducing the standby time and extending the WL (Figs. 11(*c*)–11(*e*)), resulting in a longer processing time, the percentage of energy consumption and CE attributable to welding increases, thus contributing more significantly to the overall carbon emissions.

In absence of filler wire, the standby time is less relevant on the consumption balance between operational and non-operational phases (comparison between Figs. 11(*b*), 11(*d*), and 11(*f*)). This result explains also the more pronounced effect of the non-operation phase of group D with respect to group A, that is due to the wire. Figure 12 shows the gCO_2eq for welding processes without filler wire at different powers, speeds, and weld lengths. When examining the final values of CE_{eq}, WL on the *x*-axis exhibits the most pronounced influence.

Nevertheless, with an increase in WL, the impacts of power and laser speed also intensify. Indeed, as WL rises, the slopes of the lines defining the CE_{eq} ranges decrease, indicating a more effective control of speed on process consumption.

4.3 Selection Criteria for Welding Setup Definition. Referring to the results presented in the previous paragraphs, it is now possible to define more easily which welding conditions to consider

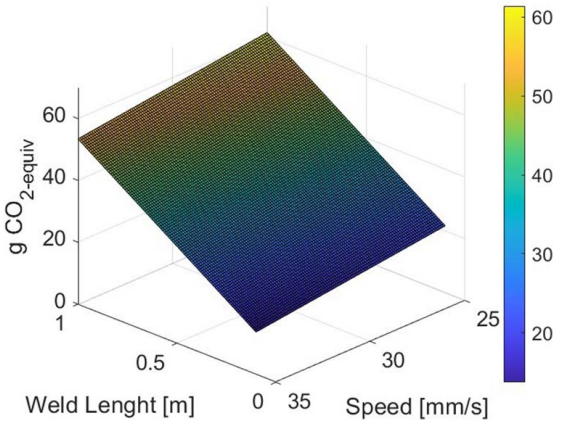

Fig. 12 Influence of laser speed and weld length when welding with filler wire. The weld length is the variable that exerts the most significant influence.

optimal in the various scenarios outlined in Fig. 3. If the prerequisites to the process are stringent, the primary selection criterion is joint quality. In this situation, as highlighted in Sec. 4.1 (particularly through Fig. 4), the optimal welding condition will involve the use of filler material and the wobbling motion strategy (group D). Conversely, if there are no requirements regarding the mechanical strength of the joint, the primary selection criterion, as mentioned earlier, can be related to minimizing CO_2 emissions. Following the results of Sec. 4.2, the choice will then fall on welding without filler material and linear motion (group A).

These two opposing options encompass a wide range of "intermediate" cases, where no clear initial constraint is declared. In this scenario, the industrial context serves as the guiding principle for action. Plant productivity can thus be incorporated among the selection criteria for the welding process. Following the results of Sec. 4.2, the industrial scenario can be characterized by either a low or high-productivity plant, depending on the ratio value between the processing time t^p and standby time t^s.

By analyzing the results obtained when all three criteria are included (Fig. 13), namely (i) productivity, (ii) weld quality, and (iii) CO_2 emissions, it becomes evident how productivity can serve as an excellent tradeoff criterion.

Figure 13(*a*) displays a CO_2 emissions/porosity graph obtained by calculating the emissions produced by welds from groups A and D in a plant with a process-to-standby time ratio of 55% (WL = 1 m, $t^s = 60$ s). Figures 13(*b*) and 13(*c*) present the same data calculated for t^p/t^s ratios of 6% (WL = 0.1 m, $t^s = 60$ s) and 0.5% (WL = 0.01 m, $t^s = 60$ s), respectively. By looking at data, it is evident that a decrease in productivity (lower t^p/t^s ratios) leads to the convergence of the two $CO_{2,eq}$ curves for A and D weld groups. The emission gap (ratio between $CO_{2,eq}$ of groups A and D) between these two welding modes decreases from higher t^p/t^s ratios (Fig. 13(*a*)) to lower t^p/t^s ratios (Fig. 13(*c*)). Assuming that $CO_{2,eq}$ gap emission variation is set below 10%, the two curves, hence the two processes, can be considered comparable due to the simplifications of the model applied. Hence, a t^p/t^s ratio of 2% can be identified as a fair tradeoff value. The framework presented in Fig. 3 can thus be completed and redefined based on the results obtained, as illustrated in Fig. 14.

5 Discussion

One of the main issues currently facing laser welding of dissimilar aluminum alloys is the definition of a sustainable industry-ready process capable of assuring high-quality joints with good productivity. In light of this challenge, the presented work aims to assess the feasibility of laser technology for joining thin sheets in a dissimilar configuration, specifically involving commercial 082-T6 sheet and stress-relieved AlSI10Mg sheets. The primary objective was to establish the correlation between bead quality and energy consumption, with the goal of identifying the optimal welding setup that simultaneously optimizes these two crucial aspects. The effects of filler wire, laser motion, and welding parameters were studied in terms of both mechanical properties and equivalent carbon emission consumption. The paper reports the optimal process parameters that guarantee a weld bead with porosity less than 4% for all the configurations tested, except for the case of linear laser motion without filler wire. This specific configuration proved unsuitable and was consequently excluded from our final considerations. Concerning weld bead quality, the employment of filler wire brings low aspect-ratio weld beads, particularly when wobbling is activated. Wobbling induces larger widths because of its stirring effect on the melt pool, resulting in an overall reduction in penetration depth. A similar effect was observed in joints performed without filler wire, but the stirring effect of wobbling is less pronounced. In terms of welding parameters and their impact on weld quality, increasing the welding speed and/or lowering laser power reduces both the size and quantity of pores. With this general trend established, the tested process conditions showed that joints with porosity below 4% can be achieved, and optimized parameters facilitate a reduction in porosity to below 2%. Notably, the two contrasting conditions—"wire with wobbling" (group D) and "direct and linear" (group A)—exhibit a broader process operating window for Class B joints, as illustrated in Fig. 4. Samples from group D are characterized by a high resistivity. Tensile-shear tests resulted in the highest failure load (5.9 kN ± 0.37) and equivalent US (204 MPa ± 9.8). Second for the highest failure load value are the welds in group A with 5.3 kN, exhibiting a failure load of 196 MPa. Slightly lower mechanical strength was registered for optimized group B samples, with a failure load and ultimate strength of 4.8 kN and 191 MPa, respectively. Group A configuration proves to be very interesting from a sustainable process perspective. The carbon emissions for the mentioned welding setups

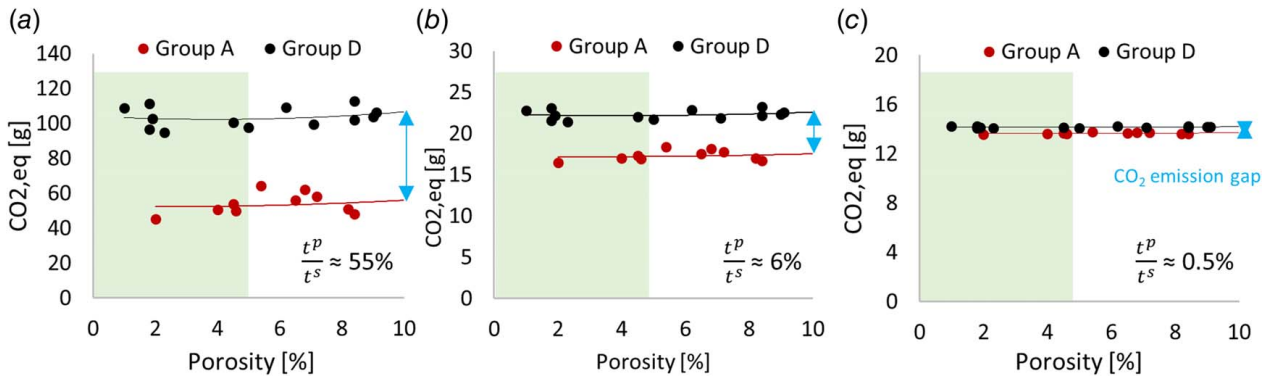

Fig. 13 Analysis of the tradeoff in the choice of welding condition

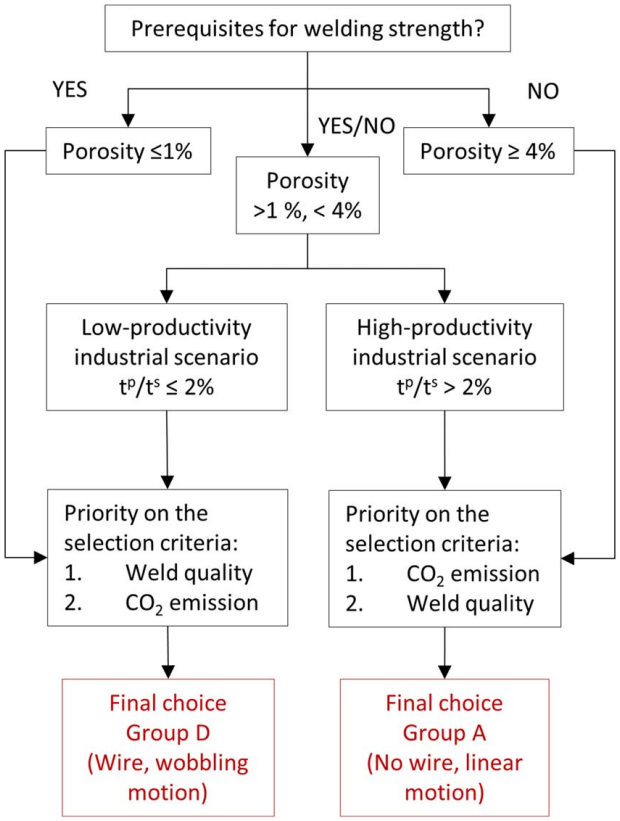

Fig. 14 Final definition of priority in the selection criteria

were computed utilizing the data from Tables 6 and 7, employing the approach and assumptions outlined earlier, and have undergone cross-verification. Taking into account the optimal process parameters for each group, the measured and estimated total carbon emissions per unit of welding length are as follows: 45.4 gCO_2eq/m for group A, 94.8 gCO_2eq/m for group B, and 108.9 gCO2eq/m for group D. The absence of filler material, coupled with the lowest power (2 kW) and the highest speed (35 mm/s) that optimized this welding condition, contributes to a low CE_{eq} consumption for group A. The CE_{eq} difference between optimized groups A and D is 140%. This disparity is mainly attributed to emissions related to wire material production (66.7%) estimated by α_w coefficient (Table 3). It is followed by the impact of scanning speed which ranges from 25 mm/s to 35 mm/s (20.6%) and finally by a decrease in laser power from 2.2 kW to 2 kW (~ 6%). In this scenario, Fig. 9 compares the estimated carbon emissions of each subsystem. The primary contributor of carbon emissions is electricity consumption, with a significant impact from the laser beam generation system, followed by energy consumption in the cooling system. The motion systems, both related to laser motion and wire feeder, make a minimal contribution due to the relatively light load on the robot arm, and the low energy requirements for the wire feeder system. Other emission costs are related to the material consumption, both in terms of compressed gas and filler wire. Groups B and D make use of filler material, which represents one of the most cost-effective factors in terms of emissions. The other non-operative addendums become significant when the integrated industrial scenario is characterized by low productivity and fast processing of components (i.e., shorter welding length). Hence, reducing the standby time of the system also improves the carbon emission performance.

Productivity assumes a significant role when maximum quality or maximum sustainability requirements are no longer sufficient to identify a preferable welding condition. Section 4.3 has indeed highlighted that the relationship between process time and standby time (or non-operational time) allows for identifying industrial scenarios where the choice of the best welding process varies. More specifically, in scenarios where high productivity is in demand, the combination of linear movement and no filler wire makes welding condition a preferable option, allowing a faster process and large CO_2 emission savings.

On the other hand, the impact of CO_2 emissions decreases as the weight of processing time drops in the ratio of process time to standby time. This leads to the choice toward a setup (group D) that ensures better quality without significant environmental impact disadvantages.

6 Conclusion

This study investigates laser welding of dissimilar aluminum alloy sheets using linear scanning and laser beam wobbling, both with and without filler wire. Different process parameters are tested for various configurations, with the main aim of identifying the optimal welding configuration that achieves the required strength, minimal defects, suitable morphology, and low equivalent carbon emissions.

Defects, such as porosity <2%, are minimized with filler wire, employing both linear and wobbled scanning strategies, as well as without wire and linear motion. The optimal process parameters were identified for each of these scenarios; however, when considering the strength and environmental sustainability criteria, the opposite "wire and wobbling" and "no wire and linear" scenarios are the most interesting. Specifically, laser power and welding speed required for high-quality welding were 2200 W and 25 mm/s in the "wire and wobbling" configuration and 2000 W and 35 mm/s in the "no wire and linear" configuration, highlighting the beneficial effect of linear motion on productivity. On the other hand, porosity determined the highest joint strength when welded in a "wire and wobbling" configuration. The emission analysis results indicate that the use of filler wire leads to a significant increase in carbon emissions, with a more significant effect than that due to direct power consumption. The welding speed is the process parameter that has the biggest impact, which is the dominant factor that influences the carbon efficiency of the laser welding system because the gradient of welding speed is greater than that of laser power. The faster the welding speed is, the higher the carbon efficiency the laser welding system will reach. In conclusion, laser welding with filler wire and wobbling motion enables joining in a broad process window, achieving the highest mechanical properties; however, linear welding may also be a preferable option for achieving high productivity and low environmental impact.

Conflict of Interest

There are no conflicts of interest.

Data Availability Statement

The datasets generated and supporting the findings of this article are obtainable from the corresponding author upon reasonable request.

Nomenclature

r_w = wire radius
v_l = laser scanning speed
v_w = wire feeding rate
Q_{gas} = gas flowrate
$t_l^s = t^s$ = standby duration of laser and chiller systems
$t_l^p = t^p$ = processing time of laser and chiller systems (equal to the welding time)
t_r^s = standby duration of robot
t_r^p = standby duration of laser and chiller systems

t_w^p = wire feeder processing time (equivalent to t_f^p)
P_c^s = chiller mean power during standby state
P_c^p = chiller mean power during welding
P_w^p = power emission during wire feed motion
$P_r^s = P_r^p = P_r$ = robot mean power
WL = weld length
CE_{eq} = total equivalent carbon emission
CE_e = total carbon emissions due to electricity consumption
CE_m = total carbon emissions due to material consumption
$CE_{e\text{-}l}$ = carbon emissions due to electricity consumption of laser
$CE_{e\text{-}c}$ = carbon emissions due to electricity consumption of chiller
$CE_{e\text{-}r}$ = carbon emissions due to electricity consumption of the robot
$CE_{e\text{-}l}^s$ = carbon emissions due to electricity consumption of laser in standby state
$CE_{e\text{-}l}^p$ = carbon emissions due to electricity consumption of laser during welding
CE_{eq} = total equivalent carbon emission
CE_e = total carbon emissions due to electricity consumption
CE_m = total carbon emissions due to material consumption
$CE_{m\text{-}g}$ = carbon emissions due to gas consumption
$CE_{m\text{-}w}$ = carbon emissions due to wire consumption
α_e = coefficient of carbon emission for energy consumption
α_g = coefficient of carbon emission for gas consumption
α_w = coefficient of carbon emission for wire consumption
ρ_w = wire density

References

[1] IEA, n.d., "Global CO_2 Emissions From Energy Combustion and Industrial Processes, 1900–2022," IEA, Paris. https://www.iea.org/data-and-statistics/charts/global-co2-emissions-from-energy-combustion-and-industrial-processes-1900-2022.
[2] IEA, 2023, "World Energy Outlook 2023." https://iea.blob.core.windows.net/assets/66b8f989-971c-4a8d-82b0-4735834de594/WorldEnergyOutlook2023.pdf.
[3] Chen, Q., Lai, X., Gu, H., Tang, X., Gao, F., Han, X., and Zheng, Y., 2022, "Investigating Carbon Footprint and Carbon Reduction Potential Using a Cradle-to-Cradle LCA Approach on Lithium-Ion Batteries for Electric Vehicles in China," J. Clean. Prod., **369**, p. 133342.
[4] Goffin, N., Jones, L. C. R., Tyrer, J., Ouyang, J., Mativenga, P., and Woolley, E., 2021, "Mathematical Modelling for Energy Efficiency Improvement in Laser Welding," J. Clean. Prod., **322**, p. 129012.
[5] Capello, E., 2008, "Le lavorazioni industriali mediante laser di potenza."
[6] Cao, X., Jahazi, M., Immarigeon, J. P., and Wallace, W., 2006, "A Review of Laser Welding Techniques for Magnesium Alloys," J. Mater. Process. Technol., **171**(2), pp. 188–204.
[7] Liverani, E., Ascari, A., and Fortunato, A., 2023, "The Role of Filler Wire and Scanning Strategy in Laser Welding of Difficult-to-Weld Aluminum Alloys," Int. J. Adv. Manuf. Technol., **128**(1–2), pp. 763–777.
[8] Saariluoma, H., Piiroinen, A., Unt, A., Hakanen, J., Rautava, T., and Salminen, A., 2020, "Overview of Optical Digital Measuring Challenges and Technologies in Laser Welded Components in EV Battery Module Design and Manufacturing," Batteries, **6**(3), p. 47.
[9] ISO, 2006, "14044:2006-Environmental Management – Life Cycle Assessment – Requirements and Guidelines."
[10] Yilbas, B. S., Shaukat, M. M., Afzal, A. A., and Ashraf, F., 2020, "Life Cycle Analysis for Laser Welding of Alloys," Opt. Laser Technol., **126**, p. 106064.
[11] Sproesser, G., Chang, Y. J., Pittner, A., Finkbeiner, M., and Rethmeier, M., 2015, "Life Cycle Assessment of Welding Technologies for Thick Metal Plate Welds," J. Clean. Prod., **108**, pp. 46–53.
[12] Sangwan, K. S., Herrmann, C., Egede, P., Bhakar, V., and Singer, J., 2016, "Life Cycle Assessment of Arc Welding and Gas Welding Processes," Proc. CIRP, **48**, pp. 62–67.
[13] Xydea, E., Panagiotopoulou, V. C., and Stavropoulos, P., 2024, "A Strategy Framework for Identifying Carbon Intensive Elements in Welding Processes," Proc. CIRP, **121**, pp. 103–108.
[14] Wei, H., Zhang, Y., Tan, L., and Zhong, Z., 2015, "Energy Efficiency Evaluation of Hot-Wire Laser Welding Based on Process Characteristic and Power Consumption," J. Clean. Prod., **87**, pp. 255–262.
[15] Feng, S., Senthilkumaran, K., Brown, C., and Kulvatunyou, B., 2014, "Energy Metrics for Product Assembly Equipment and Processes," J. Clean. Prod., **65**, pp. 142–151.
[16] Ge, W., Li, H., Cao, H., Li, C., Wen, X., Zhang, C., and Mativenga, P., 2023, "Welding Parameters and Sequences Integrated Decision-Making Considering Carbon Emission and Processing Time for Multi-characteristic Laser Welding Cell," J. Manuf. Syst., **70**, pp. 1–17.
[17] Ge, W., Cao, H., Li, H., Zhang, C., Li, C., and Wen, X., 2022, "Multi-Feature Driven Carbon Emission Time Series Coupling Model for Laser Welding System," J. Manuf. Syst., **65**, pp. 767–784.
[18] Wu, J., Zhang, C., Giam, A., Chia, H. Y., Cao, H., Ge, W., and Yan, W., 2024, "Physics-Assisted Transfer Learning Metamodels to Predict Bead Geometry and Carbon Emission in Laser Butt Welding," Appl. Energy, **359**, p. 122682.
[19] Chen, C., Liu, Y., Kumar, M., Qin, J., and Ren, Y., 2019, "Energy Consumption Modelling Using Deep Learning Embedded Semi-Supervised Learning," Comput. Ind. Eng., **135**, pp. 757–765.
[20] Li, J., Cao, L., Hu, J., Sheng, M., Zhou, Q., and Jin, P., 2022, "A Prediction Approach of SLM Based on the Ensemble of Metamodels Considering Material Efficiency, Energy Consumption, and Tensile Strength," J. Intell. Manuf., **33**(3), pp. 687–702.
[21] Wu, J., Zhang, C., Lian, K., Cao, H., and Li, C., 2022, "Carbon Emission Modeling and Mechanical Properties of Laser, Arc and Laser–Arc Hybrid Welded Aluminum Alloy Joints," J. Clean. Prod., **378**, p. 134437.
[22] Yan, W., Zhang, H., Jiang, Z., and Hon, K. K. B., 2017, "Multi-Objective Optimization of Arc Welding Parameters: The Trade-Offs Between Energy and Thermal Efficiency," J. Clean. Prod., **140**, pp. 1842–1849.
[23] Peng, S., Li, T., Zhao, J., Lv, S., Tan, G. Z., Dong, M., and Zhang, H., 2019, "Towards Energy and Material Efficient Laser Cladding Process: Modeling and Optimization Using a Hybrid TS-GEP Algorithm and the NSGA-II," J. Clean. Prod., **227**, pp. 58–69.
[24] Zhang, C., Zhou, Z., Tian, G., Xie, Y., Lin, W., and Huang, Z., 2018, "Energy Consumption Modeling and Prediction of the Milling Process: A Multistage Perspective," Proc. Inst. Mech. Eng. B, **232**(11), pp. 1973–1985.
[25] Huang, Z., Cao, H., Zeng, D., Ge, W., and Duan, C., 2021, "A Carbon Efficiency Approach for Laser Welding Environmental Performance Assessment and the Process Parameters Decision-Making," Int. J. Adv. Manuf. Technol., **114**(7–8), pp. 2433–2446.
[26] Sun, T., Franciosa, P., Sokolov, M., and Ceglarek, D., 2020, "Challenges and Opportunities in Laser Welding of 6xxx High Strength Aluminium Extrusions in Automotive Battery Tray Construction," Proc. CIRP, **94**, pp. 565–570.
[27] Daintith, J., 2009, *A Dictionary of Physics*, 6th ed., Oxford University Press, Oxford, UK.
[28] Wang, G. G., and Shan, S., 2007, "Review of Metamodeling Techniques in Support of Engineering Design Optimization," ASME J. Mech. Des., **129**(4), pp. 370–380.
[29] Bastos, J., Lo Vullo, E., Muntean, M., Duerr, M., Kona, A., and Bertoldi, P., 2020, "GHG Emission Factors for Electricity Consumption," European Commission, Joint Research Centre (JRC) [Dataset] PID. http://data.europa.eu/89h/919df040-0252-4e4e-ad82-c054896e1641
[30] Janjua, R., and Maciel, F., 2023, CO2 Data Collection, Review 2022. World Steel Association, https://worldsteel.org/climate-action/climate-action-data-collection/.
[31] International Aluminium Institute (IAI), 2023, "Greenhouse Gas Emissions Intensity-Primary Aluminium, Reference Period: 2022." https://international-aluminium.org/statistics/greenhouse-gas-emissions-intensity-primary-aluminium